Analysis and Modelling of the Impact of Plasma RF Harmonics in Semiconductor Plasma Processing

A Thesis

Submitted to
Dublin City University

For the degree of
Doctor of Philosophy (Ph D)

By
Md. Nasim Ahmed Dewan, *B.Sc. Eng., M.Sc. Eng.*

School of Electronic Engineering
Dublin City University

Research Supervisor

Dr. Patrick J. McNally, *BE, ScM, PhD, CPhys, MInstP, CEng, MIEI, MIEEE*

July 2001

DECLARATION

I hereby certify that this material, which I now submit for assessment on the programme of study leading to the award of Ph D is entirely my own work and has not been taken from the work of others save and to the extent that such work has been cited and acknowledged within the text of my work

Signed _____   ID No   96971339

Md Nasim Ahmed Dewan

Date   3 July 2001

ACKNOWLEDGEMENTS

DEDICATION

To

my beloved parents

CONTENTS

(

Analysis and Modelling of the Impact of Plasma RF Harmonics in Semiconductor Plasma Processing

Md Nasim Ahmed Dewan, *B Sc Eng , M Sc Eng*

ABSTRACT

Reactive ion etching (RIE) has been used extensively in the last few decades in the microelectronics industry for integrated circuit fabrication However, the monitoring and control of this process is quite challenging because the plasma process is complex and not fully understood The use of a newly developed Plasma Impedance Monitor (PIM) to monitor the RIE process is reported The sensitivity and the usefulness of the PIM to detect the end point of a RIE are tested in a SF_6 plasma in a capacitively coupled planar reactor with silicon (Si) and silicon dioxide (SiO_2) samples The measurement of harmonic components of the current-voltage (I-V) characteristics are tested as parameters to monitor the RIE processes and detect the end point when a SiO_2 layer on a Si substrate undergoes SF_6 RIE The parameter used for the end point detection is empirically modelled as a polynomial equation of the input factors (i e , RF source power, chamber pressure and gas flow rate) using the *Box-Behnken* experimental design The end point can be predicted from the modelled equation of the parameter used for the end point detection

An analytical solution for a *non-symmetric*, capacitively coupled plasma driven by a *non-sinusoidal* radio frequency (RF) current is obtained under the assumptions of time-independent, collisionless ion motion, inertialess electrons and uniform current density Modelling is developed considering that the RF current can be expressed as a summation of the Fourier components whose frequency is exactly an integer multiple of the fundamental frequency The different plasma parameters obtained from the present model are compared with those of an established model developed by Lieberman [M A Lieberman, *IEEE Trans Plasma Sci ,* vol 16, p 638, 1988] The present model always found the even harmonic components of RF voltage and hence the overall RF impedance, whereas the Lieberman model found no even harmonic component of RF voltage The sheath resistance and capacitance could always be estimated using the present model, whereas the Lieberman model fails to relate either of these parameters while considering the harmonic frequencies

The overall RF impedance and RF voltage obtained from the present model are verified with experimental values The relative magnitudes of RF voltage and impedance harmonics determined by the present model are shown to follow qualitatively the values measured in the experiment The values of the normalized RF voltage and impedance harmonics assume lower values both for calculated and measured quantities as the asymmetry of the plasma chamber decreases

CHAPTER 1

INTRODUTION

1 1 Introduction

The ever-shrinking dimensions of microelectronic devices have mandated the use of plasma processing in integrated circuit (IC) factories worldwide Today revenues in the plasma-processing industry have grown to over \$3 billion p a , well in excess of predictions made only a few years ago [1] Besides the use of plasmas in etching and depositing thin films, other processes include the removal of photoresist remnants after development (descumming), stripping developed photoresist after pattern transfer (ashing), and passivating defects in polycrystalline material [2] Plasma based surface processes are also critical for the aerospace, automotive, steel, biomedical and toxic waste management industries Materials and surface structures can be fabricated that are not attainable by any other commercial method, and the surface properties of materials can be modified in unique ways

Very few laboratory plasmas behave initially in the manner predicted by their designer The large number of degrees of freedom in a plasma makes it virtually impossible to take into account all the essential parameters in the theory or design of the experiment There is a degree of opportunism in many plasma experiments Sometimes a theoretical analysis or a plausible physical argument serves as the basis for design of a plasma experiment The experiment may behave as predicted, but generally it will not This discrepancy between the predicted and actual outcome of experiments has been one of the prime movers in plasma research Frequently the outcome of the actual experiment suggests new theoretical models, or more importantly, results in the discovery of new phenomena, which can then be analyzed

Capacitively coupled radio-frequency (RF) plasmas play an important role in a number of material processing applications in the microelectronics industry [3] Typical discharge parameters are pressure $p \approx 10\text{-}300$ mTorr, RF frequency $f \approx 13\ 56$ MHz, and

RF voltage $V_{RF} \approx 50\text{-}500$ V Almost all the applied voltage is dropped across capacitive RF sheaths at the discharge electrodes Accurate modelling is necessary to predict the behaviour of the discharge and to control the overall plasma processes In order to develop adequate models for these discharges, it is important to determine the dynamics and current-voltage characteristics of the plasma

The growth in use of plasma processes has led to the need for real-time, *in situ* techniques to monitor processing and to detect processing end points These techniques are needed to increase tool use and process uniformity instead of depending on off-line wafer inspections

Current-Voltage (I-V) characteristic measurement is a very good tool to monitor the plasma process without perturbing the plasma process which can be easily done by a newly developed monitoring system, called Plasma Impedance Monitoring (PIM) The PIM utilized in this study can read different I-V parameters (RF voltage, RF current, discharged power, plasma impedance and the phase) directly up to the fifth harmonic quantity with great accuracy The I-V parameters maintain almost fixed values if the environment in the plasma chamber remain unchanged The environment includes the RF power, the pressure in the chamber, gas flow rate and the material being processed in the chamber These parameters change significantly if the processing material in the chamber is changed even when all the other conditions remain identical As a result the I-V parameters can be used for observing a Reactive Ion Etch (RIE) end point when the interface between two materials is reached

To detect the end point of a process it is necessary to predict the value of the monitoring parameter used as the end point detector The monitoring parameters can be modelled as polynomial equations of input factors i e , RF power, chamber pressure and gas flow rate The *Box-Behnken* [4] experimental design methodology is a good method for a 3 factors, 3 level design Using this method the parameters can be modelled for the fixed range of values of the input factors It is possible to predict the value of a monitoring parameter with good precision from the modelled equations if the values of the input factors are known The modelled equations are valid only within the specified range of input factors considered for the model This will be outlined in Chapter 4

If one can predict the value of the monitoring parameters used to detect the end point of a process it should be possible to control the system automatically

1 2 Review of Plasma Modelling

Efforts on correlating the electric characteristics of parallel-plate discharges with an equivalent circuit model were made as early as 1954 [5] Plasma sheaths were investigated in connection with RF plasma probes Butler and Kino [6] introduced a model including the capacitive nature of the sheath, Gould [7] considered the motion of the sheath and its capacitance in an equivalent circuit model For low-pressure RF sputtering discharges, Koenig and Maissel [8] developed an equivalent circuit model defining dark spaces with a sheath capacitance, and Keller and Pennebaker [9] developed a theory relating measurable electric properties to the plasma and sheath characteristics of this class of discharge Klynko et al and Roth et al [10-11] carried out electrical characterization of processing plasmas Keller and Pennebaker also pointed out in their work that these discharges could not be sustained by secondary electrons liberated from the target, but were maintained instead by ionization in the glow or by "surf riding" of the electrons on the oscillating edge of the sheath This latter mechanism had already been suggested and investigated in detail by Godyak [12] Metze, Ernie, and Oskam [13] recently developed a very detailed time-dependent model of the sheath region which, however, is valid only for the frequency range where ions still can follow the electric field Again using an equivalent electrical circuit, the relation between operating parameters, electrical characteristics, and the resulting etching characteristics were treated by Zarowin [14,15], among others Van Roosmalen, van der Hoek, and Kalter [16] used equivalent circuits to model their large area oxygen discharge and compared it to physically measurable quantities, such as the discharge impedance and optical dark space thickness They considered several energy deposition mechanisms, including oscillating sheaths, and found that none could account for the much larger measured input power The difference between the frequency range below the ion transit frequency and the range above it has been investigated by Flamm and Donnelly [17,18] as part of their extensive research on etching (electronegative) plasmas In their research they did not include the capacitive effect of electrode sheaths Thompson and Sawin [19,20] have also investigated electronegative discharges and derived plasma characteristics from equivalent electrical circuits For the case of an SF_6

discharge they also assumed the voltage drops across the sheaths were negligible. A simple equivalent circuit with a capacitance representing the electrode sheaths was presented by Bletzinger and Flemming [21] which were derived from measurements of current and voltage waveforms as a function of operating frequency, gas pressure, and input power.

Various authors have developed analytical models to account for the electron and ion dynamics within the sheaths [22-29]. However, the non-linear ion and electron dynamics are not treated self-consistently within these models. Lieberman developed an analytical, self-consistent solution for the collisionless RF sheath considering a single sinusoidal RF current source [30]. This model was based on a symmetrically driven, parallel plate RF discharge (equal-area plates). The effect of asymmetrical sizes of the two plates was not considered in the Lieberman model. Smirnov and Orlov [31] developed another self-consistent model of low-pressure capacitive discharge. The effects associated with stochastic heating of electrons and the non-local nature of the electrical field were taken into account in this model.

1.3 Research Objectives and Summary

Although plasma processes are widely used in industry, the general understanding of these processes is poor and process control is difficult. The ability to etch fine lines, and the control of anisotropy, etching rate, uniformity, selectivity and end point detection are obtained by experimental trial and error. Plasma chemistry is very complicated and many of the surface processes are not clearly understood. Moreover, investigations often are unable to define the basic parameters which are important in a given plasma process.

In reality most reactors used for plasma processing are asymmetrical [32], where the powered electrode area is smaller than the grounded electrode area. Again, due to the complex behaviour of the plasma sheaths, the input RF source current always contains some harmonics [33-38] which contribute significantly to each of the plasma parameters. To date little work has been carried out on the analysis of the behaviour of the sheath beyond the fundamental frequency of the source current. In this work we have developed an analytical solution for a collisionless RF plasma considering a non-

symmetric capacitive discharge and all harmonics of the RF current We obtained expressions for the time-averaged ion and electron densities, electric field and electric potential within the sheath, nonlinear oscillation motion of the electron sheath boundary, nonlinear oscillating sheath voltage and the effective sheath impedance Finally, we have included the impedance of the bulk plasma to determine the overall impedance between the two plates Assuming equal plate areas it is also possible to obtain solutions for the symmetrical discharge from this model For the calculation of different parameters a comparison is made with the Lieberman model [30]

A self biased capacitively coupled planar plasma reactor was run in Reactive Ion Etching (RIE) mode with unequal plate areas The harmonics (up to the 5th harmonic, where fundamental frequency = 13 56 MHz) of RF I-V parameters (current, voltage, impedance etc) were measured using a Plasma Impedance Monitor This experiment was repeated for different powered electrode areas while the grounded electrode area remained unchanged The results obtained from the experiments are compared with the modelled parameters

Current-Voltage (I-V) characteristics (i e plasma voltage, plasma current, plasma impedance and the phase difference between plasma voltage and current) are examined in this work for use as end point detectors when RIE is performed, in order to completely etch a layer of material situated on a dissimilar material The different harmonic components of the I-V parameters, together with a number of derived process parameters, were tested to find out the best end point detector The Plasma Impedance Monitoring technologies were used to measure these parameters up to the 5th harmonic component of the fundamental frequency (13 56 MHz)

Before the above experiment we also tested the sensitivity of the PIM to the size of the sample being processed in the plasma chamber For this purpose the RIE was carried out for Si samples of different sizes in a SF_6 plasma

To predict the RIE end point values of I-V parameters, we empirically modelled the I-V parameters in terms of RF power, chamber pressure and the gas flow rate The Box-Behnken (3 factors, 3 level design) experimental design methodology was chosen for this modelling The prediction errors were also calculated in this work

Finally, we suggest a simple semi-automated computer-based system to be used for controlling the plasma etch The computer sends and receives signals via the system circuitry to turn on and off the plasma operation

1 4 Organisation of This Thesis

This thesis is organised into six chapters and one appendix

♦ The review of plasma modelling, the research objectives and the summary of this thesis have been described in this introductory chapter

♦ Since the plasma process is a complicated system, it is considered appropriate to provide some fundamental concepts of a plasma, plasma systems and plasma processes in Chapter 2

♦ In Chapter 3 the usefulness of the PIM to monitor the plasma processes is investigated The plasma current-voltage harmonics are analysed to ascertain the best monitoring parameter to be used as an end point detector when SiO_2 on a Si substrate undergoes SF_6 RIE

♦ In Chapter 4 the monitoring parameters used for the end point detection are empirically modelled as polynomial equations of the operating input factors (i e , RF source power, chamber pressure and the gas flow rate) The predicted values of the monitoring parameters obtained from the modelled equations are compared with the actual values while SiO_2 on a Si substrate undergoes SF_6 RIE and the end point is reached

♦ In Chapter 5 an analytical model for the plasma is obtained based on an asymmetrically driven, parallel plate RF discharge driven by a non-sinusoidal RF current Different sheath parameters obtained from the model are compared with the Lieberman model The current-voltage characteristics of the plasma are calculated using this model and verified with the experimental results

♦ Chapter 6 presents the conclusions of this work and offers suggestions for further research

♦ Appendix A presents a simple semi-automated computer based operation of RIE

FUNDAMEMTAL CONCEPT OF PLASMAS

2 1 Introduction

In this chapter a brief description on some fundamental concepts of plasma, plasma systems, plasma processes and plasma diagnostic techniques are presented

2 2 Plasma the Fourth State of Matter

At a non-zero absolute temperature any gas has a certain number of ionized atoms, that is, some charged particles— electrons and ions— are present along with the neutrals However, the charged particles substantially affect the properties of the gas only at concentrations at which the space charge formed by them restricts their motion As the concentration increases, this restriction becomes more and more stringent, and at sufficiently high concentrations the interaction of positively and negatively charged particles results in persistent macroscopic neutrality in volumes commensurate with that of the gas Then any disturbances of macroscopic neutrality induce strong electric fields, which quickly restore it An ionized gas at such concentrations is called a *plasma* This term was first proposed by Tonks and Langmuir [39] in 1929

Thus, at sufficiently high charged particle concentrations, an ionized gas turns into a plasma The most natural method for obtaining a plasma is to heat the gas to temperatures at which the average energy of the particles is comparable with the ionization energy of the atoms or molecules At temperatures much below the ionization energy the ratio between the concentration of ions and neutral atoms is small It increases with temperature, and when the average particle energy approaches the ionization energy, the gas almost completely turns into an ionized plasma

Because a plasma can be obtained by heating a substance in the gaseous state (the third state of aggregation), it is sometimes called *the fourth state of matter* The state of

an equilibrium plasma, as well as that of any gas, depends on its composition, component concentration, and temperature Let us denote the partial concentration of the plasma components by n_α, where the subscript α stands for a (neutral particles), i (ions), or e (electrons), as the case may be Generally speaking, a plasma may contain more than one species of atoms and ions Unless otherwise specified, we refer here to the so-called *simple plasma*, which consists of neutral particles of one species, single-charged ions of the same species, and electrons [40] Then the *degree of ionization* η can be defined as the ratio of the ion concentration to the total concentration of ions and neutral atoms

$$\eta = \frac{n_i}{n_i + n_a} \tag{2 1}$$

The plasma temperature T is expressed in energy units, it is related to the generally used expression for the temperature

$$T = kT_K \tag{2 2}$$

where T_K is the Kelvin temperature and k is the Boltzmann constant The relationship between the average energy of thermal motion of particles W and the plasma temperature is given, as for any equilibrium gas, by the following equality

$$W = \frac{3}{2}T \tag{2 3}$$

In an equilibrium plasma the prescribed concentrations and temperature completely characterize its state The temperature of such a plasma determines not only the average energy, but also the particle velocity distribution (Maxwellian distribution) From the plasma concentration and temperature one can find the degree of ionization, the concentration of ions, excited atoms, photons, and so on However, a plasma cannot always be considered to be at equilibrium In particular, a gas-discharge plasma, which is usually obtained in the laboratory, greatly deviates from equilibrium One occasionally comes across so-called partial equilibrium, at which the velocity distribution of charged and neutral particles is Maxwellian, but the temperatures determining this distribution for the electrons and heavy particles are different For such a non-isothermal plasma one can introduce the electron and ion temperatures T_e, and T_i In the general case of a non-equilibrium plasma, the velocity distribution of charged particles may be essentially non-Maxwellian But here, too, we speak of the temperature of the plasma components, defining it as the measure of the average energy of random motion of particles in accordance with eqn 2 3 Naturally, to obtain complete

9

information on the behaviour of a non-equilibrium plasma it is not sufficient to know the average energies (temperature) of the components, it is also necessary to know the particle velocity distribution function

2 3 Brief Survey of Plasmas

Although plasmas are not common terrestrially, they do represent the most ubiquitous form of matter in the universe Because electrons play such an important role in plasmas, it is useful to categorize plasmas by electron densities and electron energies In a number of cases, the electrons have a Maxwellian distribution [41], which can be described in terms of the electron energy ε as,

$$f(\varepsilon) = 2(\varepsilon/\pi)^{\frac{1}{2}} (kT_K)^{-\frac{3}{2}} \exp\left(-\frac{\varepsilon}{kT_K}\right) \tag{2 4}$$

where $f(\varepsilon)$, the electron energy distribution function, is proportional to the number of electrons having an energy between ε and $\varepsilon + d\varepsilon$, k is Boltzmann's constant, and T_K is the electron temperature The electron kinetic energy is given by

$$\varepsilon = (1/2)mv^2 \tag{2 5}$$

where m is the electron mass and v is the magnitude of the electron velocity The constants in eqn (2 4) are such that if we integrate over all energies, we get

$$\int f(\varepsilon)d\varepsilon = 1 \tag{2 6}$$

The average energy can be obtained by the integral

$$\int \varepsilon f(\varepsilon)d\varepsilon = \frac{3}{2}kT_K \tag{2 7}$$

Thus, the electron temperature T_K for a Maxwellian electron energy distribution is a measure of the average energy of the electrons

The Maxwellian distribution is also called the *equilibrium* distribution, because it represents a case where the electrons are in thermodynamic equilibrium In a number of cases, especially weakly ionized plasmas, $f(\varepsilon)$ will not be Maxwellian, however, it is quite common to still speak of an electron temperature T_K when referring to the average electron energy [42]

A convenient unit for electron temperature is the electron volt (eV) which is equivalent to a temperature of approximately 11600 K In Fig 2 1, typical values of electron densities and temperatures are shown for a variety of plasmas They range from the very rarefied and cold interstellar plasmas up to the dense and hot plasmas used for controlled fusion The plasmas of interest here are the process plasmas, which have electron densities in the range of 10^9 to 10^{12} cm^{3}, and average electron energies between 1 and 10 eV The degree of ionization for these plasmas varies from about 10^{6} to as high as 0 3 At the lower end of the density, energy, and ionization scale are the discharges that are formed between planar electrodes, while the upper end of this scale applies to discharges sustained at a frequency that corresponds to some natural frequency for the plasma (such as electron cyclotron resonance plasmas)

2 4 Plasma Parameters in Engineering

Various kinds of gas discharges find wide application in technology and experimental investigations These are primarily stationary or pulsed electrode discharges— so called glow discharges with cold electrodes, which occur at relatively low currents, and arc discharges characterized by high currents and strong electrode heating This type of discharge has been used for a long time in radio engineering, current commutation, and machining Relatively recently it found use in the pumping of gas lasers Gas discharge plasma sources—plasmatrons- have lately acquired extensive application in many chemical engineering ventures, primarily for triggering high temperature chemical reactions (in so called plasma chemistry) Along with the traditional electrode discharges, use is made of a plasma induced by high frequency fields under the effect of laser radiation (laser discharges) Table 2 1 presents the typical parameters of some kinds of gas discharge plasmas

Plasmas are used in many experiments Investigations on plasma confinement by means of a magnetic field and on its heating have been conducted in recent years in connection with nuclear fusion They embrace a wide range of conditions corresponding to different schemes, from quasi-stationary to single action pulsed ones Extensive plasma investigations are also being carried out in connection with magneto-hydrodynamic and thermionic energy conversion, the development of plasma jet engines, and spacecraft propulsion through the atmosphere
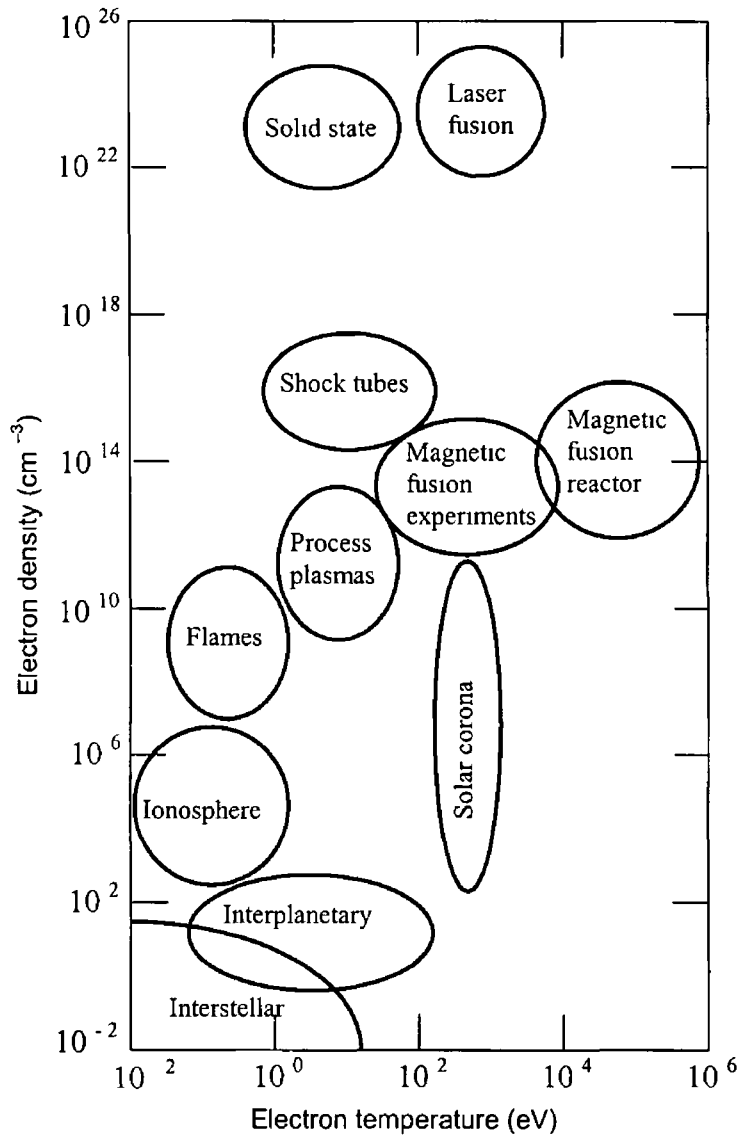
Figure 2 1 *Electron density and temperature ranges for a variety of natural and man-made plasmas The region labelled "Process plasmas" delineates the parameter ranges for the plasmas used for thin film deposition and etching [42]*

2 5 Plasma Processing in Microelectronics

A cross section of one cell of a CMOS circuit is shown schematically in Fig 2 2 This is just one of the many complex microelectronic structures now being fabricated It provides a good example of the different process steps used in the microelectronics industry We will concentrate here on these steps which directly involve the use of plasmas Although ion implantation is a very important step, it utilizes plasmas only

Table 2 1 *Parameters of gas-discharge plasma (from [40])*

Type of discharge	p (mm Hg)	I (A)	P (W/cm^3)	n_e (cm^{-3})	T_e (eV)	T_a (eV)	λ_e (cm)
Low pressure discharge	10^{-2}	1	10	10^{11}	$3-7$	3×10^{-2}	1
Glow discharge	1	10^{-2}	10^{-1}	10^{10}	1-3	3×10^{-2}	10^{-2}
Arc discharge	1	10	$10 - 10^2$	10^{13}	$0\,5-2$	10^{-1}	10^{-2}
Ultrahigh frequency discharge	10	--	10	10^{12}	$1-3$	5×10^{-2}	10^{-3}
High pressure discharge	10^3	1	10^2	10^{15}	$0\,5-1$	$0\,5$	10^{-4}
Super high pressure discharge	10^5	1	$10^3 - 10^4$	10^{17}	$0\,5-1$	$0\,5-1$	10^{-6}
Stationary laser plasma	10^3	--	10^4	10^{17}	$1-3$	$1-3$	10^{-4}

Note - 1 The table lists tentative characteristics of discharges in some typical regime They may vary appreciably depending on the regime and gas filling The parameter values are given with an accuracy to one order of magnitude

2 In the table p is the gas pressure, I is the discharge current, P is the power introduced into a unit volume of the plasma, T_e is the electron temperature, T_a is the gas temperature, and λ_e is the electron mean free path

indirectly The ions for implantation are generated by a plasma in the source However, they are extracted from this plasma, analyzed and accelerated through a high vacuum region to the substrate to be implanted While the efficient extraction of high ion current densities is an important topic in the design of implanters, since it affects wafer capacity, there is no direct effect of the plasma on wafer processes Therefore, ion implantation will not be discussed here

There are two aspects of plasmas which are important in processes physical and chemical Any plasma contains positive and negative charges in equal number densities Because electrons have a much higher mobility, any surface in contact with the plasma will develop a negative potential with respect to the plasma The resulting electric field reduces the electron current density to the surface until it equals the ion current density and the electrical neutrality of the plasma is thus maintained The electric field accelerates the ions to the surface, they arrive with an energy up to a maximum value of eV_f, where $-V_f$ is the floating potential of the surface relative to the plasma In DC discharge plasmas, V_f is normally a few Volts, and the effect of these low energy Ar^+ ions, for example, may be insignificant However, the ion energy can easily be increased by applying a potential $-V_b$ (relative to ground) to the surface, the ion energy
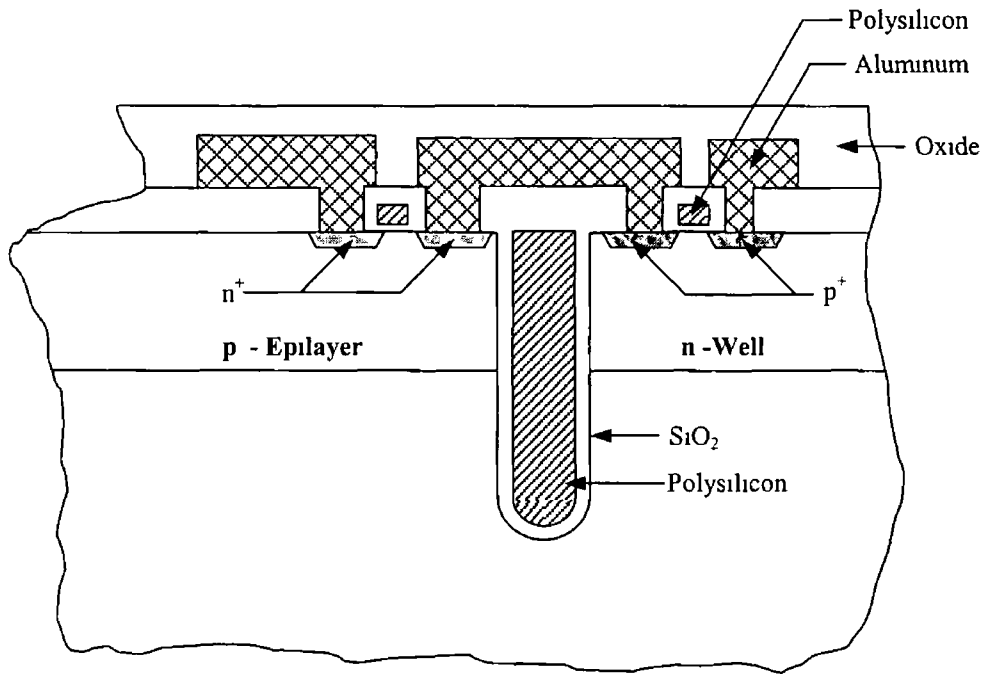
Figure 2 2 Schematic cross section of a basic cell of a CMOS circuit with a nominal transistor gate width of 1 μm [42]

is then $e(V_b + V_f)$ and this may have a significant effect on the surface For example, sputtering will take place when this energy exceeds about 20 eV In RF discharges, floating surfaces may develop even higher negative potentials, so that sputtering may occur even without deliberately supplying a bias to the sample The actual potential depends on the geometry of the system and the frequency of the supply voltage In most plasma systems, the electric field becomes normal to the substrate and ions therefore reach the sample at normal incidence Thus, some parts of a surface may be affected much less, or remain unaffected, by ions because of the substrate geometry An example is shown in Fig 2 3(a), no physical sputtering can occur in the region which is essentially masked by the mask overhang

The chemical effect of plasmas results from the chemical activity of species which can be generated by mechanisms within the plasma, such as ionization by electron collision with molecules For example, N_2^+ ions are very easily produced in the plasma When N_2^+ impinges on a substrate, it may dissociate into N atoms, which are very reactive While molecular N_2 is a very stable molecule which is unlikely to react with any substrate material, the addition of the same gas to a discharge produces highly

reactive N atoms For example, refractory materials such as AlN and TiN are readily formed when N_2^+ ions impinge on Al or Ti surfaces whereas N_2 does not react with Al even at elevated temperatures and even then only incompletely with Ti More complex gases, such as CF_4 , may be introduced into a plasma, producing different molecular ions (CF_3^+, CF_2^+ and CF^+) each of which will have different reactivities In addition to ions, uncharged radicals may be generated which are extremely reactive e g atomic oxygen in an O_2 plasma or CF_x in a CF_4 plasma These radicals reach surfaces isotropically from any direction and cause reactions there For example, In Fig 2 3(b) the sidewall of the mask is eroded by reaction with a radical, the result being a gaseous species

(a)

(b)
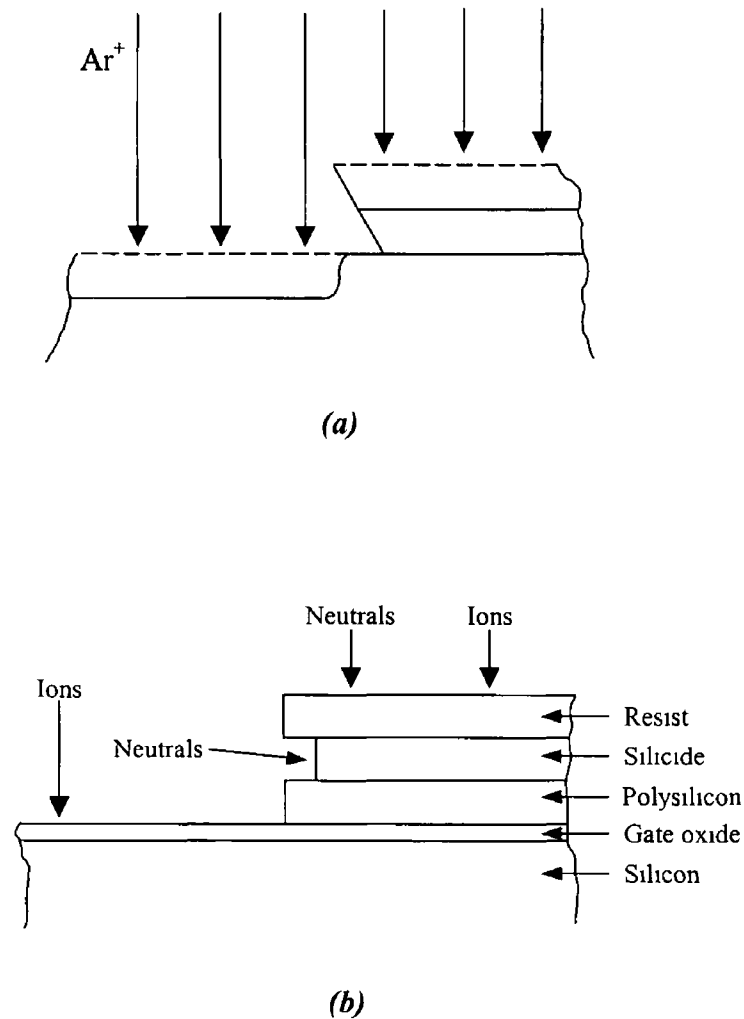
Figure 2.3 (a) Physical effects caused by the plasma The substrate is sputtered by energetic (>20eV) ions, except in the region protected by the mask overhang because the ions are at normal incidence on the substrate (b) Removal of material from under the mask due to chemical reaction with a neutral radical generated in the plasma Since they are uncharged, they can reach all surfaces

Care must be taken to ensure that no unexpected reactions take place For example, water vapour is the most common constituent of the background gas in most vacuum systems after pumpdown It is adsorbed on the chamber walls, when a system is open, or on the surfaces introduced into the system (e g substrates and holders) the water vapour then desorbs from the surface in the vacuum system, the desorption rate may be increased by substrate heating or by ion bombardment from the plasma Water vapour is then dissociated within the plasma into O, OH and H fragments Both O and OH are very reactive with many metals to form oxides the remaining hydrogen is not efficiently pumped in many vacuum systems, and is easily incorporated in many film materials

In most plasma situations, both the physical and chemical effects may be important and should be considered carefully Thus, combined effects of the situations shown in Fig 2 3 can occur The relative importance of the physical and chemical effects will, of course, depend on the circumstances of each case the reactivities, the substrate potential, and the ion species in the plasma are the important parameters However, these depend in turn on the plasma volume, gas flows, excitation volume, etc

With these two effects of plasmas m mind, we may consider their application in microelectronics processing Here we briefly review the various process steps required in fabricating the device in Fig 2 2 and the plasma requirements

2 5 1 Cleaning

Successful fabrication of complex ICs requires many lithography steps in which each mask is accurately aligned with the previous patterns on the wafer A sequence of a number of individual masks may be required to complete the process For each stage, the wafer is covered with a layer of photoresist which is exposed using the mask and the resulting pattern developed, producing areas which are free from photoresist This pattern is used in the next process step For example, the remaining resist may prevent etching of a SiO_2 layer from the Si wafer in these areas After etching, the photoresist is removed, leaving the SiO_2 layer in selected areas, as required for the next process step Alternatively, the mask may be used to selectively deposit films in unmasked areas when the photoresist is removed, the excess metal is removed

Following the etching or deposition step the photoresist must be thoroughly removed, both before etching the SiO_2 and before proceeding to the next process step If it is not thoroughly removed in the first case, regions of SiO_2 will remain, after etching, in additional uncontrolled areas

Photoresists are hydrocarbon-based polymers, with cross-linking being determined by the exposure and development All traces of polymer should be removed by the developer or the photoresist stripper However, this is often not the case, particularly when the photoresist has been subjected to extreme conditions The last traces of hydrocarbon can be removed in a suitable oxidizing atmosphere, by conversion to CO_2 and H_2O The process for this should ideally not require high temperatures nor produce damage to either the Si or SiO_2

An oxygen plasma supplies atomic oxygen which reacts rapidly with the hydrocarbon to form volatile CO_2 and H_2O Although any O_2 plasma would provide the necessary reactive oxygen, substrate damage is minimized by ensuring that O_2^+ ions do not reach the surface being etched

2 5 2 Deposition

The fabrication of a CMOS circuit involves the deposition of a variety of films, including polycrystalline silicon, Si_3N_4, and SiO_2 which may be doped with elements such as B and P, Al-Si alloys and possibly diffusion barriers such as TiN Other microelectronic devices require different materials to be deposited for example, Au/Ge/Ni on epitaxial GaAs and WSi_x for GaAs integrated circuits Some of these films (e g Al-Si, WSi_x) can be deposited by a purely physical method, such as sputtering or evaporation, while others require a chemical method, such as plasma enhanced chemical vapour deposition (PECVD) Reactive sputtering, which is widely used to deposit TiN, combines both chemical and physical aspects Evaporation is preferred for lift-off processes because of the line-of-sight deposition However, it is difficult to control alloy composition, and the adhesion of the film is often low, requiring the use of additional adhesion layers

2 5 2 1 Sputtering

Evaporation was the first method used to deposit metals for microelectronics, such as Al, for interconnect conductors With the increased complexity of integrated circuits came the need for different materials Alloys of Al-Si or Al-Si-Cu have been widely used to obtain smaller line widths and to decrease electromigration in the conductors However, the elemental constituents of alloys evaporate independently and the individual evaporation rates are proportional to the respective vapour pressures at the source temperature

It is difficult to obtain an evaporated flux ratio from an alloy source which represents the original alloy composition and the source composition changes with time Initially, the more volatile component evaporates from the charge and the flux is enriched in this component but the flux will eventually become rich in the other component as the source nears exhaustion The scarcity of alloys which evaporate congruently (i e without change in composition) makes evaporation unattractive for alloy deposition [42]

The situation for sputtering is quite different because of the momentum transfer processes responsible for ejecting atoms from the alloy target The sputtering yields S_A and S_B for the two elements in the binary alloy target AB represent the probabilities of these atoms being ejected The numbers which are ejected are, therefore, proportional to the product of these probabilities and the numbers of A and B atoms which are present within the sputtering depth In equilibrium, the surface composition of the target changes such that the composition of the elements in the sputtered flux is the same as the original alloy composition [42]

The sputtering mechanism is therefore clearly advantageous for the deposition of alloys Two points must be emphasized, however First, the sputter mechanism alone is responsible for producing the correct flux ratio and other target effects will change this ratio If the target temperature is too high, diffusion will occur and will modify the surface composition, so that the sputtered flux has a different composition from the alloy target Second, the sputtering process responsible for the correct equilibrium flux requires that the target be a homogeneous alloy and not simply a mixture of the two

components Sintered powder composite targets do not satisfy this requirement although they are sometimes used for deposition of silicides If the target used to deposit $TaSi_2$ contains grams of Ta and Si, even if they are extremely small (< 5nm), the alloy sputtering mechanism does not apply because sputtering occurs within individual Ta and Si grains rather than from an alloy in which atoms are homogeneously mixed Then, the relative fluxes of Ta and Si will depend on the area ratio of Ta and Si grains and the elemental sputter yields for Ta and Si Although the resulting film is a Ta-Si alloy, the sputtering process does not make use of the inherent advantage of the alloy sputtering process and there is no reason to expect the film to have the desired $TaSi_2$ composition However, a constant composition (i e Ta/Si ratio) may be obtained if the relative areas of Ta and Si in the target are constant [42]

Since the vapour pressure of metals is very low except at elevated temperatures, the sticking coefficient for the different species in the sputtered fluxes is effectively unity and the film composition will be the same as the composition of the flux However, the film composition may differ from the incident flux if energetic ions and neutrals reach the substrate and cause sputtering there

The sputtering process is basically simple, although practical systems are actually quite complex because substrates must be transported, and gases and pressures controlled A plasma is generated by applying either DC or RF power in a suitable geometry and the target is biased to accelerate ions of the sputtering gas to it At present, most systems use a magnetron target arrangement, a magnetic field constrains the electrons to generate ions within a few millimeters of the target surface [42]

2 5 2 2 Reactive sputtering

By adding a gas which reacts with a sputtered metal in the presence of the plasma, compound films can be deposited using basically the same sputtering system as that used for metals As an example, TiN is often used as a diffusion barrier because it is refractory and has high conductivity It is deposited quite easily by adding N_2 while sputtering a Ti target provided a sufficient N_2 supply is maintained N_2^+ ions are formed in the plasma and bombard both the target and substrate the N atoms resulting from the

impact dissociation react with the Ti The energy and flux of the N_2^+ ions are determined by the sputtering parameters such as bias potentials and power [42]

2 5 2 3 Step coverage

In microelectronics, films are often deposited onto a patterned wafer on which there are many steps which must be covered For conductors, for example, the alloy must be continuous over each step and it is desirable that the film thickness be the same on the vertical wall of the step as on the flat surface since this will minimize high resistance regions at each step However, this is obviously difficult because it would require that the sputtered flux normal to the side wall be the same as the flux to the wafer surface In the usual system geometry, the substrate is parallel to the target and the sputtered atom flux is predominantly normal to the substrate surface so that the flux to the sidewall is quite small (Fig 2 4)
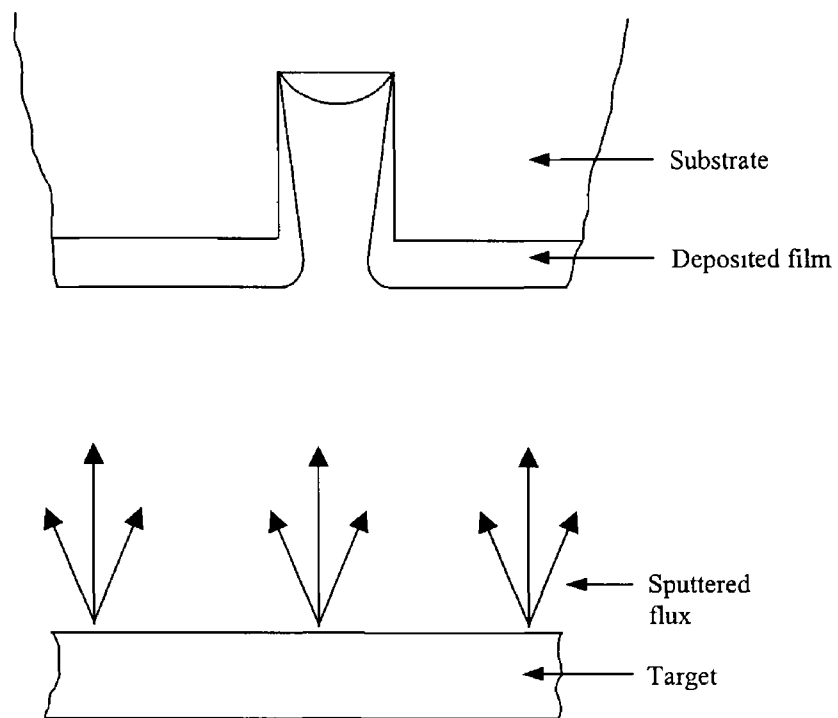
Figure 2 4 Schematic of the problem of step coverage during sputtering

By applying a bias to the substrate, ions are accelerated to the substrate and cause sputtering (usually termed resputtering) of the film If the resputtering ratio is high (i e the thickness removed from the flat surface is comparable to the thickness deposited), the film thickness on the side walls will be increased by collecting the resputtered atoms, while the thickness on the top wafer surface is reduced However, the alloy composition can be changed significantly by the resputtering In fact, the step coverage by Al-Si alloys is greatly improved by applying substrate bias even when the resputtering ratio is negligible

The ability to improve step coverage is a significant advantage and is easily implemented because of the plasma environment in which the sputter deposition is carried out It should be noted, however, that the enhancement of step coverage by bias sputter deposition may be incompatible with some masking techniques

2 5 2 4 Plasma enhanced chemical vapour deposition (PECVD)

Chemical vapour deposition has been used in IC fabrication almost since it began, and is still used in many cases In its simplest form, it requires increasing the temperature of the substrate to a value at which a required chemical reaction takes place at a useful rate in a controlled manner In PECVD, the chemical effects of the plasma allow the reactions to proceed at much lower temperatures Lower temperatures are desirable to prevent diffusion of dopants during these subsequent processes Films deposited by PECVD have increased in importance for IC processing as device dimensions have decreased and imposed the requirement for much tighter tolerances on the dopant location In depositing these films, it is the chemical aspects of the plasma which are usually of prime importance

Films can be deposited at temperatures determined by the plasma environment and the heat generated by the reactions While no elevated temperatures are required for the chemical reaction, the film properties may be improved by heating For example, silicon films deposited from SiH_4 will be amorphous and will contain a significant fraction of hydrogen, in the form SiH_x, unless the substrate temperature is above 600°C SiO_2 films are deposited from SiH_4 and N_2O, just as in the chemical vapour deposition

(CVD) case However, silicon nitride can be deposited using either NH_3 or N_2 Whereas N_2 cannot be used in CVD because of its low reactivity, its reactivity in the plasma is high due to dissociation processes [43] There are advantages to using N_2 in reducing NH bonding in the Si_3N_4 films as well as being more convenient

2 5 3 Etching

The selective removal of one material from another is an important part of IC processing For example, the SiO_2 has to be removed from the underlying silicon but it is important that no significant amount of silicon be removed Typically the dopants necessary for device operation are within 100 nm of the wafer surface and must remain there throughout processing Thus, while it is possible to remove the SiO_2 by a physical method, such as sputtering, this is not acceptable for a process step since sputtering will etch the silicon at a faster rate than it removes the SiO_2 and may also introduce damage or impurities into the exposed Si

For selectivity, a chemical reaction is required which etches one layer (e g SiO_2) but not the other (e g Si) For wet chemical etching, this often involves mixtures of several chemicals which engage in competing interactions with the exposed surfaces Just as chemical reactions for depositing films are made possible by injecting suitable gases into a plasma, so are chemical reactions for etching The chemical reaction must, in this case, convert the material to be removed into a volatile gas which will thus desorb from the surface within the plasma environment and be pumped out of the system A wide variety of gases are used in reactive plasma etching to etch different materials For example, BCl_3, $SiCl_4$, Cl_2 and CCl_4 are all used to etch Al alloys and CF_4, C_2F_6, CHF_3, SF_6, SiF_4, $CFCl_3$, CF_2Cl_2 and CF_3Cl are used to etch SiO_2 Mixtures of gases, such as $CF_4 + O_2$ are also used [44] Due to the variety of reactions that may occur, a large number of species may exist in the plasma

As discussed with reference to Fig 2 3, the type of etching which takes place will depend on the balance between the physical and chemical effects in the plasma One effect not considered was the deposition onto a side wall of a non-volatile product, such as a polymer or C [45] If this polymer or carbon compound does not react chemically with the etch gas species, it will remain on the wall, preventing any further reaction

22

because it cannot be sputtered away since the ions do not reach the side wall This can be used to the advantage of the operation in that it inhibits undercutting of masks and results in a more anisotropic etch

2 6 An Elemental View of Plasma Reactors

Although we will consider a number of aspects of plasmas and discharges in this chapter, we are primarily interested in these topics as they relate to the plasma reactors that are used for thin film processes Therefore to provide some general framework for what is to follow, we will consider here some general characteristics of the most common types of reactors

2 6 1 Planar reactors

Perhaps the most ubiquitous class of plasma reactor is one in which the plasma is formed between planar parallel electrodes [46,47], which are attached to the power source This includes configurations with a single electrode in a metallic containment vessel, the latter comprising the second electrode

The importance of the plasma electrons in generating chemically active species in the plasma volume, and the edge electric fields accelerating ions into the substrate suggests a schematic picture in which a reactor is decomposed into two regions The embodiment of this for a planar geometry is shown in Fig 2 5 Here, we see the plasma volume where chemically reactive species (and/or ions) are generated, in which there is only a small electric field Adjacent to this is a "plasma free" sheath region of strong electric field Although this picture is only approximate, it represents a useful framework for examining relevant plasma and sheath phenomena It also underlies the approach to many of the advanced plasma deposition and etch tools which are constructed to afford independent or nearly independent control of the two regions

The operation of planar reactors can be enhanced by the addition of magnetic fields This is usually accomplished by introducing a magnetic field that is nominally parallel to an electrode, as in a magnetron sputter source [48] or a magnetically

enhanced reactive ion etcher [49] The magnetic field increases the ionization efficiency of the electrons This results in higher density plasmas with decreased sheath voltage
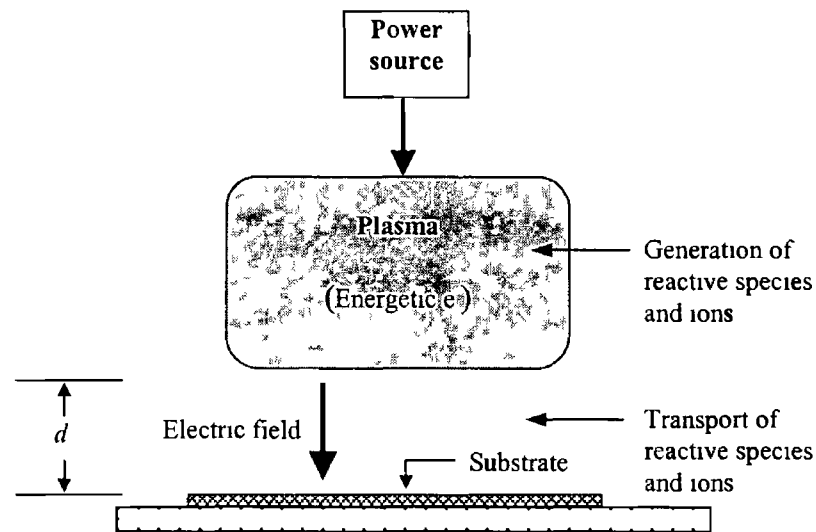
Figure 2 5 Generic plasma reactor for thin film deposition and etching A power source supplies energy to the main plasma discharge where reactive species and ions are generated These species are transported to the substrate or wafer for deposition or etching In many configurations there is an electric field in the vicinity of the substrate which accelerates the ions

2 6 2 Barrel reactors

A barrel reactor [50] is a tubular-shaped structure, in which a plasma is sustained either by inductively coupling an ac power supply through a coil which surrounds the reactor (Fig 2 6(a)), or by capacitively coupling via external rings (Fig 2 6(b)) For this configuration, the electric field is established inside the non-conducting vacuum vessel without internal electrodes Consequently, this reactor does not develop the larger sheath electric fields that a planar reactor does, so that ion bombardment usually plays little or no role The main application of barrel reactors is for isotropic etching, including the removal of organic materials as in resist stripping

2 6 3 Downstream plasma reactors

A relatively recent addition to plasma processing in production applications is the
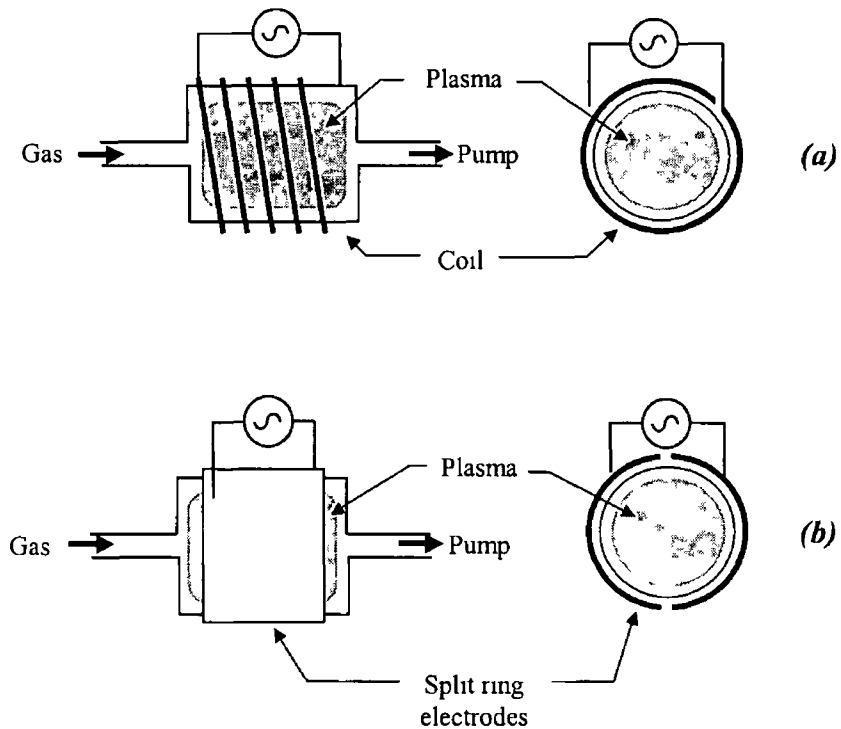
Figure 2 6 *(a) Inductively coupled plasma reactor (b) Capacitively coupled plasma reactor*

downstream plasma reactor [51-53], a generic diagram of which is shown in Fig 2 7 In the traditional barrel and planar reactors discussed above, the wafer is situated in the plasma generation chamber and is therefore immersed within the plasma In downstream reactors, the wafer is separated from the plasma chamber, so it is "downstream" from the region of plasma generation Such plasmas are usually electrodeless, being sustained by microwaves introduced by some radiation launching structure An important example of the downstream plasma reactor is the electron cyclotron resonance (ECR) plasma reactor [52,53] This apparatus includes a magnetic field Electrons are heated by a microwave source which is applied at a frequency that corresponds to that of the electrons circulating in the magnetic field

Oftentimes in the downstream geometry, ion bombardment of the substrate is not wanted Owing to the separation of the plasma from the substrate, this is easily accomplished The downstream configuration represents an even further emphasis on separating the bulk plasma from the environment of the substrate For this reason, the downstream configuration is an important approach to advanced deposition and etch tools
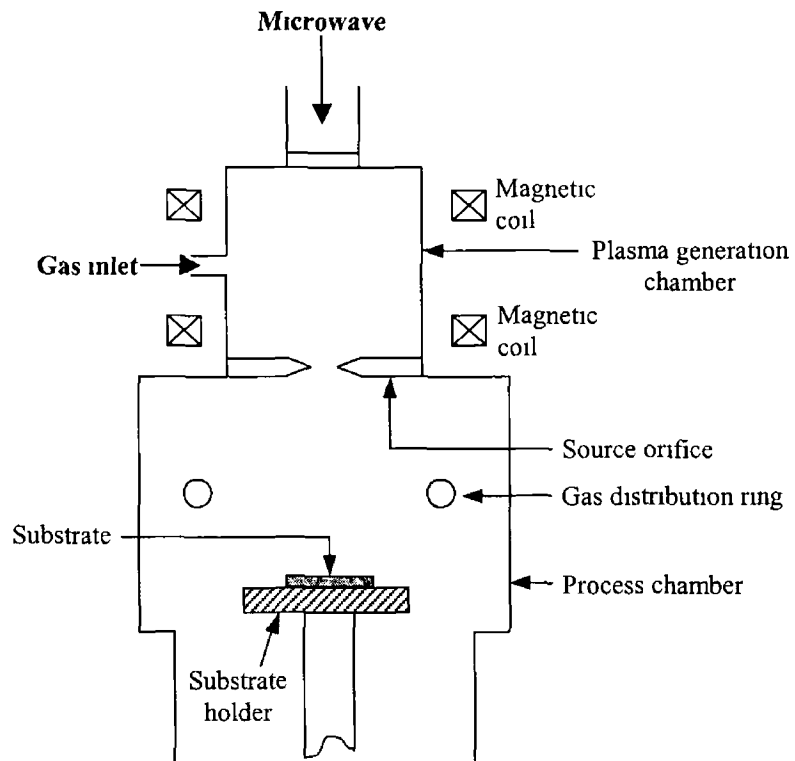
Figure 2 7 Downstream plasma reactor

2 7 Fundamental Plasma Discharge Concepts

In this section, we will review fundamental plasma discharge concepts which underlie the operation of plasma reactors for deposition and etching The concepts discussed here are covered extensively in a number of excellent plasma physics texts [40,41,54-56] and therefore, in some cases, we will present results with only limited derivations

2 7 1 Debye shielding

In general, the characteristics of plasmas will differ greatly depending on things like the constituent atoms and molecules, densities, energies, and degree of ionization There is, however, one universal plasma characteristic the free charges in the plasma will move in response to any electric field in such a way to decrease the effect of the field In particular, electrons are usually lighter and more mobile in response to electric fields, and the ions are assumed stationary That means the tendency of plasma electrons

is always to decrease any presence of electric fields There will not be regions of a plasma with excess positive or negative charge, because if there were, an electric field would arise that would move electrons to effectively eliminate any charge imbalance This feature is called *quasi-neutrality*

If a *test* positive charge is inserted in a plasma (Fig 2 8), the charge will attract a cloud of electrons, and repel the local ions, so that it is completely shielded from the rest of the plasma Outside the cloud there will be no electric field This is the phenomenon of *Debye shielding* We can find a self-consistent solution for the electrostatic potential Φ, which arises from the test charge Q
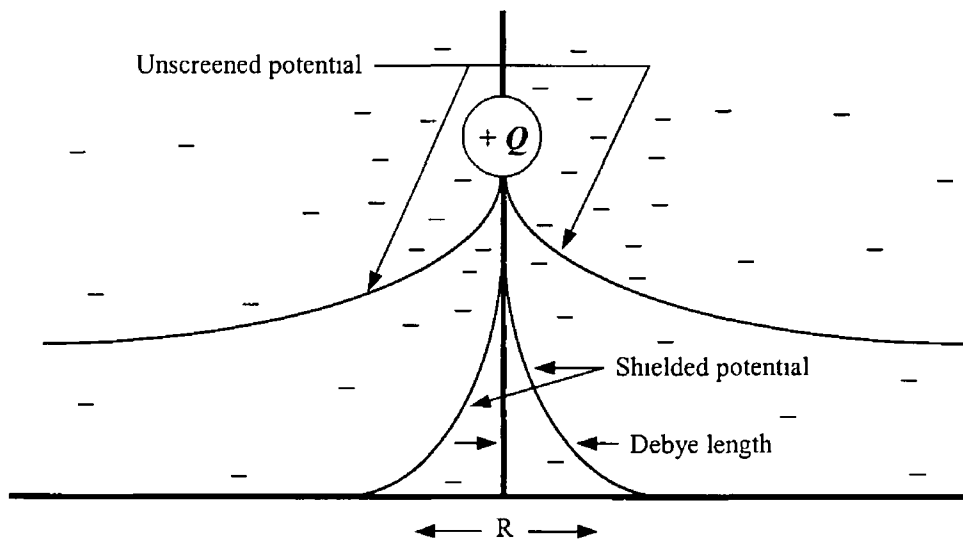
Figure 2 8 Schematic of the unshielded electrostatic potential from a point charge +Q compared to the Debye shielded potential that occurs when the charge is immersed in a plasma The electron density increases in the vicinity of the charge, creating the exponential fall-off in the potential

Using Boltzmann's equation, $n(E)=n_0 \, exp(-E/kT)$ where k is Boltzmann's constant, we can write the equations for ion density (n_i) and the electron density (n_e) as

$$n_i = n_0 \, exp\,(-e\Phi\,/\,kT\,) \qquad (2\ 8a)$$

$$n_e = n_0 \, exp\,(\,e\Phi\,/\,kT\,) \qquad (2\ 8b)$$

where n_0 represents the value of both particles at equilibrium The charge density ρ is given by

$$\rho = e(n_i - n_e) = -2n_0 e\, sinh(e\Phi / kT)$$ (2 9)

where we have used the identity $sinh(x) = \frac{1}{2}(e^x - e^{-x})$ Using Poisson's equation,

$$\nabla^2 \Phi = -\frac{\rho}{\varepsilon_0}$$ (2 10)

Substituting eqn (2 9) in eqn (2 10), we obtain,

$$\nabla^2 \Phi = \frac{2n_0 e}{\varepsilon_0} sinh(e\Phi / kT)$$ (2 11)

Near the edge of the cloud, and beyond, the electrostatic energy $e\Phi$ associated with Q is much less than the electron thermal energy kT i e, $e\Phi/kT \ll 1$ We can then approximate $sinh(e\Phi/kT) \approx e\Phi/kT$, so that eqn (2 11) becomes

$$\nabla^2 \Phi = \frac{2}{\lambda_D^2} \Phi$$ (2 12)

where we define the *Debye length*, λ_D as

$$\lambda_D = \left(\frac{\varepsilon_0 kT}{n_0 e^2} \right)^{\frac{1}{2}}$$ (2 13)

The solution of eqn (2 12) is [57]

$$\Phi = \frac{Q}{r} exp\left(-\sqrt{2}r / \lambda_D\right)$$ (2 14)

By eqn (2 14), the Debye length λ_D is a measure of the range of the effect of the test charge Q If follows from eqn (2 13) that this range is greater in a hot diffuse plasma than in a cool dense plasma This is to be expected if T is large, more electrons in the cloud at a given distance from Q will be able to escape, so that Q is less efficiently screened, if n_0 is small electrons will have to be drawn from a larger volume in order to shield a given charge Q

2 7 2 Plasma oscillations

If a charge imbalance does occur in a plasma, we have seen how the electrons will move to shield out its effects This does not happen instantaneously, however A

28

reasonable estimate of the time it takes for the shielding to "get in place", would be the time required for an electron to move a Debye length This time t_p is [42]

$$t_p = \lambda_D / u_e = \left(\frac{\varepsilon_0 m_e}{n_0 e^2} \right)^{\frac{1}{2}}$$
(2 15)

where u_e and m_e are the electron velocity and mass respectively Furthermore, we might imagine that the electrons, moving under the force of the electric field from the charge imbalance, may "overshoot" and execute an oscillatory motion A more rigorous treatment of this problem [54] reveals that this is the case The electrons will oscillate at a frequency which is just the inverse of t_p called the *plasma frequency* ω_p, which can be given by the equation

$$\omega_p = \frac{1}{t_p}$$
(2 16)

Collisions will damp out this oscillatory motion, so that the shielding electrons will eventually assume the static distribution in eqn (2 14)

In the absence of magnetic fields, this is the only "normal mode" of a plasma In the presence of magnetic fields, however, plasmas display a number of additional oscillatory modes A detailed discussion of these, which is beyond the scope of this chapter, can be found in a number of excellent references [55,58] We note here the general observation that the plasma will screen out an oscillating field with a frequency below ω_p, but above this frequency, the electrons cannot respond fast enough to accomplish the shielding

2 7 3 Collisional processes

Collisions are generally characterized by a cross section σ which has the dimensions of area If an electron collided with a "hard sphere" of radius a, then $\sigma = \pi a^2$ (Fig 2 9) The cross section is a measure of the probability that a given process will occur For some complicated processes there may not be a corresponding physical picture as Fig 2 9, although a still will have units of area If we are considering electron-neutral collisions where N is the neutral density, then the quantity,

$$\lambda = (N\sigma)^{-1}$$
(2 17)

29
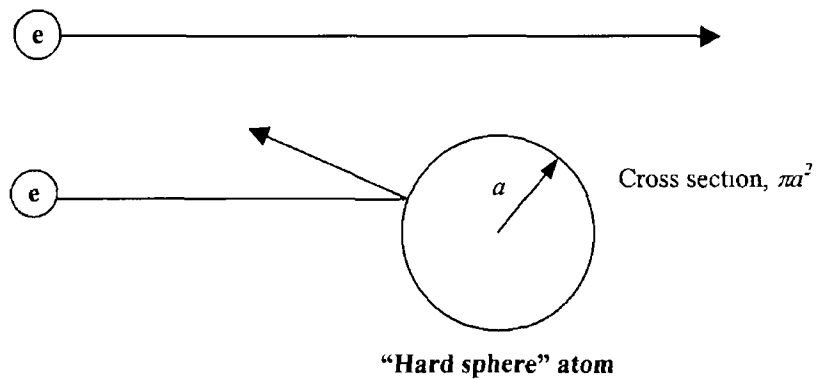
"Hard sphere" atom

Figure 2 9 Hard sphere atom cross section Only those electrons that approach within distance 'a' from the centre will undergo a collision

is the collision *mean free path* This is the average distance travelled by the electron between collisions or processes

Another important quantity which is related to the cross section is the *collision frequency* If u_e is the electron velocity, then the collision frequency v is defined by [42]

$$v = N\sigma u_e \qquad (2\ 18)$$

and has units of s^{-1} The time between collisions is just v^{-1}

Collisions fall into two general categories *elastic collisions,* which are those for which the internal energy of the colliding partners is unchanged by the collision, and *inelastic collisions,* in which internal energy changes Internal energy refers to electronic excitations in atoms or electronic, vibrational, and rotational excitations in molecules Ions will, in general, have different states of internal energy, however, an electron does not

In weakly ionized plasmas ($n_e / N < 10^{-4}$), collisions between electrons and neutrals will be very important in establishing the electron energy distribution function In fact, the dominance of electron-neutral collisions is responsible for the general character of these glow discharges, which behave very differently from plasmas with higher degrees of ionization, where electron-electron collisions dominate

30

In what follows we will consider examples of some important collision processes
Additional information can be found in the references [59,60]

2 7 3 1 Electron-neutral collisions

The elastic cross section for electron-neutral collisions σ_N will depend on the
electron velocity Examples of σ_N for the rare gases are shown in Fig 2 10 For rare
gases heavier than He, the cross section has a minimum at low electron velocities, rises
to a peak which increases with mass, and then falls off at higher velocities The
minimum is called the Ramsauer effect and arises from the quantum mechanical wave
nature of the electron [61] The increase in the maximum cross section with mass is
related to the increased size of the atom At higher electron velocities, the interaction
time is shortened, so that the collision has less effect on the electron
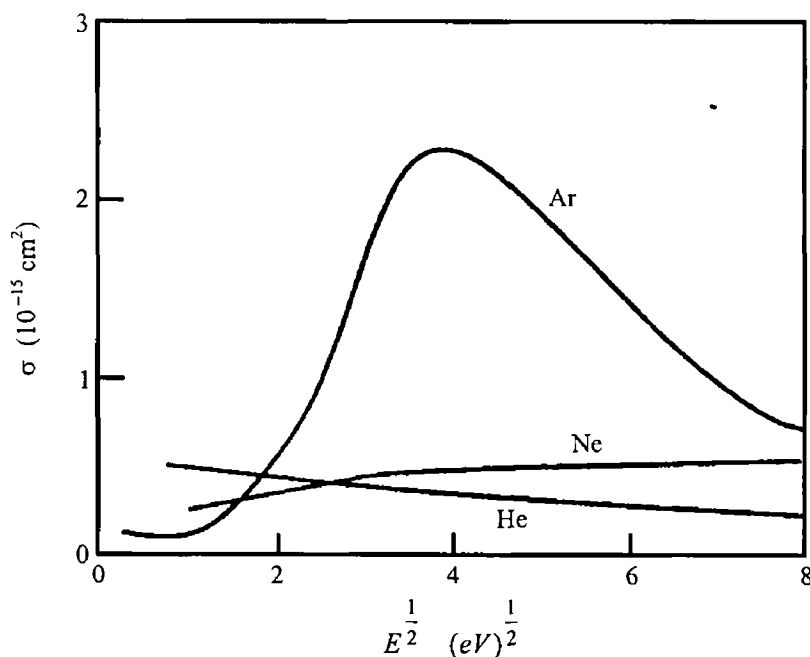
Figure 2 10 *Elastic scattering cross sections for electrons of energy E
incident on He, Ne and Ar [59]*

The average amount of energy transferred from the electron to the neutral is E_t,
given by [48]

$$E_t = \delta E \qquad (2\ 19)$$

E is the electron energy and δ is given by

$$\delta = \frac{2m}{M} E$$ (2 20)

where m and M are the electron and neutral mass respectively Since the neutral mass is much larger than the electron mass (e g , for Ar, $(2m/M) = 1/40,000$), very little energy is transferred to the neutral in an elastic collision However, the electron will experience a large change in the direction of its velocity, and hence its momentum is changed

From eqn (2 18), we can write the collision frequency for electron-neutral elastic collisions v_N, as

$$v_N = N\sigma_N u_e$$ (2 21)

where u_e is the electron velocity From eqn (2 21) we can see that v_N will depend on the neutral gas pressure because the neutral density N is inversely proportional to the gas pressure

2 7 3 2 Electron-electron collisions

Electron-electron collisions are characterized by a cross section $\sigma_{e\,e}$ which is given by [42]

$$\sigma_{e-e} = \frac{e^4 \ln \Lambda}{4\pi\varepsilon_0^2 \left(mu_e^2\right)^2}$$ (2 22)

where

$$\Lambda = \frac{12\pi\left(\varepsilon_0 kT / e^2\right)^{\frac{3}{2}}}{\sqrt{n}}$$ (2 23)

and m, e, u_e, n, T are the mass, charge, velocity, density and temperature of the electrons, respectively The collision frequency for electron-electron elastic collision can be given, from eqn (2 18) as

$$v_{e-e} = n\sigma_{e-e} u_e$$ (2 24)

In electron-electron collisions, since the masses are equal, the electrons can exchange energy very effectively, unlike an electron-neutral collision, where there is a large mass difference Hence, electron-electron collisions will become important even at

low degrees of ionization This is quantified by a parameter P, which is the ratio of the rate of electron energy loss by electron-electron collisions to that for electron-neutral collisions When $P > 1$, electron-electron collisions will become important This condition occurs for degrees of ionization around 10^{-4} or 10^{-3} In ECR discharges, where the degree of ionization is above this, electron-electron collisions will dominate, while in planar reactors, with lower degrees of ionization, electron-neutral collisions will be most important This will have important implications for the electron energy distribution function

2 7.3 3 Electron impact inelastic collisions

Though the inelastic cross sections are often much smaller than the elastic ones, the electron can lose a much larger fraction of its energy given by [42]

$$\frac{M}{m+M}E \tag{2 25}$$

where m and M are the electron and the neutral mass respectively Since $M \gg m$, virtually all of the electron energy is available for inelastic processes

As a first example, we will consider the inelastic processes that result when an electron impacts an atom like He In the He atom, the electrons occupy certain discrete states, as in Fig 2 11

There are a number of important processes shown here The first is ionization,

$$e + He \rightarrow He^+ + 2e,$$
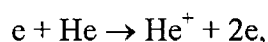
where ions and additional electrons are created Another process is electronic excitation,
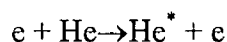
$$e + He \rightarrow He^* + e$$

where the electrons in the He atom are promoted to excited states The lifetime of many of the He excited states is very short (typically 100 ns or less), so that excitation is frequently followed by radiative decay,
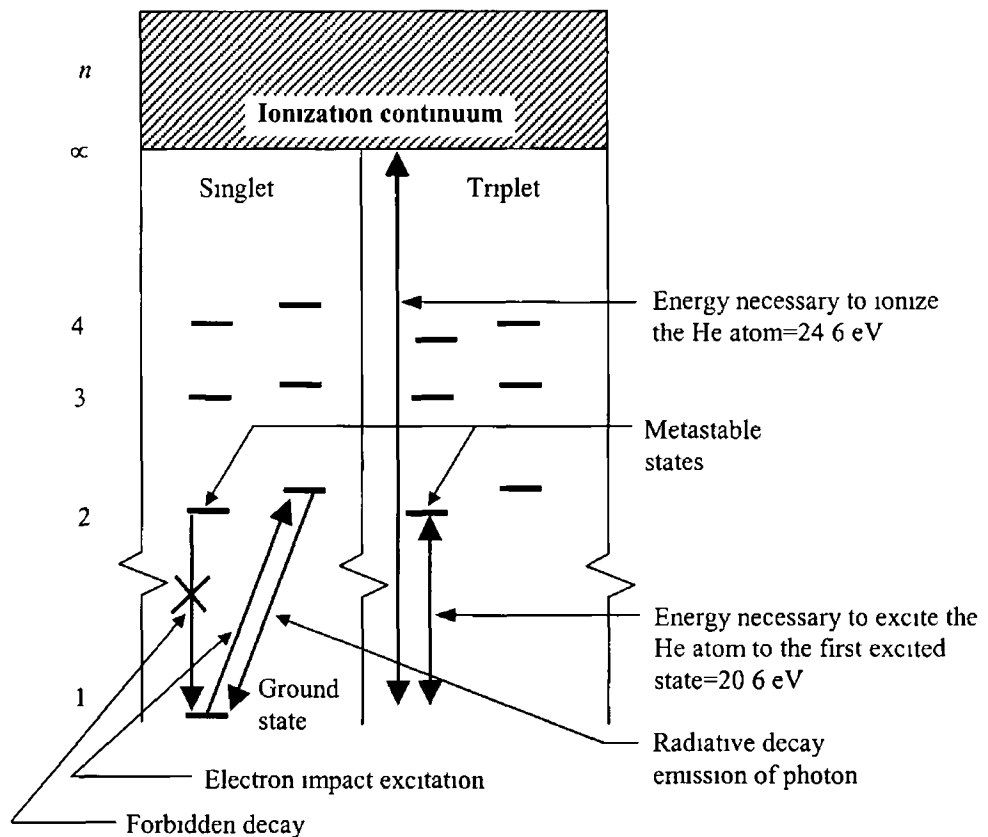
Figure 2 11 *Atomic energy levels for He, showing the singlet and triplet series (not to scale) The energy necessary to ionize He atom is 24 6 eV, while the energy for the first electronic excitation of He atom is 20 6 eV Excited atomic states, which are forbidden from decaying to the ground state, have long lifetimes and are called metastable states*

$$He^* \rightarrow He + h\nu$$

where a photon of frequency ν is emitted Certain states in He have much longer lifetimes These *metastable* states, which are shown in Fig 2 11, can have lifetimes of 1 ms or longer The metastable states also have considerable energy (e g , 20 eV for He) and if they collide with ground state neutrals, they may cause excitation or ionization These are the *Penning processes*, which, for metastable species A^* colliding with species B look like

$$A^* + B \rightarrow A + B^* \quad \text{(Penning excitation)}$$

$$A^* + B \rightarrow A + B^+ + e \quad \text{(Penning ionization)}$$
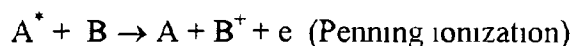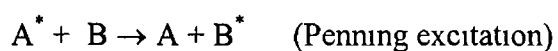
These processes will increase the ionization rates and excitation rates in plasmas, and this is one of the reasons why rare gases like He and Ar are added to process plasma discharges

The inverse processes, where electrons are lost by recombination can also be important One example is three body recombination,

$$He^+ + 2e \rightarrow He + e,$$
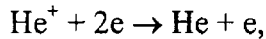
where two electrons are necessary to conserve momentum Another recombination process is *radiative recombination*,

$$He^+ + e \rightarrow He + h\nu,$$
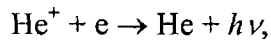
where energy and momentum are balanced by emission of a photon after recombination [59,60,62,63]

An important process for electron loss that can occur in a plasma where the neutral species has a high electron affinity (such as halogen discharges) is electron capture [59,60,62,63], shown here for fluorine

$$F + e \rightarrow F$$
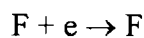
Each process will have a cross section associated with it In all of these processes, the incident electron will lose an amount of energy equal to that required for the inelastic process For the electron loss processes, the entire energy of the electron is lost

In rare gas atoms, electron excitation requires an amount of energy which is very close to that for ionization, and therefore, the cross sections are quite similar Owing to this, for rare gas plasmas, we can reasonably assume that where light is emitted (radiative decay following electron excitation), ionization is probably also occurring

When an electron collides with a molecule (which we will represent as AB), a number of processes may occur *Dissociation,* such as

$$e + AB \rightarrow A + B + e$$
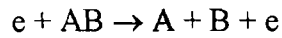
can result in the formation of chemically reactive radicals Another important process is *dissociation ionization,*

$$e + AB \rightarrow A^+ + B + 2e$$

where ions and radicals may be formed The dissociation products of molecules may react to form additional species The chemically active species may also undergo surface reactions, as in etching or deposition

Some electron loss processes associated with molecules are *associative recombination*

$$e + (AB)^+ \rightarrow AB$$
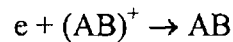
and *dissociative attachment*

$$e + AB \rightarrow (AB)^-$$
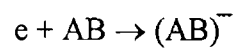
2 7 3 4 Ion collision processes

There are a few ion impact processes which are crucial to the discharge The first is secondary electron emission from a surface bombarded by an energetic ion [63] This process is usually characterized by a coefficient λ which is the ratio of the number of electrons emitted for each incident ion Typically λ lies between 0 05 and 0 1 Another important ion process is that of charge transfer

$$A^+ + B \rightarrow A + B^+$$
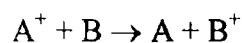
where A and B can be the same species This process is an important loss mechanism for energetic ions in the sheath region of discharges

2 7 4 Diffusion of particles

Whenever there is a concentration gradient of particles, the random motion of the particles results in a net flow down the gradient. This is the phenomenon of *diffusion* The resulting ion and electron current densities in the presence of a diffusion gradient dn/dx (assumed in one dimension for simplicity) can be written [64]

$$J_e = -eD_e \frac{dn_e}{dx} \qquad (2\ 26)$$

$$J_i = -eD_i \frac{dn_i}{dx} \qquad (2\ 27)$$

where, D_e and D_i are the diffusion coefficients of the electrons and ions respectively. It is possible to show that the diffusion coefficient and mobility μ (the drift velocity in unit electric field) are related by temperature [64]

$$\frac{D}{\mu} = \frac{kT}{e} \qquad (2\ 28)$$

This is *Einstein's relation* We already know that the mobility of the electrons is very much greater than that of the ions, and therefore the electron diffusion coefficient will be very much greater than the ion diffusion coefficient. One might expect as a result that, in a region of concentration gradient, the electrons would stream out very much faster than the ions. This is initially true, but the exodus of the electrons leaves the rest of the plasma more positive and sets up a restraining electric field which grows large enough to equalize the diffusion rates of the ions and the electrons. Therefore, the collective behaviour of the ions and electrons causes them to move with the same diffusion coefficent. This is the phenomenon of *ambipolar diffusion* In the extreme limit, which occurs for electron densities above $10^9\ \text{cm}^{-3}$, both electrons and ions diffuse at twice the slower ion rate [54,55,65]

2 7 5 Sheaths

2 7 5 1 Sheath near a non-conducting or isolated surface

We have already examined the effects of Debye shielding which occurs inside the plasma volume. We will now explore the manifestation of this effect at the plasma edge. At the boundary, electrons and ions will diffuse out of the plasma, as noted in section

2 7 4, owing to their thermal energies From simple kinetic theory, the particle flux Γ is [62]

$$\Gamma = \frac{1}{4} n \overline{u}$$ (2 29)

where, n is the particle density and $\overline{u}$ is the average velocity of the particle which is given by [66]

$$\overline{u} = \left(\frac{8kT}{\pi m} \right)^{\frac{1}{2}}$$ (2 30)

with T the (ion or electron) temperature and m the mass In the absence of any sheath effects, and for electron temperatures equal to or greater than the ion temperature, the electron velocity will be much greater than the ion velocity

Let's consider what happens near a non-conducting wall (or an isolated conducting wall) The electron flux to the wall will be higher initially, owing to their greater thermal velocities However, this will cause the plasma to become more positive, since there is an excess of positive ions left behind An electric field will develop which will retard the electrons and accelerate the ions, in such a way to make the net current zero The magnitude of the potential which the plasma acquires is about $(3kT_e/e)$ [42], where T_e is the electron temperature As we might guess, this potential falls off from the wall into the plasma over a distance of the Debye length λ_D (eqn 2 13), as shown in Fig 2 12
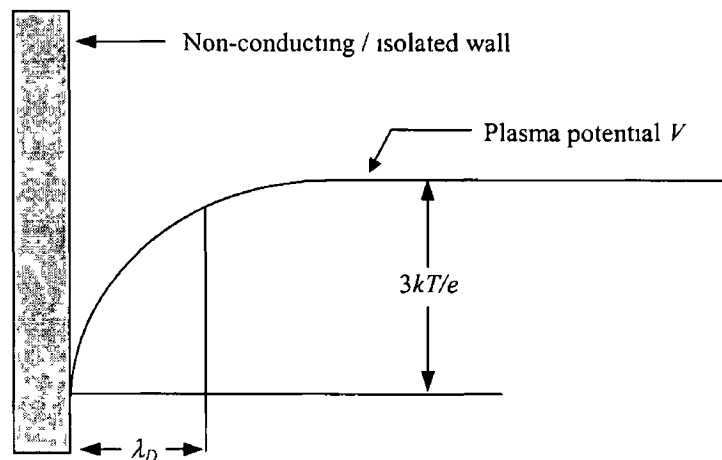
Figure 2 12 Behaviour of the plasma potential in the vicinity of a non-conducting or isolated wall The characteristic fall-off distance for the sheath potential is the Debye length

38

2 7 5 2 Sheath near a conducting electrode

Let us now consider the case of a surface across which current flows (e g , the cathode in a dc glow) The form of the potential in this region can be found from Poisson's equation The structure of the DC sheath is shown m Fig 2 13
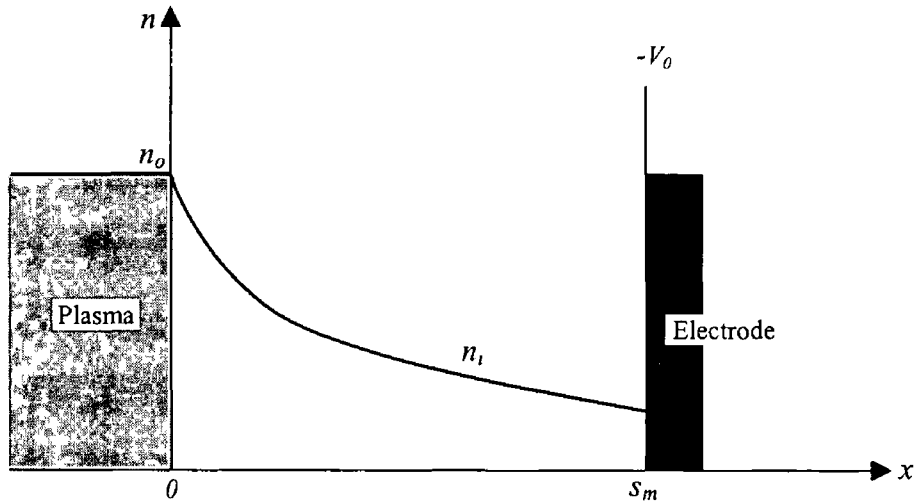
Figure 2 13 *Structure of the high voltage DC sheath*

We will assume that the potential on the electrode is negative and large, which will have the effect of attracting ions and repelling electrons Ions crossing the sheath boundary at $x = 0$ accelerate within the sheath and strike the electrode at $x = s_m$ We will take the electron density in the sheath region to be zero The current density J is then given by

$$J = en_i u_i \tag{2 31}$$

where n_i is the ion density, e is the electronic charge, and u_i is the ion velocity The potential $V(x)$ at any position x obeys Poisson's equation and we can write

$$\frac{d^2 V}{dx^2} = -\frac{en_i}{\varepsilon_0} \tag{2 32}$$

The ion velocity is related to the potential V by conservation of energy

$$\frac{1}{2} Mu_i^2 = -eV \tag{2 33}$$

where M is the ion mass From these three equations, we have

$$\frac{d^2V}{dx^2} = -\frac{J}{\varepsilon_0}\left(-\frac{M}{2eV}\right)^{\frac{1}{2}}$$ (2 34)

Multiplying this equation by (dV/dx) and integrating,

$$\left(\frac{dV}{dx}\right)^2 = \frac{4J}{\varepsilon_0}\left(\frac{M}{2e}\right)^{\frac{1}{2}}(-V)^{\frac{1}{2}}$$ (2 35)

where we have chosen $dV/dx = -E = 0$ at $V = 0$ ($x = 0$) Taking the (negative) square root (since dV/dx is negative) and integrating again, we obtain

$$-V^{\frac{3}{4}} = \frac{3}{2}\left(\frac{J}{\varepsilon_0}\right)^{\frac{1}{2}}\left(\frac{M}{2e}\right)^{\frac{1}{4}} x$$ (2 36)

Letting $V = -V_0$ at $x = s_m$ ($=$ the sheath width) and solving for J, we obtain

$$J = \frac{4}{9}\varepsilon_0\left(\frac{2e}{M}\right)^{\frac{1}{2}}\frac{V_0^{\frac{3}{2}}}{s_m^2}$$ (2 37)

which is the well-known Child Law for space charge-limited current flow The resulting sheath thickness s_m will be many times the Debye length

In addition to this "free fall" sort of sheath, in which we assumed that the ions did not make any collisions, it is also possible to have a mobility-limited sheath, where the ion velocity is determined by its mobility [54]

2 7 6 Heating mechanisms

The exact mechanisms by which the plasma sustains itself, although mainly due to ionization and excitation, are quite complex At low pressures a mechanism called 'sheath heating' is responsible for maintaining the plasma, while at medium pressure localized ionization dominates [67] At high pressure and voltages secondary electrons emitted from the electrodes cause ionization throughout the plasma In this case the plasma resembles a dc glow discharge and is known as the γ regime

2 7 6 1 Sheath heating

For a fixed gas, electrode gap and material, and driving frequency, the heating regime can be determined by the gas pressure and current density At low pressures, of the order of 10 - 40 mTorr, currents of the order of 3 mA/cm^{-2} and with an electrode gap of 6-8 cm a collisionless regime for plasma electrons occurs [67] Here, stochastic heating in the sheath dominates while collisional heating due to electron-atom collisions is small The sheaths in an RF plasma move with speeds up to ~5x10^{7} cm/sec Low energy electrons are gently pushed by the bulk electric field towards the electrodes as the sheath retreats during the positive part of the cycle Some electrons move too slowly to catch the retreating sheath and so they bounce and lose energy When the sheath expands during the negative part of the cycle the electrons are unable to move away and so collide with the sheath as it passes, gaining energy [68,69]

For argon this heating regime is enhanced by the previously mentioned phenomenon known as the Ramsauer effect [40,61,70] The cross section for elastic collisions, for slow electrons is unusually small in inert gases as shown in Fig 2 14 The low energy group of electrons therefore have an extremely low electron-atom collision frequency These electrons oscillate collisionlessly in the bulk of the plasma, trapped by the ambiploar potential well and unable to gain energy from the sheaths or the RF field The fast electrons can however overcome these barriers and effectively interact with the argon atoms in ionizing collisions They then compensate for their energy losses through collisions with the oscillating plasma sheath [71-73] Most heating occurs during expansion of the sheaths for this process However a mechanism known as anomalous sheath heating has been shown to occur, where heating during the retreating part of the cycle arises [74] This anomalous effect is due to the presence of a large field reversal at the retreating sheath edge This field reversal occurs because of collisional drag forces which prevent the electrons from responding instantly to the fields

2 7 6 2 Bulk heating

If the pressure of the plasma is increased above ~ 50 mTorr, again with a 6-8 cm

41
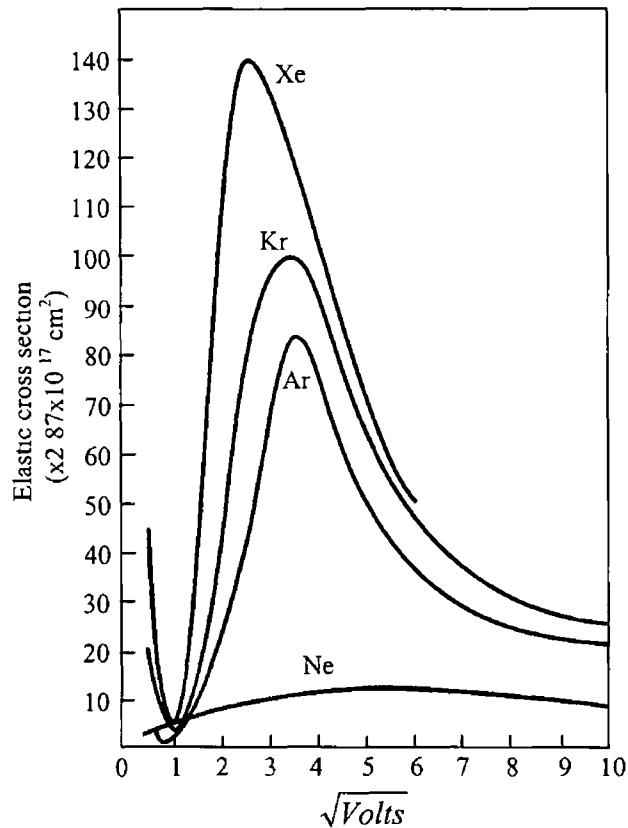
Figure 2 14 *Elastic scattering cross section for Ne, Ar, Kr and Xe (after [59])*

electrode gap, for the system used in [67], the conditions of this regime are determined by the pressure and discharge length, and ohmic or bulk heating becomes the dominant heating regime In this case ionization occurs locally in the bulk of the plasma as the mean free path of the electrons is less than the chamber dimensions The electrons are heated by the bulk electric field giving them a higher temperature than they had in the stochastically heated regime The transition in pressure between the collisional and non-collisional regimes can be characterized by a parameter pd where p is the gas pressure and d the half width of the bulk plasma [75] The transition normally occurs in the range $pd = 0\ 1$ to $0\ 2$ Torr cm

2 7 6 3 γ regime

If the pressure of the plasma is increased to $\sim 0\ 5$ Torr and the driving voltage is also increased, the heating mode of the plasma changes abruptly from the α (bulk electron heating) to the γ mode In this regime the ions bombard the surface of the

42

electrodes emitting secondary electrons These electrons are then accelerated by the sheath field to very high energies, enter the bulk plasma causing ionization mainly at the plasma sheath boundary but also to some extent in the bulk The ions produced are then accelerated towards the electrodes causing more secondary electrons The abrupt change in heating mode is also accompanied by a dramatic change in light emission from the plasma, a sharp drop in the electron temperature and an increase in the plasma density [76,77]

2 7 7 Breakdown

In the following sub-sections we will consider the breakdown processes that precede the formation of DC and RF glow discharges

2 7 7 1 DC breakdown

We will examine DC breakdown by considering, as an example, Ar at 30 mTorr in a system, shown in Fig 2 15, comprising two electrodes connected to a DC power supply with voltage V_{ps} through a ballast resistor R
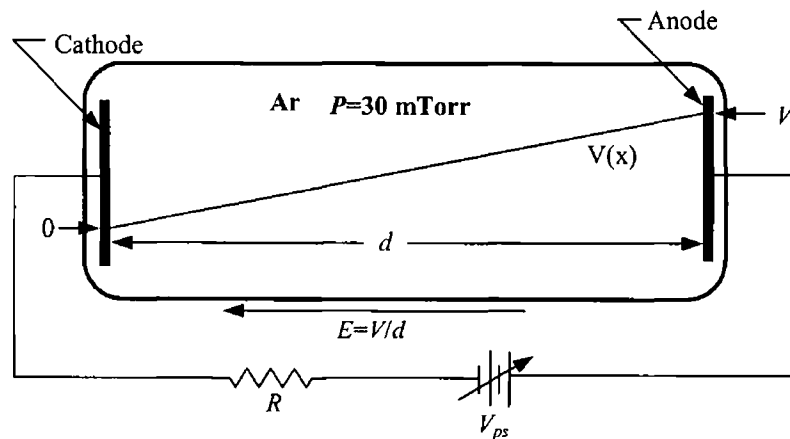
Figure 2 15 Schematic of an Ar discharge prior to breakdown The resistance of the Ar is much greater than that of the ballast resistor R, so almost the entire voltage is dropped across the discharge tube

Initially, the resistance of the neutral gas will be much greater than that of R, so the voltage across the discharge $V \approx V_{ps}$ Let us assume that there is one free electron,

43

formed perhaps by a cosmic ray or some UV photon, near the cathode The electric field will accelerate the electron towards the anode Let α be the probability per unit length that ionization will occur The quantity α is called Townsend's first ionization coefficient, and represents the net ionization probability, including losses As a result of the acceleration by the electric field, the electron will gain energy and produce ionization This will lead to a multiplication of the number of electrons as shown in Fig 2 16
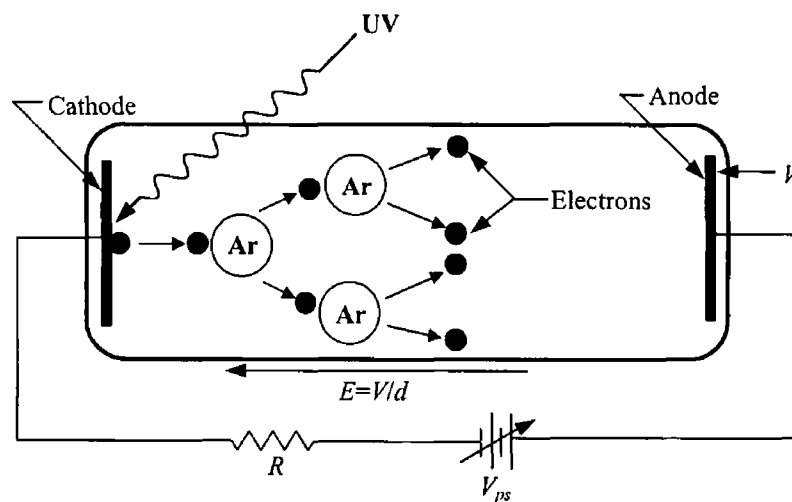
Figure 2 16 *Behaviour of the discharge at breakdown An electron is created by photodesorption at the cathode The electron is accelerated by the electric field and causes ionization, creating ions and additional electrons*

The current at the anode arising from an electron current I_0 emitted from the cathode is given by [42,78]

$$I_d = I_0 \, exp(\alpha d)$$

(2 38)

The electric field will also accelerate ions, and when ions strike the cathode, electrons will be emitted by ion impact secondary electron emission with a probability γ The total number of ions created by the first electron multiplication is ($exp(\alpha d)$ -1) This will give rise to γ($exp(\alpha d)$ -1) secondary electrons, which will also be accelerated by the electric field and cause more ionization and consequently more ions If we add up this sequence of successive generation of secondary electrons giving rise to more ions giving rise to more secondaries, etc , we find that the total current arriving at the anode is

$$I_d = \frac{I_0 \, exp(\alpha d)}{1 - \gamma[exp(\alpha d) - 1]}$$ (2 39)

If $exp(\alpha d) \gg 1$, we can write eqn (2 39) as

$$I_d = \frac{I_0 \, exp(\alpha d)}{1 - \gamma \, exp(\alpha d)}$$ (2 40)

When $\qquad\qquad 1 - \gamma \, exp(\alpha d) \approx 0$ $\qquad\qquad$ (2 41)

the current I_d tends to increase rapidly, a condition arises referred to as breakdown

2 7 7 2 RF breakdown

Breakdown in an RF field is actually somewhat simpler than that for the DC case, if most of the electrons are able to undergo their oscillatory motion without colliding with a wall In this case, the oscillating electric field puts directed energy into the electrons, which then heat up by undergoing collisions with neutrals In this way the electrons are heated up sufficiently to produce the required amount of ionization which must balance the losses due to diffusion to the walls, volume recombination, electron attachment, etc

2 7 8 Glow discharges

Prior to breakdown, we started with a homogenous neutral gas with a constant electric field and a linear voltage drop Following breakdown, a discharge forms, and rearranges itself into characteristic regions to provide optimally for particle generation and energy input to balance losses For a DC discharge, just at breakdown, the current will increase with little increase in the voltage This is called the Townsend discharge [79] and precedes the avalanche that signifies "full" breakdown The first "state" after breakdown is a glow discharge Initially, the glow will not completely cover the cathode surface It operates at near constant voltage in this regime, with the current increasing as the cathode coverage increases Eventually, the glow expands to fill the cathode surface, and subsequently, further increases in power will result in increases in both voltage and current The salient characteristic of a glow discharge is that electrons are created by

iomzation and secondary electron generation from ion impacts on surfaces If the power is increased further, the cathode will begin to heat Eventually, thermionic emission will occur, and become the dominant electron creation process At this point the discharge voltage will decrease and the glow has evolved into an arc

In the following sections, we will consider the main characteristics of DC and RF glow discharges In particular, we will look at those features which pertain to our application of glow discharges to the deposition and etching of thin films

2 7 8 1 DC glow discharge

It is convenient and traditional [54] to picture the glow discharge as comprising a number of distinct regions Of course, this is an artificial construct, in reality the discharge is a continuous entity Fig 2 17 shows the DC glow schematically We will now consider each region

2 7 8 1 1 The cathode region

A narrow luminous layer is often observed adjacent to the cathode The light emitted from this region is thought to be due to excitation of the neutral gas followed by a radiative decay and surface bombardment by ions Beyond this luminous region is the Crooke-Hittorf cathode dark space, which extends to the next luminous region, the negative glow

Whereas originally the voltage was dropped uniformly across the entire discharge tube, in the glow phase, almost the entire voltage appears across the cathode dark space or sheath This voltage will accelerate ions from the negative glow region to the cathode where they will cause secondary electron emission with a probability of approximately 0 1 to 0 05 The secondary electrons will be accelerated back through the cathode region by the potential and will gain very high energy These high energy electrons will cause more iomzation and excitation in the bulk near the sheath The radiative decay of these excited atoms results in the negative glow

46
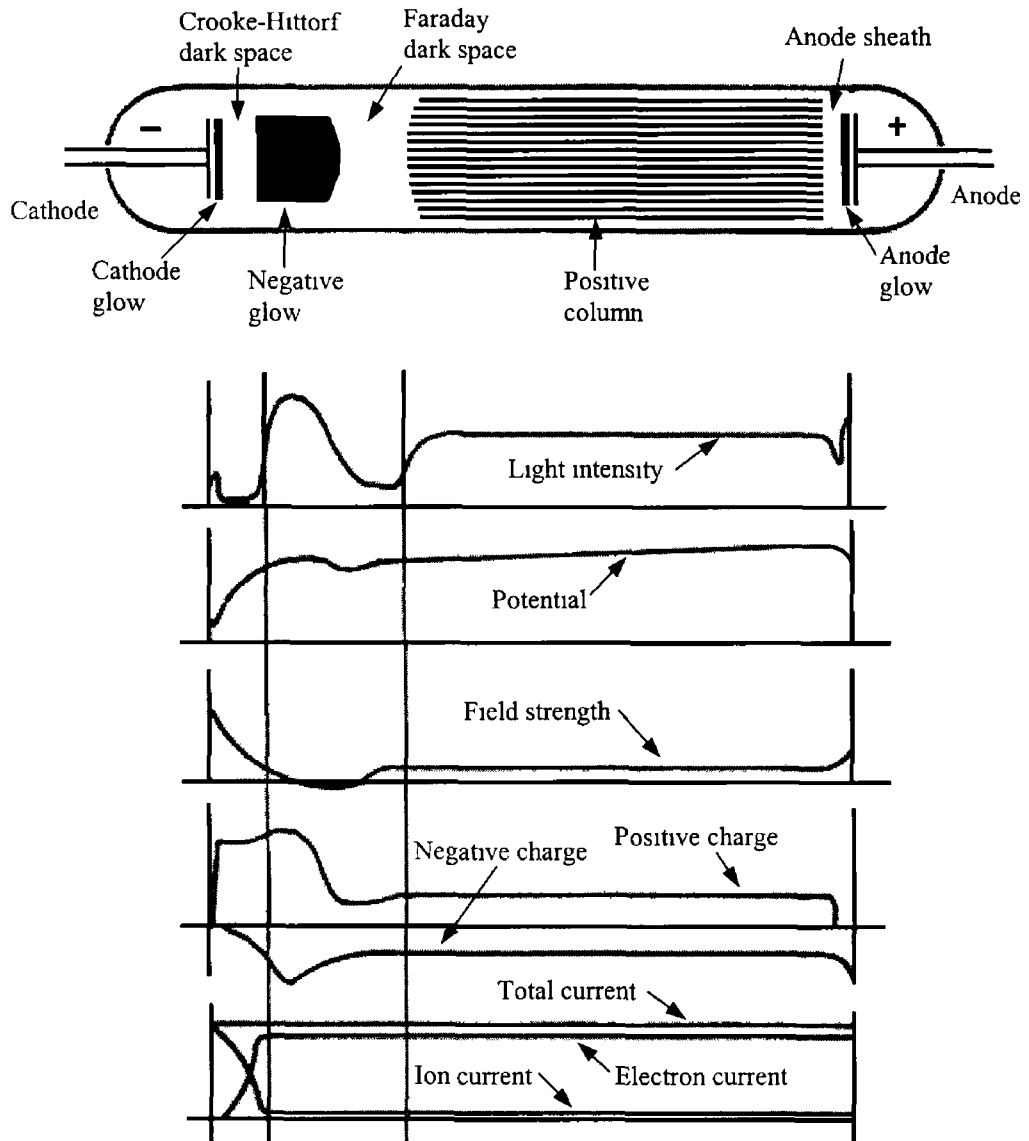
Figure 2 17 Classical picture of the architecture of a DC glow discharge After breakdown, the discharge arranges itself into characteristic regions to provide for particle and energy input Most of the potential is dropped across the cathode sheath region, which contains ions but very few electrons There are approximately equal number of ions and electrons in the negative glow, Faraday dark space and positive column (after [80])

Owing to the large electric field that exists in the cathode dark space region, the electron density is small, and the ion current is determined by space charge-limited flow or mobility-limited flow as described in Sect 2 7 5 2 Assuming that we have a free fall condition (i e , the ions do not suffer collisions in the sheath), we can use eqn (2 37) to write the Child-Langmuir expression for the ion current density at the cathode,

$$J = \frac{4}{9}\varepsilon_0 \left(\frac{2e}{M}\right)^{\frac{1}{2}} \frac{V_0^{\frac{3}{2}}}{s_m^2} \qquad (2\ 42)$$

where V_0 and s_m are the potential drop across the cathode sheath and the sheath width, respectively

2 7 8 1 2 Secondary electron generation

Ion bombardment of the cathode will cause secondary electron generation The secondary electron yield, which is the ratio of secondary electrons emitted per incident ion will depend upon the material and the ion energy It will also depend critically on the condition of the surface, including both the crystal orientation and the degree of surface contamination Some materials can have secondary electron coefficients which exceed unity The energy of the secondary electrons is generally quite low, typically peaking around 2-5 eV [81]

2 7 8 1 3 Ionization in the cathode sheath

One of the greatest debates in the area of low-temperature plasma behaviour is whether there is significant ionization in the cathode sheath Much of the older literature has assumed that virtually all of the ionization needed to supply the ions which are accelerated to the cathode (and therefore lost at the cathode) occurs in the sheath [82] One observation that supports this position is that the product of the dark space thickness and the neutral pressure is constant for a given supply voltage On the other hand, for species like Ar, excitation will accompany ionization, since the energy threshold for the first excited state is similar to that for ionization (11 5 eV and 15 6 eV respectively) Thus, if there is no emission, there will be little or no ionization This point of view is consistent with that of Chapman, who uses a simple calculation of ionization rates to conclude that ionization in the sheath cannot account for the observed electron density [63]

This apparent conflict may be resolved by the numerical modelling of the DC glow performed by Graves and Jensen [83] They developed a continuum model which they applied to a DC Ar discharge at 500 mTorr While the identification of their results

does not exactly follow the schematic description of the DC glow given above, they do show a sheath region of high electric field and a bulk region which seems to be identified with the negative glow region (see next section) The ionization does occur in the sheath region, however, upon close inspection, the high electric field extends beyond the sheath region into the negative glow, as does the ionization source From their results, it would appear that ionization does occur in the sheath and in the region of the sheath-glow interface In general, in a DC discharge sufficient ionization must occur due to the secondary electrons to sustain the plasma

2 7 8 1 4 Ion charge exchange in the cathode sheath

Ions which are being accelerated through the sheath will, in general, undergo charge exchange collisions with the neutral species as

$$Ar^+ + Ar \rightarrow Ar + Ar^+$$
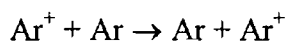
This will alter their energy distribution at the cathode, since an ion produced by charge exchange somewhere in the sheath will not receive the full acceleration of the sheath drop This problem has been studied both theoretically and experimentally by Davis and Vanderslice [84]

2 7 8 1 5 The anode sheath

Before considering the negative glow and positive column regions of the discharge, let us consider the anode sheath region (see Fig 2 17) The anode sheath is, more or less, a Debye sheath That means that there will be a voltage drop of typically $3kT_e/e$ (see Section 2 7 5) For a typical discharge with $T_e = 3-4$ eV, the plasma will be at a potential of about 9-12 V above the anode Since there is a current flowing through the plasma, which for the DC case must be constant everywhere, then there must be a net electron current at the anode equal to the ion current at the cathode We note, however, that there will also be an ion current at the anode, given the fact that the discharge is at +10V with respect to the anode From the numerical calculations [83], the ion current is about 10% of the electron current at the anode In any case, the energy

of the ions bombarding the anode is sufficiently low as to not cause secondary emission Some of the secondary electrons created at the cathode and accelerated by the cathode sheath may pass through the discharge and strike the anode with enough energy to emit additional secondary electrons This can be an important process at low pressures

2 7 8 1 6 The negative glow region

The luminous negative glow is a plasma region characterized by nearly equal electron and ion densities, typically in the range of 10^9 - 10^{11} cm^3 where the electron temperature measurements within the glow show typical values of 2 - 10 eV Since this region is a plasma, the electric field is small The sources of energy input to the glow include the energetic secondary electrons emitted from the cathode and accelerated across the sheath, and direct acceleration of the electrons in the glow by the electric field

The strong electric field in the cathode region is responsible for energy input to the negative glow, both through acceleration of secondary electrons, and by acceleration of glow electrons near the glow edge Thus, the magnitude of this field will be determined self-consistently by the plasma's requirements for ionization to sustain itself

A magnetic field nominally parallel to the cathode, as found in a magnetron configuration [42,85,86] will cause the electrons to undergo gryo orbits, providing the collision frequency is below the cyclotron frequency As a consequence, the electrons will spend more time in the vicinity of the cathode and their ionization efficiency will be increased This will result in a decrease in the sheath field and potential, and will also produce a higher density discharge

The continuum model for the DC glow [83] displays a negative glow region adjacent to the sheath and extending to the anode The calculated temperature for this region is about 0 7 eV, which is considerably less than is typically measured

The negative glow region, along with the cathode and associated dark space comprise a self-sustaining discharge configuration as shown in Fig 2 18 The sheath field will accelerate ions formed in the negative glow These ions will cause secondary

electrons to be emitted at the cathode The secondary electrons will be accelerated across the sheath and represent the main energy input to the plasma These high-energy secondary electrons will generate more ionization in the negative glow Thus the discharge is sustained
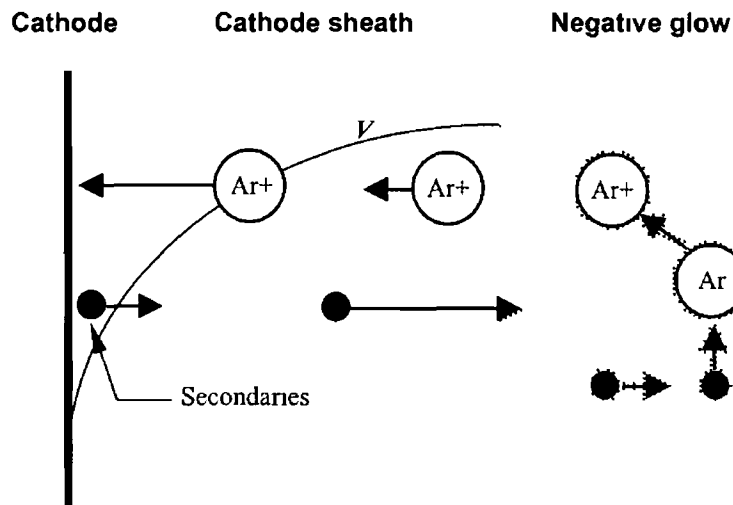
Figure 2 18 Schematic of the discharge behaviour in the cathode sheath-negative glow regions Ions from the negative glow fall through the cathode sheath causing secondary electron emission The secondaries are accelerated back through the sheath and comprise the main energy input to the negative glow which supports the ionization process These regions comprise a self-sustaining combination

2 7 8 1 7 Beyond the negative glow

Although a dc glow discharge may end with the negative glow, in general it does not Beyond the negative glow is another dark space, called the Faraday dark space, followed by the positive column and the anode sheath Although the positive column is not typically found in processing plasma discharges, we will now consider briefly the so-called Faraday dark space and the positive column

Regardless of whether the energetic secondary electrons formed at the cathode, and accelerated through the (Crooke-Hittorf) dark space directly cause ionization, or whether they transfer their energy to the electrons in the negative glow which then cause ionization (or whether it is a combination of both types of processes), it is clear that the energetic electrons represent the main source of energy input to the glow The extent of

51

the negative glow is determined by the range over which the energetic electrons lose their energy This determines the location of the cathode end of the Faraday dark space There is, however, a small electric field in the plasma regions of the discharge, and this electric field will increase the temperature of the electrons by acceleration and subsequent scattering We note that it will take a certain distance to travel before the electrons reach their equilibrium energy as a result of the electric field acceleration Where the electrons have not yet equilibrated, we would expect no light Until they drifted that far, the electron energy will be below that necessary to excite inelastic processes, such as excitation, and hence no light will be visible in that region Since this distance is longer than the negative glow region, there is another dark space, namely the Faraday dark space

2 7 8 1 8 The positive column

In the positive column (see Fig 2 17), the electrons have equilibrated with the electric field where the electron energy becomes sufficient for inelastic processes, such as excitation The local electric field accelerates the electrons and represents the main energy input source The main losses are diffusion to the walls and radiation from line emission In electronegative discharges, electron attachment may be an additional important loss mechanism Since many plasma processes involve halide-containing gases, this is an important consideration

The positive column may be arbitrarily long [54], or absent entirely, and serves to connect the anode electrically to the remainder of the discharge The positive column and other features beyond the negative glow do not usually play an important role in plasma processing (although they are very important for discharges used as light sources)

2 7 8 2 RF glow

In a DC glow discharge, most of the input power is used to accelerate the ions through the sheath, and appears as heat when the ions strike the cathode If the secondary electron coefficient were 0 1, then, to a good approximation, only 10% of the power will end up in the negative glow from the secondary electrons which are

accelerated in the sheath In this sense, the DC glow is a rather inefficient plasma generator, though for processes which depend on ion bombardment, such as sputtering, this is not a problem

An even more serious limitation of a DC glow discharge is the necessity of conducting net current to sustain the discharge This requirement generally precludes the use of insulating materials in sputtering targets, substrates, or deposited films, because the insulators would prevent DC current conduction If the insulators did not cover the entire electrode surface, it may be possible to sustain a DC discharge, but the insulators will build up a charge, making processes difficult to control

The use of an AC power source can alleviate both these shortcomings of the DC glow discharge Let us start by considering a very low frequency AC power source, with a period which is long compared to the time it takes for the plasma particles to come to equilibrium with the electric field We will further assume that there are no insulators present In this case, the AC discharge will be very similar to the DC discharge, except that the current will reverse every half cycle A sheath will form at the electrode which is negative during the particular half cycle of the AC power, and ions will be accelerated across this sheath The ions, which are able to cross the sheath in a short time compared to the AC period, will gain an amount of energy roughly equal to the instantaneous AC voltage Thus, the ions striking the electrodes will have a distribution of energies, which will extend to approximately the peak AC voltage

If we now consider what happens if we have an insulating electrode, we would find that current would flow until the insulator charged up and terminates the discharge On the next half cycle, however, the insulator would discharge, and current would flow in the opposite direction until the insulator charged up again The insulator behaves like a capacitor that is charged in alternate directions by the plasma If the AC frequency is increased to the point where the charging time is much longer than the AC period, current will flow in the plasma for the entire AC cycle A frequency of about 50 - 100 kHz is usually sufficient to achieve this condition In this case, also, we would find that sheaths would form and ions would be accelerated by the instantaneous field, and arrive at the electrodes with a distribution of energies up to approximately the peak AC voltage

As the frequency of the AC source is increased, new phenomena begin to appear The details of the various frequency-dependant effects have been reviewed by Flamm [87], and have been reported for a few specific processes [81,88,89] However, due to the fact that most commercial RF plasma equipment is designed to work at the internationally assigned frequency of 13 56 MHz, the use of different frequencies has not been exploited and remains an untapped opportunity for optimizing processes We will not consider this topic further here, but will instead explore the salient features of plasma operation at 13 56 MHz At this frequency, the massive ions have too much inertia to respond to the instantaneous electric field in the sheath regions, while the lighter electrons will Owing to the differences in mobilities of the ions and the electrons, however, a time-average bias will arise for certain configurations

2 7 8 2 1 Self bias and plasma potential

To see how this comes about, let us consider a discharge system with one small electrode connected to an RF power source through a coupling capacitor shown in Fig 2 19 The characteristic response of the plasma to a voltage V is given by the curve in Fig 2 20 Owing to the much greater mobility of the electrons compared to the ions, a given positive voltage will result in a much larger electron current than the ion current which flows for the same negative voltage In effect, the plasma behaves like a leaky diode, showing a much larger effective resistance for ion current than for electron current
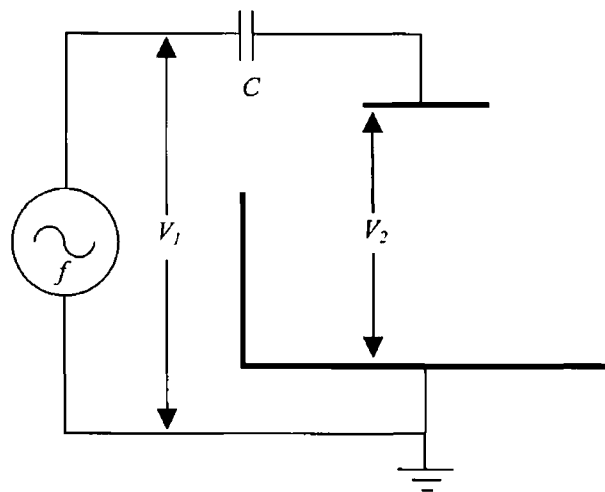
Figure 2 19 Schematic of electrode configuration for an RF glow discharge An RF power supply is capacitively coupled to the electrodes

I

Electron saturation

V

Ion saturation
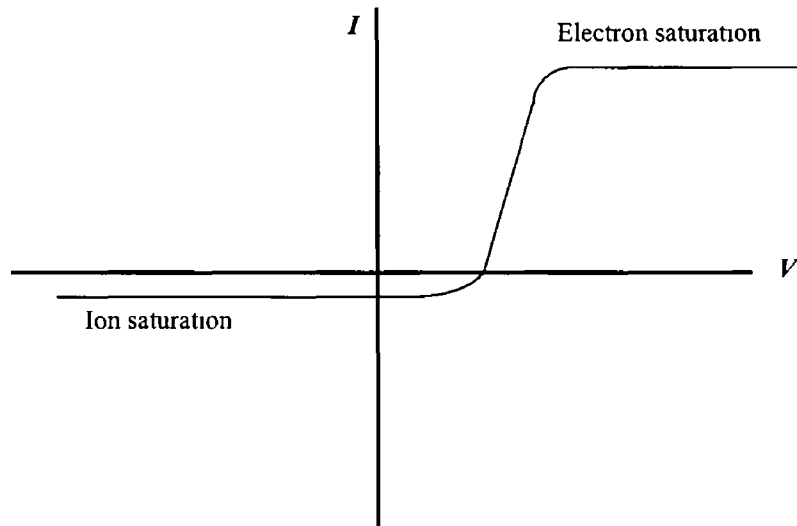
Figure 2 20 Electron and ion current as functions of the applied potential V The greater mobility of the electrons compared to the ions results in a larger electron current for a given positive voltage than the ion current which flows for an equal negative voltage

Let us now apply a square wave with peak amplitude V_0 (See Fig 2 21) Initially, when the applied voltage goes to $+V_0$, the potential across the plasma is V_0 The capacitor will be charged through the effective resistance of the plasma for electron current flow, and the plasma potential V_2 will drop as shown in Fig 2 22 When the power supply changes sign, the voltage across the plasma drops instantaneously by - $2V_0$, after which the voltage decays with the longer time constant associated with the higher effective resistance ion current flow As shown in Fig 2 22, this continues until the time average electron and ion currents are equal, a condition which results in time-average negative bias on the electrode [8] Although the derivation was presented with a square wave power source, a similar effect holds for a sine wave, as in Fig 2 23

Implicit in this derivation is the fact that the area of the large electrode was sufficient to permit all of the necessary currents to flow during each cycle In other words, the limiting impedance for current flow on both half cycles occurs at the small area electrode It is important to note that the features of the RF discharge which resulted in the self bias were the presence of the coupling capacitor (which ensures a time-average zero current), and the fact that one of the electrodes was much smaller
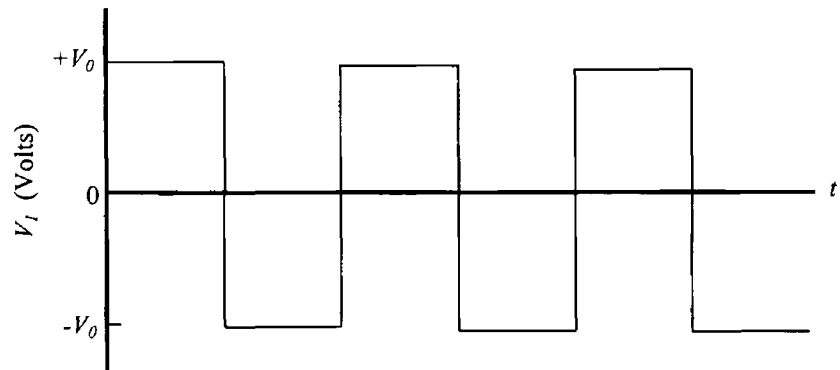
Figure 2 21 *Output square wave of peak voltage V_0 which is used for the circuit shown in Fig 2 19*
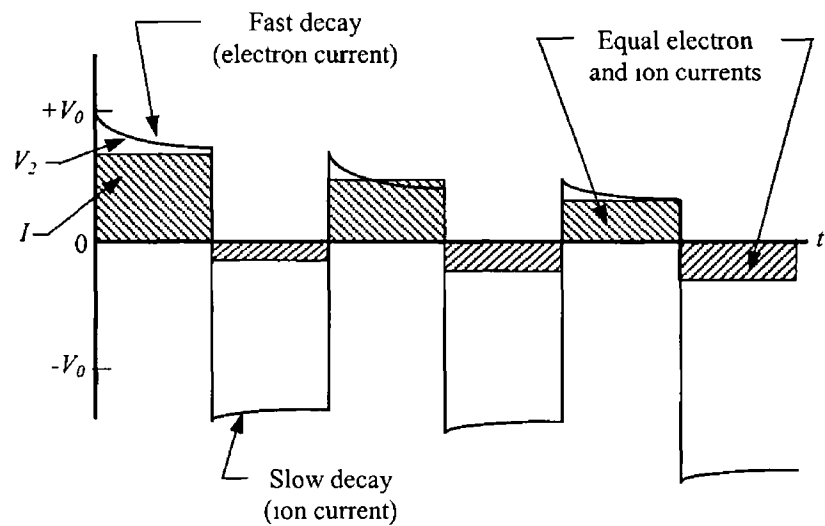
Figure 2 22 *Behaviour of the discharge voltage V_2, as the self bias develops to produce equal electron and ion currents On each half cycle, the current decays as the capacitor charges from the plasma On the half cycle where electron current flows, the decay is faster, because the plasma has an effectively lower impedance owing to the greater mobility of the electrons*

Applied voltage, V_1

V_0

Volts

0

t

$-V_0$

Voltage on small electrode, V_2
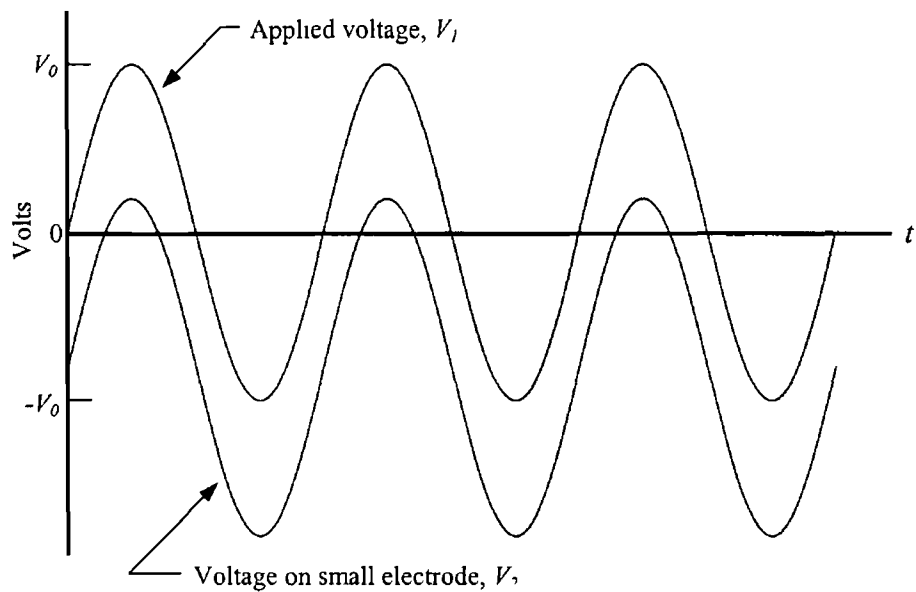
Figure 2 23 Self bias for a sine wave driven system

than the other The driven electrode is not necessarily the one where the bias occurs
The location of the capacitor is similarly irrelevant in determining the bias In fact, if the
apparatus were symmetric and totally decoupled from ground, there would be no self
bias The grounded electrode can have a bias if there is a coupling capacitor somewhere
in the circuit and the grounded electrode is smaller than the driven electrode

The plasma prefers to be more positive that the most positive surface Then, for
the case of a large bias, we would expect the plasma potential to behave as shown in
Fig 2 24 Even with the self bias, the small electrode is positive for some fraction of a
cycle, so the time average plasma potential is usually higher than for the DC case Ions,
which cannot respond on the fast RF time scale will bombard the small electrode with
an energy given by the difference between the time-average plasma potential and the
time-average self bias

The magnitude of the bias will depend on the neutral pressure [90] As the
pressure is increased with constant power into the discharge, the bias will decrease This
is due in part to decreases in the RF voltage, because the plasma impedance decreases as
the neutral density increases Another way of looking at this phenomenon is that at high

densities, the discharge does not require as high a sheath field to sustain itself, because it is able to put energy directly into the glow electrons
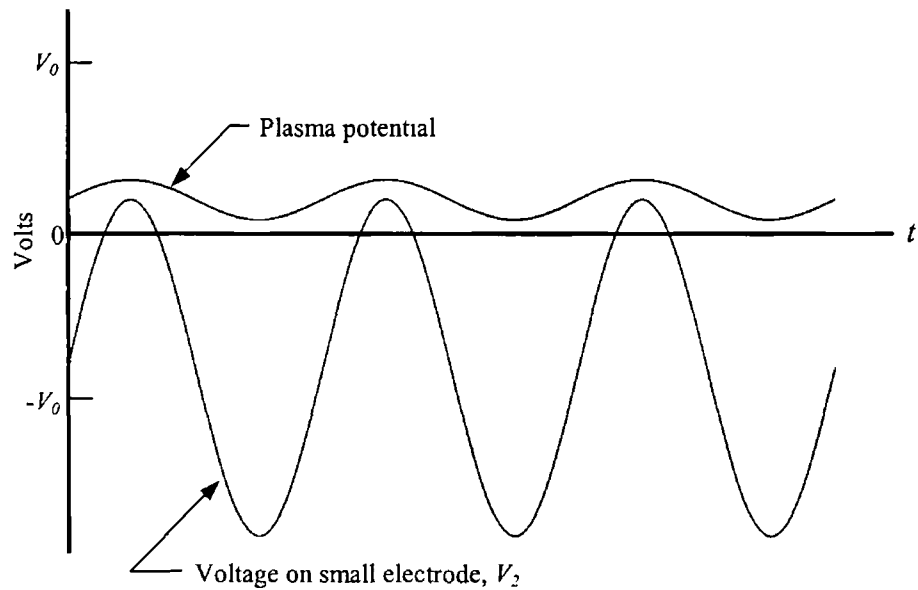
Figure 2 24 Time variation of the plasma potential shown with the self bias voltage on the small electrode In the absence of collisions in the sheath, the ion energy at the small electrode will be the difference between the average potential and average self bias

The asymmetric RF discharge configuration, which results in high bias, is the chosen configuration for reactive ion etching [91], where ion bombardment produces anisotropic etching The highest bombardment energies are obtained as the pressure is lowered Since excessive ion energy can result in damage to a wafer, however, some reactive ion etch processes are operated at higher pressures (200-300 mTorr), to reduce the ion energy both through a lower bias and collisions in the sheath The latter effect, however, tends to destroy the directionality of the bombarding ions, which reduces their utility for anisotropic etching

For the case of a symmetric discharge (equal area electrodes), where there is no self bias, the plasma potential appears as in Fig 2 25 Here we see that the time average plasma potential will be much greater than for the DC case, and, even though there is no bias, there will be energetic ion bombardment which will occur at both electrodes In this apparatus, energetic ion bombardment occurs primarily due to the large plasma

potential An excellent summary of the self bias and plasma potential behaviour has been given by Kohler *et al* [92]
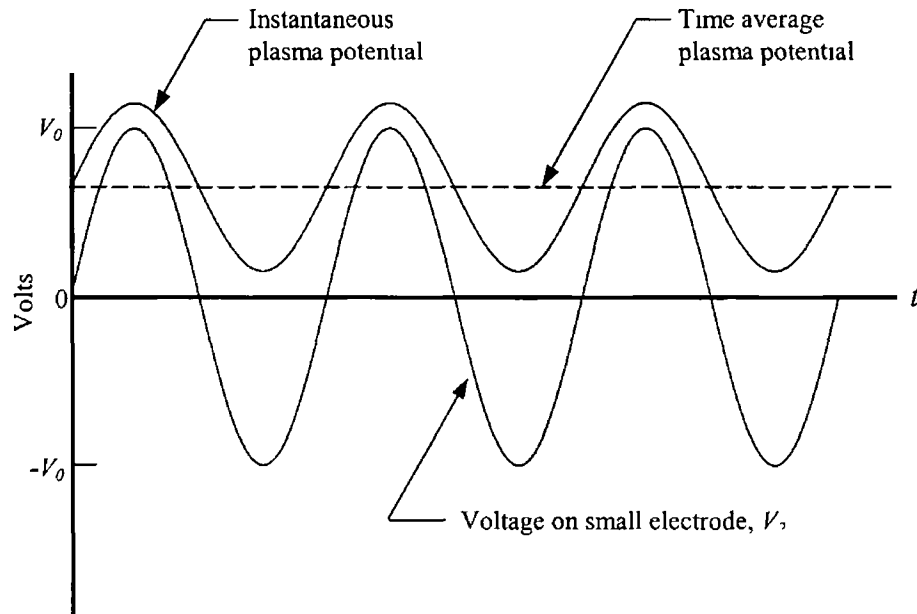
Figure 2 25 Plasma potential and self bias voltage for a symmetric discharge configuration There is no self bias in this case, but the plasma potential is higher than for the asymmetric case

The sheaths in an RF discharge have large RF displacement currents flowing through them, but rather small conduction currents The sheaths will behave like capacitors with some leakage current The main part of the RF glow will be resistive, much as the negative glow and positive column in a DC discharge The self bias voltage will divide between the two electrodes in a fashion inversely proportional to the capacitance of the sheath regions

$$\frac{V_a}{V_b} = \frac{C_b}{C_a}$$

(2 43)

where a and b denote the two electrodes The capacitance of the sheath regions is roughly given by

$$C = \frac{\varepsilon_0 A}{s}$$

(2 44)

where A is the area of the sheath and s is the sheath thickness There are two effects which make this expression difficult to use in practice (1) the effective area of the

sheath will depend on (unavoidable) stray coupling from the electrode to other surfaces, and (2) s will depend in a complicated way on the discharge parameters Koenig and Maissel [8] attempted to relate s to the voltage by requiring that the Child-Langmuir space charge-limited currents at each electrode be equal

$$\frac{V_a^{\frac{3}{2}}}{s_a^{2}} = \frac{V_b^{\frac{3}{2}}}{s_b^{2}} \tag{2 45}$$

From eqns (2 43), (2 44) and (2 45) we obtain

$$\frac{V_a}{V_b} = \left(\frac{A_b}{A_a}\right)^4 \tag{2 46}$$

This concludes that the bias divides between the electrodes in such a manner as to be inversely proportional to the fourth power of the ratio of the electrode areas The caveats noted above, however, conspire to render this simplistic derivation much less than adequate More sophisticated models have been presented by Horwitz [93] and Kohler *et al* [92]

2 7 8 2 2 Discharge characteristics

Owing to the self bias, there will be energetic ion bombardment of the smaller electrode, with attendant secondary electron emission (In addition, there will also be some bombardment of the larger electrode) In this respect, an RF discharge can be similar to the DC discharge there will be a cathode sheath and a quasi-negative glow which is energized by the accelerated secondaries There are differences, however Although the ions are typically going slowly enough that they will respond only to the time average potential, the electrons will generally cross the sheath region in a fraction of the RF period This can give rise to time dependent phenomena In particular the edge of the sheath will generally oscillate Some researchers believe that this mechanism can put energy directly into the electrons by a "surf riding" effect [94]

One characteristic which distinguishes the RF discharge from the DC discharge is that, because the RF field is changing direction in time, it can put energy into the electron energy distribution function more readily than the DC field In the DC case an electron had to drift a considerable distance in the field to come into equilibrium with it This is the reason that the positive column is separated from the negative glow In the

RF case, however, the electrons will not experience a net drift, since the field is changing direction They will equilibrate after a characteristic time Owing to this, the RF discharge is more efficient than the DC discharge In a sense, the negative glow and positive column regions overlap

2 7 8 2 3 Summary of the RF glow discharge

The RF glow discharge embodies many of the same qualitative features of the DC glow discharge, with the formation of sheaths in which strong electric fields will accelerate ions and electrons At low frequencies, where ions can follow the changing electric fields, the discharge will behave similarly to the DC case As the frequency increases, the ions will no longer be able to follow the instantaneous electric field, but will instead respond to the time averaged fields Here, for discharge configurations with unequal electrode areas and where the electrons are the dominant negative charge carriers, a self-bias will arise which will produce a time-average negative voltage on the smaller electrode Ions will be accelerated by the difference between the time-average plasma potential and the time-average bias In general, the energy of the bombarding ions in an RF discharge will increase as the neutral pressure is decreased

Energy input to the RF discharge occurs through three mechanisms Energetic ions striking the electrode will cause the formation of secondary electrons These electrons can be accelerated through the sheath and cause ionization as in the sheath and negative glow regions of the DC discharge The oscillating electric fields in the glow can input energy directly into the electrons, much in the same way as the positive column of the DC discharge Finally, the oscillating sheath electric field will accelerate electrons in the glow This "surf-riding" mechanism has no direct analog in the DC discharge

Several enhancement schemes for the RF discharge are possible The addition of a magnetic field nominally parallel to the electrode surface will result in confinement of the electrons Such schemes are used for magnetically enhanced reactive ion etching [44] Their principle advantage is that the presence of the magnetic field increases the electron ionization efficiency This results in a lowering of the sheath potential and

concomitant lowering of the bombarding ion energy, with no degradation of plasma performance

It is also possible to use microwave power, typically at 2 45 GHz, to operate a discharge In these schemes, the power can be coupled radiatively, obviating the need for electrodes One very important such configuration is the electron cyclotron resonance reactor [53], which includes a magnetic field and a microwave at a frequency which is matched to the cyclotron frequency of the electrons

2 7 9 Electronegative discharge

The electronegative plasma is different from the electropositive plasma (e g Ar discharge) due to the fact that there is an additional type of particle present in this plasma together with the positive ions, electrons and the neutral atoms This additional particle is the negative ion Due to the presence of the negative ions the entire plasma chemistry is changed and therefore the plasma parameters become completely different from those of the electropositive discharge The commonly used electronegative gases in plasma processes include halogens and halogen containing compounds (e g Cl_2, BCl_3, CF_4, SF_6), oxygen and others [95] There has been much work done on electronegative gases [96-99] SF_6 is a very common electronegative gas used for the reactive ion etching of materials [100-104] High selectivity is obtainable using the SF_6 gas or a mixture of SF_6 and other gas due to the presence of a greater fluorine content This selectivity may be further enhanced by adding a small amount of Cl containing gases (such as $CFCl_3$, Cl_2 and C_2F_5Cl) which substantially reduces undercutting effects [105-107]

2 8 Measurement of Plasma Properties

Once a plasma has been created (or even while it is being created) in the laboratory or in nature, it is usually desirable to be able to measure a variety of the properties of that plasma As a state of matter, plasma is a complex medium, and the measurement of its properties in a clear and unambiguous manner is correspondingly difficult In addition to shape and location, the plasma properties to be measured include density, temperature, thermal conductivity, dielectric tensor, radiation rate, radiative-

absorption coefficient, collision frequency, ordinary and anomalous resistivity, velocity-and configuration-space diffusion coefficients, distribution function, and the stability or instabilities of the plasma Of course, some of these properties are related, and a measurement of one determines one or more of the others There are many techniques for measuring plasma properties Only a few important of them are described here [108-111]

2 8 1 Current and voltage measurements in plasmas

Since a plasma consists of mobile ions and electrons, the application of an electric field to a plasma causes these charged particles to move, resulting in an electric current The ratio of the discharge potential to current is the impedance of the plasma Impedance is one of the important plasma characteristics and depends on the collision frequency and density in simple plasma models Thus the measured impedance can be compared with theoretical values to verify or study plasma properties In some instances the current or voltage measured in the external circuit of the electrical apparatus used to create the plasma can provide useful information concerning the state of the plasma [41]

The current in a plasma discharge is usually measured by means of a current transformer, which can be air-core, ferrite-core, or iron-core, depending on the rise-time requirements in a given experiment A current transformer generates a voltage proportional to the derivative of the current through the loop The voltage from the current transformer can be recorded directly on an oscilloscope and integrated graphically, or the signal can be integrated electronically by means of a passive (or active) circuit integrator before it is recorded An air-core current transformer is shown schematically in Fig 2 26, together with a passive circuit integrator

In some cases a small current coil is used instead of a current transformer allowing the main discharge current to flow through it This gives direct measurement of the discharge current The schematic diagram of the apparatus for a current-voltage measurement used by Mlynk and Hess [10] is shown in Fig 2 27 The operating impedance bridge in Fig 2 27 includes a filter which is tuned for a bandwidth of 5-15 MHz Thus any harmonics of the 13 56 MHz signal were removed
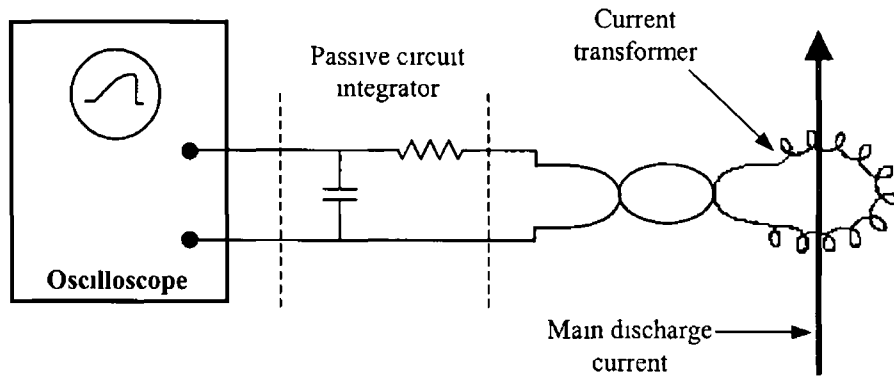
Figure 2 26 *Schematic of measuring RF current using current transformer [41]*
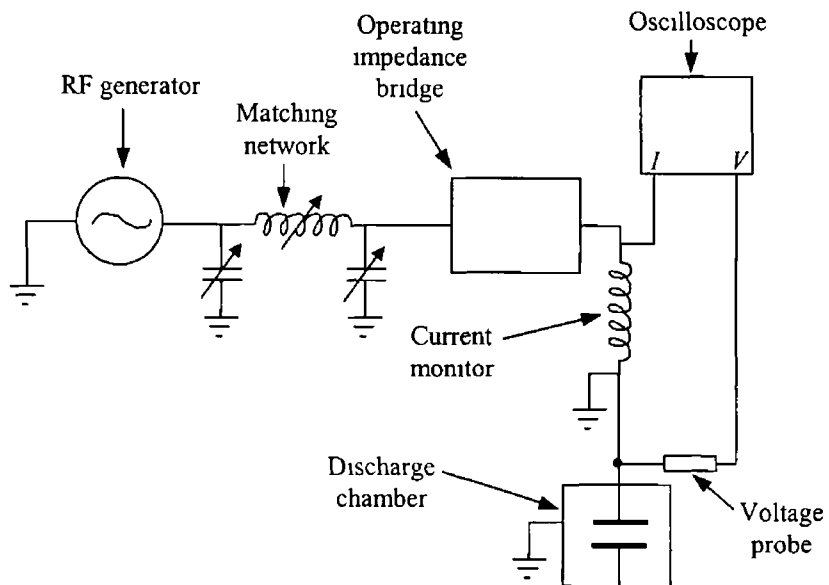
Figure 2 27 *Schematic of an experiment showing method of measuring RF current and voltage associated with the discharge*

Roth *et al* [11] used commercial voltage (Phillips PM9100) and current (Pearson 2878) probes (Fig 2 28) to measure the RF voltage and current Both probes have sufficient bandwidth to measure the fundamental frequency of 13 56 MHz and up to four harmonics They are housed in an aluminium box, called a probe station, in order to provide shielding from stray radiation The box is designed so that it may be inserted in series with the coaxial cable delivering RF power to the powered electrode
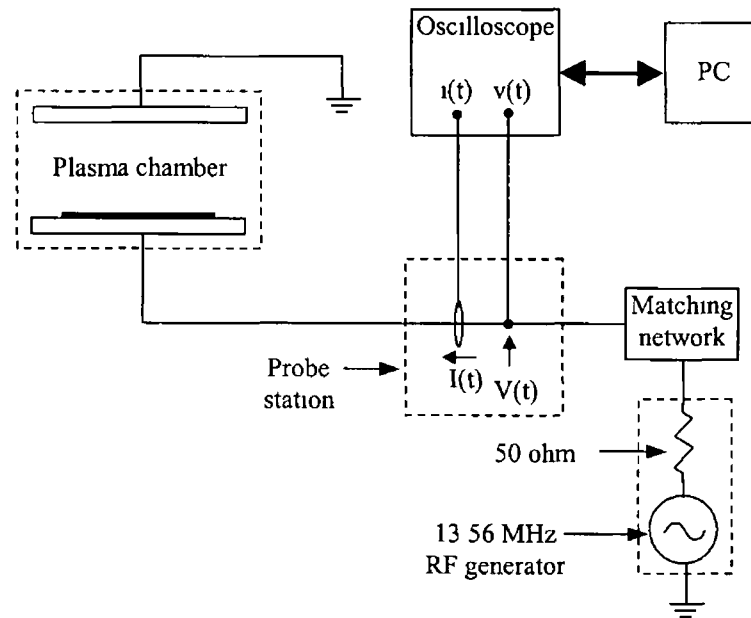
Figure 2 28 Schematic of an experiment showing method of measuring RF current and voltage using commercial probes

A commercially developed new method of measuring plasma current and voltage is Plasma Impedance Monitoring [112-114] The main parts of this system include (i) I-V sensor, (ii) acquisition and control unit, and (iii) microcomputer The I-V sensor is a post-match current-voltage sensor I-V sensors are located between the matching network and the driven electrode of the plasma reactor (Fig 2 29) The sensors measure current and voltage signals that are proportional to the plasma RF current and voltage The signal is fed to the acquisition and control unit Microprocessor based analysis routines operate on the acquired signals to yield the Fourier components of the fundamental and the first four harmonic components The phase angle between the harmonic components is also computed The basic RF plasma parameters (current,

65

voltage and phase angle) are then transferred to the microcomputer via an interface cable for display and further analysis A detail description of the Plasma Impedance Monitoring System is given in chapter 3
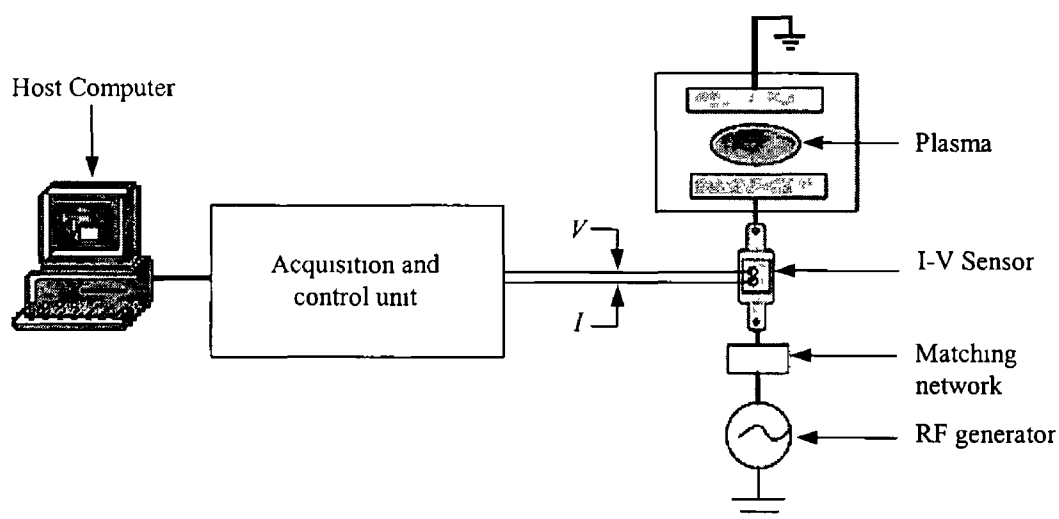
Figure 2 29 Schematic diagram of measuring RF current and voltage using Plasma Impedance Monitoring

2 8 2 Plasma probes

There are a variety of probes used to measure plasma properties They all share the feature of being inserted into the plasma medium in order to sample plasma properties in a local region Most probes perturb the plasma in some way, and care must be exercised to ensure that the plasma measured in the presence of the probe is the same as the plasma before the probe was introduced The two simplest probes used in plasma measurements are electrostatic (or Langmuir) and magnetic probes

2 8 2 1 Electrostatic or Langmuir probes

Figure 2 30 is a schematic of an electrostatic probe, together with the electric circuit needed to bias the probe to different voltages relative to the plasma while measuring the current collected by the probe Langmuir and Mott-Smith [115],

developed the theory of such probes and showed that they could be used to measure the electron density n_e, the ion density n_i, the electron temperature T_e, the plasma potential V_p, the plasma floating potential V_f (i e , the potential of the probe for zero net current) and the random electron and ion current densities It was through this work that such probes became known as Langmuir probes Many improvements in their design and in the sophistication of electronic instrumentation associated with their use have been made over the years [108] They are a simple and still useful tool in the study of laboratory plasmas
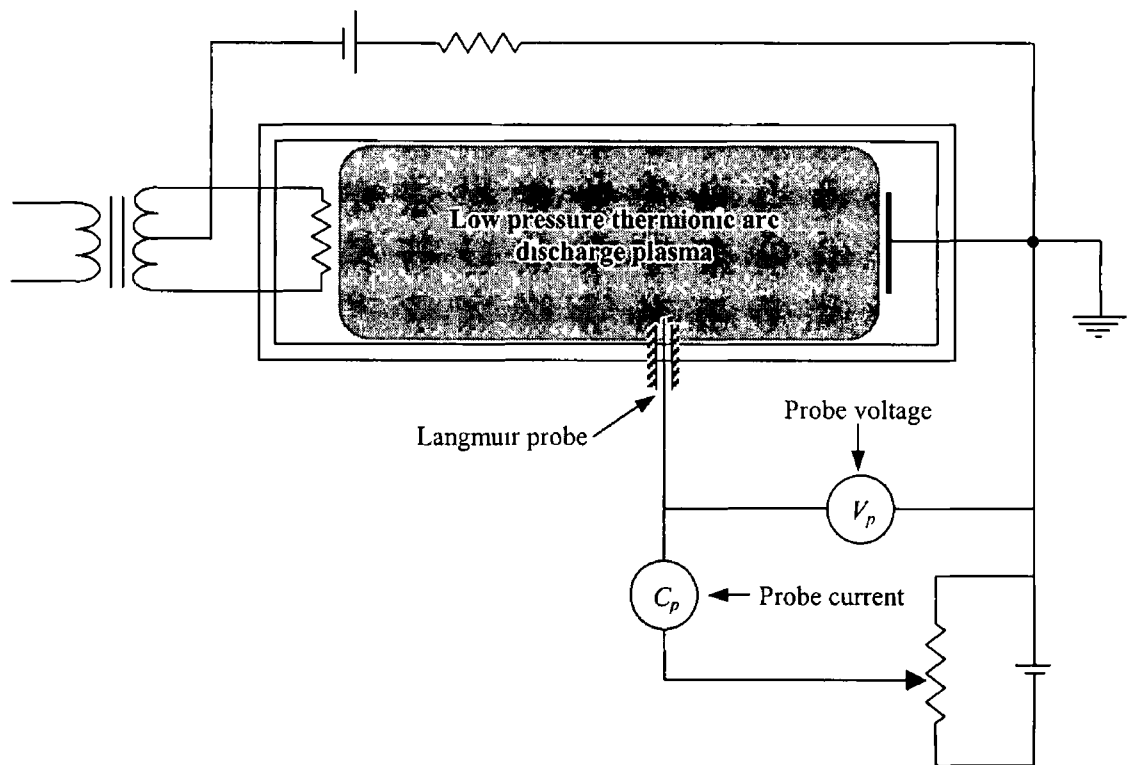
Figure 2 30 *Schematic of a Langmuir electrostatic probe in a plasma showing biasing arrangement*

Generally, a Langmuir probe is a small-diameter insulated tungsten wire with a small exposed region at its end to collect electrons or ions from the plasma, depending on the potential of the probe relative to the plasma Figure 2 31 is a schematic of typical current-voltage characteristics obtained with a Langmuir probe in an unmagnetized plasma If the potential of the probe is much larger than the local potential of the plasma, the probe attracts electrons and repels ions, forming a sheath region around the probe, which is electron-rich This sheath region is a few Debye lengths thick and
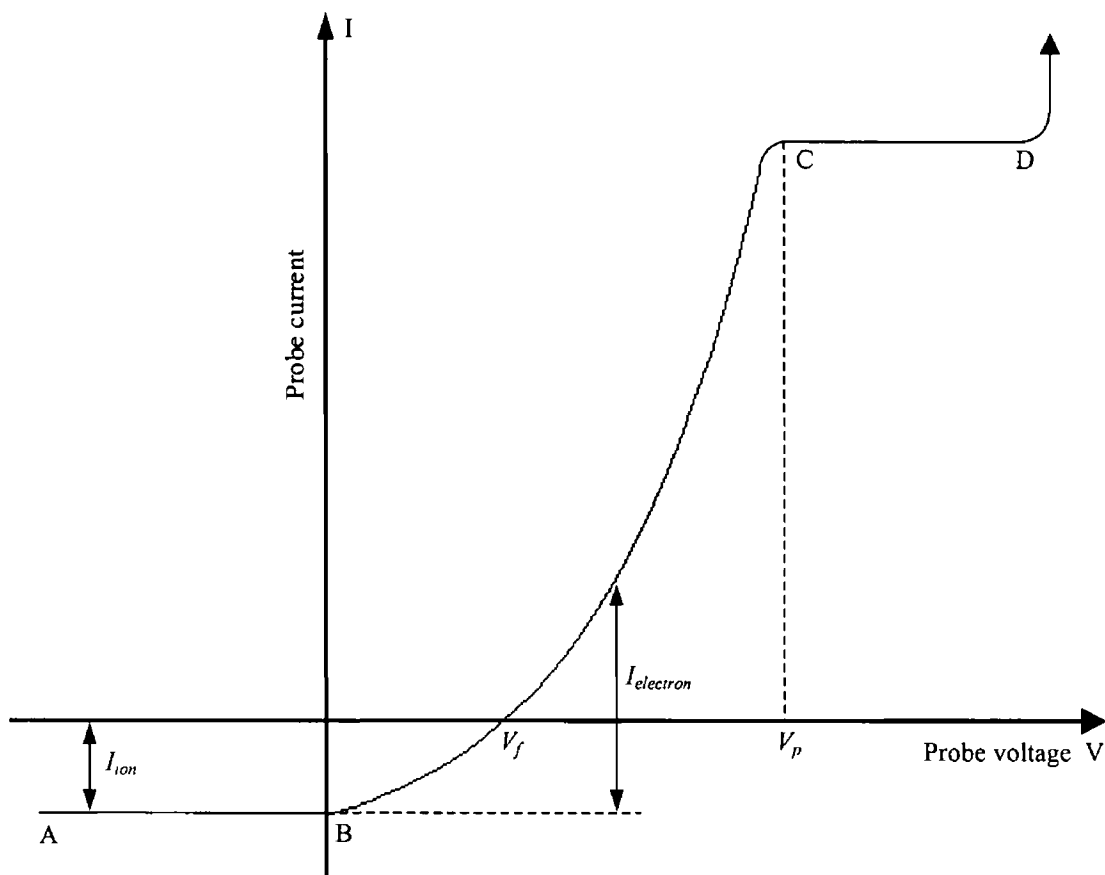
Figure 2 31 Volt-ampere characteristic of a probe in a low-density arc-discharge plasma Diagram is not to scale since the maximum electron current is usually 1,000 times the maximum ion current [41]

occurs for the same reason that a given charged particle in a plasma is shielded, as described in section 2 7 1 Thus the influence of a probe in a plasma is limited to a region about one Debye length from the probe The region AB in Fig 2 31 represents saturated ion current for a probe biased negatively with respect to plasma floating potential The curve BC is the true electron current, since the probe no longer repels electrons for potentials above B The region CD is nearly horizontal, since at these probe potentials all the random electron current entering the probe sheath is collected Above D, the voltage drop across the sheath is greater than the ionization potential, and the electrons moving toward the probe ionize the background gas, resulting in a probe arc

2 8 2 2 Magnetic probes

Magnetic probes are used to sample the magnetic fields in or around plasmas The probe usually consists of a few turns of wire arranged in a loop, which may be a millimeter in diameter or larger, as required for the measurement These magnetic probes operate on the principle that a time-changing magnetic field induces a voltage in the loops, the magnetic field can be determined from a measurement of the induced voltage These magnetic probes, which sample the magnetic field in a given direction, are most generally used in fast-compression plasma experiments, such as the dynamic pinch [41,116] Fig 2 32 is a schematic of a magnetic probe as it might be used in a dynamic pinch If the probe is oriented so as to be sensitive to the θ component of the magnetic field, the signal detected by the probe will be zero until the current sheet associated with the collapsing plasma passes the probe position The magnetic field at the probe position then rapidly jumps to the value associated with the discharge current If the probe is small and movable, it is possible to measure the location of the current shell as a function of time, and compare the results with the theoretically predicted collapse rate

One difficulty connected with the use of magnetic probes is that they generate a voltage proportional to dB/dt rather than B This problem is usually solved by integrating the probe signal with a passive circuit integrator, as shown in Fig 2 32 Care must be exercised to shield magnetic probes electrostatically so that electric fields associated with the discharge are not also detected Such shielding limits the maximum frequency of magnetic field fluctuations that can be detected by the probe system Many other details concerning magnetic probes must be understood in order to avoid errors in their use [108]

2 8 3 Other methods of measurement of plasma properties

2 8 3 1 Photography and atomic spectroscopy

In many cases plasmas emit radiation from atomic transitions in the visible region of the electromagnetic spectrum with sufficient intensity ($>10^4$ Joule/m^2 at the film) so that the plasma can be photographed to determine its position and motion Fig 2 33 is
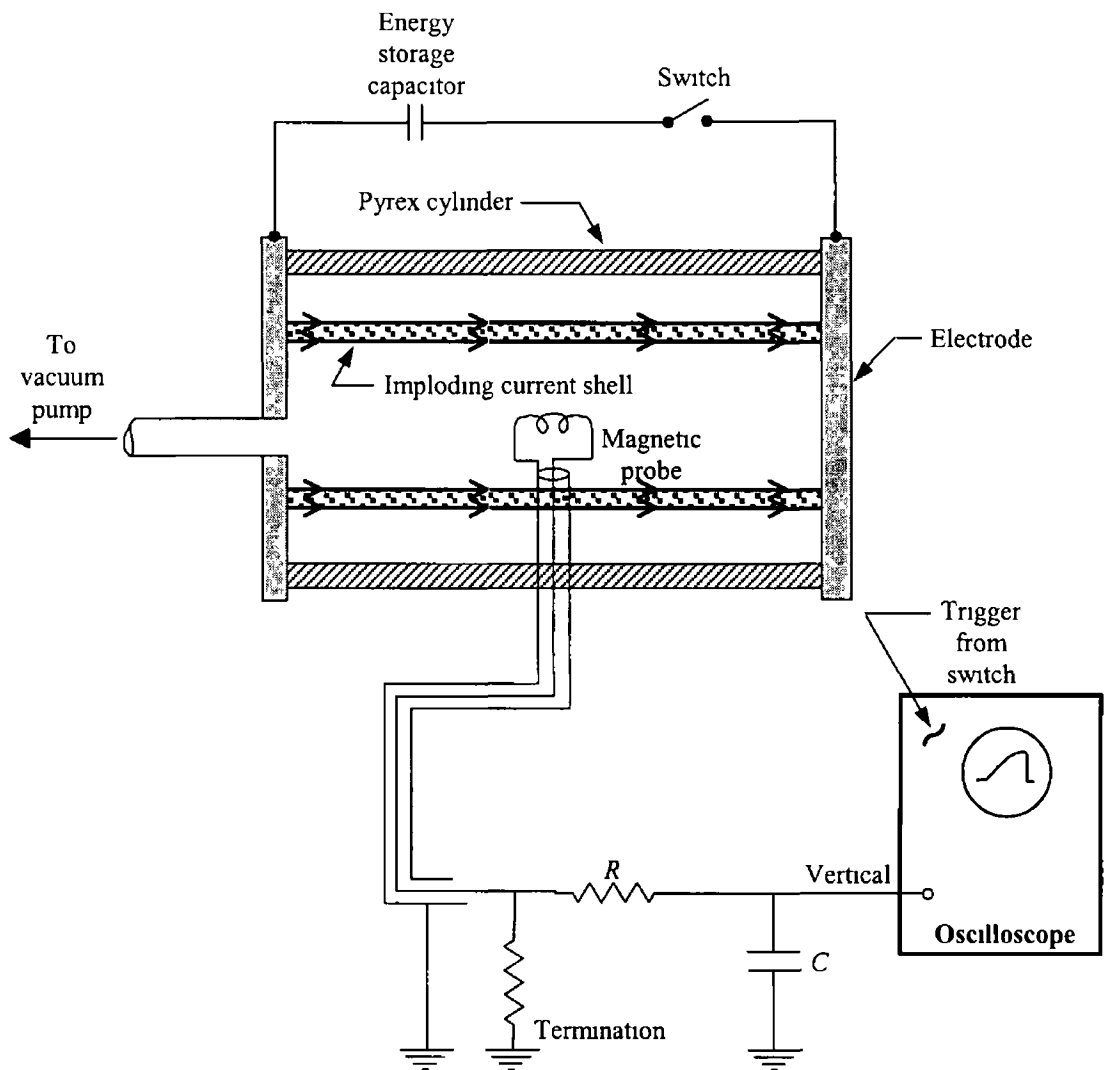
Figure 2 32 *Schematic of a dynamic-pinch experiment showing a magnetic probe used to measure the time when the collapsing plasma passes a given point (from [41])*

an example where the time development of a plasma instability in a pinch experiment can be followed, and the modal pattern that develops compared with theory [117] Gribkov et al [118] used high-speed interferometric photography of a plasma, recording the interferograms on a magnetic video tape The method made it possible to obtain rapid information about the state of the plasma in the instrument Chen et al [119] studied the dynamics and chemical reactions in a laser-ablated $PbTiO_3$ plume by optical-wavelength sensitive CCD photography The radiation that occurs from atomic transitions also occurs in the vacuum ultraviolet and soft x-ray regions of the electromagnetic spectrum, depending on the temperature and density of the plasma The

presence of this line radiation and the profiles of the emission or absorption lines can be used to measure plasma density and temperature [110]
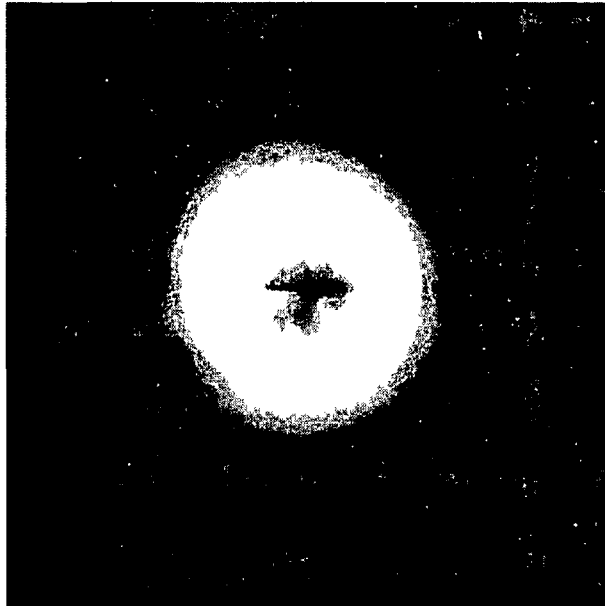
Figure 2 33 Photograph of a linear pinch, taken through a hollow electrode, looking down the hole in the center of the plasma cylinder In this experiment an axial (directed out of the page) magnetic field was applied to "stiffen" the collapsing plasma (from [117])

2 8 3 2 Radiation measurements

Plasmas also emit radiation in the microwave ($\lambda\approx1$ cm) and millimetre-wave ($\lambda\approx1$ mm) regions of the electromagnetic spectrum This radiation can be detected in a variety of ways, depending on its intensity and duration For example, a magnetically confined hot electron plasma ($T_e\approx50$ keV) has mildly relativistic electrons and emits radiation at the cyclotron frequency and its harmonics The radiation can be detected with a conventional superheterodyne system with mixer, local oscillator, and intermediate-frequency amplifier or by a cryogenically cooled indium antimonide photodetector [120] and grating monochromator system This latter system works best in the 8 to 0 1 mm wavelength portion of the spectrum, and the superheterodyne system works best for wavelengths greater than 4 mm

Lichtenberg et al [121] used a cryogenic photodetector system to investigate the spectral distribution of synchrotron radiation from a magnetically confined plasma Figure 2 34 is a plot of the absolute intensity of synchrotron radiation measured using such a cryogenic photodetector system Cottrell [122] measured the plasma ion temperature from Balmer alpha charge-exchange radiation during neutral injection Garbuzov et al [123] measured the plasma temperature from thermal UHF radiation in solid-fuel magneto-hydrodynamic (MHD) generators
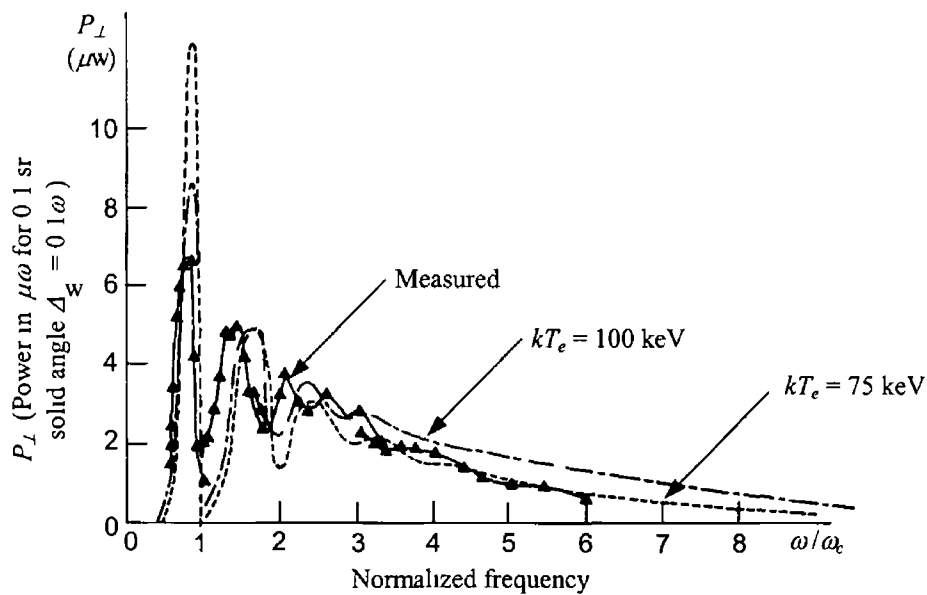
Figure 2 34 Spectrum of synchrotron radiation emitted by a hot-electron plasma in a 5-T magnetic field, compared with theoretical spectra for a two-dimensional Maxwellian distribution at 75 and 100 keV [121]

There are many other methods for the measurement of electromagnetic radiation emitted or absorbed by plasmas This is an active area of experimental and theoretical research in plasma physics [124]

2 8 3 3 Single particle measurements

Magnetically confined plasmas frequently emit charged or neutral particles, depending on the plasma density and temperature and the background gas pressure in which the plasma resides For example, a magnetic-mirror experiment [41] has a velocity-space diffusion mechanism that drives particles into a loss cone, which results

in their escape along the magnetic field lines As they escape, the particles can be collected, energy-analyzed, and counted by a variety of methods, such as quadrupole mass spectrometers, crystal detectors, particle multipliers, etc The properties of the escaping particles can be related to the properties of the plasma still in the magnetic mirror

Neutral particles are also sometimes emitted by plasmas when conditions are right Generally, low-density hot ions in a good vacuum lead to the proper conditions The fast-escaping neutrals are created by the resonant charge-exchange collision of a fast ion and a slow neutral These two particles exchange an electron, thus creating a fast neutral and a slow ion If the mean free path for the fast neutral is greater than the size of the experiment, the fast neutral will escape where it can be analyzed and counted This charge-exchange process is an energy-loss mechanism that must be minimized in any fusion reactor, but which leads to a useful measurement tool in the meantime

Although there are some subtleties in the interpretation of plasma properties in terms of escaping single particles, the methods are generally quite useful and important [108]

2 8 3 4 Light scattering

The invention and subsequent development of high-power lasers brought about a new means of measuring the density and temperature of plasmas This new means is based on the scattering of electromagnetic waves by free electrons The intensity of electromagnetic radiation scattered from a small-amplitude electromagnetic wave by a free electron is given by the Thomson cross section (s $_{Th} = \frac{8}{3}\pi r_0^2$), where r_0 is the classical electron radius If the scattering electron is moving with a low velocity ($v \ll c$), the scattered radiation is Doppler-shifted to a higher or lower frequency, depending on the angle of observation This Doppler shift of the scattered radiation is used to measure the temperature or velocity distribution of dense low-temperature ($T_e < 1$ keV) plasmas [125] (by measuring the Doppler broadening of the laser line width for radiation scattered from a laser beam by a plasma) A Maxwellian plasma-distribution

function produces a Gaussian-shaped spectral distribution of scattered radiation whose width is proportional to the plasma temperature

For plasmas with electron temperatures greater than 10 keV, the spectrum of scattered radiation is not Gaussian in shape, but rather is skewed and shifted to shorter wavelengths The wavelength of radiation scattered by a given high-velocity electron in a particular direction depends only on that electron's velocity However, in a laboratory-size hot-electron plasma (T_e > 10 keV), electrons will pass completely through the scattering region during the observation time, and as a result there is a correction to the intensity of scattered radiation that must be taken into account in determining the number of electrons in each velocity class [126]

2 9 Conclusion

Despite the apparent anomaly of subjecting an IC, during processing, to an environment containing charged species, plasmas obviously play an important role in IC fabrication The two process attributes, physical and chemical, are important although their relative importance will change with the application, the plasma equipment and the gases being used A plasma is, however, a very complex environment in which to carry out these processes Only an improved understanding of the plasma environment will make it possible to fully utilize the various process methods and to develop new methods

The basic theory of RF plasmas has been examined Different system configurations have been introduced to show the effect of both chamber geometry and power coupling to the plasma Processes within the plasma have also been reviewed for the benefit of understanding the analysis and results presented in the following chapters A brief review of plasma measurements is also presented for understanding the diagnostic and control techniques of plasma processes

CHAPTER 3

EARLY RESULTS AND ANALYSIS OF PLASMA CURRENT-VOLTAGE HARMONICS MONITORING BY PIM

3 1 Introduction

Due to its inherent ability for anisotropic etching, reactive ion and plasma etching have found wide application in fabricating very and ultra large-scale integrated circuits As increasing accuracy of etching is required, it is necessary to have an *in situ* tool that automatically monitors the uniformity of etching and determines an accurate end point for the etch At the present time, the available techniques for end-point detection include laser reflection interferometry [127], optical emission spectrometry [128,129], mass spectrometry [130], ellipsometry [131], plasma impedance monitoring [132-135], thermal imaging [136] and infrared laser absorption spectroscopy [137] The plasma impedance technique eliminates the need for optical windows or extensive system modification and can be easily adopted for automation However, little work has been reported in the area of plasma impedance monitoring for end-point detection in [132-134] Patel *et al* [135] demonstrated end-point detection based on monitoring the change in plasma composition for polycrystalline silicon (polysilicon) and Si_3N_4 etching in an SF_6 plasma and photoresist stripping in an O_2 plasma They used three separate units of commercial equipment for the measurement of RF voltage, RF current and phase difference between RF voltage and current In this chapter, we demonstrate the successful end-point detection of reactive ion etching of a SiO_2 layer on a Si wafer in SF_6 plasma with a planar capacitive discharge using a newly developed commercial plasma impedance monitoring (PIM) system End-point conditions are tested in a novel fashion by monitoring several harmonic components of the RF parameters (RF current, RF voltage and the phase between RF voltage and RF current) and the best parameter is proposed for use as a tool for the end point detection of SiO_2 etching

At the beginning of this chapter the sensitivity of the Plasma Impedance Monitor (PIM) to the reactive ion etching process is investigated Thereafter, the effectiveness of the PIM for the detection of end points is tested when a SiO_2 layer deposited on a Si substrate undergoes RIE processes Since PIM is relatively new equipment for plasma monitoring, a brief description of this equipment as well as the RIE equipment used in this work is presented in the early sections of this chapter In the later sections of this chapter we used the Infra-Red (IR) spectroscopy technique to confirm the end points of the RIE processes and to see whether there was any non-uniformity in etching of the SiO_2 layer on Si A short description of the IR spectroscopy technique is also presented in the early sections

3 2 Reactive Ion Etching Equipment

The experimental equipment consists of a planar, capacitively coupled reactive ion etching system coupled with a Plasma Impedance Monitoring (PIM) system Figure 3 1(a) and 3 1(b) show a photograph and the schematic diagram of the apparatus, respectively The RIE system consists of two water-cooled circular aluminium electrodes separated by 6 cm The diameter of the upper electrode is 28 5 cm whereas the lower electrode is 24 cm in diameter A Pyrex cylinder seals the whole plasma chamber For RIE operation the upper electrode is grounded and the lower electrode is supplied by a 13 56 MHz RF generator An impedance matching circuit is placed between the RF generator and the lower electrode to minimize the reflected power from the plasma chamber A dark space shield is installed below the lower electrode to eliminate any unwanted discharge effects A mass flow controller unit controls the flow of inlet gasses into the chamber where a rotary pump maintains the necessary vacuum in the chamber

3 2 1 Plasma Impedance Monitor (PIM)

The Plasma Impedance Monitor is a similar type of equipment as used in [35, 37, 112, 138-141] for the measurement of plasma I-V parameters It comprises a Smart PIM^{TM} unit interfaced to a personal computer which was developed by Scientific Systems Ltd , Ireland The Smart PIM^{TM} is a microprocessor-based electronic system

(a)
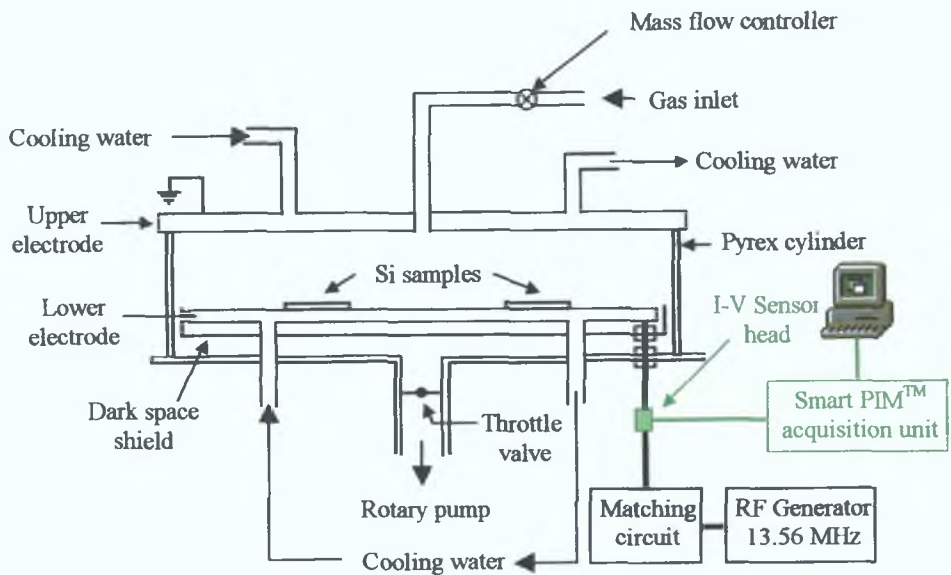
(b)

***Figure** 3.1 Capacitively driven, parallel plate, RIE system with the Plasma Impedance Monitoring system: **(a)** Photograph, and **(b)** Schematic diagram.*

for measuring RF plasma parameters of RF laboratory and industrial electrical plasmas. The PIM measures in real time the true plasma impedance, current, voltage and phase in process reactors. The system monitors power spectra, generated by the non-linear plasma impedance. Figure 3.2 shows the basic Smart PIM^{TM} unit along with its accessories. These furnished accessories are: (i) Smart PIM^{TM} acquisition unit, (ii) Current-Voltage (I-V) sensor head and cable, (iii) RF vector integrator, (iv) copper interface cable, and (v) data analysis and acquisition software.
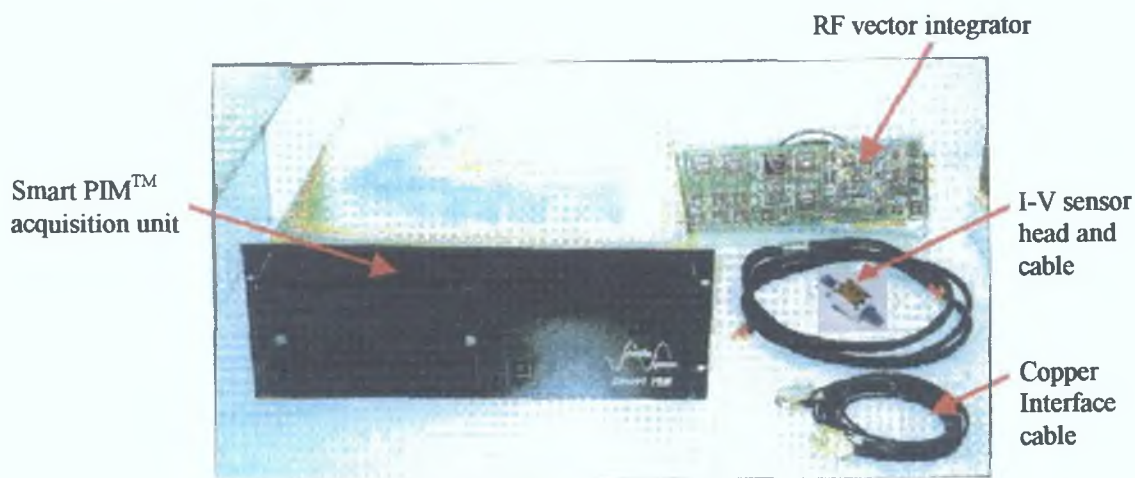
Figure 3.2 Smart PIM^{TM} system accessories.

The I-V sensor is a post-match current-voltage sensor. The sensor head is located between the matching network and the driven electrode of the plasma reactor (shown in green colour in Fig. 3.1(b)). The basic electrical circuit representing the sensor head is shown in Fig. 3.3.

To measure the RF current a small coil is placed near the main RF current carrying conductor. The magnetic flux produced by the main RF current induces a small voltage across the coil which induces a small current to flow through a high resistance R. The voltage across the resistor R is directly proportional to the main RF current. The voltage across the resistor (v_I) is measured.

To measure the RF voltage a conducting material is placed near the main RF current-carrying conductor separated by an insulating material. This conducting material together with the main RF current-carrying conductor and the insulator forms a

78
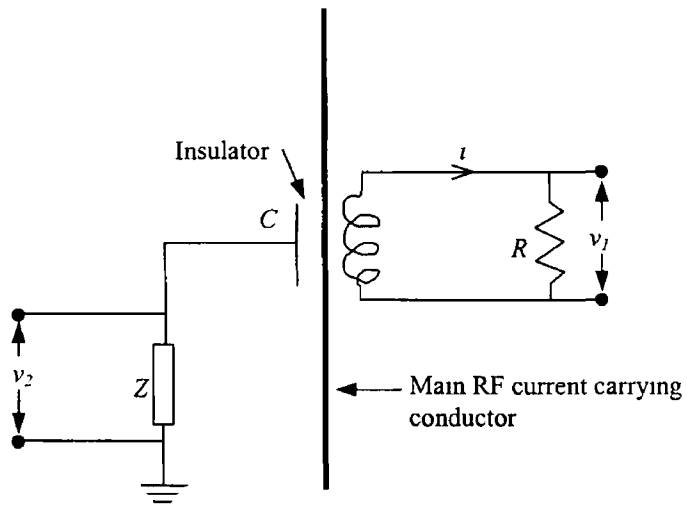
Figure 3 3 Electrical representation of the I-V sensor head

capacitor (shown as C in Fig 3 3) The insulating material is chosen so that the capacitive reactance of C is very high compared to the main plasma impedance Another small impedance Z is connected in series with C which could be a small resistor or a combination of a resistor and a capacitor A very small amount of current will flow through the capacitor C which is proportional to the main RF voltage This current will induce a voltage across the impedance Z which is also proportional to the RF voltage The voltage across Z (v_2) is measured

The sensor head measures current and voltage signals (v_1 and v_2, respectively) that are proportional to the plasma RF current and voltage The signal is fed via the I-V cable to the radio frequency vector integrator (RFVI), which is housed in the PIM acquisition electronics unit The RFVI board implements a proprietary sampling technique providing phase resolution of better than 0 001 degrees [142] In operation the RFVI captures one cycle of the I-V signal and measures accurately the phase angle between the two signals

Microprocessor based analysis routines operate on the acquired signals to yield the Fourier components of the fundamental and the first four harmonic components The phase angle between the harmonic components is also computed Several measurement speeds are provided, each measurement or sample yields the fundamental and the first four harmonic components of the current and voltage signals and the phase angle

79

between the respective components The PIM does not require frequency scanning to capture the harmonic spectra of the basic RF plasma parameters—current, voltage and phase angle The basic RF plasma parameters are transferred to the user's host PC via an RS232 communication link (copper interface cable) for display and further analysis using the Scientific Systems Windows™ based software, PIMSoft™

PIMSoft™ provides a complete platform required for displaying and analysing the acquired RF plasma parameters Simple point and click mouse operations allow monitoring of derived parameters including the plasma load power and impedance The user can also generate additional derived parameters using the PIMSoft™ function calculator A Smart PIM unit can control four vector integrators and sensor heads This feature allows for monitoring the plasma process at the source and chuck electrodes in multiple process reactors PIMSoft™ allows simultaneous display and control of data from the multi-sensor heads

3 3 Infrared Spectroscopy

Electromagnetic radiation is a good means towards an understanding of the bonding structure of compounds when it interacts with the atoms of that compound The interaction of matter with electromagnetic radiation of wavelength between 1 and 300 µm [143] induces either rotational or vibrational energy level transitions, or both, within the molecules involved The frequencies of infrared radiation absorbed by a molecule are determined by its rotational energy levels and by the force constants of the bonds in the molecule Since these energy levels and force constants are usually unique for each molecule, so also the infrared spectrum is usually unique

The infrared region is used primarily for analysis of organic compounds because they have unique and complex spectra In infrared spectroscopy, the film is irradiated by light with frequencies in the infrared region of the spectrum The molecules in the film will only absorb the radiation energy at specific frequencies, which match the natural vibrational frequencies of the molecule These occur, as mentioned before, in the infrared region of the electromagnetic spectrum

For a vibration to be IR active, it is necessary to induce a change in the dipole moment The dipole moment is defined as the magnitude of either charge in a dipole multiplied by the charge spacing If an atom has the same number of protons and electrons, it is electrically neutral and does not contribute to the dipole moment The chemical forces that exist in the molecule tend to redistribute the electrons so that a given atom may have a deficit or an excess of electrons, being considered as a particle with a small positive or negative charge When applying IR excitation, this charge may change due to molecular vibration If the negatively charged atom vibrates in one direction, and the positively charged one in the opposite direction, the vibration is IR active However, if the molecule retains the centre of symmetry so that the dipole moment remains unchanged, the vibration is IR inactive The degree of absorption depends on the concentration of IR active bonding within the sample, the molecular absorption coefficient and the thickness of the sample according to the equation [144]

$$I = I_0 e^{-\alpha c t}$$

(3 1)

where I_0 is the light intensity without absorption, I is the intensity of light which has passed through the sample, t is the sample thickness, α is the molecular absorption coefficient and c is the concentration of material under test

Infrared spectroscopy is one of the best analytical tools for the measurement of impurities in silicon and to study the structural characteristics of thin oxides in particular It is a non-destructive and highly sensitive optical characterization technique It is optical in the fact that it studies the response to light It is a good method to use as the optical beam can be easily manipulated and the samples do not get damaged

Long-wavelength light is directly absorbed at band features by phonons and impurities In infrared spectroscopy the intensity of absorbed light is measured versus wavelength or frequency, which provides a capacity for good analysis

3 3 1 Theory of infrared spectroscopy

The key optical component of an infrared spectrometer is a Michelson interferometer consisting essentially of two mirrors and a beam-splitter as shown in Figure 3 4 Both mirrors reflect the beams back to the beam-splitter where they are

recombined These two beams may add either constructively or destructively depending upon whether they are in phase or out of phase A Michelson mteferometer varies the relative phase of one beam to the other by adjusting mirror M_1 If the light source is monochromatic, scanning the movable mirror M_1 causes the output beam intensity to rise and fall periodically, as the relative phase of the two recombining beams in the interferogram shifts The frequency of the signal is proportional to the wavenumber of the monochromatic light source as discussed in Bomem, 1989 [145]

Moving
Mirror, (M_1)

x

Beam splitter

IR Source

Stationary
Mirror, (M_2)

Detector
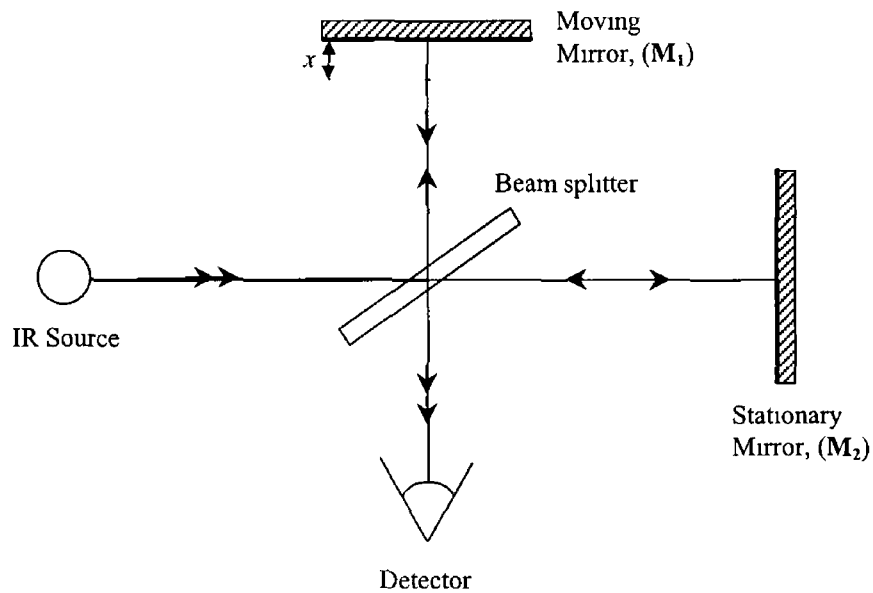
Figure 3 4 Schematic diagram of Michelson interferometer

The output beam intensity can be given by [146]

$$I(\delta) = \frac{I_0}{8}[1 + Cos(2\pi\delta\sigma)]$$ (3 2)

where, $I(\delta)$ = intensity measured for an optical path difference δ in the interferometer,

σ = wavenumber of the light source = λ^{-1}, and

I_0 = incident light intensity

When the light source used contains many frequencies, the intensity measured as a function of optical path difference is a summation (or in the limited case, an integral) over all frequencies, i e [146],

$$I(\delta) = \int_0^\infty S(\sigma)\frac{I_0}{8}[1 + Cos(2\pi\delta\sigma)]\,d\sigma \qquad (3\ 3)$$

where $S(\sigma)$ is the intensity function of the light with wavenumber σ The interferogram measured by the spectrometer is [146]

$$I(\delta) = \frac{I_0}{8}\int_0^\infty S(\sigma)Cos(2\pi\delta\sigma)\,d\sigma \qquad (3\ 4)$$

We can re-write eqn (3 4) as [146]

$$I(\delta) = \frac{I_0}{16}\int_{-\infty}^\infty S(\sigma)e^{J2\pi\delta\sigma}\,d\sigma \qquad (3\ 5)$$

This equation is related to the frequency spectrum of the light by the Fourier Cosine transformation, [146]

$$S(\sigma) = \int_{-\infty}^\infty I(\delta)e^{-J2\pi\delta\sigma}\,d\delta \qquad (3\ 6)$$

For a more detailed discussion of Fourier Transformation see Brighan, 1974 [147]

Since "the spectrogram (irradiance versus wavenumber), of the light incident on a Michelson interferometer is the Fourier transform of the interferogram (irradiance versus path difference) as a function of mirror movement" it enables one by detecting the interferogram $I(\delta)$ to determine the spectral irradiance $S(\sigma)$ as a function of wavenumber σ by Fourier transform methods [148]

The Fourier transform methods refer in particular to the Fast Fourier Transform (FFT) The FFT is an algorithm that can compute the Discrete Fourier Transform (DFT) faster than other available algorithms as reported by Cochran *et al* [149] Thus using the FFT, the DFT of the interferogram curve is calculated, giving the more familiar frequency spectrum

3 4 Experiment for Sensitivity Test

Before the original experiment the plasma chamber was cleaned by running the system in Reactive Ion Etching (RIE) mode with Ar gas at 200 Watts RF power, 72 mTorr chamber pressure and 8 6 sccm gas flow rate To determine the sensitivity of the Plasma Impedance Monitor to process variations, the RIE was carried out for Si wafer samples of different sizes in the reactor with SF_6 plasma Different RF powers were

used, while the chamber pressure and the inlet gas flow rate were kept identical (i e , chamber pressure = 80 mTorr and gas flow rate = 3 9 sccm) for each experiment The harmonics of plasma discharged power, plasma impedance and phase between RF voltage and current were recorded with corresponding RF power supplied for each of the sample sizes used for the experiment Each of these measurements was made a few minutes later after the plasma was initiated, while the plasma chemistry inside the chamber became stable and fell into time zone-II (different time zones for plasma chemistry are explained in section 3 7)

3 5 Results and Discussion of Sensitivity Test

Figures 3 5(a)-3 5(d) show a selection of the harmonic components of plasma discharged power, i e , P_1, P_2, P_3 and P_4, figures 3 6(a)-3 6(d) show the corresponding harmonic components of the plasma impedance, i e , Z_1, Z_2, Z_3 and Z_4, whereas figures 3 7(a)-3 7(d) show the same harmonic components of the phase, i e , ϕ_1, ϕ_2, ϕ_3 and ϕ_4, for the SF_6 RIE of Si wafers of different sizes at 80 mTorr operating pressure and 3 9 sccm gas flow rate The different subscripts used here indicate the corresponding harmonic components, for example, subscript '1' indicates the fundamental component, subscript '2' indicates the second harmonic component and subscript '3' indicates the third harmonic component, etc From these figures it is seen that the data for no sample in the chamber (i e , fraction = 0) can be more easily isolated from the other data, in particular, for the case of the first two harmonics of each parameter (i e , discharge power, plasma impedance and phase) But the trends in the experimental data points for ¼, ½, ¾ and a complete wafer cannot be easily separated This suggests that the PIM is sensitive to the presence of silicon This is because the presence of silicon in the chamber changes the constituents of the plasma and hence the impedance of the plasma But in general the PIM is not very sensitive to the size of the sample, possibly because the plasma chemistry inside the chamber does not vary significantly with the variation of the sample size Also, the impedance of the lower electrode sheath is very little changed with the wafer size as ¼, ½, ¾ and a complete wafer of Si cover only 4 34%, 8 68%, 13 02% and 17 36%, respectively, of the lower electrode

84
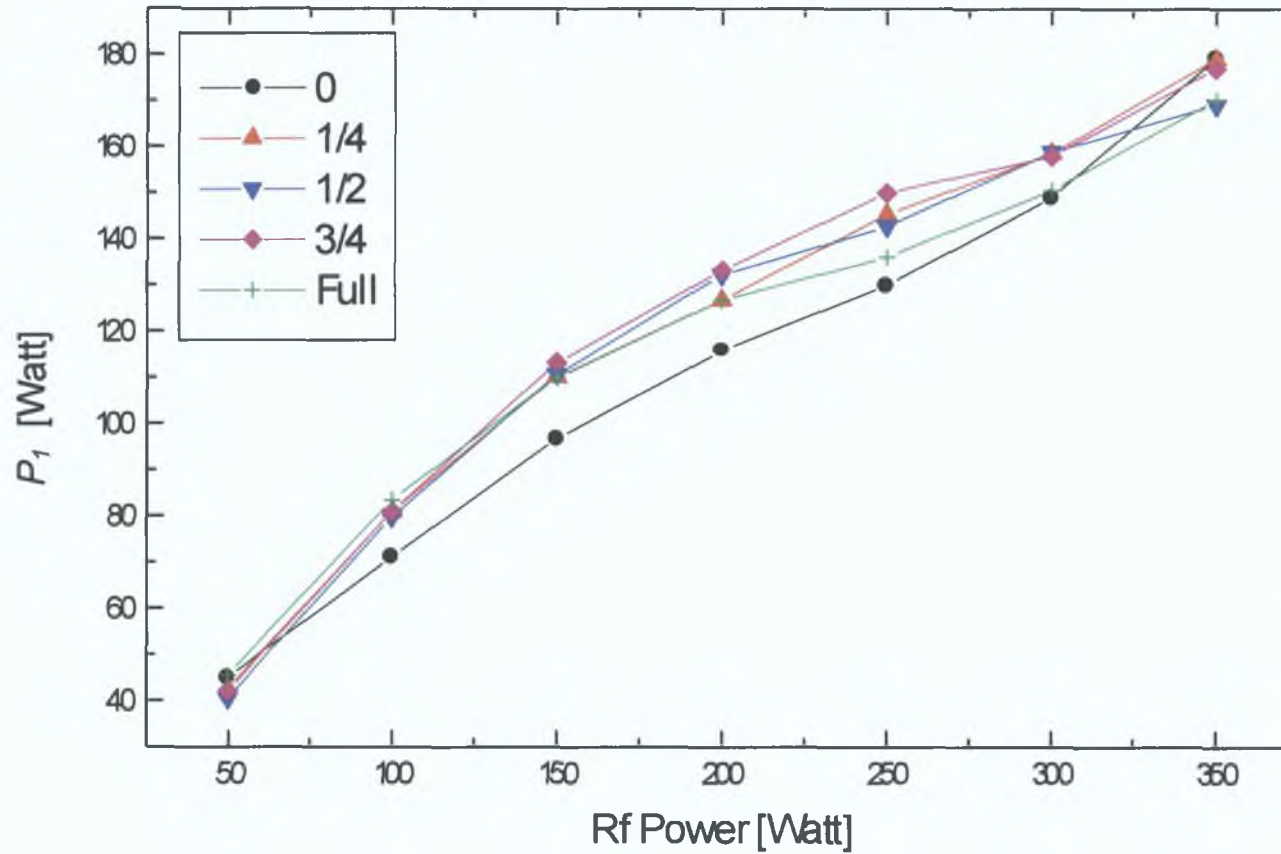
Figure 3.5(a) *Fundamental component of plasma discharged power versus RF supplied power for SF₆ RIE of 0, ¼, ½, ¾ and full fraction of a 100mm diameter Si wafer at 80 mTorr pressure and 3.9 sccm gas flow rate.*
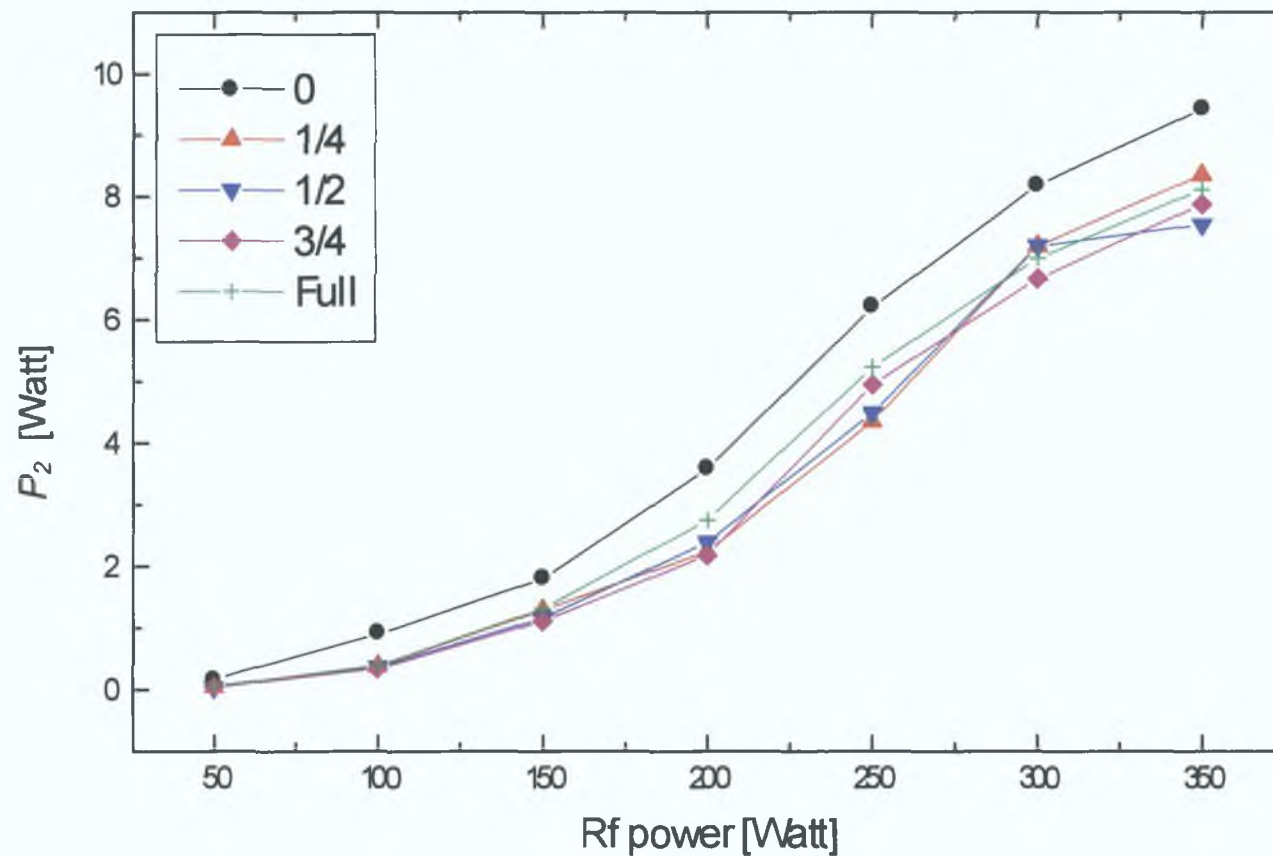
Figure 3.5(b) *Second harmonic component of plasma discharged power versus RF supplied power for SF$_6$ RIE of 0, ¼, ½, ¾ and full fraction of a 100mm diameter Si wafer at 80 mTorr pressure and 3.9 sccm gas flow rate.*
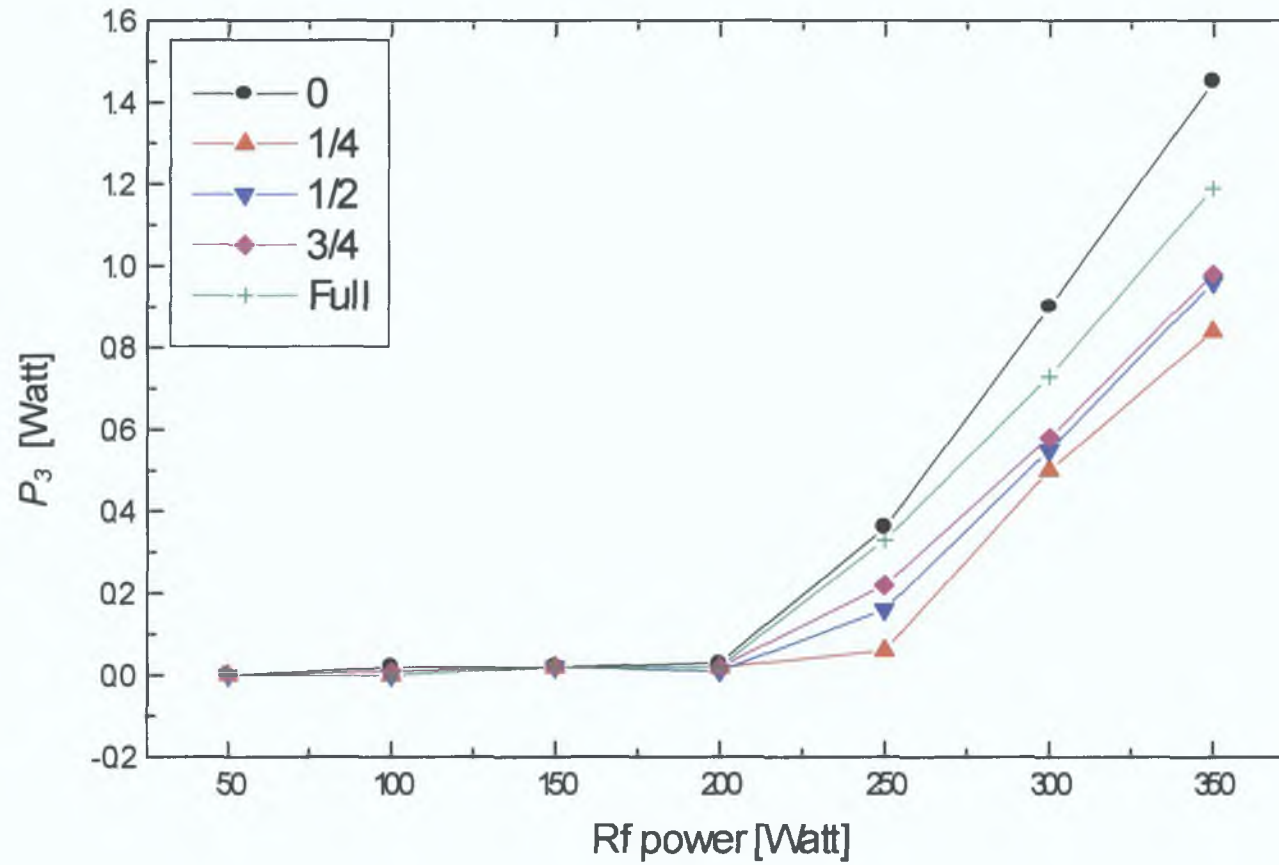
Figure 3.5(c) *Third harmonic component of plasma discharged power versus RF supplied power for SF$_6$ RIE of 0, ¼, ½, ¾ and full fraction of a 100mm diameter Si wafer at 80 mTorr pressure and 3.9 sccm gas flow rate.*
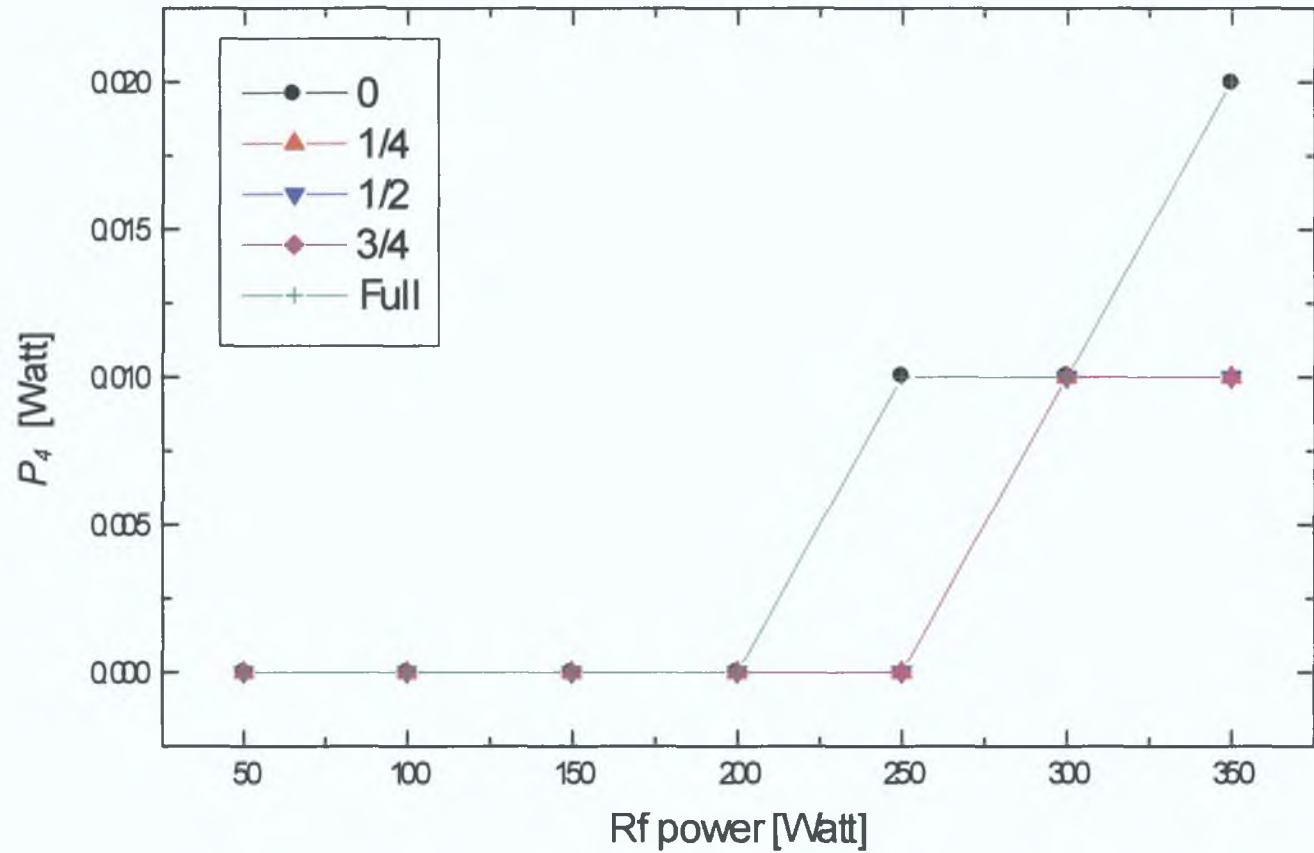
Figure 3.5(d) *Fourth harmonic component of plasma discharged power versus RF supplied power for SF$_6$ RIE of 0, ¼, ½, ¾ and full fraction of a 100mm diameter Si wafer at 80 mTorr pressure and 3.9 sccm gas flow rate.*
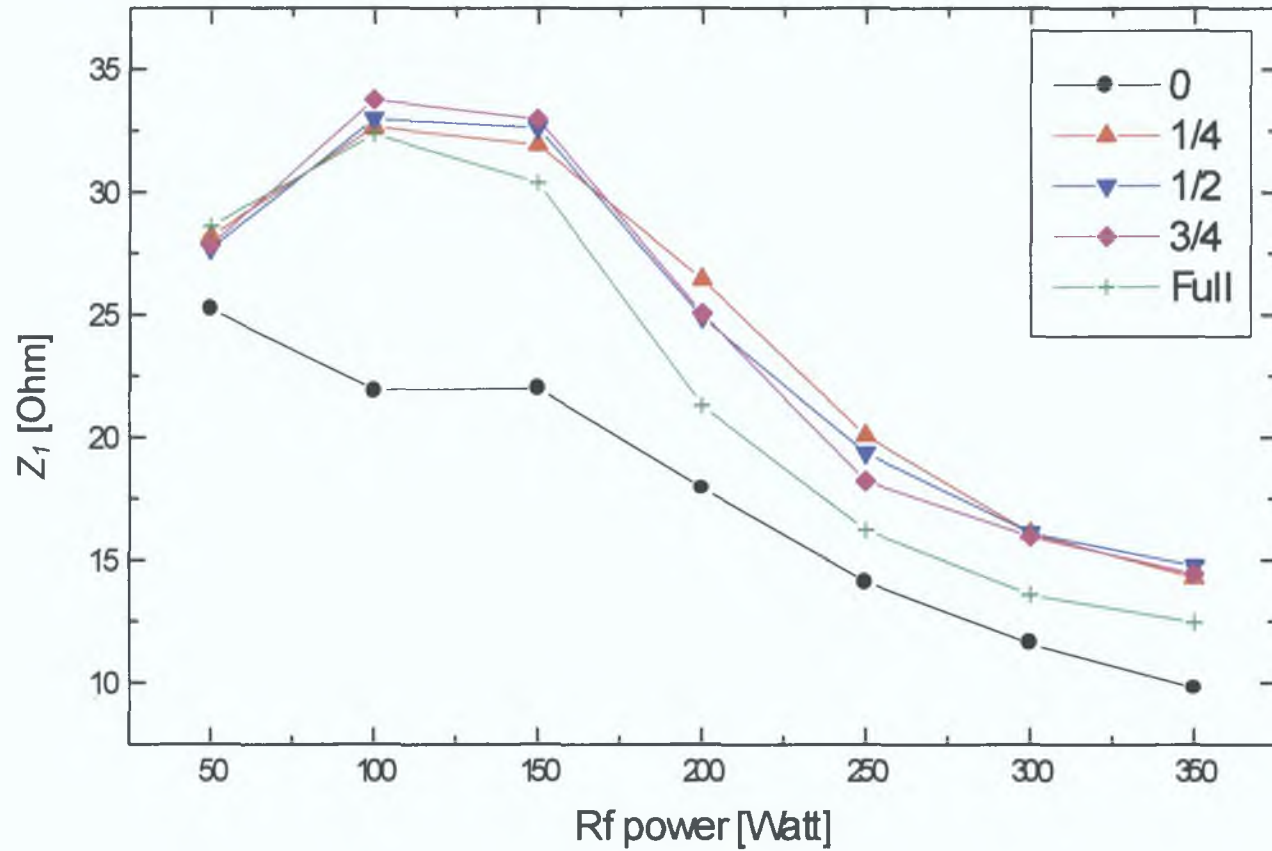
Figure 3.6(a) *Fundamental component of plasma impedance versus RF supplied power for SF_6 RIE of 0, ¼, ½, ¾ and full fraction of a 100mm diameter Si wafer at 80 mTorr pressure and 3.9 sccm gas flow rate.*
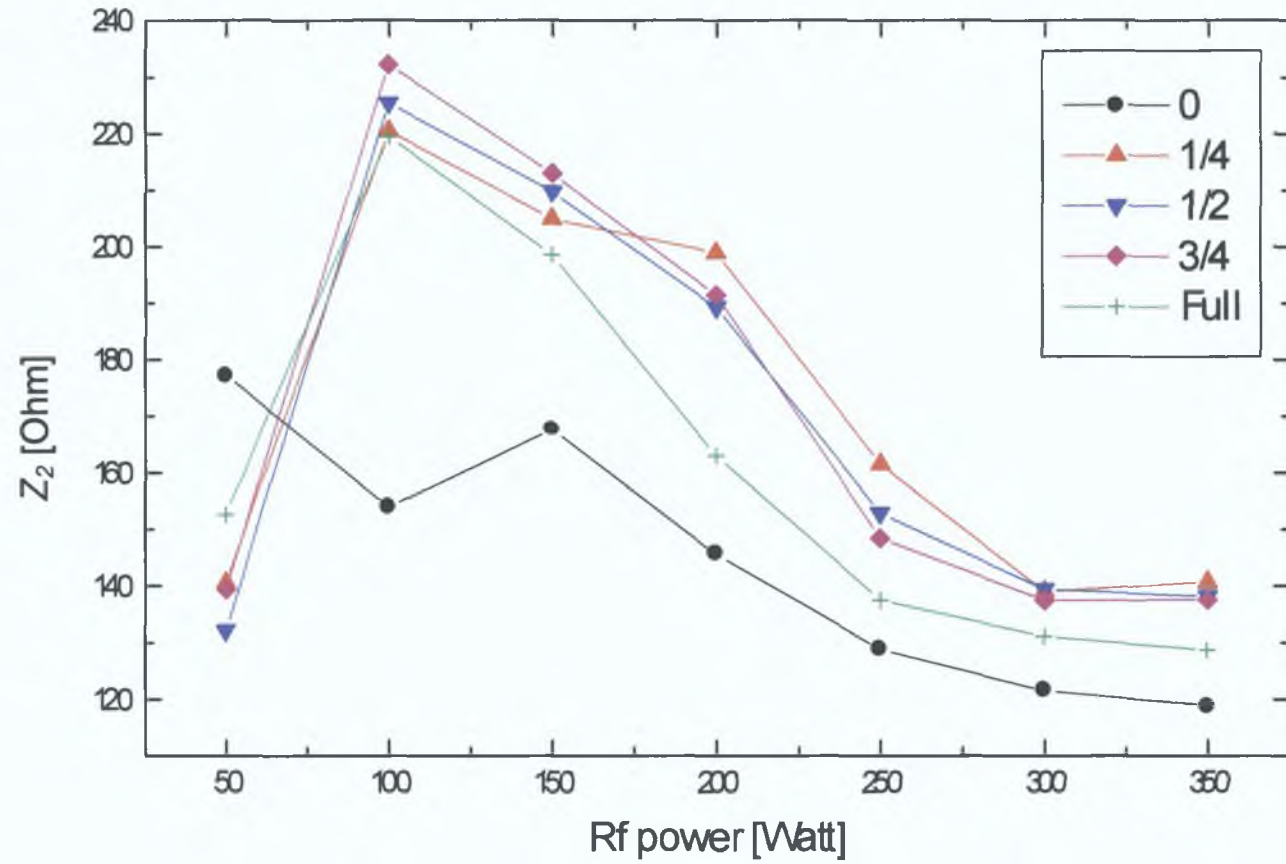
Figure 3.6(b) *Second harmonic component of plasma impedance versus RF supplied power for SF$_6$ RIE of 0, ¼, ½, ¾ and full fraction of a 100mm diameter Si wafer at 80 mTorr pressure and 3.9 sccm gas flow rate.*
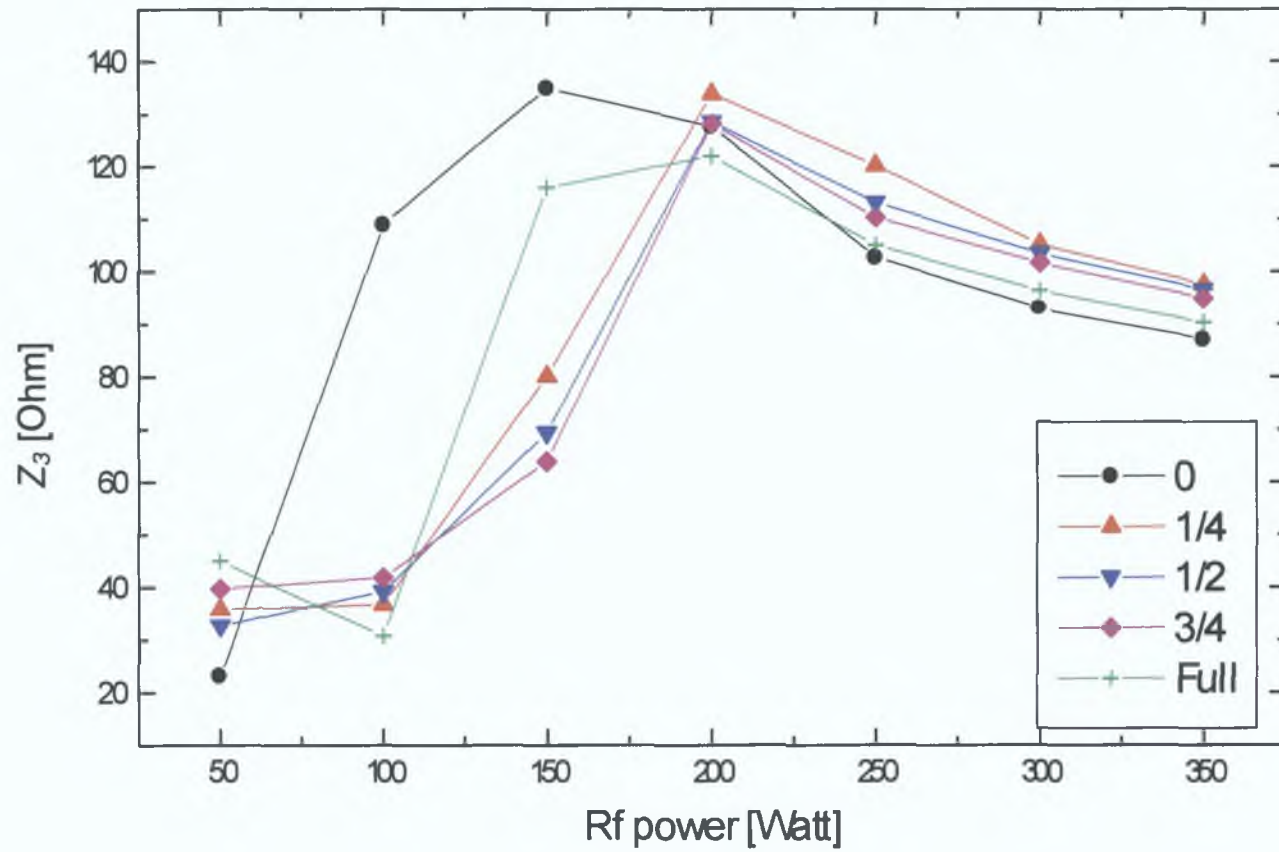
Figure 3.6(c) *Third harmonic component of plasma impedance versus RF supplied power for SF_6 RIE of 0, ¼, ½, ¾ and full fraction of a 100mm diameter Si wafer at 80 mTorr pressure and 3.9 sccm gas flow rate.*
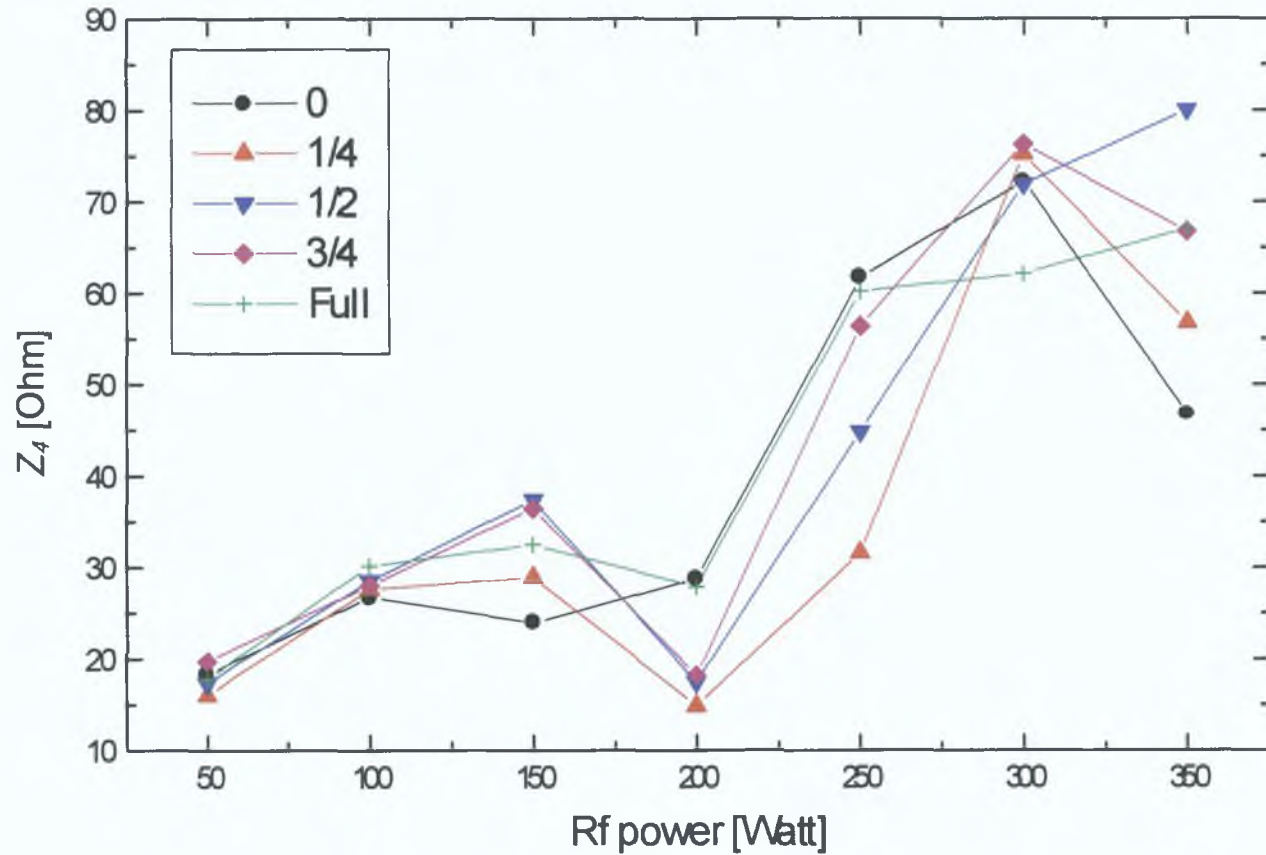
Figure 3.6(d) *Fourth harmonic component of plasma impedance versus RF supplied power for SF₆ RIE of 0, ¼, ½, ¾ and full fraction of a 100mm diameter Si wafer at 80 mTorr pressure and 3.9 sccm gas flow rate.*
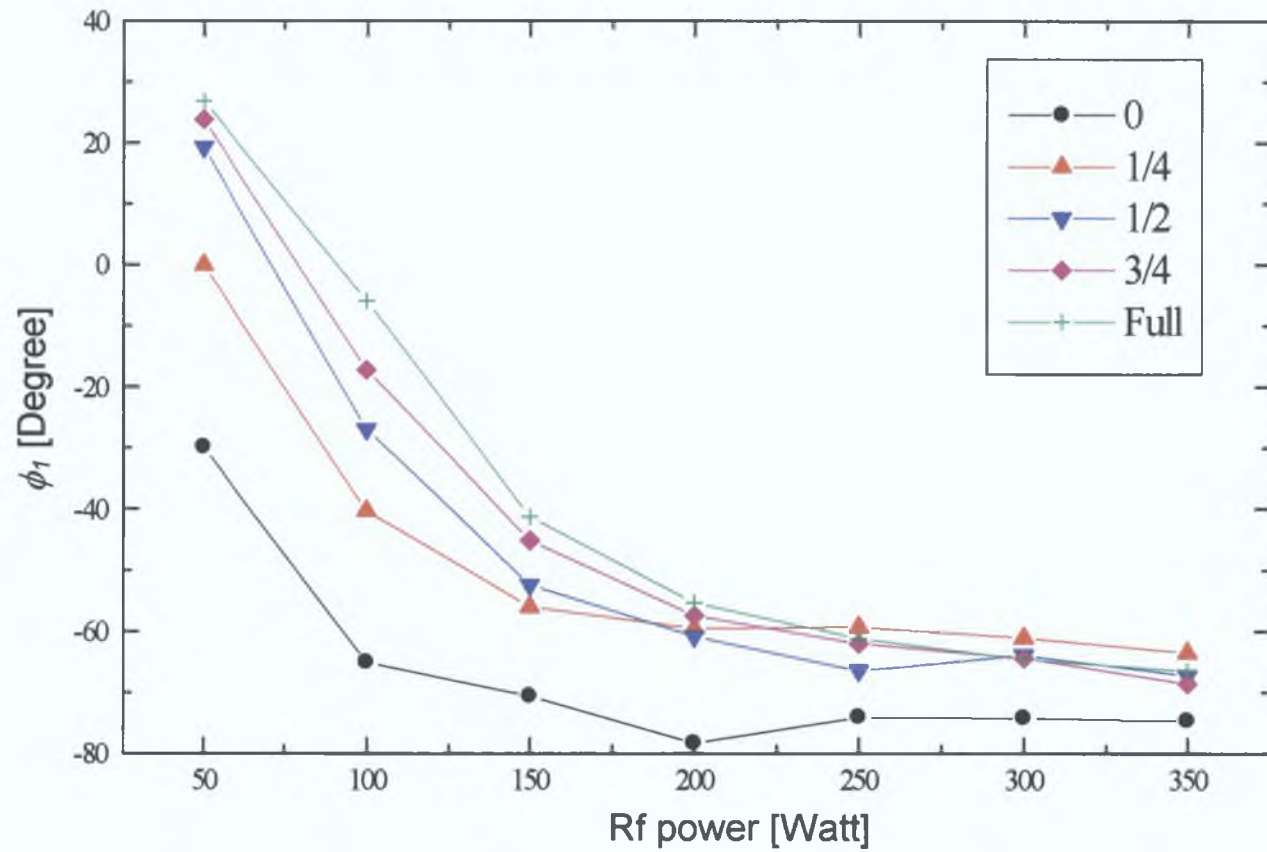
Figure 3.7(a) *Fundamental component of phase versus RF supplied power for SF_6 RIE of 0, ¼, ½, ¾ and full fraction of a 100mm diameter Si wafer at 80 mTorr pressure and 3.9 sccm gas flow rate.*
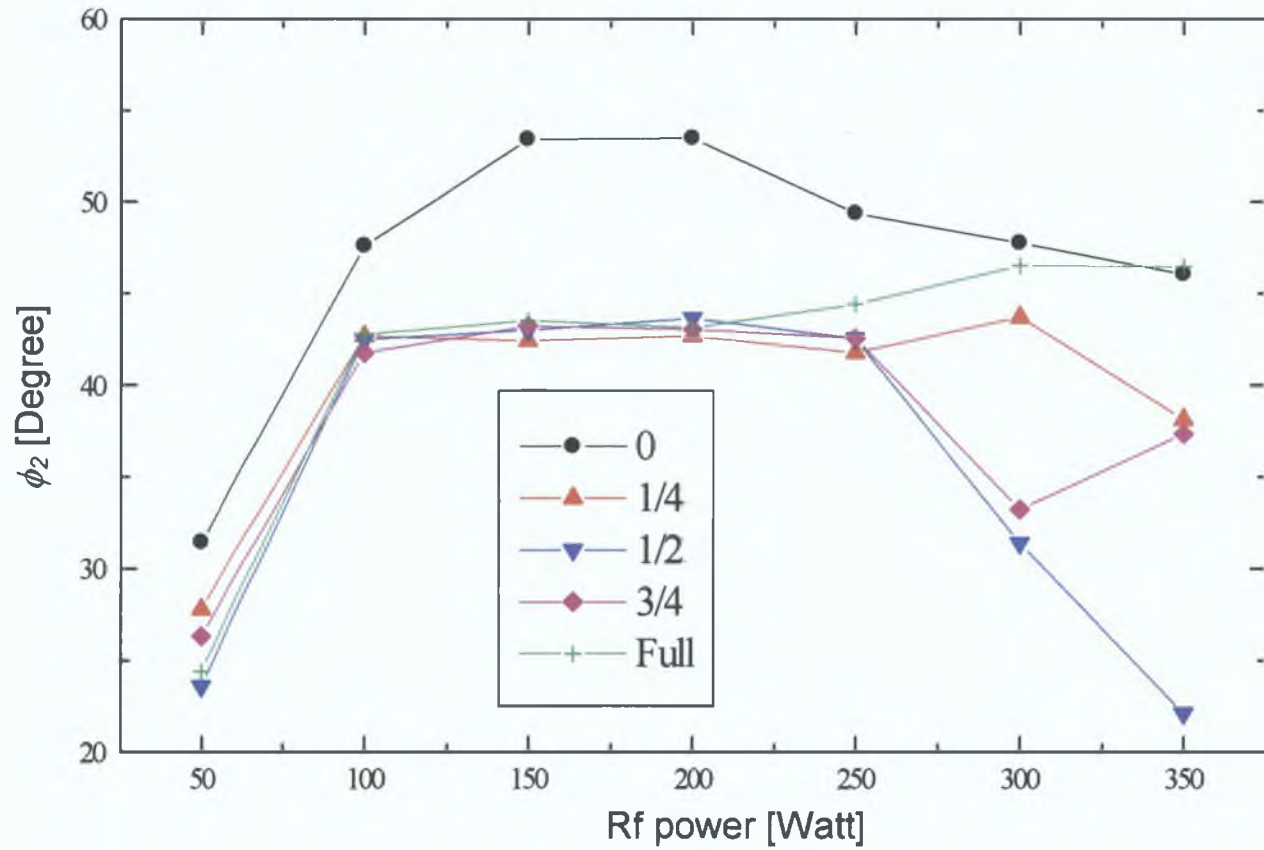
***Figure* 3.7(b)** *Second harmonic component of phase versus RF supplied power for SF$_6$ RIE of 0, ¼, ½, ¾ and full fraction of a 100mm diameter Si wafer at 80 mTorr pressure and 3.9 sccm gas flow rate.*
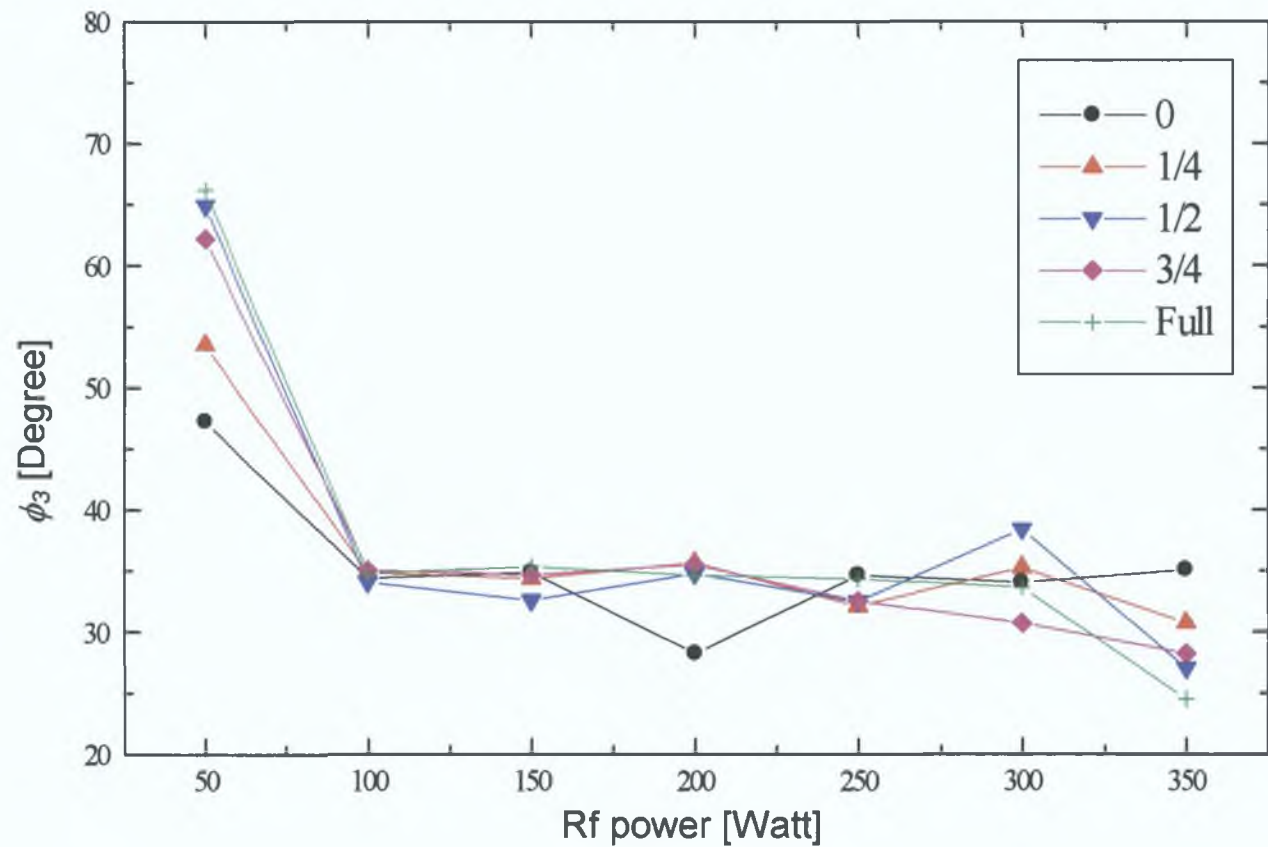
Figure 3.7(c) *Third harmonic component of phase versus RF supplied power for SF_6 RIE of 0, ¼, ½, ¾ and full fraction of a 100mm diameter Si wafer at 80 mTorr pressure and 3.9 sccm gas flow rate.*
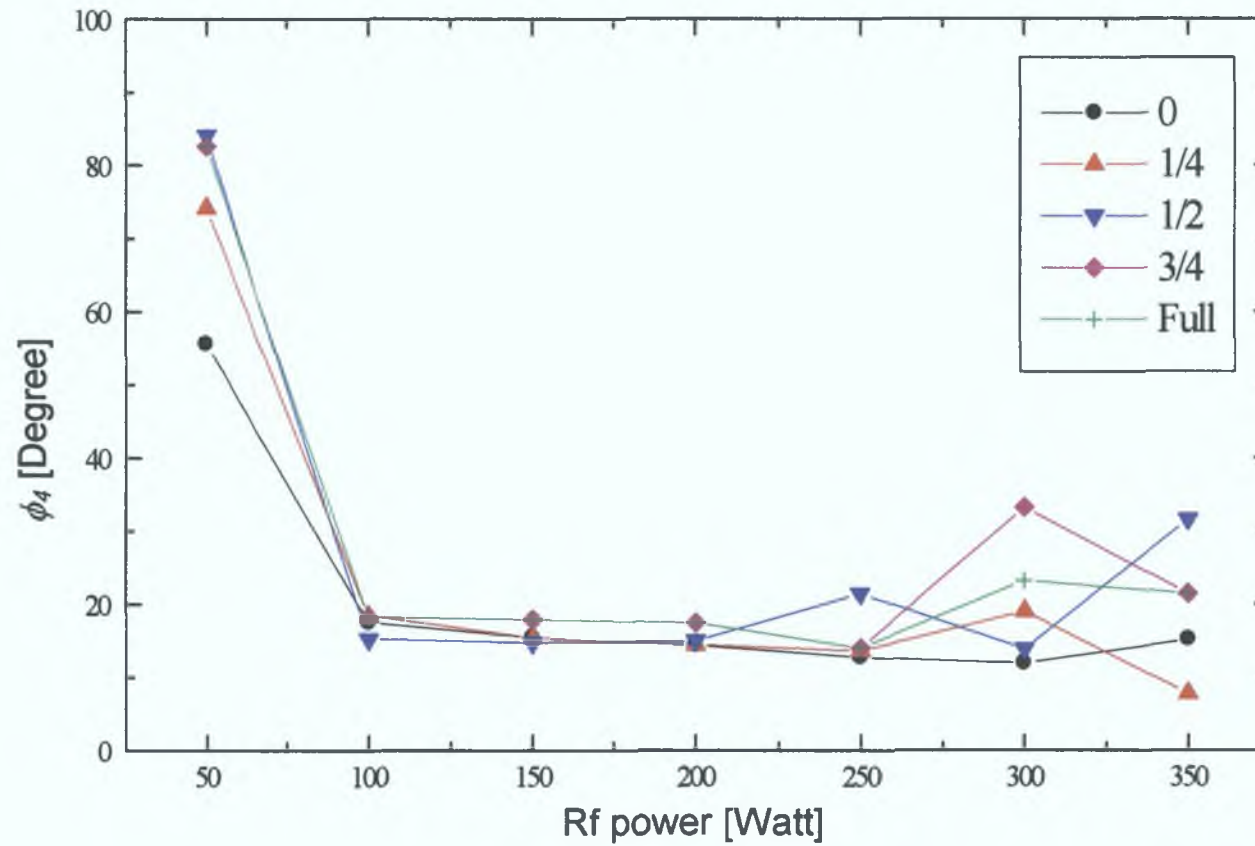
Figure 3.7(d) *Fourth harmonic component of phase versus RF supplied power for SF$_6$ RIE of 0, ¼, ½, ¾ and full fraction of a 100mm diameter Si wafer at 80 mTorr pressure and 3.9 sccm gas flow rate.*

The sensitivity of the PIM is much better when using P_2, Z_1 and ϕ_1 compared to P_1, Z_2 and ϕ_2 Because the data for no Si sample in the chamber for the parameters P_1, Z_2 and ϕ_2 are separable from the other data only for a specific range of RF power, for example, P_1 for ~100-300 Watt, Z_2 for >100 Watt and ϕ_2 for <350 Watt The higher harmonic components (i e , 3rd, 4th and 5th harmonic) of any of the measured plasma parameters (i e , discharge power, plasma impedance and phase) were not found to be applicable for use as monitoring parameters because the corresponding data do not follow any particular trend with the sample size However, the PIM showed a little sensitivity to the presence of silicon while using P_3 and Z_3 parameters in the range of >200 Watt and ~100-200 Watt, respectively The different sensitivity behaviours of the PIM to the different I-V parameters mentioned above are not clearly understood These sensitivities can be again different if the plasma environments (i e , gas and/or sample inside the chamber) are changed

It was of interest to investigate whether there is any derived process parameter which gives better sensitivity to the PIM Ratios of a particular harmonic component of discharge power to the same harmonic component of plasma impedance were tested for that purpose up to the fifth harmonic component The results for the first four harmonic components are shown in figures 3 8(a)-3 8(d) (the ratio of the appropriate plasma discharge power harmonic to the same harmonic of plasma impedance, i e P_i/Z_i, $i =$ 1,2,3 and 4) It was seen that these derived parameters could be useful in monitoring the etch process while considering the harmonic components corresponding to the first two harmonic frequencies The sensitivity of the PIM to these parameters appears to be greater at higher RF power levels The derived parameter for the 3rd harmonic frequency (i e , P_3/Z_3) is also useful as a monitoring parameter only at higher power levels (in this case, greater than 200 Watts) because the data points are not clearly separated in the lower power regimes But if we compare figure 3 5(c) with the figure 3 8(c) we can see that the two figures are almost the same That means the use of P_3/Z_3 shows the same sensitivity as P_3 So, there is no added advantage in using P_3/Z_3 instead of P_3 as a monitoring parameter, as it requires more calculations Again, the sensitivity to differences in sample sizes is not great enough (nor indeed is there a clear functional dependence upon wafer size) to suggest their confident usage in this regard It is also
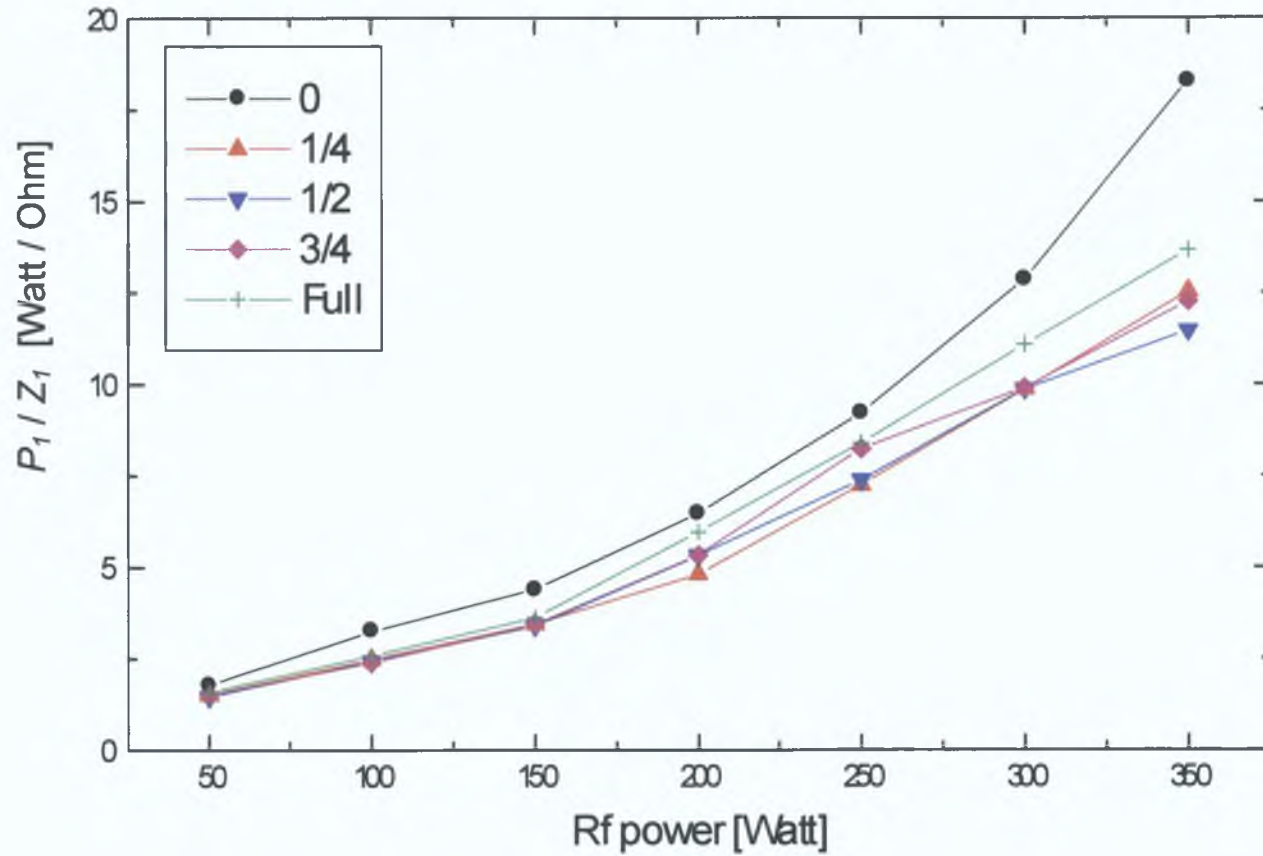
Figure 3.8(a) P_1 / Z_1 *versus RF generated power for SF_6 RIE of 0, ¼, ½, ¾ and Full fraction of a 100mm diameter Si wafer at 80 mTorr pressure and 3.9 sccm gas flow rate.*
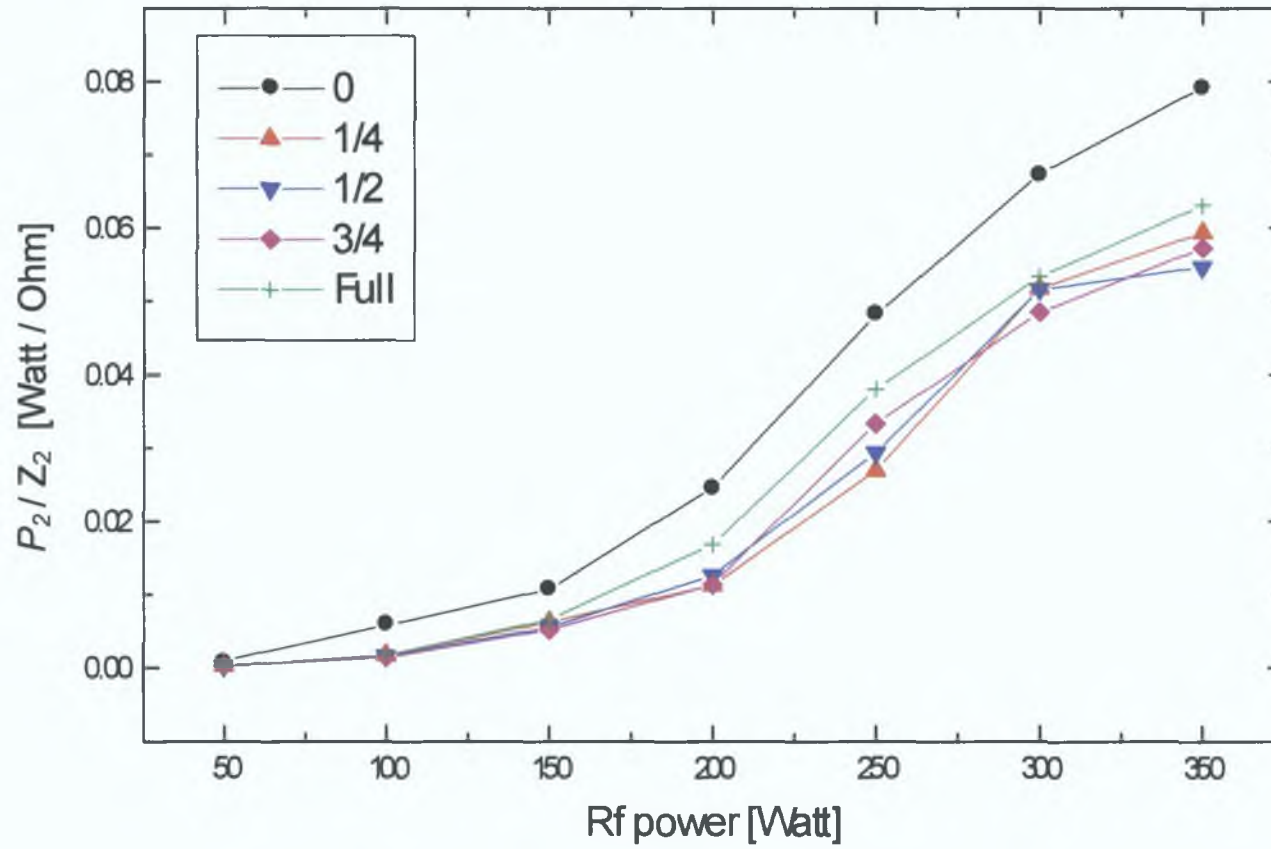
Figure 3.8(b) *P_2 / Z_2 versus RF generated power for SF_6 RIE of 0, ¼, ½, ¾ and Full fraction of a 100mm diameter Si wafer at 80 mTorr pressure and 3.9 sccm gas flow rate.*
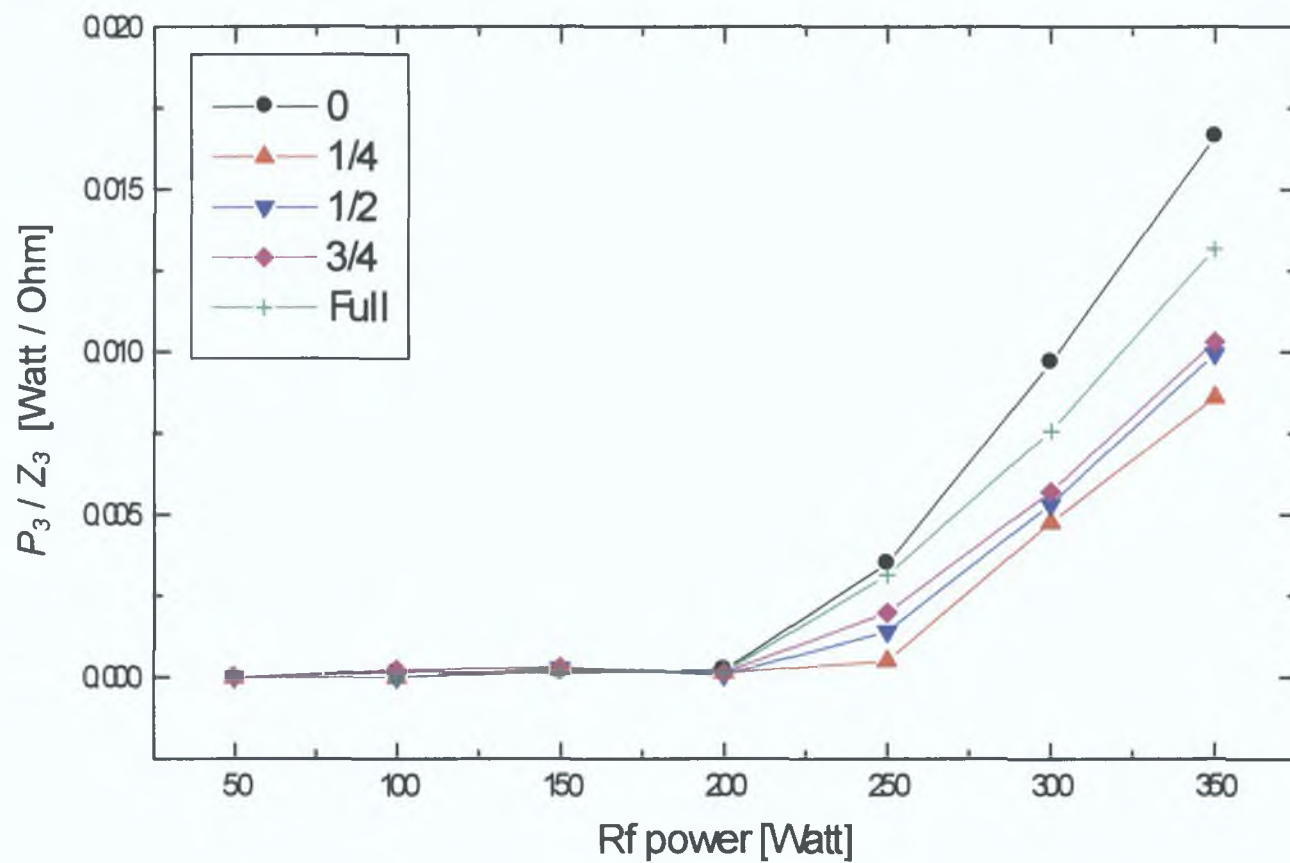
Figure 3.8(c) P_3 / Z_3 *versus RF generated power for* SF_6 *RIE of 0,* ¼, ½, ¾ *and Full fraction of a 100mm diameter Si wafer at 80 mTorr pressure and 3.9 sccm gas flow rate.*
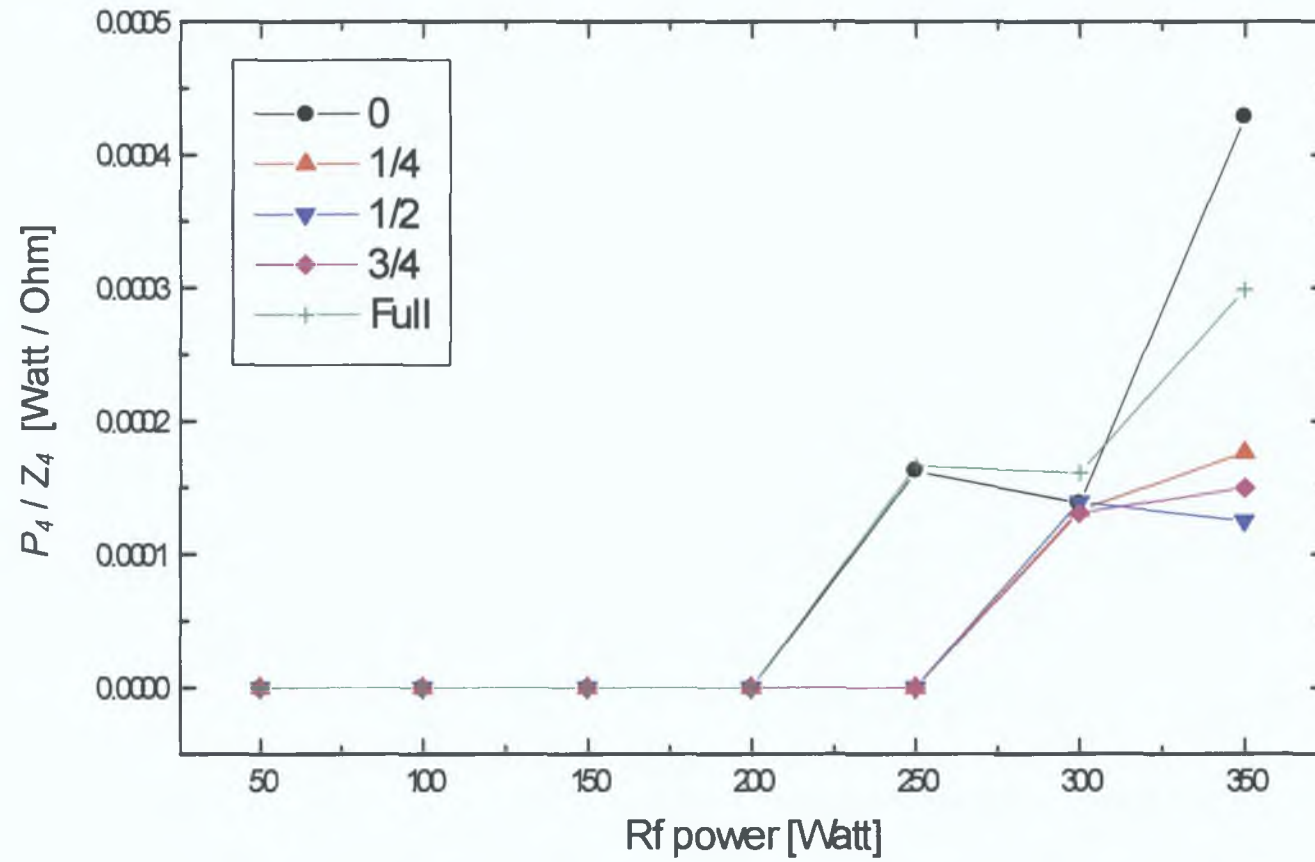
Figure 3.8(d) *P_4 / Z_4 versus RF generated power for SF_6 RIE of 0, ¼, ½, ¾ and Full fraction of a 100mm diameter Si wafer at 80 mTorr pressure and 3.9 sccm gas flow rate.*

true for this case that the derived parameters for higher harmonics (beyond third) are not useful as monitoring parameters

3 6 Experiments for Testing the PIM for End Point Detection

In this experiment tests were carried out to determine the efficacy of fundamental and harmonic component measurements of RF I-V parameters as a means of establishing controllable and repeatable end point detection within an RIE process In order to establish this, SF_6 RIE was carried out on half of a 100 mm diameter Si wafer covered with a 1 32 μm thick SiO_2 layer for different RF powers, chamber pressures and gas flow rates given by Table 3 1 The different settings of RF power, chamber pressure and gas flow rate in Table 3 1 were chosen according to a 3-factor, 3-level *Box-Behnken* experimental design for the operating range 100-150 Watt RF power, 40-60 mTorr chamber pressure and 3 9-6 5 sccm gas flow rate (we will discuss this in detail in Chapter 4) Before the original experiment the plasma chamber was cleaned, similarly as before, by running the system in RIE mode with Ar gas at 200 Watts RF power, 72 mTorr chamber pressure and 8 6 sccm gas flow rate During each run of the RIE processes the experiment was continued until the SiO_2 layer was completely removed We also allowed the experiments to continue until some of the upper Si layers were etched away to confirm that there was no more SiO_2 on top of the Si sample after the etch process The values of different harmonics of I-V parameters were recorded and plotted against time to examine the change in values of the parameters while the SiO_2 overlayer was being completely etched away

3 7 Results and Discussion of the Use of PIM as End Point Detector

We plotted all the I-V parameters (i e , RF voltage, RF current, RF power, RF impedance and phase) up to the 5th harmonic against time to see whether there is any change in those parameters when the Si-SiO_2 interface is reached during the etch process But we could not find any significant difference in values in any of the harmonics of these parameters *except* the fundamental components of RF impedance (Z_l) and the phase (ϕ_l) All except Z_l and ϕ_l change their values in an uncorrelated manner and cannot be used as monitoring parameters for end point detection For

Table 3 1 Design matrix of the experimental run for the end point detection experiments

Run	RF Power (Watt)	Chamber Pressure (mTorr)	Gas flow rate (sccm)
1	100	40	5 2
2	100	60	5 2
3	150	40	5 2
4	150	60	5 2
5	100	50	3 9
6	100	50	6 5
7	150	50	3 9
8	150	50	6 5
9	125	40	3 9
10	125	40	6 5
11	125	60	3 9
12	125	60	6 5
13	125	50	5 2

simplicity of discussion we have included only the plots for Z_I and ϕ_I in this section Figures 3 9-3 21 display both Z_I and ϕ_I, plotted against time for the different RF powers, chamber pressures and gas flow rates as the SF_6 RIE was carried out on the Si wafer covered with a 1 32 µm SiO_2 layer, in accordance with the experimental "Runs" defined in Table 3 1

First, if we consider only ϕ_I we see from the figures that the value of ϕ_I varies according to a fixed pattern for all the experimental conditions In order to facilitate an explanation the total time period used for each experiment can be subdivided into four time zones as shown in the figures After the plasma is initiated the value of ϕ_I varies continuously and becomes stable after a certain period of time This is marked as time zone I This variation is due to the time required to reach a steady-state discharge condition for the plasma [135] The main reason of this change is due to the chemical effects imposed by the cleaning of the chamber surface just after the initiation of the plasma In time zone II the constituents inside the plasma chamber are stable and fixed because only the SiO_2 is being etched away This is why ϕ_I maintains almost a fixed value throughout this zone At the end of this zone the SiO_2 layer is completely removed and Si underneath the SiO_2 layer starts to be etched That means that the plasma chemistry is changed from one state to another Again, to reach another steady-state discharge a finite amount of time is required and this is what we see in time zone III In
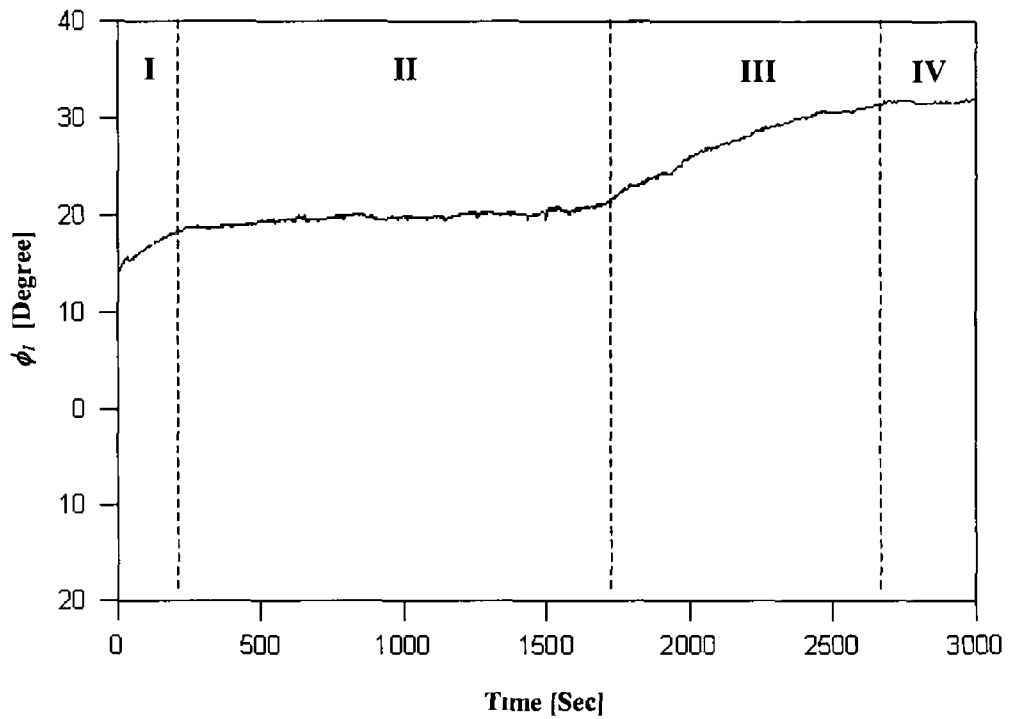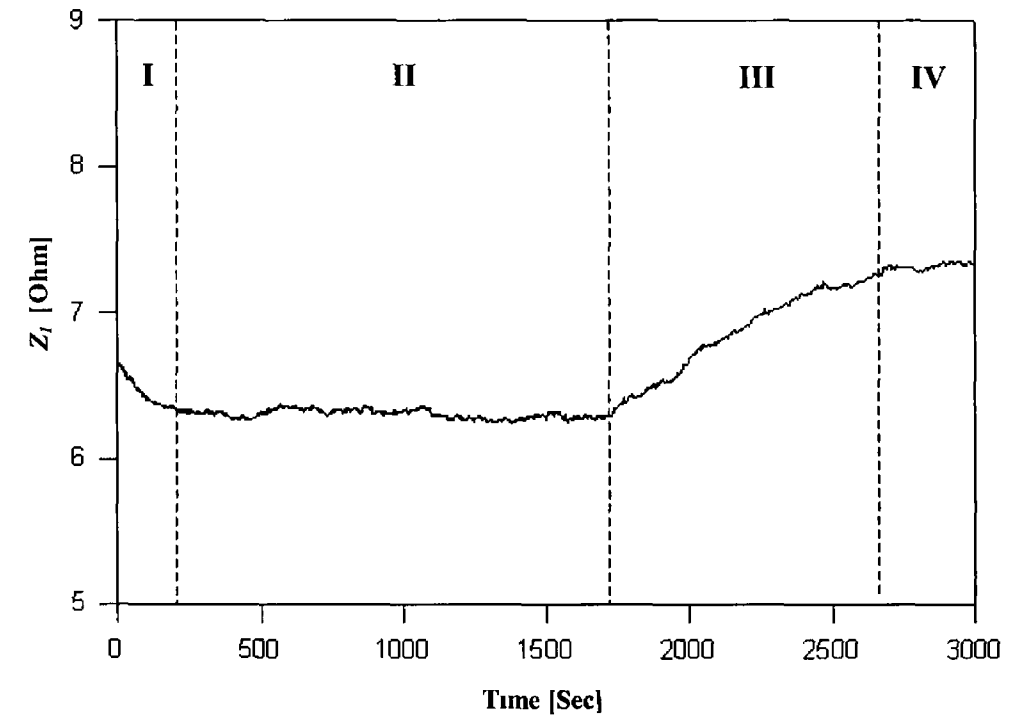
Figure 3 9 Fundamental components of RF impedance and phase plotted against time while SF₆ RIE was carried out on half of a 100mm diameter Si wafer covered with 1 32μm thick SiO₂ layer at RF power=100 Watts, chamber pressure=40 mTorr and gas flow rate=5 2 sccm (Run 1)
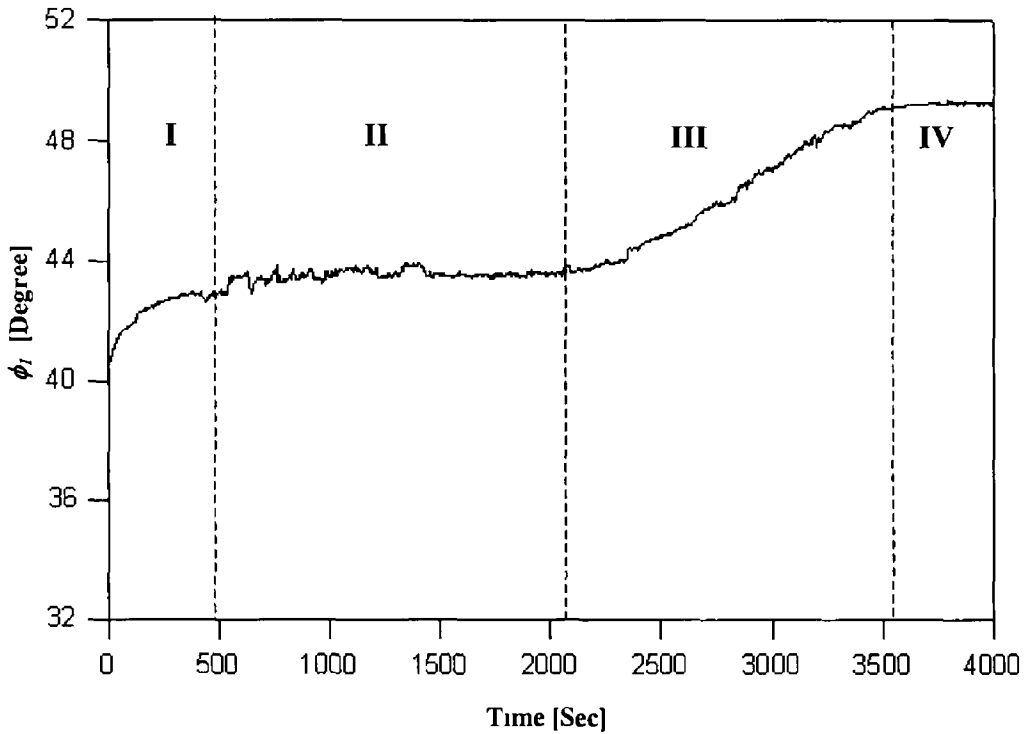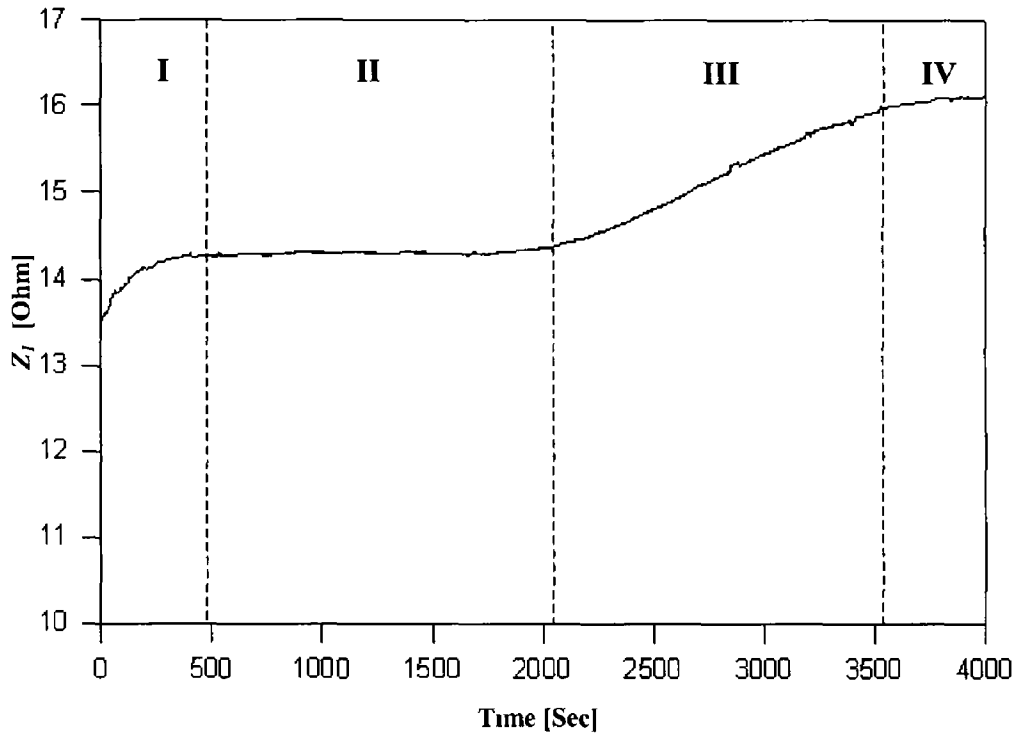
Figure 3 10 *Fundamental components of RF impedance and phase plotted against time while SF_6 RIE was carried out on half of a 100mm diameter Si wafer covered with 1 32μm thick SiO_2 layer at RF power=100 Watts, chamber pressure=60 mTorr and gas flow rate=5 2 sccm (Run 2)*
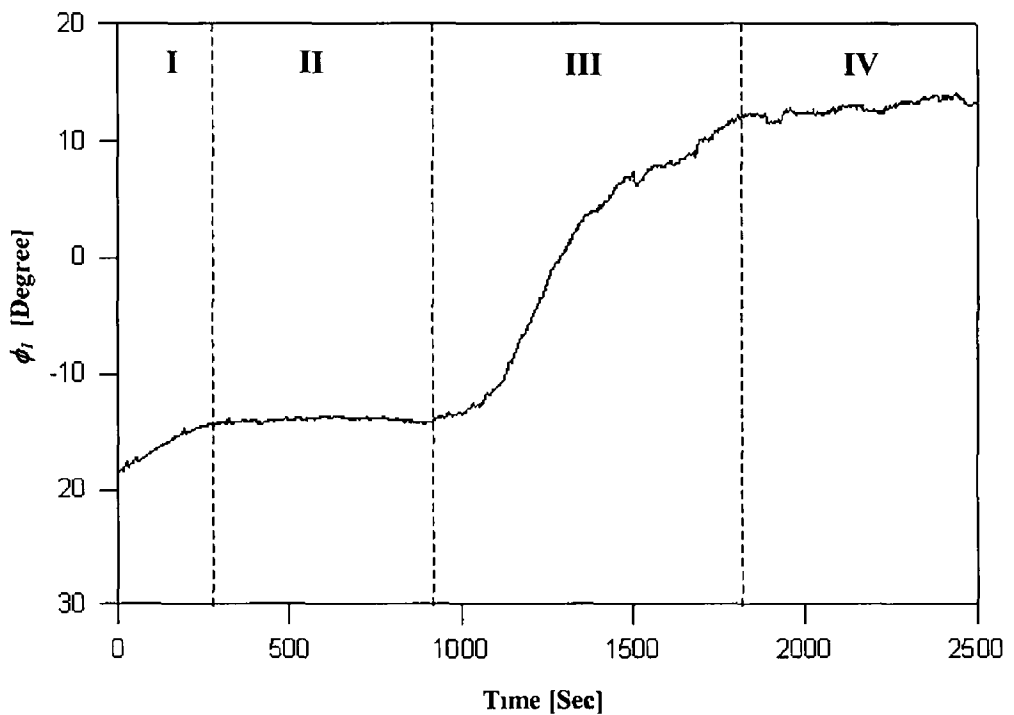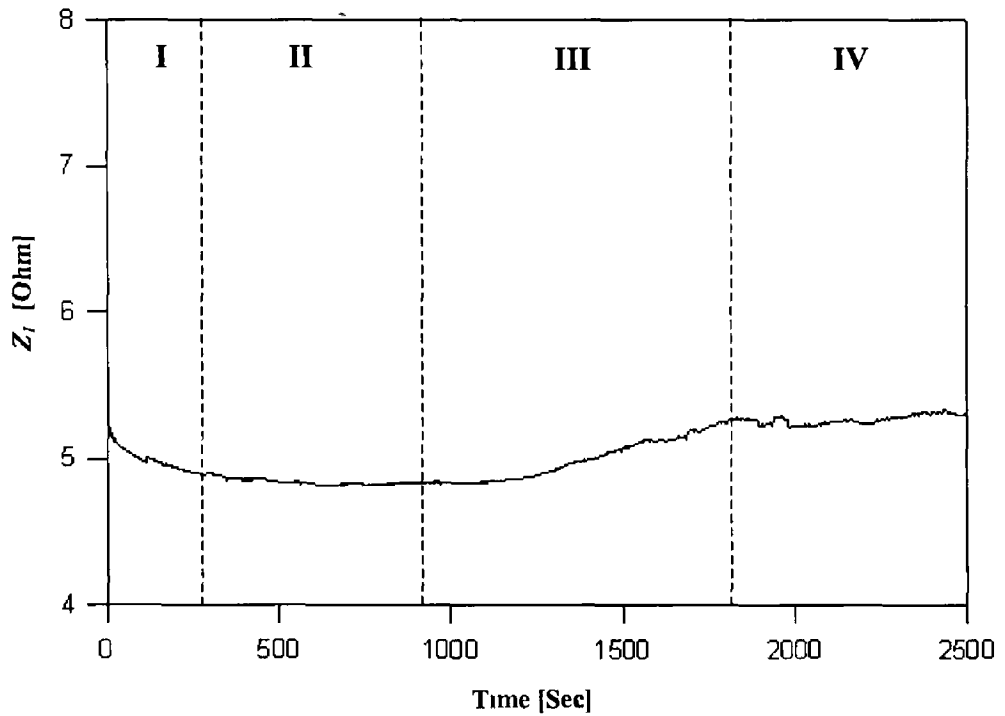
Figure 3 11 Fundamental components of RF impedance and phase plotted against time while SF_6 RIE was carried out on half of a 100mm diameter Si wafer covered with 1 32μm thick SiO_2 layer at RF power=150 Watts, chamber pressure=40 mTorr and gas flow rate=5 2 sccm (Run 3)
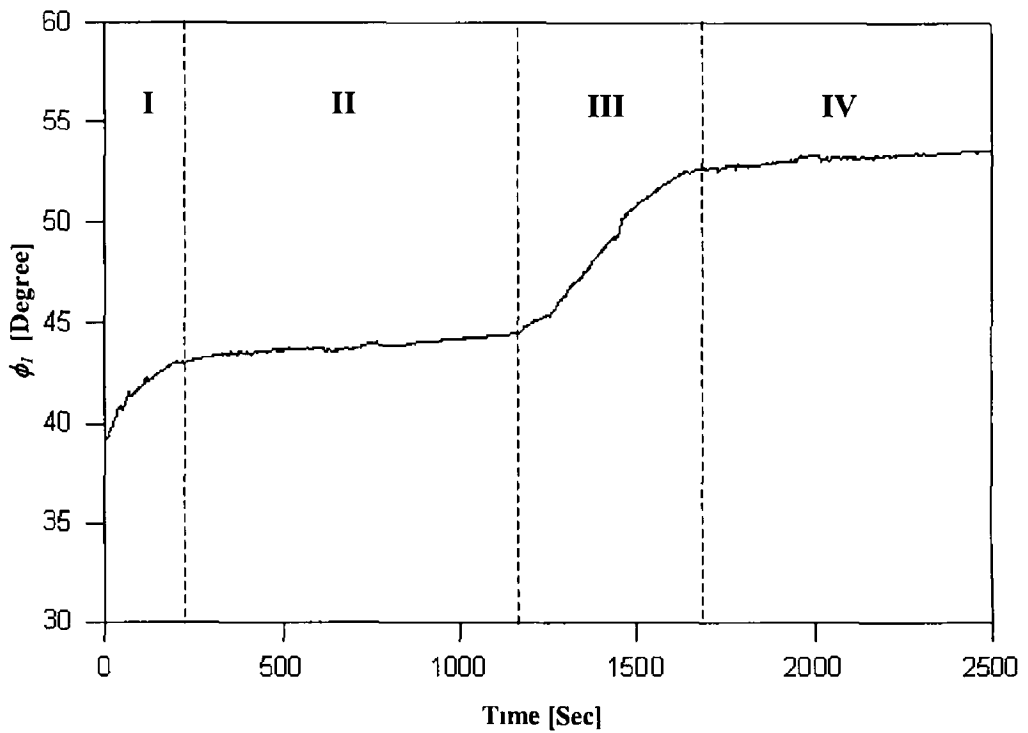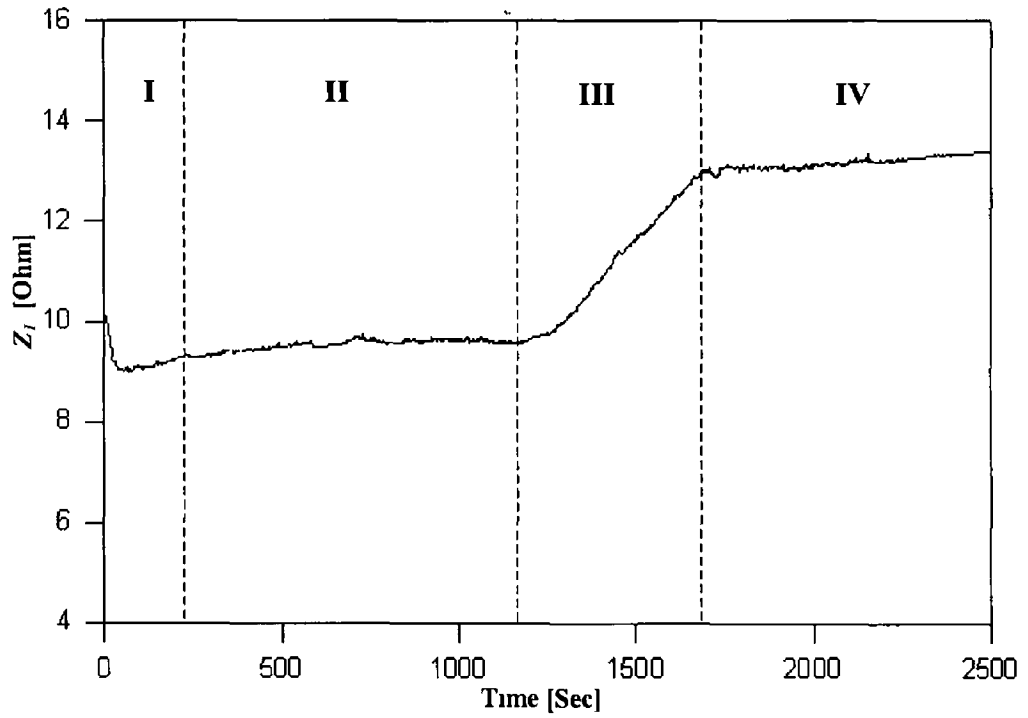
Figure 3 12 Fundamental components of RF impedance and phase plotted against time while SF₆ RIE was carried out on half of a 100mm diameter Si wafer covered with 1 32μm thick SiO₂ layer at RF power=150 Watts, chamber pressure=60 mTorr and gas flow rate=5 2 sccm (Run 4)
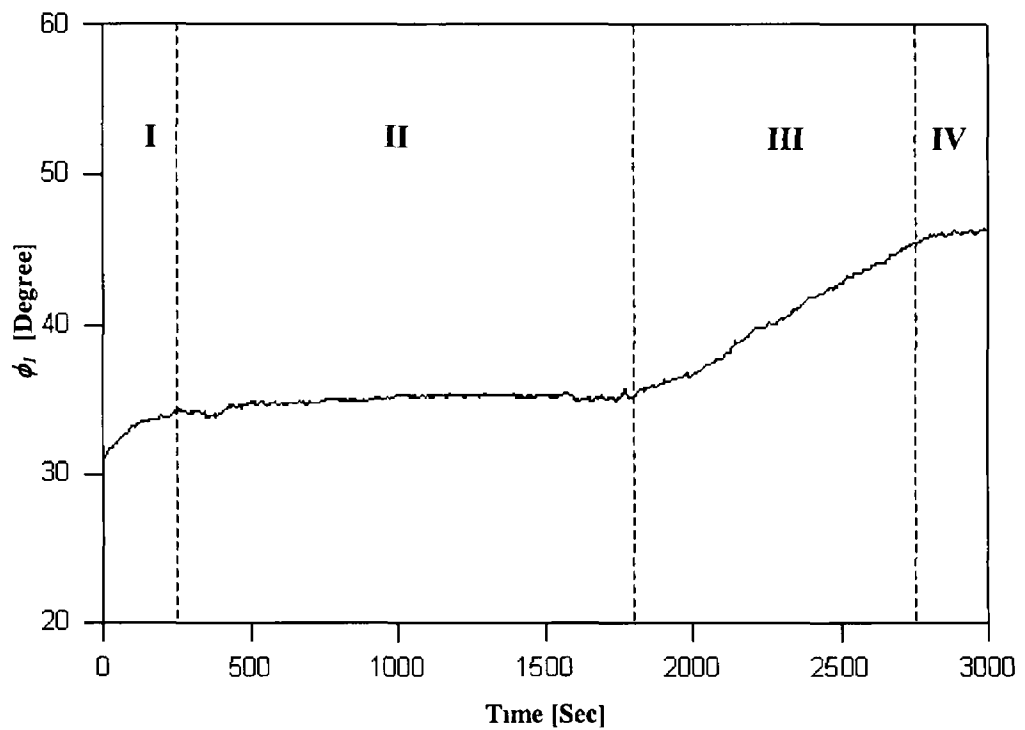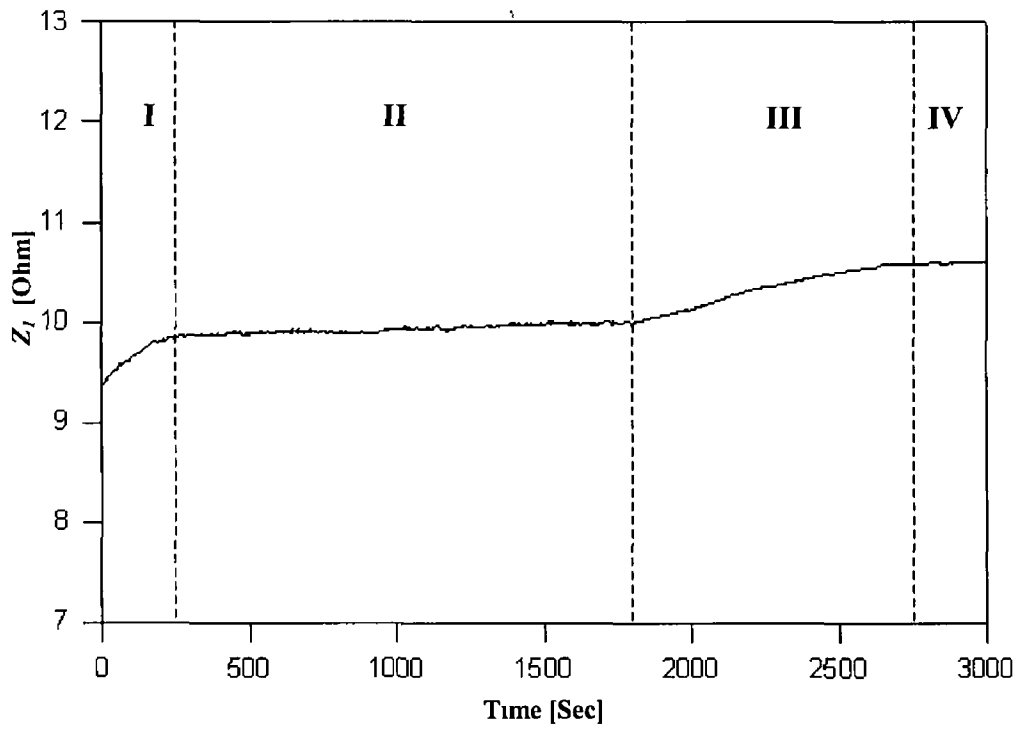
Figure 3 13 *Fundamental components of RF impedance and phase plotted against time while SF_6 RIE was carried out on half of a 100mm diameter Si wafer covered with 1 32μm thick SiO_2 layer at RF power=100 Watts, chamber pressure=50 mTorr and gas flow rate=3 9 sccm (Run 5)*
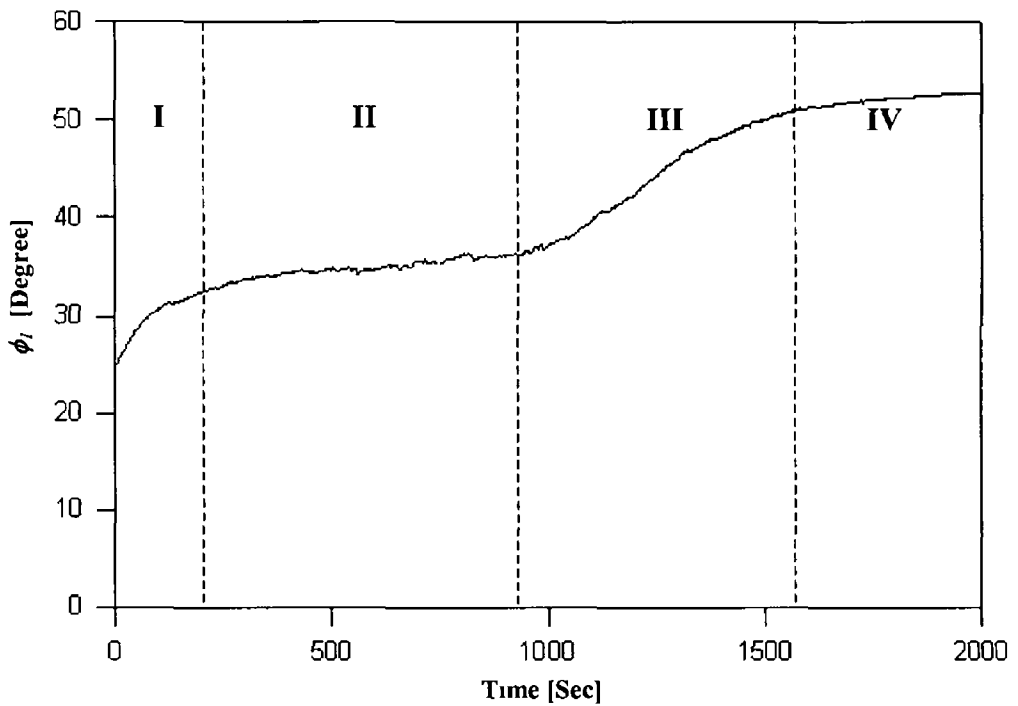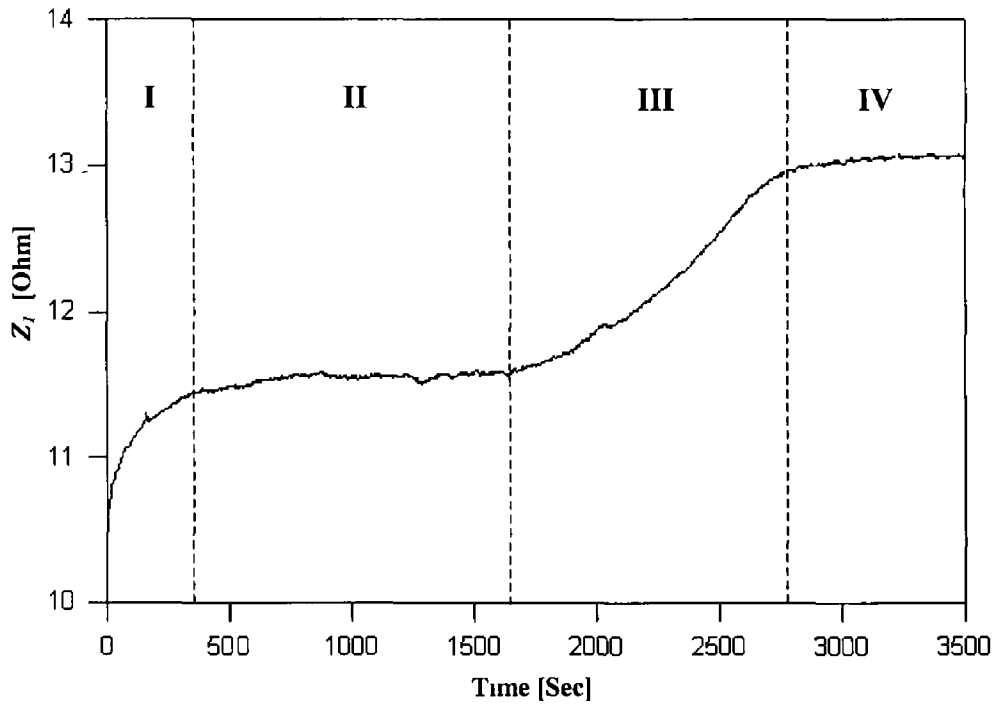
Figure 3 14 *Fundamental components of RF impedance and phase plotted against time while SF$_6$ RIE was carried out on half of a 100mm diameter Si wafer covered with 1 32µm thick SiO$_2$ layer at RF power=100 Watts, chamber pressure=50 mTorr and gas flow rate=6 5 sccm (Run 6)*
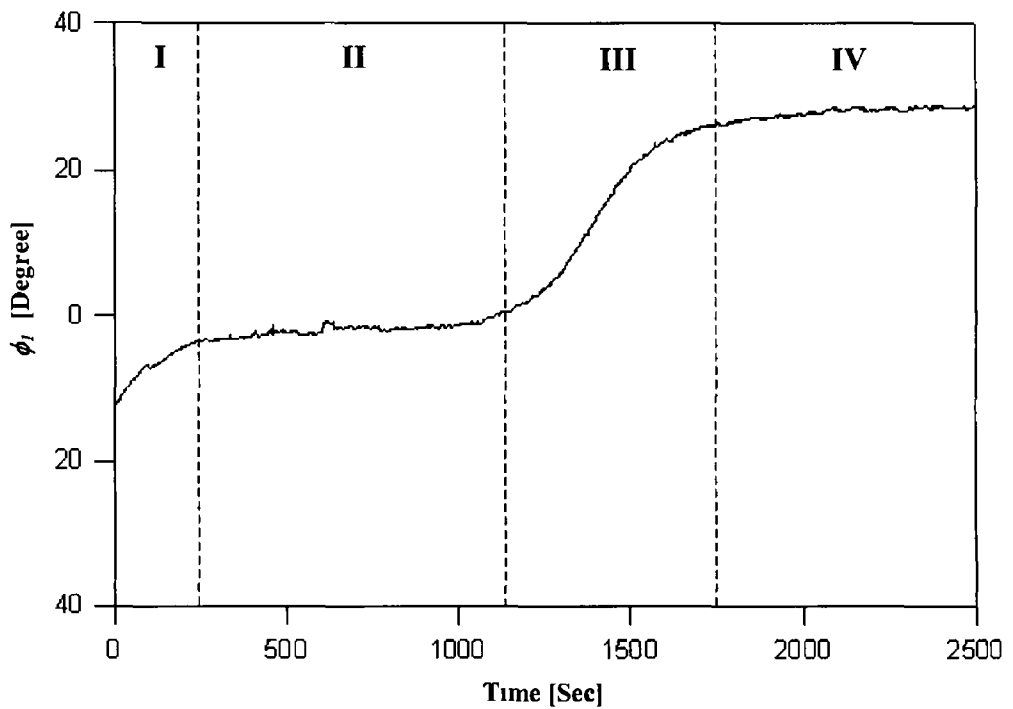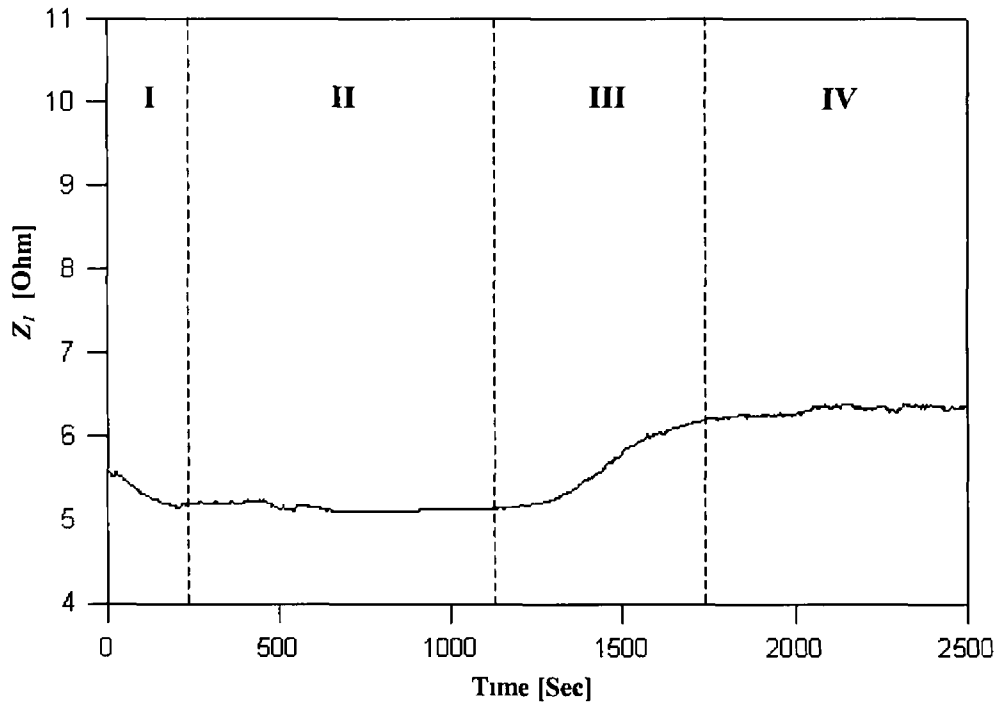
Figure 3 15 Fundamental components of RF impedance and phase plotted against time while SF_6 RIE was carried out on half of a 100mm diameter Si wafer covered with 1 32μm thick SiO_2 layer at RF power=150 Watts, chamber pressure=50 mTorr and gas flow rate=3 9 sccm (Run 7)
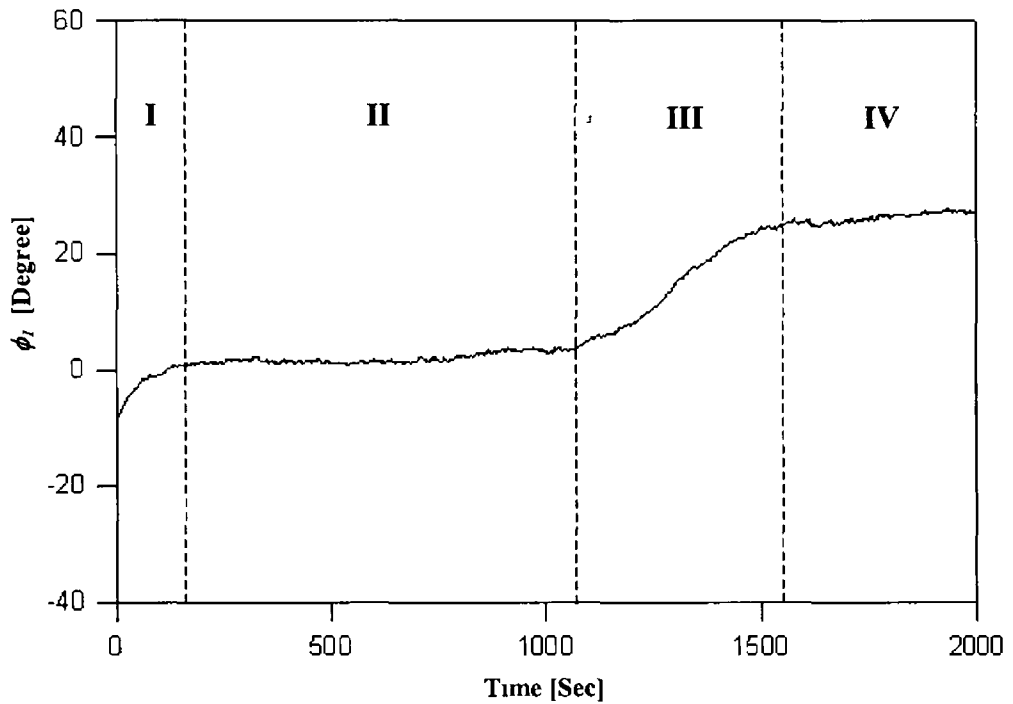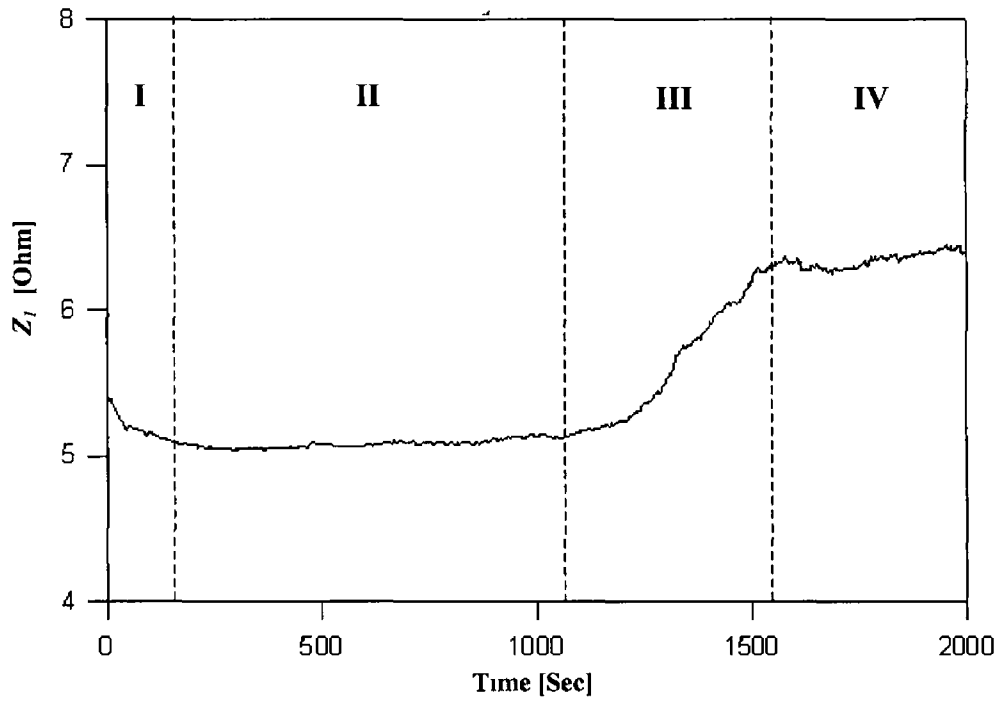
Figure 3.16 Fundamental components of RF impedance and phase plotted against time while SF₆ RIE was carried out on half of a 100mm diameter Si wafer covered with 1 32μm thick SiO₂ layer at RF power=150 Watts, chamber pressure=50 mTorr and gas flow rate=6 5 sccm (Run 8)
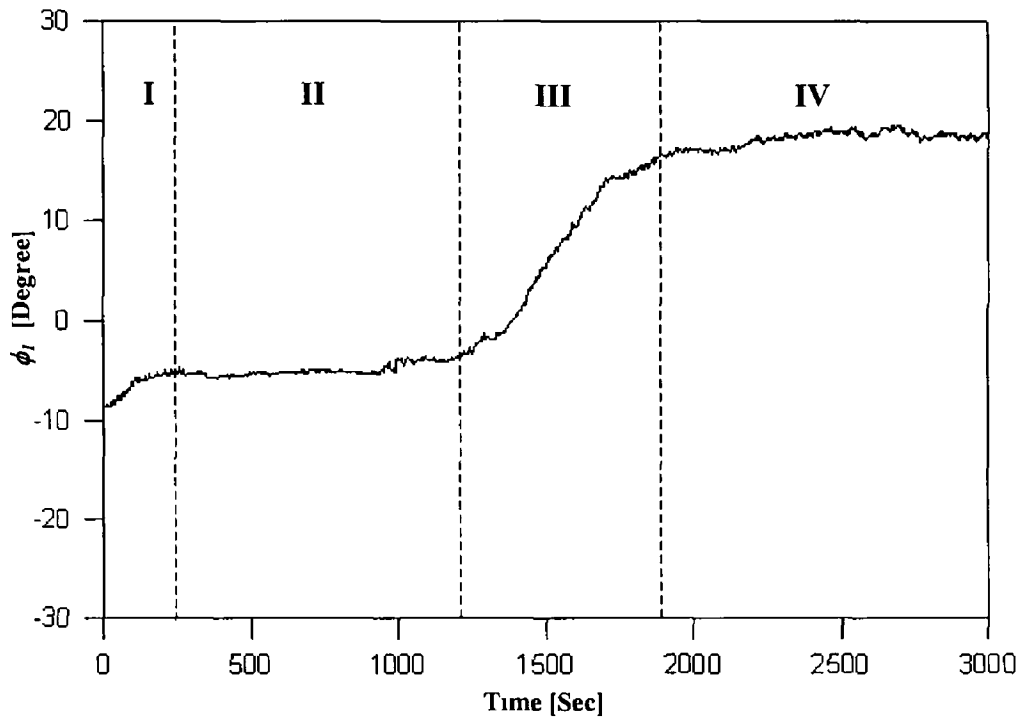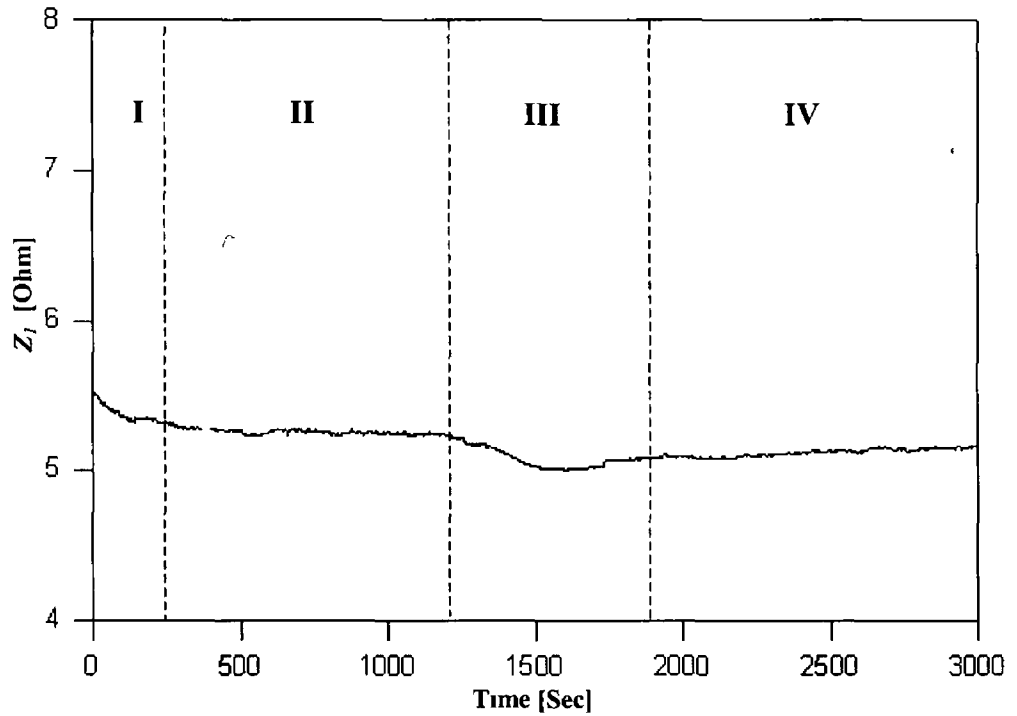
Figure 3 17 *Fundamental components of RF impedance and phase plotted against time while* SF_6 *RIE was carried out on half of a 100mm diameter Si wafer covered with 1 32μm thick* SiO_2 *layer at RF power=125 Watts, chamber pressure=40 mTorr and gas flow rate=3 9 sccm (Run 9)*

112
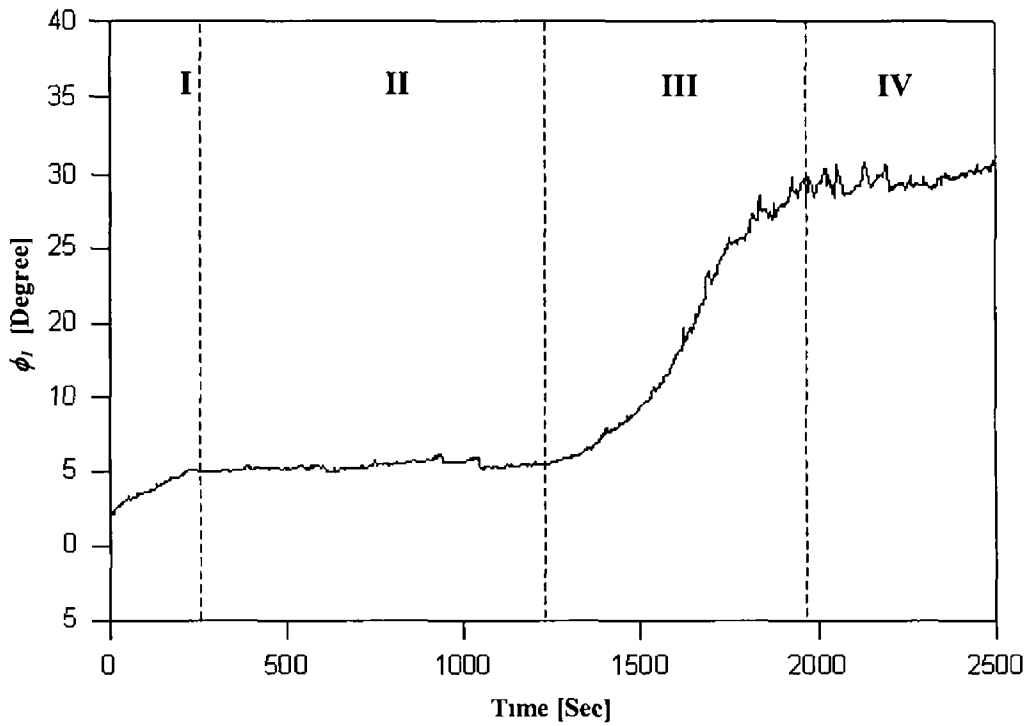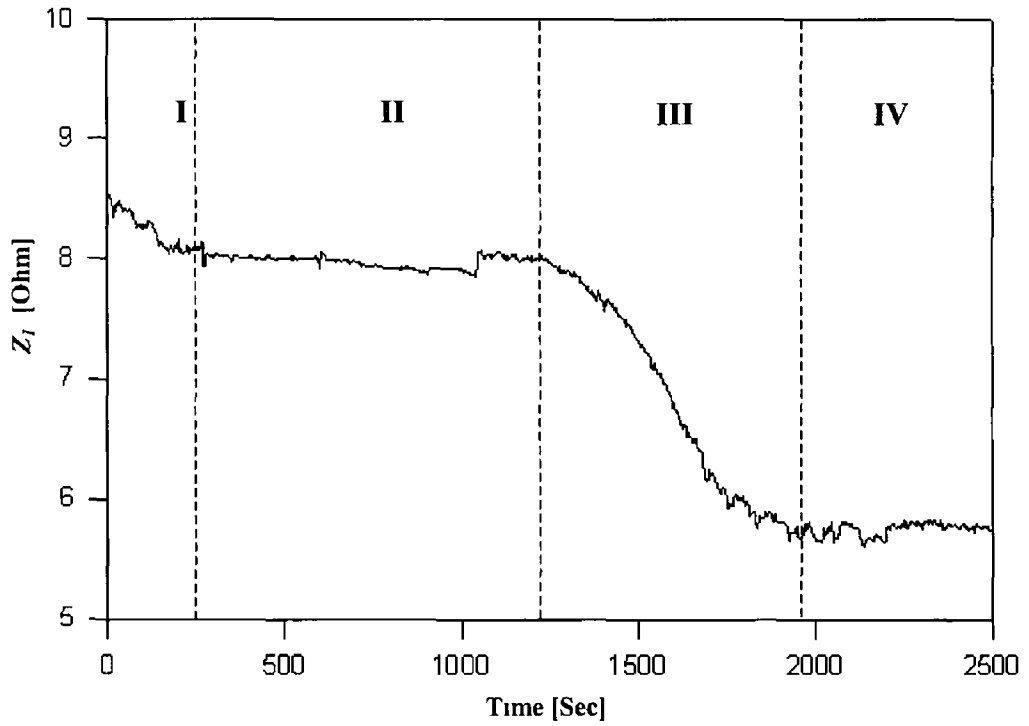
Figure 3 18 *Fundamental components of RF impedance and phase plotted against time while SF₆ RIE was carried out on half of a 100mm diameter Si wafer covered with 1 32μm thick SiO₂ layer at RF power=125 Watts, chamber pressure=40 mTorr and gas flow rate=6 5 sccm (Run 10)*
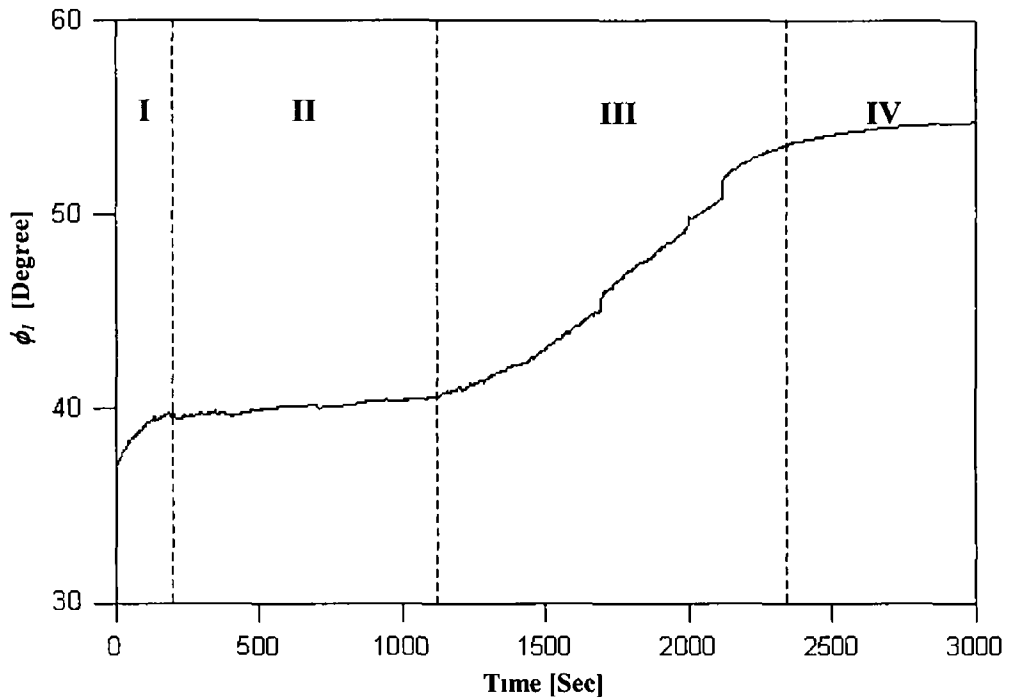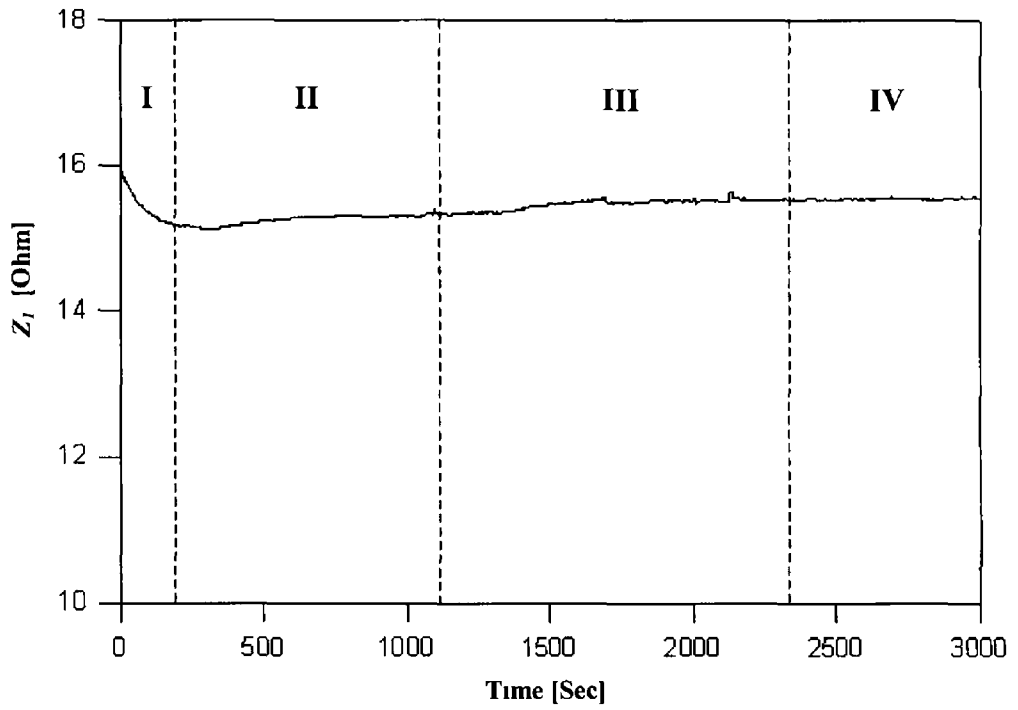
Figure 3 19 *Fundamental components of RF impedance and phase plotted against time while SF$_6$ RIE was carried out on half of a 100mm diameter Si wafer covered with 1 32μm thick SiO$_2$ layer at RF power=125 Watts, chamber pressure=60 mTorr and gas flow rate=3 9 sccm (Run 11)*
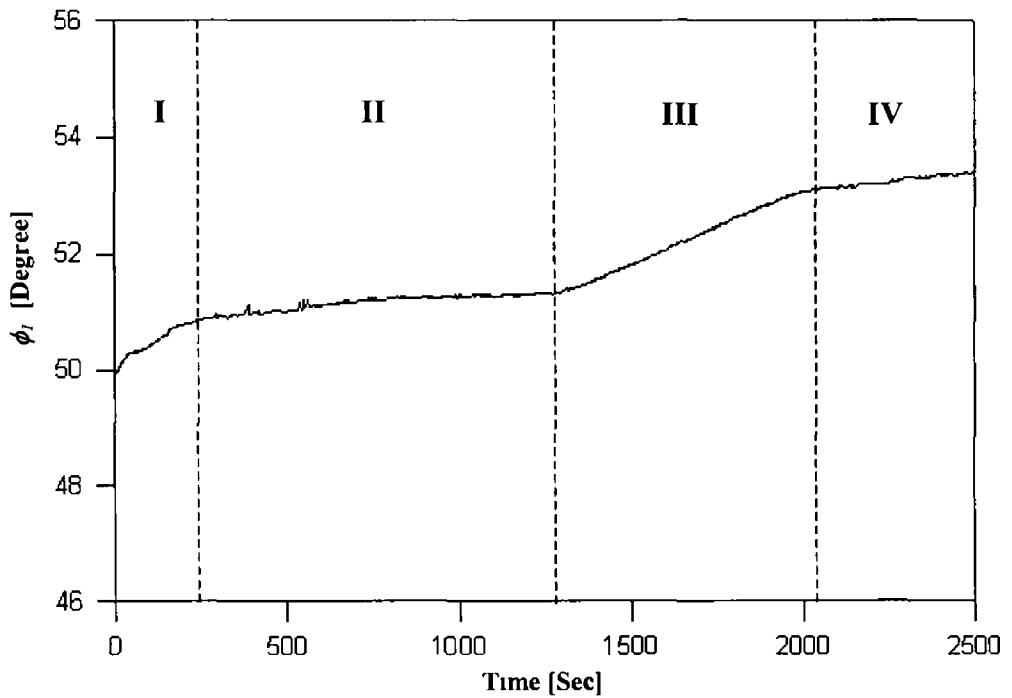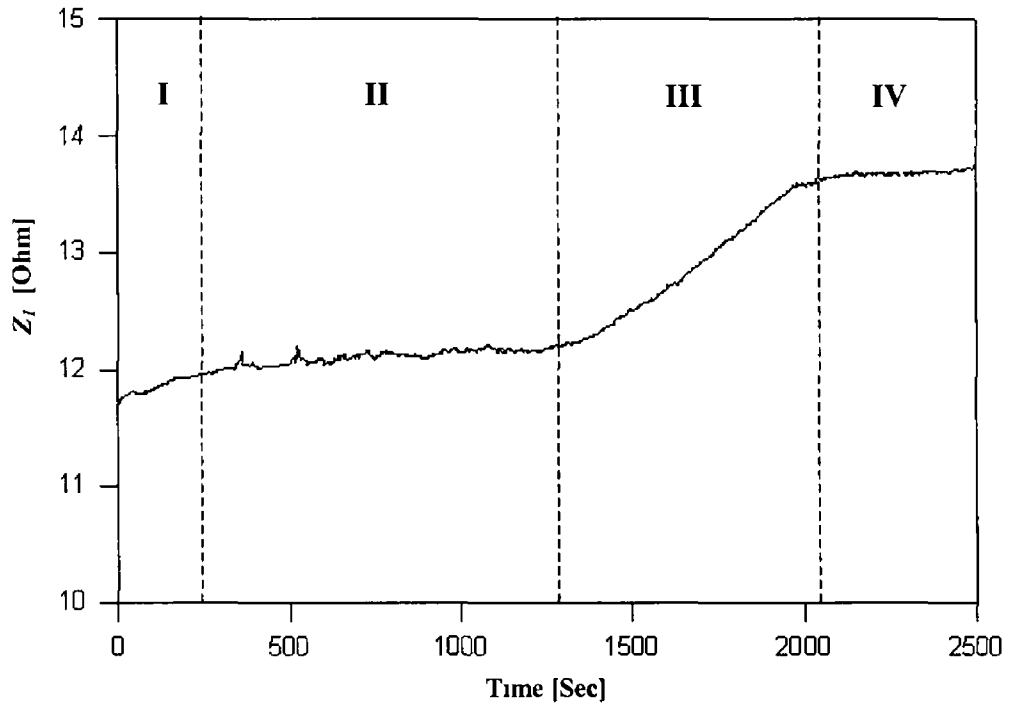
Figure 3 20 Fundamental components of RF impedance and phase plotted against time while SF_6 RIE was carried out on half of a 100mm diameter Si wafer covered with 1 32μm thick SiO_2 layer at RF power=125 Watts, chamber pressure=60 mTorr and gas flow rate=6 5 sccm (Run 12)
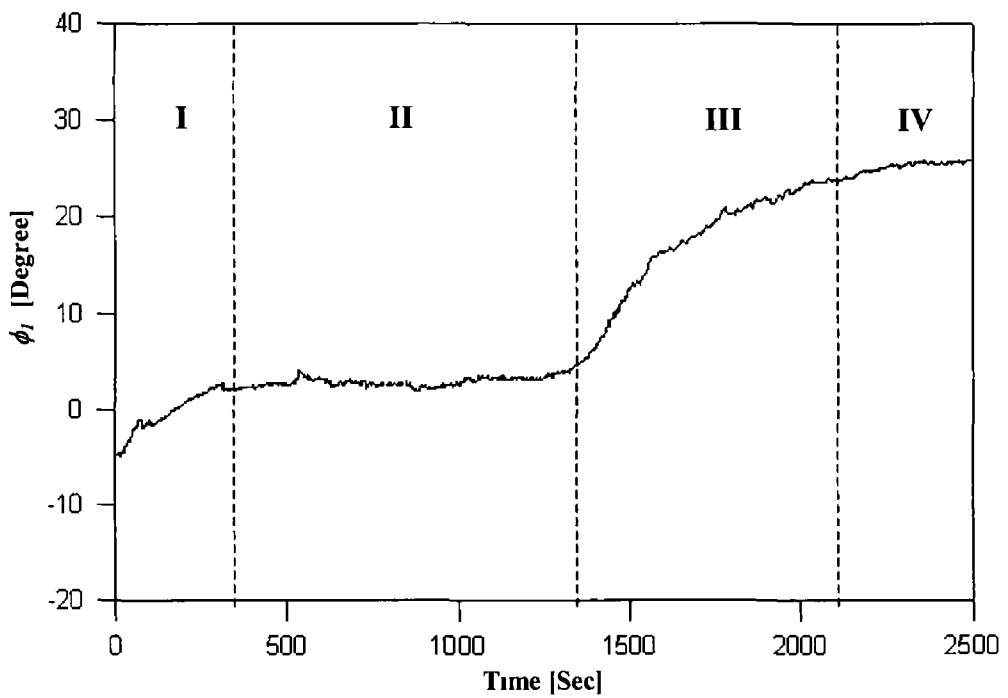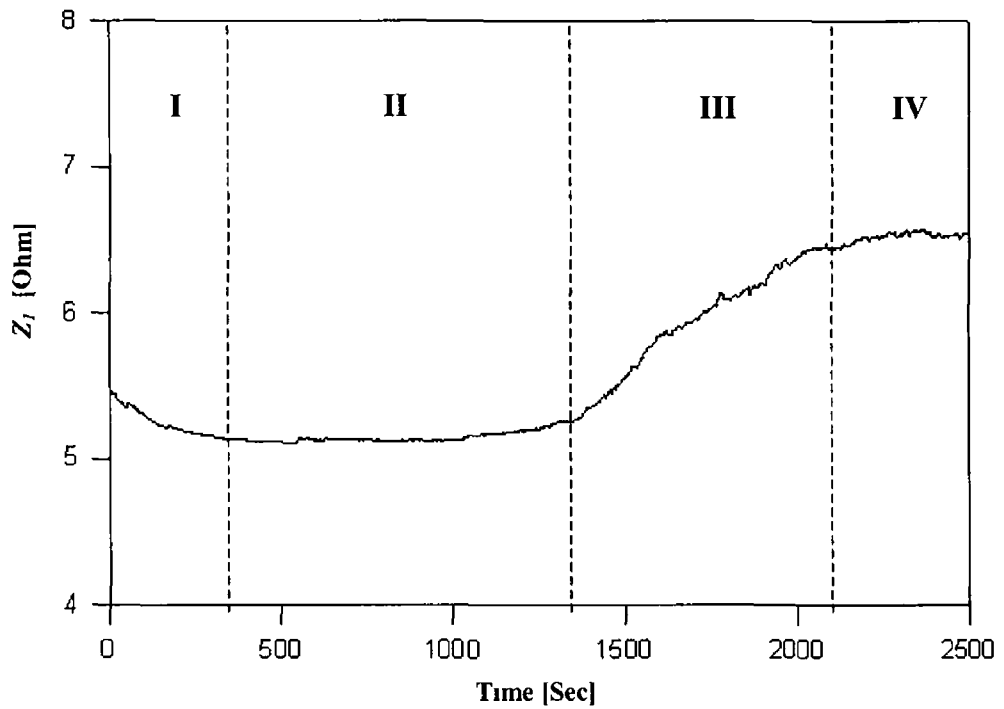
Figure 3 21 *Fundamental components of RF impedance and phase plotted against time while SF_6 RIE was carried out on half of a 100mm diameter Si wafer covered with 1 32µm thick SiO_2 layer at RF power=125 Watts chamber pressure=50 mTorr and gas flow rate=5 2 sccm (Run 13)*

this zone ϕ_l varies gradually from one steady-state value to another and at the end of this time zone it becomes stable again Throughout the time zone IV ϕ_l maintains a fixed value because the constituents of the plasma again become fixed and stable

The time required to completely etch the SiO_2 layer (or to start the transition of the ϕ_l value) depends on the etch rate, which is a function of experimental conditions i e , RF power, chamber pressure and gas flow rate That was the reason why the transition of ϕ_l from one value to another occurred at different times (after the discharge was initiated) for different experimental conditions The value of ϕ_l is also different for different experimental conditions even though the sample conditions (SiO_2 or Si) are identical For this reason the change in the value of ϕ_l, when the SiO_2-Si interface is reached, is different for different experimental conditions which can be clearly identified from the figures

If we consider Z_l as an end point detector we see from the above figures that it also adheres to the same four time zones in most of the experimental conditions but not for all the experiments In figure 3 19 it is difficult to separate the time zone III i e , there is no significant change in the value of Z_l when the SiO_2-Si interface is reached In figures 3 17 and 3 18 the value of Z_l goes downward in time zone III, whereas it goes upward in rest of the figures Although time zone I is not important for end point detection, we observed that after the initiation of plasma the value of Z_l goes downward in this zone in some of the experiments (figures 3 9, 3 11, 3 12, 3 15, 3 16, 3 17, 3 18, 3 19 and 3 21) whereas it goes upward in the other experiments (figures 3 10, 3 13, 3 14 and 3 20)

The increments of ϕ_l values in time zone I indicate that the reactive part of the plasma impedance becomes more inductive when SiO_2 is being etched than when nothing is being etched Similarly, the increments of ϕ_l values in time zone III indicate that the reactive part of the plasma impedance is more inductive when Si is being etched than when SiO_2 is being etched The relative variation of sheath capacitance with the plasma chemistry could be the major reason for these changes in ϕ_l values mentioned above (in time zones I and II) However, Z_l denotes the absolute value of the fundamental component of plasma impedance, which varies as a function of both of its

117

real and the reactive parts This can account for the fact that the Z_i values change in a somewhat complex manner compared to the ϕ_i values and do not follow the same trend for all the experiments

We should note here that during the end point experiments described in section 3 6 the harmonic components of the RF discharged power and/or the RF current were very small compared to their fundamental components For example, in run 13 given in Table 3 1, the second, third, fourth and fifth harmonic components of discharged power were ~1 21%, ~0 317%, ~0 03% and ~0 0%, respectively, of the fundamental component whereas the same harmonic components of the RF current were ~2 63%, ~1 44%, ~0 49% and ~0 24%, respectively, of the fundamental component Therefore when the plasma chemistry changes at the end point, the change in the harmonic components of I-V parameters becomes very small and cannot be identified easily by the PIM That is why the higher harmonic components of I-V parameters could not be used for end point detection

From the above discussion we can conclude that the fundamental component of phase can be used as a good controlling parameter for end point detection when Si wafers covered with a SiO_2 layer undergoes a SF_6 RIE process The fundamental component of plasma impedance can also be used for end point detection but only for specific experimental conditions The other harmonics or I-V parameters were not found to be useful as parameters for end point detection

3 8 Experimental Confirmation of the End Point Detection

To confirm that there was no SiO_2 left on the Si wafer we carried out two different experiments/observations They are described below with the results and comments

3 8 1 Observation of the plasma colour

The plasma species concentration gradually changes from one state to another when the SiO_2 layer is completely removed and the Si layer starts to be etched away (time zone III in figures 3 9-3 21) This change takes a finite amount of time when the

emission properties of the plasma also changes gradually from one state to another Due to this change a clear change in plasma colour was observed during the RIE experiments After the plasma was initiated photographs of the plasma were taken by a digital still camera at different times of the etch process Figure 3 22 shows twenty-*four* chronological pictures (numbered from 1 to 24) depicting the evolution of the plasma with time The pictures were taken at intervals of approximately 90 seconds The two relatively dark portions at the top and the bottom of each picture indicate the image of the top and the bottom electrode of the plasma chamber, respectively The intermediate portion between the two electrodes shows the image of the actual plasma During the experiment we also monitored the ϕ_i value against time Pictures 1-10 were taken in time zone II, pictures 11-17 were taken in time zone III and pictures 18-24 were taken in time zone IV The constant pinkish plasma colour shown by pictures 1-10 is consistent with no change in the plasma chemistry in time zone II In pictures 11-17 we can see that there is a gradual change in the plasma colour from pinkish to whitish which reflects the gradual change in the plasma chemistry in time zone III Pictures 18-24 maintain the same whitish colour consistent with another stable plasma condition as the RIE process is carried on From figure 3 22 we see that the plasma colour totally changed from pinkish to whitish which reflects the complete change over of the plasma chemistry This was one indication that the SiO_2 layer was completely removed after the process

3 8 2 Infra Red Spectroscopy measurements on the samples used for RIE experiments

After each of the etching experiments given by Table 3 1 we carried out a Fourier Transform Infra-Red (FTIR) measurement on the sample used for the RIE experiments to prove that there was no SiO_2 left on the surface of the sample The FTIR reflectance spectrum was obtained using a Perkin-Elmer FTIR 2000 system operating in reflection mode The scanning resolution was 2 cm ^{1} The angle of IR beam incidence was set to 35° with respect to the normal to the surface of the sample All the scans were performed at room temperature and normal atmospheric conditions The Kramers-Kronig transformation [150,151] was used to obtain the absorbance spectrum from each of the reflectance spectra For comparisons the spectra were obtained under identical
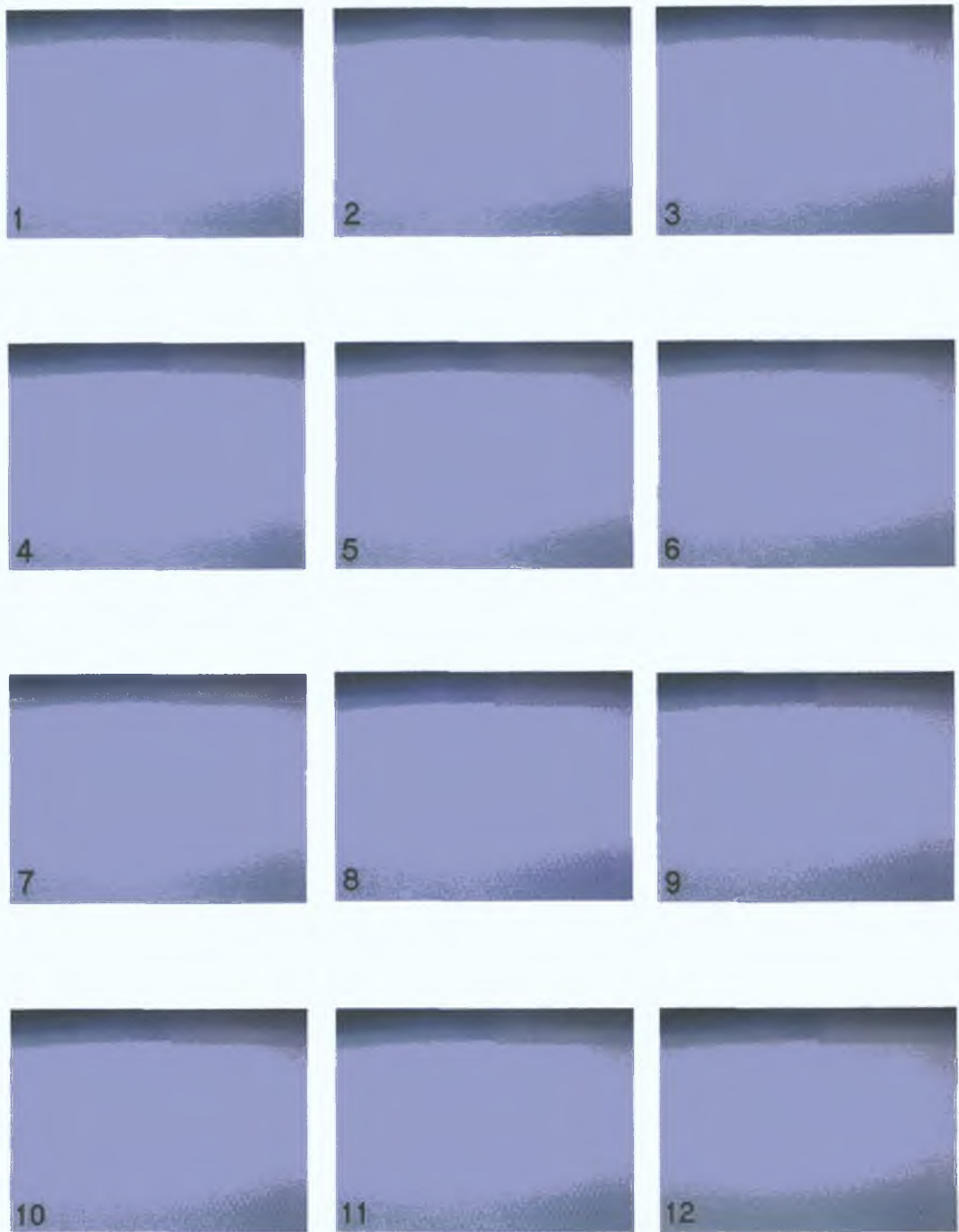
Figure 3.22 (1-12) Photograph of plasma taken by a digital still camera at different times after the plasma was initiated when Si wafer covered with 1.32 μm SiO_2 layer undergoes SF_6 RIE process. The time between the images is approximately 90 seconds.
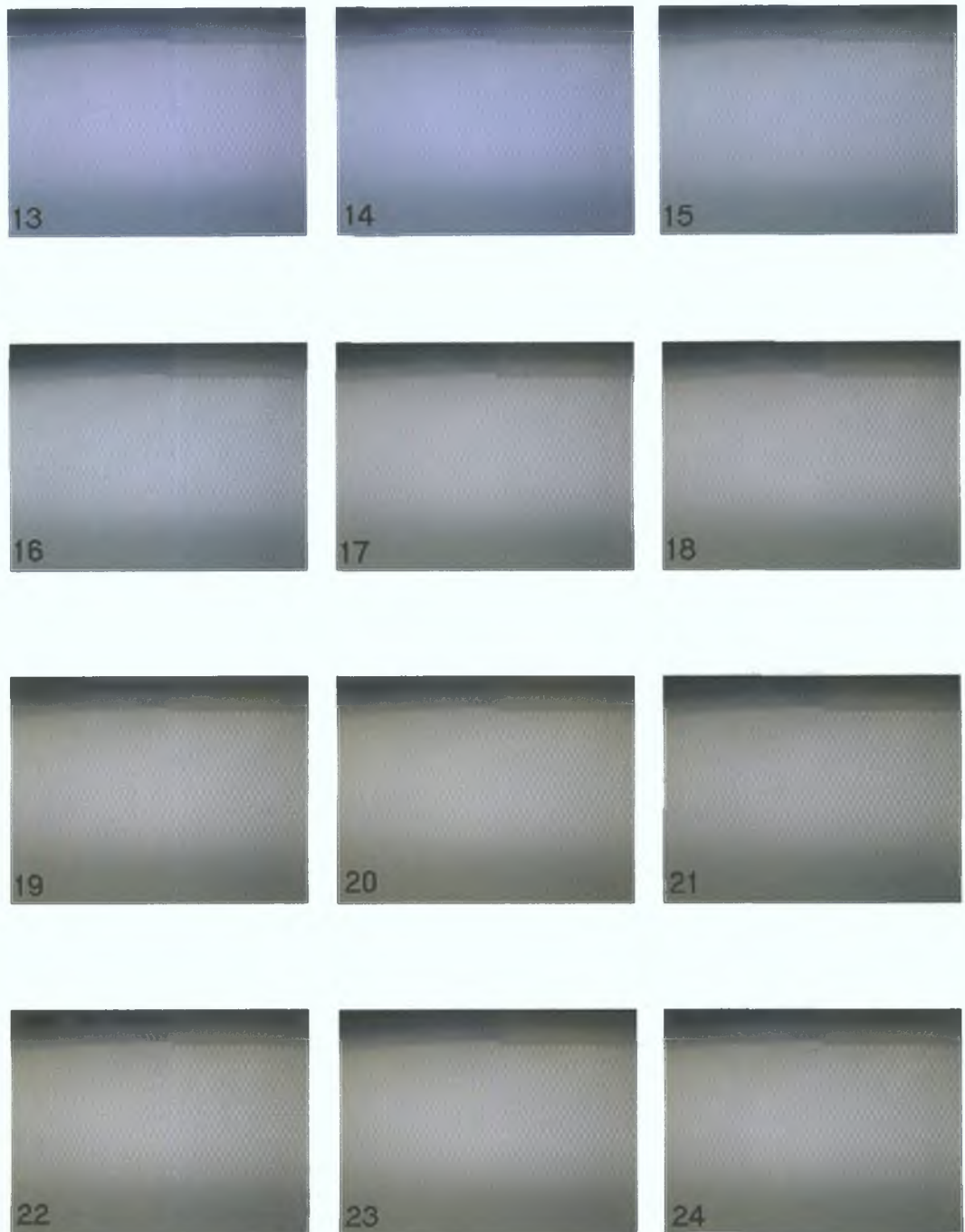
Figure 3.22 (13-24) Photograph of plasma taken by a digital still camera at different times after the plasma was initiated when Si wafer covered with 1.32 μm SiO₂ layer undergoes SF₆ RIE process. The time between the images is approximately 90 seconds.

FTIR acquisition conditions from a bare Si wafer and a Si wafer covered with a 1 32 μm thick SiO_2 layer, respectively Figure 3 23 shows five absorbance spectra plotted against wavenumber, where **a, b** and **c** represent the absorbance spectra obtained at three different locations of the Si sample used for one of the end point experiments given by Table 3 1 For our interest we repeated this particular end point experiment and stopped when the value of ϕ_l just became flat and went into zone IV (see figures 3 9- 3 21) after the transition from one value to another The different positions on the sample were so chosen that they were at different radial positions of the powered electrode of the RIE equipment during the end-point experiment—one positioned near the edge of the sample which was nearest to the centre of the electrode, one near the edge of the sample which was farthest from the centre of the electrode and the other at the middle of the sample The spectra **I** and **II** represent the same absorbance spectra taken from a bare Si wafer and a Si wafer covered with 1 32 μm thick SiO_2 layer, respectively All the spectra in figure 3 23 are plotted at the same scale except each spectrum is vertically shifted so that they can be easily compared

From figure 3 23 it is clearly evident that all three spectra (i e , **a, b** and **c**) taken from the sample are similar to that of the bare silicon (i e , **I**) That proves that there was only Si on all the surface of the sample Again, if there was any SiO_2 left on the surface of the sample, it would display a peak near 1080 cm[1] [152-154] in the absorbance spectrum, which is clearly shown in the spectrum obtained from a Si sample covered with SiO_2 layer (i e , **II**) The above discussion confirms that the SiO_2 layer was completely etched away during the RIE end point experiment

3 9 Test of Non-Uniformity of Etch Rate During the End Point Experiment

The plasma species concentration changes at the completion of the etching of the SiO_2 layer, forcing the electrical parameters to change As discussed in section 3 7 the value of ϕ_l completely reflects this change The transition time to reach the next steady state condition also depends upon the areal non-uniformity in the etching To see whether there was any non-uniformity in the etching we carried out two different experiments They are described below
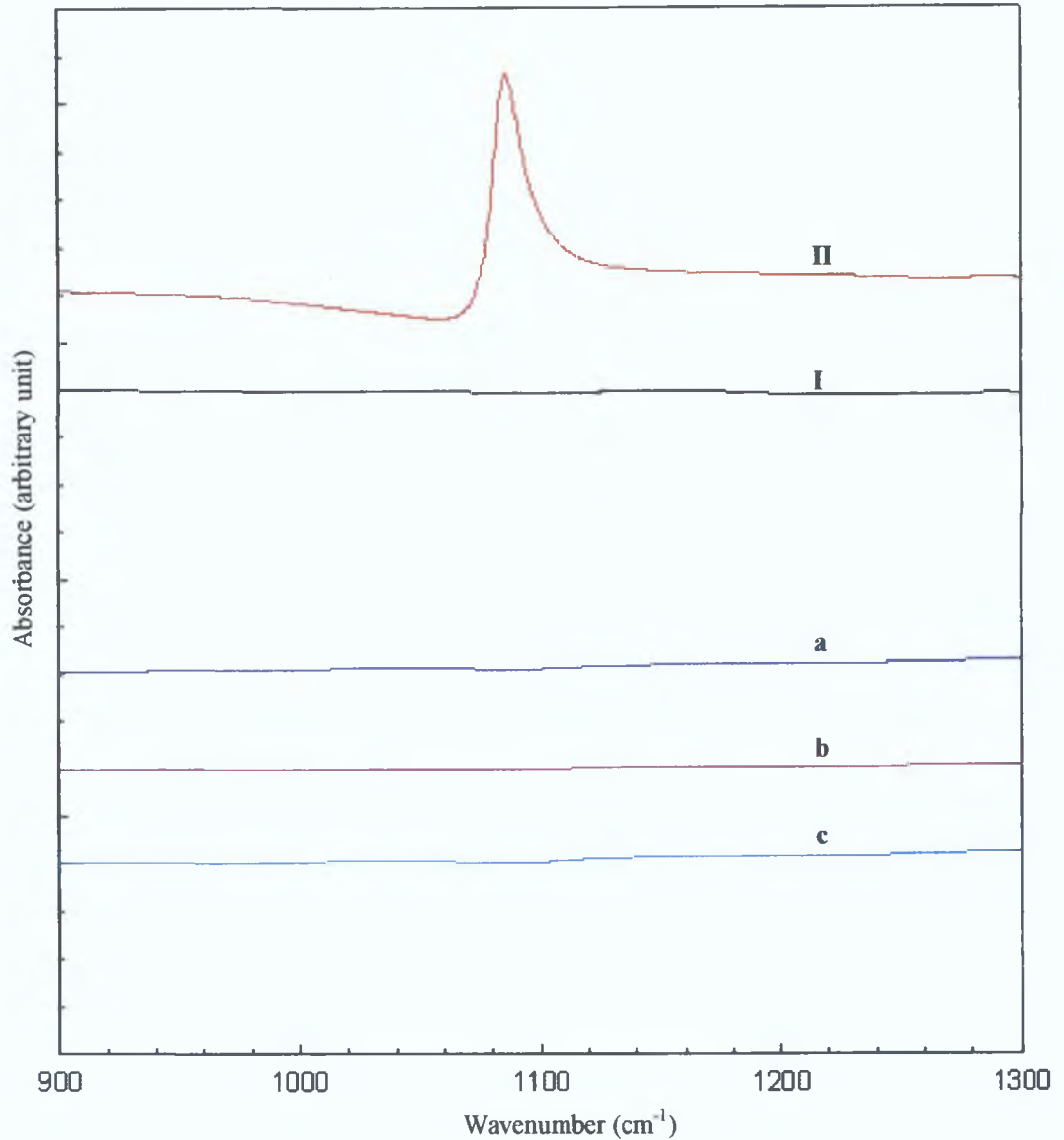
Figure 3.23 FTIR absorbance spectra of Si sample used in RIE end-point experiment (*a, b and c*) compared with the same spectra of bare Si and SiO₂ (*I and II*), respectively.

3.9.1 Fourier Transform Infra-Red Spectroscopy (FTIR) measurement for non-uniformity test

In order to examine whether there was any non-uniformity in the etching during the end point experiment, the RIE experiment described by Run 13 in Table 3.1 was carried out on half of a 100 mm dia SiO₂ sample (Si wafer covered with 1.32 μm thick

SiO_2 layer) and continued for 20 minutes (i e 1200 sec) after the plasma was initiated After that we obtained the FTIR transmission spectra at three different positions of the sample used for the RIE experiment The three positions were chosen in a similar fashion to section 3 8 2 i e , one near the edge of the sample which was nearest to the centre of the electrode, one near the edge of the sample which was farthest from the centre of the electrode and another at the middle of the sample Before the RIE experiment we obtained the same transmission spectra on the original SiO_2 sample at two different positions to see whether there was any inhomogeneity in oxide film thickness throughout the sample surface

Figure 3 24 shows the FTIR transmission spectra obtained at two different positions for the fresh SiO_2-Si sample before use in the RIE experiment mentioned above Figure 3 25 shows the same spectra obtained at three different positions on the same sample after the RIE experiment From figure 3 24 it is clear that peak heights for both the positions are almost same both at ~1080 cm^{-1} and ~800 cm^{-1} wavenumbers [154] The SiO_2 layer thickness maintains a linear relationship with the peak height of the infrared absorption spectrum [154-156], thus confirming that the oxide thickness of the original sample before RIE was the same across the surface of the sample

Now from figure 3 25 we see that there is a clear difference in the peak heights of absorbance spectrum obtained at three different positions showing the difference in oxide layer thickness at those positions This proves that the etching rate in the end point experiments described by Table 3 1 was not uniform throughout the sample surface

3 9 2 Check for areal non-uniformity in etching

As we expected a variation of etch rate with radial position of the sample on the powered electrode due to the variation of plasma particle densities [157] we repeated the end point experiment described by Run 13 in Table 3 1 four times with the same sample size (half of a 100 mm diameter Si sample covered with 1 32 μm thick SiO_2 layer) but cut into a different numbers of pieces (i e 1, 2, 4 and 6 pieces, respectively) We placed all the pieces at approximately the same radial position on the powered
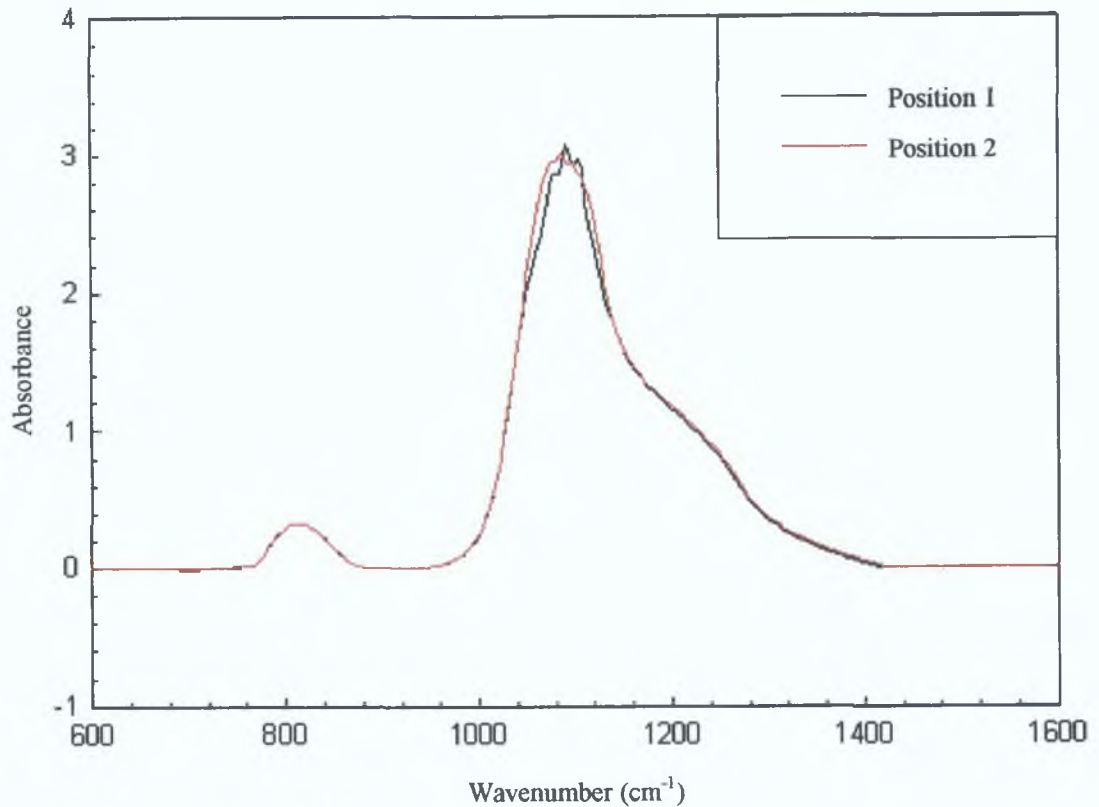
Figure 3.24 *FTIR transmission spectra taken at two different positions of a Si wafer covered with a 1.32 μm thick SiO₂ layer.*

electrode (shown by Figure 3.26) during the experiment. Thus, more of the sample area was at the same radial position on the powered electrode as the sample was cut into a greater number of pieces. For the same reason we expected a smaller transition time (the total time in zone **III** in figures 3.9-3.21) for ϕ_l for the sample cut into more pieces.

Figure 3.27 shows the transition time for ϕ_l as a function of the number of pieces of the sample during the check for areal non-uniformity in the etching experiment. It is evident that the transition time of ϕ_l becomes smaller as we increase the number of pieces of the sample placed at the same radial position of the powered electrode. This result unambiguously confirms that the etch rate varies as a function of radial position on the powered electrode of the RIE equipment.
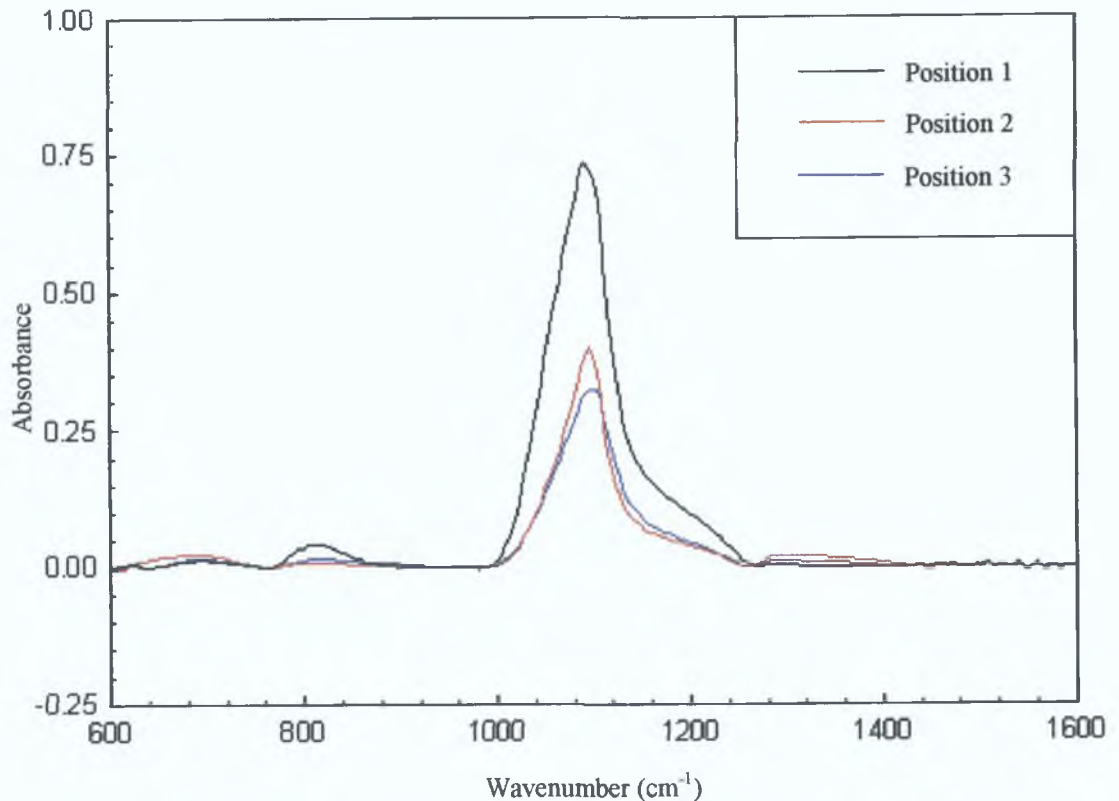
Figure 3.25 FTIR transmission spectra taken at three different position of a Si-SiO$_2$ sample (Si wafer covered with 1.32 μm thick SiO$_2$ layer) etched for 20 minutes at an experimental condition given by Run 13 in Table 3.1.

3.10 Sources of Error

As the RF power and the chamber pressure of our RIE equipment are manually controlled a slight drift of those input parameters might have occurred at each of the end point and RIE experiments mentioned in this chapter. However, we tried to keep those paramters constant as much as posible throughout each of the experiments by continuous tracking. The changes of these parameters were very small and can be neglected.

3.11 Conclusion

It is shown that the use of I-V harmonic evaluation via Plasma Impedance Monitoring is a useful means of monitoring RIE plasma processes. This type of analysis can detect the presence of silicon in a plasma chamber with SF$_6$ gas present, but is not
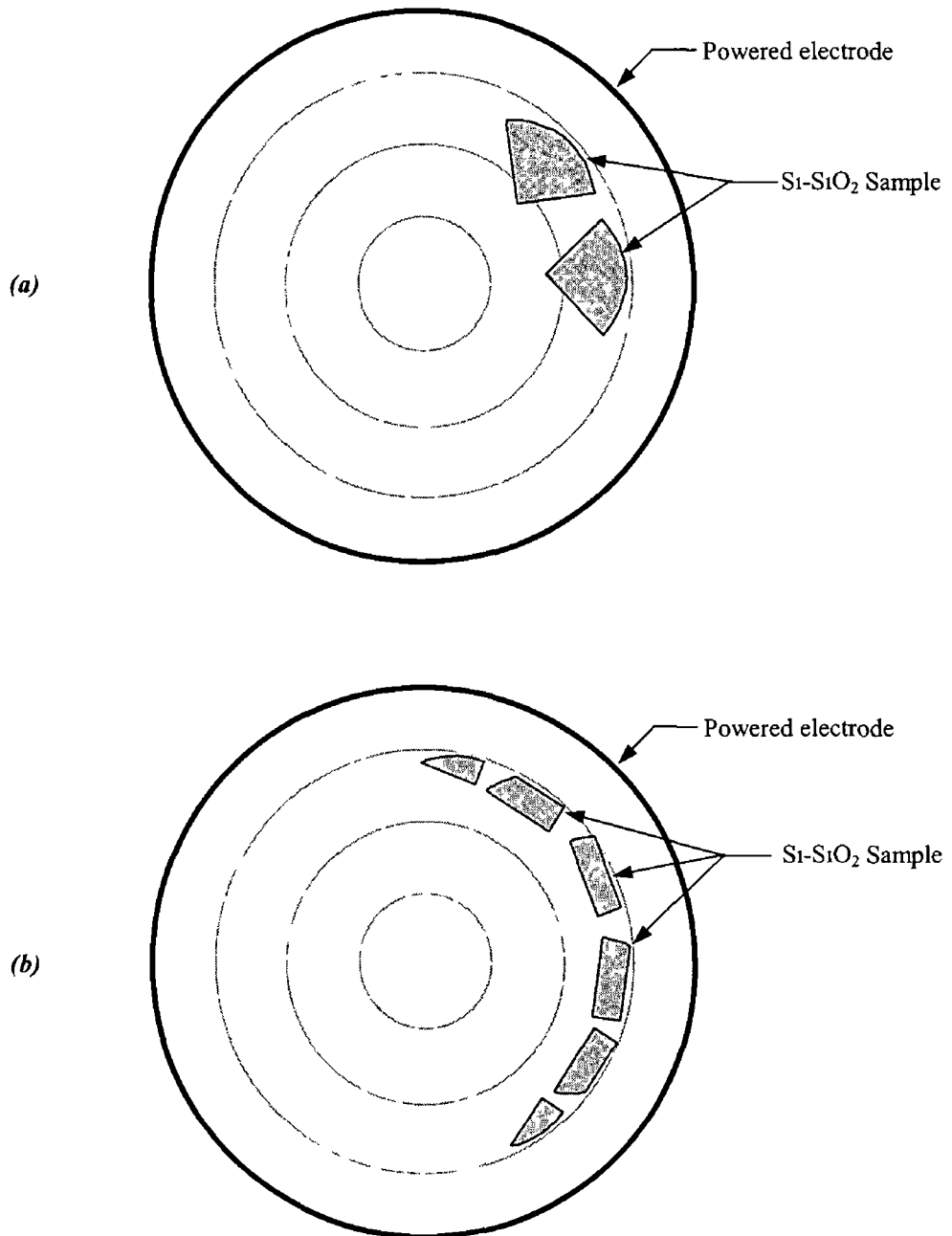
Figure 3 26 *Sι-SιO₂ sample (Sι wafer covered with 1 32 μm thick SιO₂ layer) cut into pieces and placed at approximately the same radial position on the powered electrode during the check for areal non-uniformity ιn etching experiment In (a) a smaller portion of the two bigger pieces ιs at the same radial position on the powered electrode compared to that ιn (b) containing six smaller pieces*

Transition Time (minute)

15
14 ▲
13
12 ▲
11 ▲
10 ▲
9

1   2   4   6
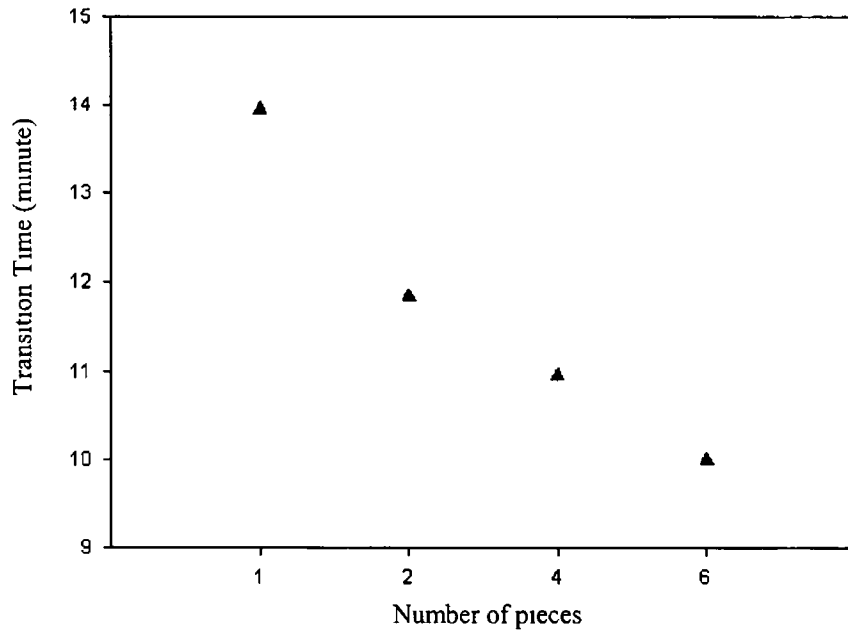
Number of pieces

Figure 3 27 Transition time required for ϕ_1 to change its value from one steady-state to the other during the end point experiment described by Run 13 in Table 3 1 as a function of the number of pieces of the sample used for the experiment

as sensitive to changes in the size of the etched silicon sample Sensitivity is high while using P_2, Z_1 or ϕ_1 parameters as the monitoring parameters The use of P_1, Z_2 or ϕ_2 also showed good sensitivity but only in specific ranges of RF power The higher harmonics (beyond second) of RF parameters were not found to be useful as monitoring parameters except where P_3 and Z_3 showed some sensitivity in specific ranges of RF power for plasma operation

If one uses a derived ratio of the discharged power to the plasma impedance of the same harmonic component while considering any of the first two harmonic frequencies, better sensitivity can also be obtained at higher power levels The use of derived parameters for higher harmonic components (beyond second) are not applicable as monitoring parameters

It is also shown that monitoring the fundamental component of phase (ϕ_1) is a useful technique for observing an endpoint of SiO_2 etching on a Si wafer using SF_6 RIE The PIM can easily detect the change in the value of ϕ_1 when the SiO_2 overlayer is

128

completely and preferentially etched away The fundamental component of plasma impedance (Z_I) also appears to give good end point detection but only for specific ranges of RF power, chamber pressure and gas flow rate The other I-V parameters or harmonic components (not shown here) were found to be of little use for the end point detection

The plasma species and their concentrations change from one steady-state condition to another at the completion of the SiO_2 layer etch, forcing the electrical parameters to change The change of ϕ_I (or Z_I) value reflects these changes The transition of ϕ_I (or Z_I) value to the next steady-state requires a finite amount of time as the plasma species and their concentrations need a finite amount time to reach their next steady-state condition The transition time also increases as the areal non-uniformity in the etching increases This transition time can be reduced by cutting the sample in many pieces and placing them at the same radial positions of the powered electrode during the end point experiments, because the etch uniformity is improved in this way

CHAPTER 4

MODELLING OF MONITORING PARAMETERS

4 1 Introduction

To reliably detect the end point of a process it is necessary to predict the value of the monitoring parameters used as the end point detector when the actual end point is reached Since our aim was to detect the end point of the SF$_6$ RIE of the Si-SiO$_2$ sample, we needed to model the monitoring parameters when the Si sample undergoes the RIE process in order to predict the value of these parameters The monitoring parameters can be empirically modelled as polynomial equations of input factors i e , RF power, chamber pressure and gas flow rate for a fixed range of their values The modelled equations are valid only within the range considered for the model It is possible to predict the value of a monitoring parameter with good precision from the modelled equations if the values of the input factors are known for a particular process This model needs specific experimental design Since in our case there were three input factors — RF power, chamber pressure and gas flow rate — the *Box-Behnken* [158] experimental design methodology was found to be appropriate for modelling the monitoring parameters

In this chapter the modelling of the monitoring parameters using the *Box-Behnken* design methodology is described The errors in the predicted value of the monitoring parameters are also investigated At the beginning of this chapter a brief description of experimental design and the *Box-Behnken* design methodology is presented

4 2 What is Experimental Design?

Experimental design consists of applying purposeful changes of inputs (factors) to a process (or activity) in order to observe the corresponding changes in the outputs (responses) The process (or activity) is defined as some combination of *machines,*

130

materials, methods, people, environment, and *measurement* which, when used together, perform a service, produce a product, or complete a task [4] Thus experimental design is a scientific approach which allows the researcher to gain knowledge in order to better understand a process and to determine how the inputs affect the response(s)

Graphically, a process appears as shown in Figure 4 1 Obviously there exist many different kinds of processes, the one provided here is representative of various applications of designed experiments
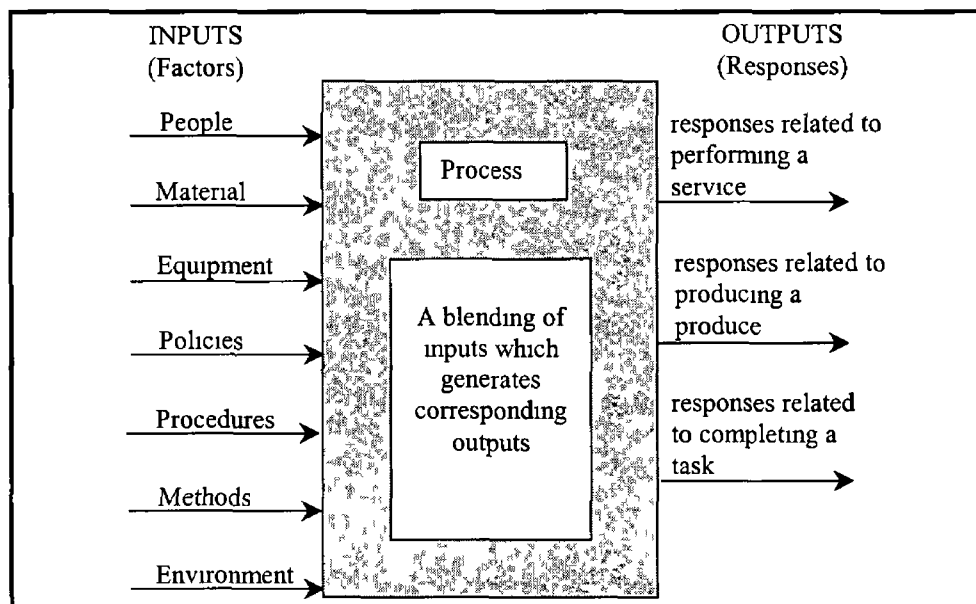
Figure 4 1 Illustration of a process

4 3 Why Use Experimental Design?

Regardless of where one works (research, development, design, quality, test, reliability, manufacturing, packaging, etc), the task for most scientists and engineers is to gain, document, and transfer product and/or process knowledge To really understand a process (or activity) one needs facts and data Collecting data through the use of one-factor-at-a-time experimentation and/or a series of trial and error tests has resulted in very inefficient and ineffective attempts to understand and optimize product designs and processes

131

For the engineer or scientist experimental designs are used as (1) the most effective method for identifying the key input factors, (2) the most efficient way to gain an understanding of the relationship between the input factors and the response(s), (3) a method for building a mathematical model relating the response to the input factors, which is often referred to as process/product characterization, (4) a means of determining the settings of the input factors which optimize the response and minimize cost, and (5) a scientific method for setting tolerances [4]

4 4 Conversion of Actual Factor Settings to Coded Values

Although the actual settings are used to run the experiment, it is necessary to standardize the different factor units and scale them before analysis The standardization is performed by coding the low actual settings as -1 and the high actual settings as $+1$ To convert from coded to actual settings and *vice versa* the following formula can be used

$$Actual = \left[\frac{Hi + Lo}{2}\right] + \left[\frac{Hi - Lo}{2}\right] x \; Coded \tag{4 1}$$

A more formal approach is presented in eqn 4 2

$$x_J = \frac{f_J - \bar{f}_J}{d_J} \quad \text{or} \quad f_J = \bar{f}_J + \frac{d_J}{2} x_J \tag{4 2}$$

where x_J is the coded setting for factor J

f_J is the actual setting for factor J

$\bar{f}_J$ is the average of all the actual settings for factor J

d_J is the distance between the largest and smallest actual settings of factor J [4]

For convenience, researchers sometimes abbreviate the "+1" and "-1" with "+" and "-", respectively, as shown in Table 4 1 Each column of factor values is referred to as a vector in the design matrix A design of n runs is considered to be *balanced vertically* when the coded values, x_{ij}, sum to zero , i e ,

$$\sum_{i=1}^{n} x_{ij} = 0 \tag{4 3}$$

Table 4 1 *Coded values for 3-factors in a 4-run design matrix*

(a) Run	Factors			(b) Run	Factors		
	A	B	C		A	B	C
1	+1	+1	+1	1	+	+	+
2	+1	-1	-1	2	+	-	-
3	-1	+1	-1	3	-	+	-
4	-1	-1	+1	4	-	-	+

for each factor (or column) j Balanced designs are desirable because they simplify the calculations during analysis, and under certain conditions they lend themselves to orthogonal designs A design matrix is said to be orthogonal if it is balanced vertically and if the dot product of all possible column pairs is zero, i e ,

$$\sum_{i=1}^{n} x_{ij} x_{ik} = 0 \qquad (4\ 4)$$

for all n combinations of columns j and k, where $j{\neq}k$ In other words, multiplying the +1 and -1 values in each row for any 2 columns should sum to zero [4]

4 5 Box-Behnken Designs

An efficient and frequently used 3-level design for modelling quantitative factors (time, temperature, pressure, flow, speed, concentration, power, etc) is the *Box-Behnken* design In their 1960 article, Box and Behnken [158] provided tabled *Box-Behnken* designs for k (number of factors) up to 16 (excluding k=8) When k=4, the design, in shorthand notation, appears as shown in Table 4 2 This design is divided into 3 orthogonal blocks of 9 runs where each ±1 refers to alternating columns of (- - + +) and (- + - +) The completed 27 run *Box-Behnken* for k=4 is shown in Table 4 3

Table 4 2 *Shorthand notation for a Box-Behnken design for 4 factors*

Factors			
A	B	C	D
±1	±1	0	0
0	0	±1	±1
0	0	0	0
±1	0	0	±1
0	±1	±1	0
0	0	0	0
±1	0	±1	0
0	±1	0	±1
0	0	0	0

Table 4 3 *Complete set of 27 runs for a Box-Behnken design based on 4 factors*

Run	A	B	C	D	
1	-	-	0	0	
2	-	+	0	0	
3	+	-	0	0	
4	+	+	0	0	
5	0	0	-	-	
6	0	0	-	+	
7	0	0	+	-	
8	0	0	+	+	
9	0	0	0	0	
10	-	0	0	-	Note Interaction and quadratic columns can
11	-	0	0	+	be developed by the appropriate column value
12	+	0	0	-	multiplications
13	+	0	0	+	
14	0	-	-	0	
15	0	-	+	0	
16	0	+	-	0	The orthogonal blocks are separated by
17	0	+	+	0	dashed lines
18	0	0	0	0	
19	-	0	-	0	
20	-	0	+	0	
21	+	0	-	0	
22	+	0	+	0	
23	0	-	0	-	
24	0	-	0	+	
25	0	+	0	-	
26	0	+	0	+	
27	0	0	0	0	

If only 3 factors were used, the design would appear graphically as shown in Fig 4 2 The *Box-Behnken* designs are nearly orthogonal The primary disadvantage of *Box-Behnken* designs is that the large number of runs required to estimate all factor second-order effects (i e, A^2, B^2, C^2 etc) and all linear 2-way interactions (i e, AB, BC, AC etc) when the number of factors is high That is why the *Box-Behnken* design will be less efficient when the number of input factors is greater than 4 [4]

A shorthand notation summary of *Box-Behnken* designs for k=3, 4 and 5 is displayed in Table 4 4

Run	A	B	C
1	-	-	0
2	-	+	0
3	+	-	0
4	+	+	0
5	-	0	-
6	-	0	+
7	+	0	-
8	+	0	+
9	0	-	-
10	0	-	+
11	0	+	-
12	0	+	+
13	0	0	0
14	0	0	0
15	0	0	0
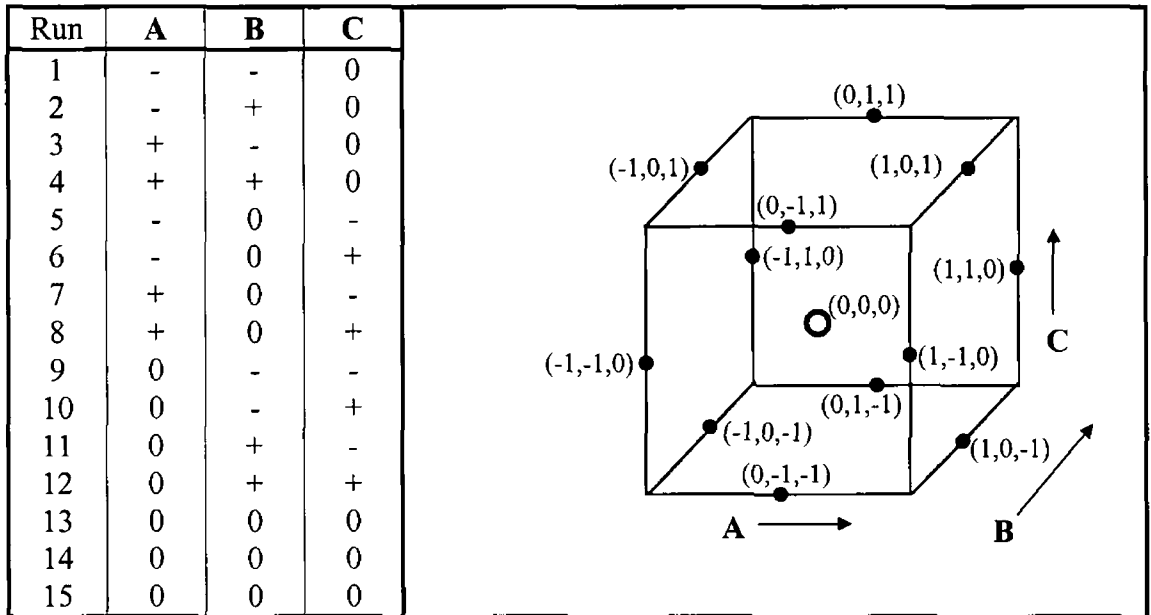
Figure 4 2 Design matrix and geometric representation of a Box-Behnken design for 3 factors

4 6 Experimental Equipment

The same experimental equipment described in section 3 2 (Fig 3 1) was used for this experiment It is consisted of the planar, capacitively coupled reactive ion etching system coupled with a Plasma Impedance Monitoring (PIM) system (see section 3 2 1) Figure 3 1 shows the schematic diagram of the apparatus

4 7 Experiment

Figure 4 2 shows the design matrix and geometric representation of the *Box-Behnken* design used for these experiments In this figure the symbols A, B and C represent the coded values of RF power, chamber pressure and the gas flow rate, respectively Four sets of experiments were carried out for different operating ranges of input factors and different sample conditions inside the chamber Table 4 5 shows the operating ranges and sample status inside the chamber used for these experiments

Table 4 4 Box-Behnken designs for k=3, 4 and 5

Box-Behnken Designs

Number of factors (k)	Design matrix					Number of points	Blocking and centre-point information
3	±1	±1	0			4	No orthogonal blocking with 3 replicated centre-points
	±1	0	±1			4	
	0	±1	±1			4	
	0	0	0			3	
						n = 15	
4	±1	±1	0	0		4	3 blocks of 9 runs each and 1 centre-point per block
	0	0	±1	±1		4	
	0	0	0	0		1	
	±1	0	0	±1		4	
	0	±1	±1	0		4	
	0	0	0	0		1	
	±1	0	±1	0		4	
	0	±1	0	±1		4	
	0	0	0	0		1	
						n = 27	
5	±1	±1	0	0	0	4	2 blocks of 23 runs each and 3 replicated centre-points per block
	0	0	±1	±1	0	4	
	0	±1	0	0	±1	4	
	±1	0	±1	0	0	4	
	0	0	0	±1	±1	4	
	0	0	0	0	0	3	
	0	±1	±1	0	0	4	
	±1	0	0	±1	0	4	
	0	0	±1	0	±1	4	
	±1	0	0	0	±1	4	
	0	±1	0	±1	0	4	
	0	0	0	0	0	3	
						n = 46	

Table 4 5 Operating ranges and sample status inside the chamber considered for modelling

Experiment	RF power (Watts)		Chamber pressure (mTorr)		Gas flow rate (sccm)		Sample status inside the chamber
	Lo	Hi	Lo	Hi	Lo	Hi	
1	50	300	40	200	1 56	7 80	No sample
2	100	200	40	100	2 60	5 20	No sample
3	100	150	40	60	3 90	6 50	No sample
4	100	150	40	60	3 90	6 50	½ of 100mm dia Si wafer

Before each set of the experiments the plasma chamber was cleaned by running the system in RIE mode with Ar gas at 200 Watts RF power, 72 mTorr chamber pressure and 8 6 sccm gas flow rate The system was subsequently run in reactive ion etching mode with SF_6 gas as per the conditions shown in table 4 5 The values of the I-V parameters were recorded at each of the experimental runs shown in figure 4 2

4 8 Modelling of Current-Voltage (I-V) Parameters

The I-V parameters were modelled using the Q-Edge^{TM} software from the values recorded in each of the experiments The resulting polynomial equations for fundamental components of discharged power and plasma impedance for each of the experiments are given below In the polynomial equations the letters **A**, **B** and **C** represent the coded values of **RF power, chamber pressure** and **gas flow rate**, respectively

Q-Edge^{TM} is a state-of-art design of experiments (DOE) software package [159] This software provides the *Box-Behnken* design for experiments of 3 or 4 input factors The response parameters of any three or four-factors experiment can be expressed as functions of the input factors The design allows only for the main effects, second order effects and the two-way interactions That means that the polynomial equations of the response parameters will contain only the linear terms (i e , **A**, **B**, **C** etc), their quadratic factors (i e , A^2, B^2, C^2 etc) and their linear products- two at a time (i e , **AB**, **BC**, **AC** etc)

The percentage errors in determining the I-V parameters from their modelled equations were calculated at each of the experimental conditions (given by figure 4 2) for each set of experiments (given by table 4 5) They are also shown following the respective polynomial equations for the I-V parameters The errors in the predicted values were evaluated using the following equation,

$$Percentage\ Error = \frac{Y_p - Y_a}{Y_a} x100 \qquad (4\ 3)$$

where, Y_a = measured value of a parameter and Y_p = predicted value of the parameter determined from the modelled equation

137

Experiment 1:

Power =	50 - 300 Watt
Pressure =	40-200 mTorr
Gas Flow Rate =	1.56 – 7.8 sccm
Sample status =	No sample inside the chamber

$$P_1 = 148.50 + 88.25A + 19.66B - 1.95C - 10.29A^2 + 1.21B^2 - 9.59C^2$$
$$+ 6.27AB + 2.68AC + 3.37BC \tag{4.5a}$$

$$Z_1 = 37.81 + 1.94A + 14.31B + 0.83C - 5.46A^2 - 11.52B^2 - 5.51C^2$$
$$+ 8.83AB + 2.07AC - 0.54BC \tag{4.5b}$$
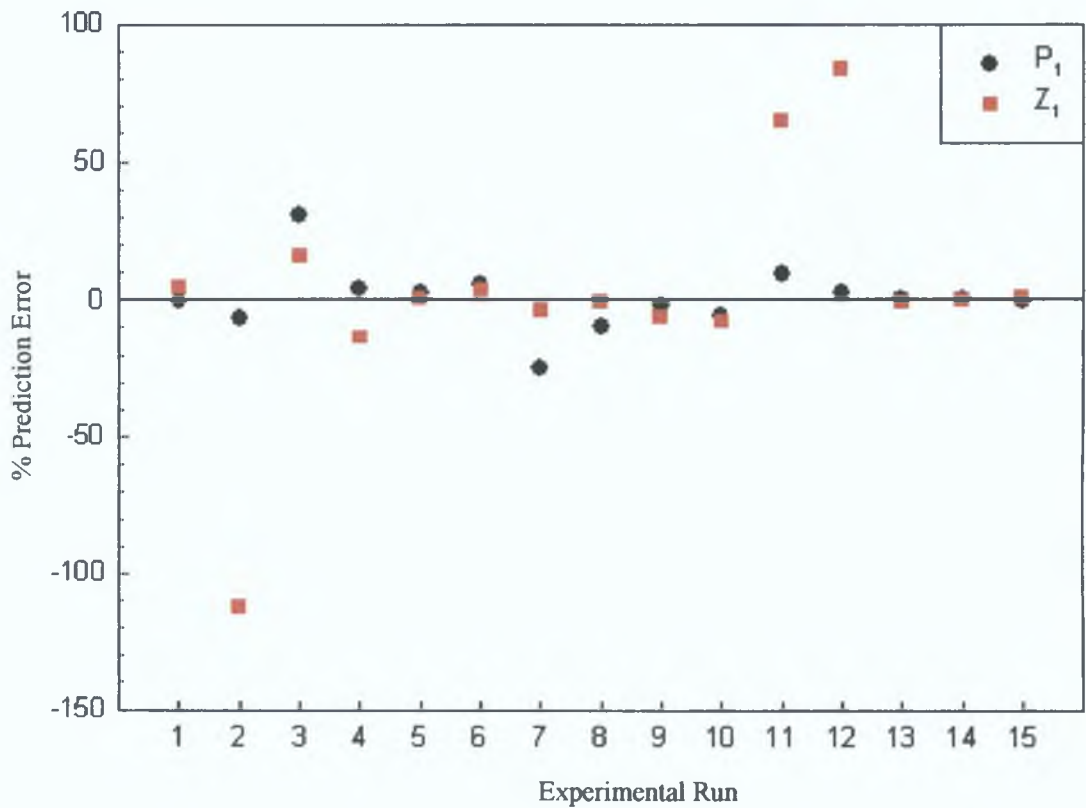
Figure 4.3 *Percentage prediction error in P_1 and Z_1 at different experimental runs of experiment 1.*

Experiment 2:

Power =	100 - 200 Watt
Pressure =	40-100 mTorr
Flow Rate =	2.6 - 5.2 sccm
Sample status =	No sample inside the chamber

$$P_1 = 97.47 + 26.22A + 15.24B - 1.67C - 2.55A^2 + 8.64B^2 - 0.39C^2$$
$$- 1.61AB - 0.19AC + 0.52BC \tag{4.6a}$$

$$Z_1 = 21.64 - 3.44A + 13.33B + 0.01C - 0.44A^2 - 0.72B^2 - 0.79C^2$$
$$+ 1.15AB + 0.26AC - 0.03BC \tag{4.6b}$$
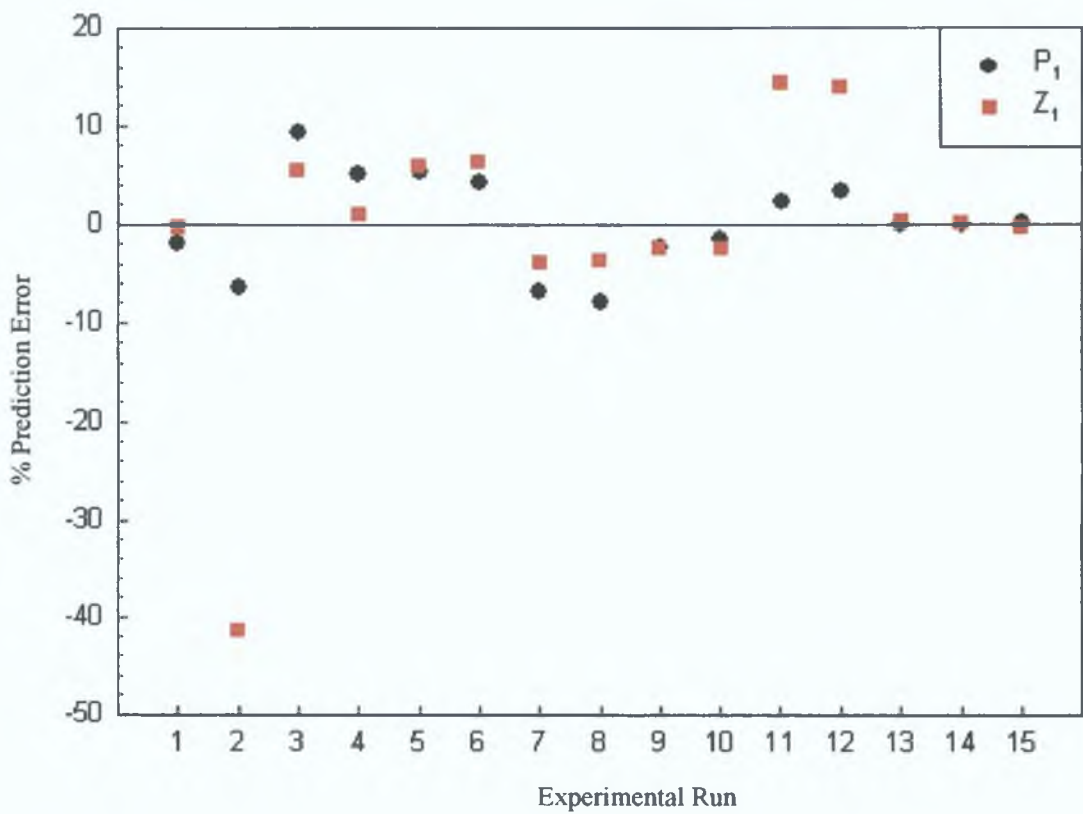
Figure 4.4 *Percentage prediction error in P_1 and Z_1 at different experimental runs of experiment 2.*

Experiment 3:

Power =	100 - 150 Watt
Pressure =	40-60 mTorr
Flow Rate =	3.9 - 6.5 sccm
Sample status =	No sample inside the chamber

$$P_1 = 73.48 + 12.98A + 2.08B + 0.30C + 0.26A^2 + 2.85B^2 + 0.04C^2$$
$$-1.85AB - 0.02AC - 0.29BC \tag{4.7a}$$

$$Z_1 = 12.49 - 2.52A + 4.74B - 0.08C + 0.05A^2 + 0.29B^2 - 0.07C^2$$
$$-0.26AB - 0.02AC + 0.18BC \tag{4.7b}$$
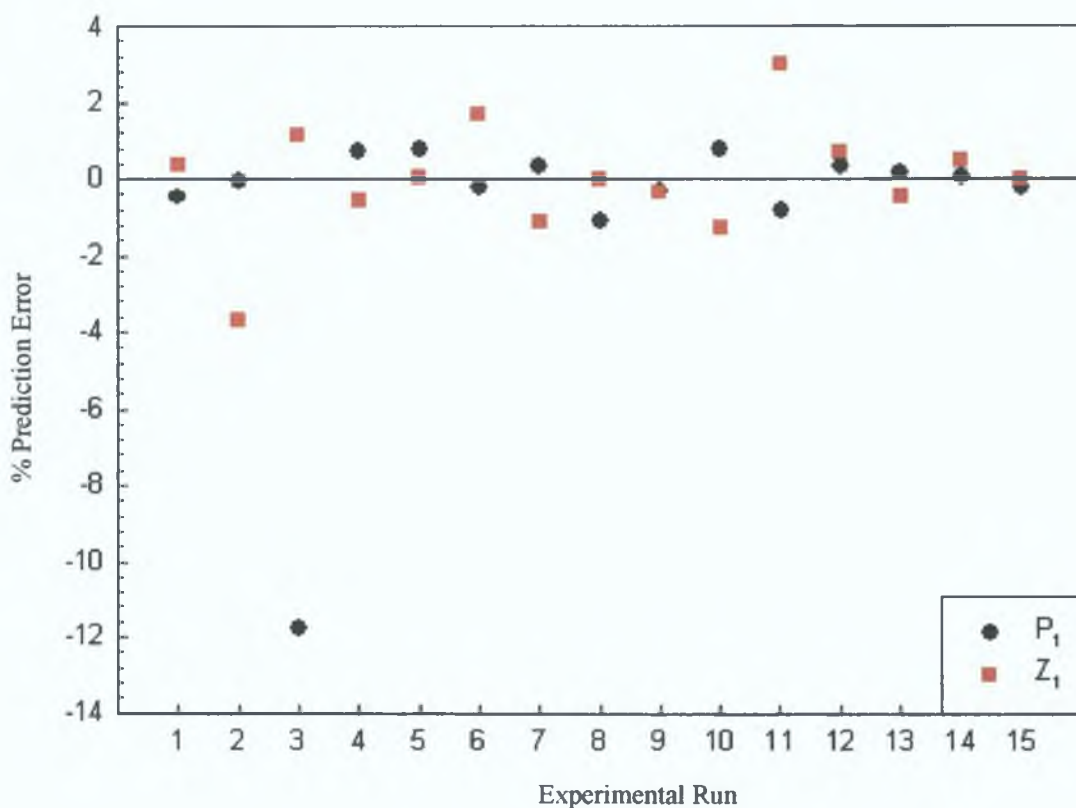
Figure 4.5 *Percentage prediction error in P_1 and Z_1 at different experimental runs of experiment 3.*

Experiment 4:

Power =   100 - 150 Watt

Pressure =   40-60 mTorr

Flow Rate =   3.9 - 6.5 sccm

Sample status =   half of 100mm diameter Si wafer inside the chamber

$$P_1 = 77.11 + 12.06A + 5.30B + 0.35C + 1.41A^2 + 3.53B^2 - 0.45C^2$$

$$- 0.93AB + 0.21AC - 0.52BC \tag{4.8a}$$

$$Z_1 = 6.45 - 2.01A + 4.35B + 0.16C + 1.48A^2 + 2.45B^2 + 1.10C^2$$

$$- 0.25AB - 0.57AC - 0.64BC \tag{4.8b}$$
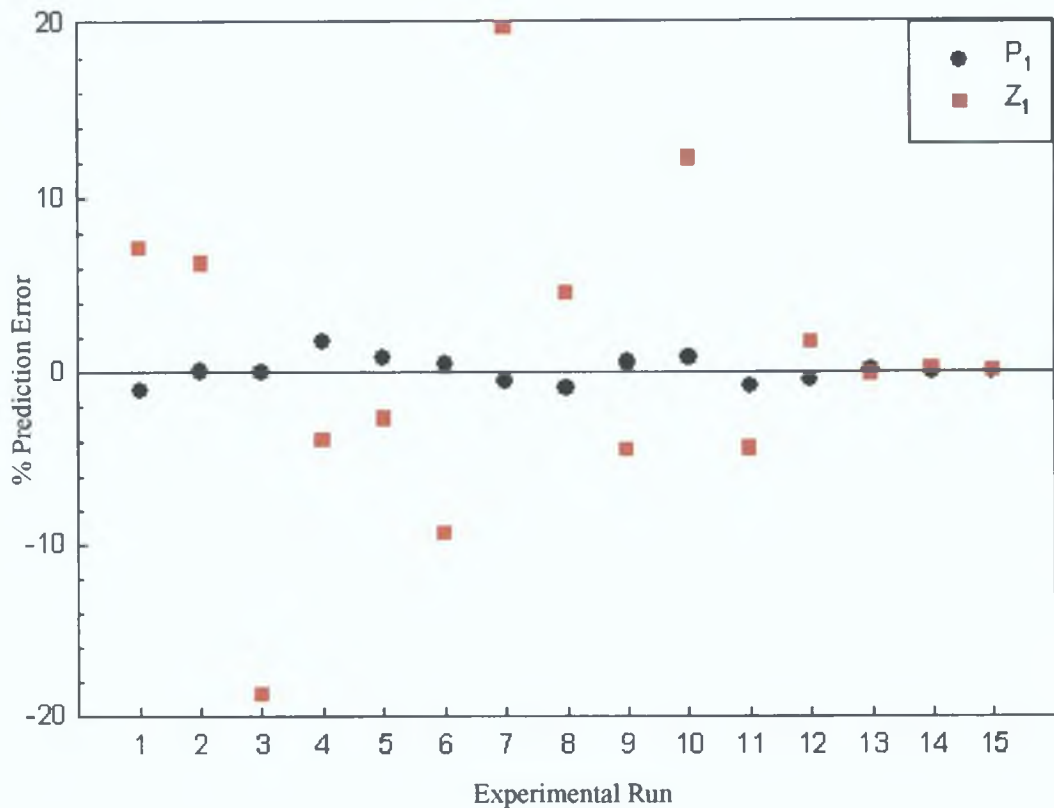
Figure 4.6 *Percentage prediction error in P_1 and Z_1 at different experimental runs of experiment 4.*

Figures 4 3-4 5 show that the errors in the predicted values of the I-V parameters determined using the modelled equation are different for the different operating ranges of input factors considered for the model outlined in table 4 5 The errors become higher for larger variations in input factors As we can see in the case of experiment 1, the prediction error is extremely high (especially for Z_i), though the error is not too high at all the experimental runs In experiment 2 the prediction improves except for a few outlying conditions (e g , runs 2, 11 and 12) This was expected because the range of parameter workspace considered here for all the three input factors was smaller than that of experiment 1 In the experiment 3 the range of parameter workspace for RF power and chamber pressure was further reduced while the gas flow variation remained the same as for experiment 2 We see that the prediction errors for both P_i and Z_i are reasonably small in this case (smaller than ±4%) except at experimental run 3 where the error in P_i reaches ~ -12%

We can conclude from the above discussion that the prediction error would be minimum where the operating workspace of the input factors considered for the experiments is smallest However, the actual parameter workspace varies little in practical operations Therefore, for experimental purposes, we considered small ranges of operation for modelling the I-V parameters in experiment 4 (see table 4 5) which now includes half of a 100mm diameter Si wafer inside the plasma chamber It is clear from figure 4 6 that the prediction errors in the P_i parameter do not exceed ±2%, though the error in the Z_i parameter became higher than that of experiment 3 This could be due to the presence of Si inside the chamber changing the plasma constituents and hence the impedance characteristics of plasma Again we saw that P_i was less affected then Z_i while we introduced half of a 100mm diameter Si wafer inside the chamber This may be due to the fact that the real part of the plasma impedance, which directly contributes to the discharged real power, does not vary significantly with the introduction of the Si wafer inside the chamber whereas the reactive part of the plasma impedance changes by a significant amount and thus also the Z_i parameter

4 9 Modelling of Phase as the End Point Detector

In Chapter 3 we found that the fundamental component of phase (ϕ_l) behaves as the best parameter for end point detection when a SiO_2 layer on a Si sample undergoes SF_6 RIE operation It would be useful to study the viability of the use of ϕ_l for end point detection and prediction For the experiments outlined in this study we need to predict the value of ϕ_l when a bare Si wafer is in the SF_6 RIE chamber The reason for this is that, at the end point, the Si underneath the SiO_2 layer would start to be etched away and the plasma condition would be same as when a bare Si wafer is etched Focusing on this fact we modelled ϕ_l for the experimental condition 4 shown in Table 4 5 as it provides a low variation of parameter workspace for the input factors In fact, if we look back to Chapter 3 we would see that the design matrix (shown by Table 3 1) of the experimental run for the end point detection experiments was the same as the design matrix given by figure 4 2 designed for the experimental condition 4 in Table 4 5 The polynomial equation for ϕ_l as a function of RF power, chamber pressure and gas flow rate is given below

$$\phi_l = 24\ 00 - 7\ 51A + 14\ 79B + 2\ 05C + 5\ 75A^2 + 6\ 85B^2 + 7\ 47C^2$$
$$+ 5\ 50AB - 1\ 57AC - 3\ 32BC \qquad (4\ 9)$$

where, A, B and C represent the coded values of RF power, chamber pressure and gas flow rate, respectively, given by eqn (4 2) Here A, B and C are unit less

At each of the end point experiments described in Chapter 3 (section 3 6) there was a finite shift of ϕ_l (Zone III) from one steady-state value (Zone II) to another (Zone IV) which was a definite measure of the end point Since our main aim was to detect this shift of ϕ_l value, we estimated the predicted shift of ϕ_l at each of the experimental conditions given by figure 4 2 (also see Table 3 1) as

$$\Delta\phi_{l\,pred} = \phi_{lf\,pred} - \phi_{li} \qquad (4\ 10)$$

where, ϕ_{li} and $\phi_{lf\,pred}$ represent the actual value of ϕ_l before the shift and the predicted value of ϕ_l after the shift (given by eqn 4 9), respectively We also determined the actual shift of ϕ_l values during the experiments as

$$\Delta\phi_{l\,act} = \phi_{lf\,act} - \phi_{li} \qquad (4\ 11)$$

where, $\phi_{1f\,act}$ represents the actual value of ϕ_1 after the shift. In figure 4 7 the predicted shift of ϕ_1 value ($\phi_{1f\,pred}$) is compared with the actual shift ($\phi_{1f\,act}$) at different experimental runs given by Table 3 1 and figure 4 2
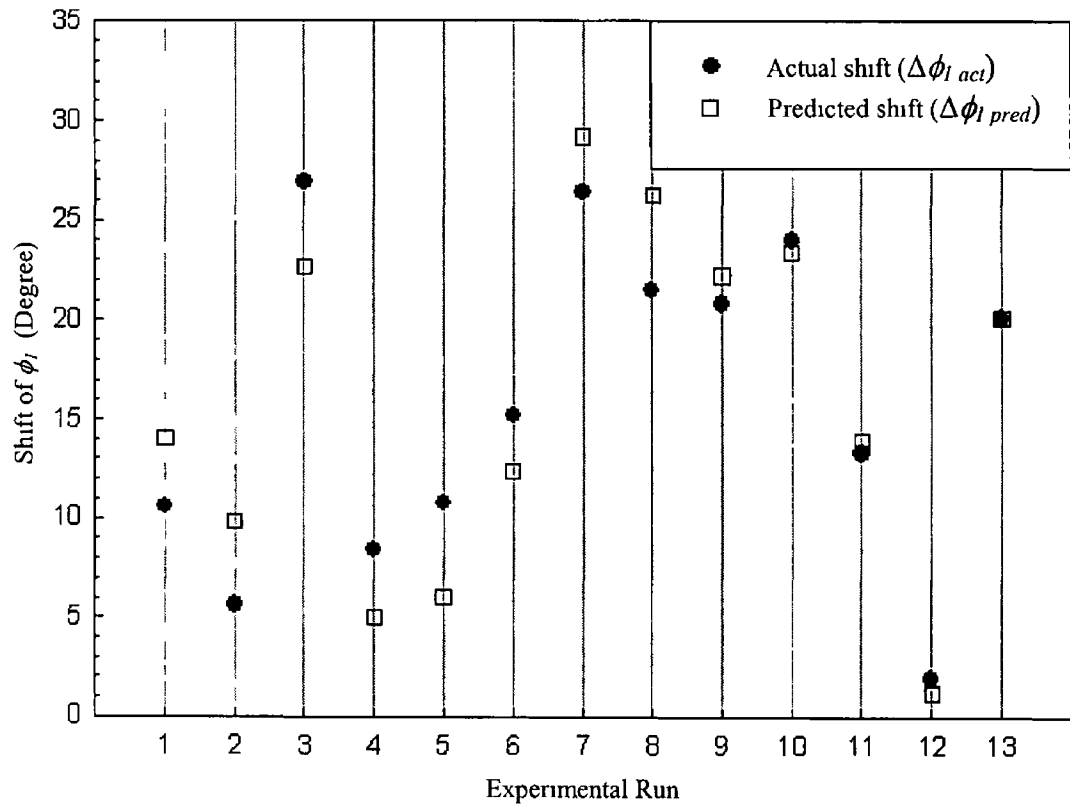
Figure 4 7 *Comparison between the predicted and the actual shifts of ϕ_1 ($\Delta\phi_1$ pred and $\Delta\phi_1$ act, respectively) at different experimental runs*

It is evident from the figure 4 7 that the predicted shift of ϕ_1 is always close to the actual shift and the difference between these two values is always smaller than the actual shift. That means that the end point can be predicted from the modelled equation and detected using the PIM while a SiO₂ layer on a Si sample undergoes SF₆ RIE and the end point is reached, and if the operating RF power, chamber pressure and the gas flow rate is known

4 10 Comments on Modelling

As the modelled equations include only the main effects (A, B and C), their quadratic factors (A^2, B^2 and C^2) and the two-way interactions (AB, BC and AC) the

predicted values of any response parameter determined by the modelled equation should and do contain some errors In order to obtain a set of equations which give errorless predictions of the response parameters we need to carry out the experiment at all possible values of the input factors and must consider all the higher order effects and interactions during the modelling However, it is possible to have an infinite number of combinations of the input factors and it is not realistic to carry out the experiment at each possible experimental condition It is also unrealistic to consider all the higher order terms and the interactions in modelling the equations as they also may be of infinite number However, if the operating space of the input factors taken into consideration is small, then it is possible to obtain a model with acceptable prediction error limits by carrying out a limited number of experiments specified by the experimental design When the operating space is smaller the data points considered for the experiments are much closer to each other and as a result more experiments are performed for a given range of input factors, thus yielding a better prediction of the response parameters than for the larger input factors workspace

4 11 Conclusion

In practice where a small variation in input factors (RF power, chamber pressure and gas flow rate) is allowed, it is possible to predict the value of monitoring parameters with reasonable precision from the modelled polynomial equations It has been shown in this study that while the Si-SiO_2 interface is reached during an SF_6 RIE of a Si wafer covered with a SiO_2 layer, the predicted shift of ϕ_l ($\Delta\phi_{l\,pred}$) is always close to the actual shift ($\Delta\phi_{l\,act}$) Therefore, using the modelled equation for ϕ_l it is possible to detect the end point of the RIE of SiO_2 lying on a Si substrate using the PIM, when the operating input factors are known In general, we can conclude that using the PIM and the modelled equation for the monitoring parameter it may be possible to detect the end point when a material lying on a dissimilar substrate undergoes RIE For this end point detection process to work the monitoring parameter should be chosen such that the value of this parameter changes significantly when the end point is reached

The prediction error in the monitoring parameters determined using the modelled equations could be minimized using a smaller input factor workspace A better

prediction could also be obtained using more sophisticated modelling which allows for a greater number of input factor interactions and more experimental runs For more than 3-4 input factors different methods of modelling (e g , central composite design [4]) could be used rather than the *Box-Behnken* method for a more accurate prediction of the monitoring parameters

PLASMA MODELLING FOR NON-SINUSOIDAL RF CURRENT

5 1 Introduction

As we discussed in the introductory chapter, the RF current source of a plasma processing system always contains some harmonics of the driving frequency These harmonics arise from nonlinearities in the plasma sheath [30] and asymmetries in the geometry of the plasma chamber [33] The harmonics occur at integer multiples of 13 56 MHz, the fundamental frequency In this chapter we present an analytical solution for a high voltage, collisionless, capacitive RF sheath driven by a non-sinusoidal RF current source under the assumption that the source current contains a finite number of harmonic components whose frequency is an integer multiple of the fundamental frequency We obtain expressions for the time-average ion and electron densities, electrical field and electric potential within the sheath, nonlinear oscillation motion of the electron sheath boundary, ion sheath thickness and the effective sheath impedance The calculated values of the above parameters were compared with those of the Lieberman model [30] Finally, we consider a non-symmetric, parallel plate, capacitive discharge and include the bulk impedance to determine the overall plasma impedance for each of the harmonic frequencies We also calculate the overall RF voltage for all the harmonic frequencies An analysis for symmetrical operation is also obtainable from this model when both electrodes are considered of equal area The calculated impedances and the RF voltages were compared with values measured in experiments

5 2 Limitations of Lieberman Model

In the Lieberman model an analytical solution was obtained for the collisionless RF sheath driven by a sinusoidal, RF current source The harmonic contents present in the driving current were ignored in this model Thus the effect of harmonic currents on

plasma parameters was not included in his model which could produce errors in the calculation of plasma parameters using this model

The Lieberman model was based on a symmetrically driven, parallel plate RF discharge The effect of asymmetrical sizes of the two plates was not considered in this model That means this model cannot be applied to all plasma systems other than a particular type having both electrodes of equal area

In reality most plasma systems utilize electrodes of unequal area and the source current contains a number of harmonic components To have a more appropriate and general model one must consider an unequal-plate-area system which will include the effect of all the current harmonics

In the following section we present a generalized model considering a capacitively coupled parallel plate plasma system having unequal-area electrode plates driven by a non-sinusoidal RF current source

5 3 Modelling of RF Plasma

5 3 1 Analysis of plasma sheath

In general, the discharge parameters, e g , electron density n_e, ion density n_i and electron temperature T_e are complicated functions of position and time Therefore, we made the following assumptions to simplify the analysis

(a) The ion motion within the sheath is collisionless The ions respond only to the time-average electric field This is a good approximation provided $\omega_{pi}^2 \ll \omega^2$, where ω_{pi} and ω are the ion plasma frequency and the fundamental driving frequency, respectively The ion sheath-plasma boundary is stationary, and ions enter the sheath with a Bohm presheath velocity $u_B = \sqrt{eT_e/M}$, where e is the ion charge, T_e is the electron temperature (in Volts), and M is the ion mass [29,30,160]

148

(b) The electrons are inertialess and respond to the instantaneous electric field. The electron Debye length, λ_D, everywhere within the sheath is assumed to be much smaller than the ion sheath thickness s_m. Since $\lambda_D \ll s_m$, the electron density falls sharply from $n_e \approx n_i$ at the plasma side of the electron sheath boundary to $n_e \approx 0$ at the electrode side. The electron sheath oscillates between a maximum thickness of s_m and a minimum thickness of a few Debye lengths from the electrode surface.

(c) There is no transverse variation (along the plates). The plasma and the current density are uniform throughout the cross-section at any particular distance from either of the two plates. This is a good approximation provided $l \ll \sqrt{A}$, where l and A are the separation between the two electrode plates and the cross-sectional area of the plate, respectively.

(d) The plasma source current is non-sinusoidal but it can be resolved into a finite number of harmonic components whose frequencies are integer multiples of the driving frequency. This is a good approximation when the current is periodic in nature in time space and the magnitude of harmonic components at very high freqencies are very small compared to the fundamental and can be neglected.

The structure of the RF sheath is shown in Fig 5 1. Ions crossing the ion sheath boundary at $x = 0$ accelerate within the sheath and strike the electrode at $x = s_m$ with high energies. Since the ion flux $n_i u_i$ is conserved and u_i increases as ions transit the sheath, n_i drops. This is sketched as the heavy, solid line in Fig 5 1.
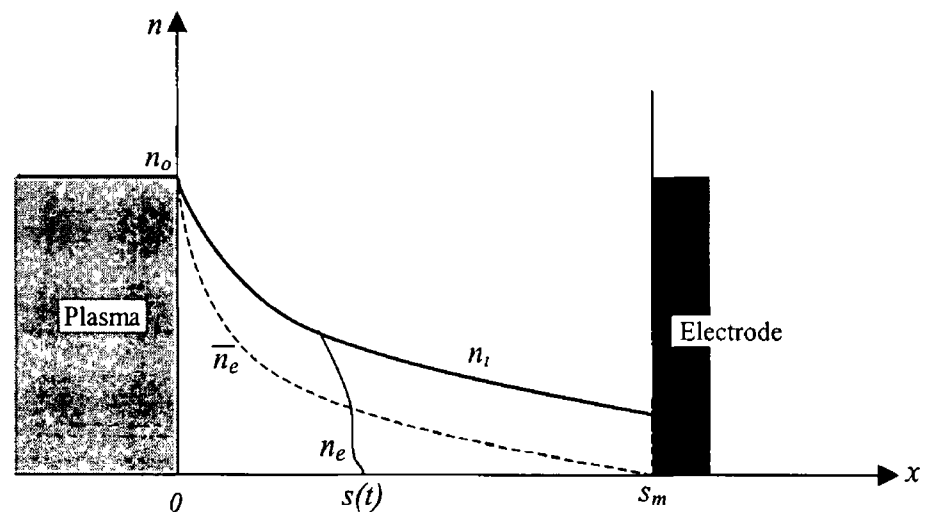
Figure 5 1 Structure of the high voltage, capacitive RF sheath

The ion particle and energy conservation equations are respectively

$$n_i u_i = n_0 u_B \tag{5 1}$$

$$\frac{1}{2} M u_i^2 = \frac{1}{2} M u_B^2 - e\overline{\Phi} \tag{5 2}$$

where n_0 is the plasma density at $x = 0$ and $\overline{\Phi}$ is the time-average potential within the sheath, $\overline{\Phi}$, n_i and u_i are functions of x From (5 1) and (5 2) we have

$$n_i = n_0 \left(1 - \frac{2\overline{\Phi}}{T_e}\right)^{-\frac{1}{2}} \tag{5 3}$$

The Maxwell equation for the instantaneous electric field $E(x,t)$ within the sheath is

$$\frac{\partial E}{\partial x} = \frac{e}{\varepsilon_0} n_i(x), \qquad s(t) < x$$

$$= 0, \qquad s(t) > x \tag{5 4}$$

Here, $s(t)$ is the distance from the ion sheath boundary at $x = 0$ to the electron sheath edge, the electron sheath thickness is $s_m - s(t)$ The instantaneous potential $\Phi(x,t)$ is determined from the equation

$$\frac{\partial \Phi}{\partial x} = -E(x) \tag{5 5}$$

Time-averaging (5 4) and (5 5) over an RF cycle, we obtain the equations for the time-average electric field $\overline{E}(x)$ and potential $\overline{\Phi}(x)$

$$\frac{d\overline{E}}{dx} = \frac{e}{\varepsilon_0} \left[n_i(x) - \overline{n}_e(x)\right] \tag{5 6}$$

$$\frac{d\overline{\Phi}}{dx} = -\overline{E} \tag{5 7}$$

where $\overline{n}_e$ is the time-average electron density within the sheath We assume that $n_e(x,t) = 0$ during the part of the RF cycle when $s(t) < x$, otherwise, $n_e(x,t) = n_i(x)$ We therefore have

$$\overline{n}_e(x) = \left(1 - \frac{2\varphi}{2\pi}\right) n_i(x) = \left(1 - \frac{\varphi}{\pi}\right) n_i(x) \tag{5 8}$$

where, $2\varphi(x) = 2\omega t$ is the phase interval during which $s(t) < x$ $\overline{n}_e(x)$ is shown as a dashed line in Fig 5 1 For x near zero, $s(t) < x$ during only a small part of the RF cycle, therefore, $2\varphi \approx 0$ and $\overline{n}_e(x) \approx n_i(x)$ For x near s_m, $s(t) < x$ during most of the RF cycle, therefore, $2\varphi \approx 2\pi$ and $\overline{n}_e(x) \approx 0$ To determine the time averages quantitatively, we

assume that the non-sinusoidal RF current consists of several *sinusoidal harmonic components* which flow along the x-axis through the sheath and can be written as [161]

$$J_{RF}(t) = -\sum_{p=1}^{N} \bar{J}_p \sin(p\omega t)$$ (5 9)

where, $J_p(t) = -\bar{J}_p \sin(p\omega t)$, the p-th harmonic component of RF current density

Equating this displacement current to the conduction current at the electron sheath boundary, we obtain the equation for the electron sheath motion

$$-en_i(s)\frac{ds}{dt} = -\sum_{p=1}^{N} \bar{J}_p \sin(p\omega t)$$ (5 10)

Integrating (5 4) we obtain

$$E = \frac{e}{\varepsilon_0} \int_s^x n_i(\xi)d\xi, \qquad\qquad s(t) < x$$

$$= 0, \qquad\qquad st) > x$$ (5 11)

Integrating (5 10) we have

$$\frac{e}{\varepsilon_0} \int_0^s n_i(\xi)d\xi = \sum_{p=1}^{N} \frac{\bar{J}_p}{p\omega\varepsilon_0}[1 - \cos(p\omega t)]$$ (5 12)

Putting $s = x$ at $\omega t = \varphi$ in (5 12) we have

$$\frac{e}{\varepsilon_0} \int_0^x n_i(\xi)d\xi = \sum_{p=1}^{N} \frac{\bar{J}_p}{p\omega\varepsilon_0}[1 - \cos(p\varphi)]$$ (5 13)

Substracting (5 12) from (5 13) we obtain

$$\frac{e}{\varepsilon_0} \int_s^x n_i(\xi)d\xi = \sum_{p=1}^{N} \frac{\bar{J}_p}{p\omega\varepsilon_0}[\cos(p\omega t) - \cos(p\varphi)]$$ (5 14)

Inserting (5 14) into (5 11) we obtain

$$E(x,\omega t) = \sum_{p=1}^{N} \frac{\bar{J}_p}{p\omega\varepsilon_0}[\cos(p\omega t) - \cos(p\varphi)], \qquad s(t) < x$$

$$= 0, \qquad\qquad s(t) > x$$ (5 15)

We note that $s(t) = x$ at $\omega t = \varphi$ and $s(t) < x$ when $-\varphi < \omega t < \varphi$ Taking the time-average we obtain from (5 15)

$$\bar{E}(x) = \frac{1}{2\pi} \int_{-\varphi}^{\varphi} E(x,\omega t) \, d\omega t$$ (5 16)

Inserting (5 15) into (5 16) we have

$$\overline{E}(x) = \sum_{p=1}^{N} \frac{\overline{J}_p}{p\omega\varepsilon_0\pi}\left[\frac{1}{p}\sin(p\varphi) - \varphi\cos(p\varphi)\right]$$
(5 17)

Using (5 7),

$$\frac{d\overline{\Phi}}{dx} = -\overline{E}(x) = -\sum_{p=1}^{N} \frac{\overline{J}_p}{p\omega\varepsilon_0\pi}\left[\frac{1}{p}\sin(p\varphi) - \varphi\cos(p\varphi)\right]$$
(5 18)

Inserting (5 3) into (5 10) with $s(t) = x$, $\omega t = \varphi$, we obtain

$$\frac{d\varphi}{dx} = \frac{e\omega n_0\left(1 - 2\overline{\Phi}/T_e\right)^{-\frac{1}{2}}}{\sum_{p=1}^{N} \overline{J}_p \sin(p\varphi)}$$
(5 19)

Dividing (5 18) by (5 19) and integrating,

$$\sqrt{1 - 2\overline{\Phi}/T_e} = 1 - \frac{1}{e\omega^2 T_e\varepsilon_0\pi n_0}\left[\sum_{p=1}^{N}\sum_{\substack{q=1 \\ q\neq p}}^{N}\frac{\overline{J}_p\overline{J}_q}{p}\left\{\frac{2p+q}{2p(p+q)^2}\sin(p+q)\varphi\right.\right.$$

$$\left.- \frac{2p-q}{2p(p-q)^2}\sin(p-q)\varphi - \frac{1}{2(p+q)}\varphi\cos(p+q)\varphi + \frac{1}{2(p-q)}\varphi\cos(p-q)\varphi\right\}$$

$$\left.+ \sum_{p=1}^{N}\sum_{\substack{q=1 \\ q=p}}^{N}\frac{\overline{J}_p^2}{p}\left\{\frac{3}{8p^2}\sin(2p\varphi) - \frac{\varphi}{4p}\cos(2p\varphi) - \frac{\varphi}{2p}\right\}\right]$$
(5 20)

Inserting (5 20) into (5 19) and integrating with $\varphi = 0$ at $x = 0$ we have,

$$e\omega n_0 x = \sum_{p=1}^{N}\overline{J}_p \int_0^{\varphi}\sin(p\varphi)d\varphi - \frac{1}{e\omega^2 T_e\varepsilon_0\pi n_0}\left[\sum_{p=1}^{N}\sum_{\substack{q=1 \\ q\neq p}}^{N}\sum_{r=1}^{N}\frac{\overline{J}_p\overline{J}_q\overline{J}_r}{p}\right.$$

$$\int_0^{\varphi}\left\{\frac{2p+q}{2p(p+q)^2}\sin(p+q)\varphi - \frac{2p-q}{2p(p-q)^2}\sin(p-q)\varphi - \frac{1}{2(p+q)}\varphi\cos(p+q)\varphi\right.$$

$$\left.+ \frac{1}{2(p-q)}\varphi\cos(p-q)\varphi\right\}\sin(r\varphi)\,d\varphi + \sum_{p=1}^{N}\sum_{\substack{q=1 \\ p=q}}^{N}\sum_{r=1}^{N}\frac{\overline{J}_p^2\overline{J}_r}{p}\int_0^{\varphi}\left\{\frac{3}{8p^2}\sin(2p\varphi)\right.$$

$$\left.\left.- \frac{\varphi}{4p}\cos(2p\varphi) - \frac{\varphi}{2p}\right\}\sin(r\varphi)d\varphi\right]$$

152

Or, $e\omega n_0 x = \sum_{p=1}^{N} \frac{\bar{J}_p}{p} \{1 - cos(p\varphi)\}$

$$-\frac{1}{e\omega^2 T_e \varepsilon_0 \pi n_0} \left[\sum_{p=1}^{N} \sum_{\substack{q=1 \\ q \neq p}}^{N} \sum_{r=1}^{N} \frac{\bar{J}_p \bar{J}_q \bar{J}_r}{p} F_1^{pqr} + \sum_{p=1}^{N} \sum_{\substack{q=1 \\ q=p}}^{N} \sum_{r=1}^{N} \frac{\bar{J}_p^2 \bar{J}_r}{p} F_2^{pqr} \right] \quad (5\ 21)$$

where,

$$F_1^{pqr} = \frac{2p+q}{4p(p+q)^2} \left\{ \frac{1}{p+q-r} sin(p+q-r)\varphi - \frac{1}{p+q+r} sin(p+q+r)\varphi \right\}$$

$$-\frac{2p-q}{4p(p-q)^2} \left\{ \frac{1}{p-q-r} sin(p-q-r)\varphi - \frac{1}{p-q+r} sin(p-q+r)\varphi \right\} + \frac{1}{4(p+q)}$$

$$\left\{ \frac{\varphi}{p+q+r} cos(p+q+r)\varphi - \frac{1}{(p+q+r)^2} sin(p+q+r)\varphi - \frac{\varphi}{p+q-r} cos(p+q-r)\varphi \right.$$

$$+ \frac{1}{(p+q-r)^2} sin(p+q-r)\varphi \bigg\} - \frac{1}{4(p-q)} \left\{ \frac{\varphi}{(p-q+r)} cos(p-q+r)\varphi \right.$$

$$- \frac{1}{(p-q+r)^2} sin(p-q+r)\varphi - \frac{\varphi}{p-q-r} cos(p-q-r)\varphi$$

$$\left. + \frac{1}{(p-q-r)^2} sin(p-q-r)\varphi \right\}$$

, when $p+q-r \neq 0$, $p-q+r \neq 0$ and $p-q-r \neq 0$ (5 21a)

$$F_1^{pqr} = \frac{2p+q}{4p(p+q)^2} \left\{ \varphi - \frac{1}{2r} sin(2r\varphi) \right\} - \frac{2p-q}{4p(p-q)^2} \left\{ \frac{1}{2q} sin(2q\varphi) - \frac{1}{2p} sin(2p\varphi) \right\}$$

$$+ \frac{1}{4(p+q)} \left\{ \frac{\varphi}{2r} cos(2r\varphi) - \frac{1}{4r^2} sin(2r\varphi) \right\} - \frac{1}{4(p-q)} \left\{ \frac{\varphi}{2p} cos(2p\varphi) - \frac{1}{4p^2} sin(2p\varphi) \right.$$

$$\left. + \frac{\varphi}{2q} cos(2q\varphi) - \frac{1}{4q^2} sin(2q\varphi) \right\} \qquad \text{, when } p+q-r = 0 \qquad (5\ 21b)$$

$$F_1^{pqr} = \frac{2p+q}{4p(p+q)^2} \left\{ \frac{1}{2p} sin(2p\varphi) - \frac{1}{2q} sin(2q\varphi) \right\} - \frac{2p-q}{4p(p-q)^2} \left\{ \frac{1}{2r} sin(2r\varphi) - \varphi \right\}$$

153

$$+ \frac{1}{4(p+q)} \left\{ \frac{\varphi}{2q} cos(2q\varphi) - \frac{1}{4q^2} sin(2q\varphi) - \frac{\varphi}{2p} cos(2p\varphi) + \frac{1}{4p^2} sin(2p\varphi) \right\}$$

$$- \frac{1}{4(p-q)} \left\{ \frac{\varphi}{2r} cos(2r\varphi) - \frac{1}{4r^2} sin(2r\varphi) \right\} \qquad \text{, when } p\text{-}q\text{+}r = 0 \qquad (5\ 21c)$$

$$F_1^{pqr} = \frac{2p+q}{4p(p+q)^2} \left\{ \frac{1}{2q} sin(2q\varphi) - \frac{1}{2p} sin(2p\varphi) \right\} - \frac{2p-q}{4p(p-q)^2} \left\{ \varphi - \frac{1}{2r} sin(2r\varphi) \right\}$$

$$+ \frac{1}{4(p+q)} \left\{ \frac{\varphi}{2p} cos(2p\varphi) - \frac{1}{4p^2} sin(2p\varphi) - \frac{\varphi}{2q} cos(2q\varphi) + \frac{1}{4q^2} sin(2q\varphi) \right\}$$

$$- \frac{1}{4(p-q)} \left\{ \frac{\varphi}{2r} cos(2r\varphi) - \frac{1}{4r^2} sin(2r\varphi) \right\} \qquad \text{,when } p\text{-}q\text{-}r = 0 \qquad (5\ 21d)$$

and,

$$F_2^{pqr} = \frac{3}{16p^2} \left\{ \frac{1}{2p-r} sin(2p-r)\varphi - \frac{1}{2p+r} sin(2p+r)\varphi \right\} + \frac{1}{8p} \left\{ \frac{\varphi}{2p+r} cos(2p+r)\varphi \right.$$

$$\left. - \frac{1}{(2p+r)^2} sin(2p+r)\varphi - \frac{\varphi}{(2p-r)} cos(2p-r)\varphi + \frac{1}{(2p-r)^2} sin(2p-r)\varphi \right\}$$

$$+ \frac{1}{2p} \left\{ \frac{\varphi}{r} cos(r\varphi) - \frac{1}{r^2} sin(r\varphi) \right\} \qquad \text{, when } 2p\text{-}r \neq 0 \qquad (5\ 21e)$$

$$F_2^{pqr} = -\frac{7}{128p^3} sin(4p\varphi) + \frac{\varphi}{32p^2} cos(4p\varphi) - \frac{1}{8p^3} sin(2p\varphi) + \frac{\varphi}{4p^2} cos(2p\varphi) + \frac{3\varphi}{16p^2}$$

$$\text{, when } 2p\text{-}r = 0 \qquad (5\ 21f)$$

Putting $x = s(t)$ and $\varphi = \omega t$ in (5 21), we obtain the nonlinear motion of the electron sheath Again using (5 21) and putting $x = s_m$ at $\varphi = \pi$ we obtain the ion sheath thickness s_m

From (5 3) and (5 20) we have,

$$n_t = n_0 \left[1 - \frac{1}{e\omega^2 T_e \varepsilon_0 \pi n_0} \left\{ \sum_{p=1}^{N} \sum_{\substack{q=1 \\ q \neq p}}^{N} \frac{\bar{J}_p \bar{J}_q}{p} \left(\frac{2p+q}{2p(p+q)^2} sin(p+q)\varphi \right. \right. \right.$$

154

$$-\frac{2p-q}{2p(p-q)^2}\sin(p-q)\varphi - \frac{1}{2(p+q)}\varphi\cos(p+q)\varphi + \frac{1}{2(p-q)}\varphi\cos(p-q)\varphi\Bigg)$$

$$+\sum_{p=1}^{N}\sum_{\substack{q=1 \\ q=p}}^{N}\frac{\bar{J}_p^2}{p}\left(\frac{3}{8p^2}\sin(2p\varphi) - \frac{\varphi}{4p}\cos(2p\varphi) - \frac{\varphi}{2p}\right)\Bigg]\Bigg]^{-1} \qquad (5\ 22)$$

Differentiating (5 17), using (5 3) and (5 19) and equating $\dfrac{d\bar{E}}{dx} = \dfrac{\rho}{\varepsilon_0}$ we obtain the net charge density,

$$\quad \rho = \frac{\varphi}{\pi}n_i e \qquad (5\ 23)$$

Now from (5 8), the time-average electron density,

$$\bar{n}_e = \left(1 - \frac{\varphi}{\pi}\right)n_i \qquad (5\ 24)$$

From (5 20), the time-average potential,

$$\frac{\bar{\Phi}}{T_e} = \frac{1}{2} - \frac{1}{2}\Bigg[1 - \frac{1}{e\omega^2 T_e\varepsilon_0\pi n_0}\Bigg\{\sum_{p=1}^{N}\sum_{\substack{q=1 \\ q\ne p}}^{N}\frac{\bar{J}_p\bar{J}_q}{p}\left(\frac{2p+q}{2p(p+q)^2}\sin(p+q)\varphi\right.$$

$$-\frac{2p-q}{2p(p-q)^2}\sin(p-q)\varphi - \frac{1}{2(p+q)}\varphi\cos(p+q)\varphi + \frac{1}{2(p-q)}\varphi\cos(p-q)\varphi\Bigg)$$

$$+\sum_{p=1}^{N}\sum_{\substack{q=1 \\ q=p}}^{N}\frac{\bar{J}_p^2}{p}\left(\frac{3}{8p^2}\sin(2p\varphi) - \frac{\varphi}{4p}\cos(2p\varphi) - \frac{\varphi}{2p}\right)\Bigg\}\Bigg]^2 \qquad (5\ 25)$$

and from (5 25), using $\bar{V} = -\bar{\Phi}(\varphi = \pi)$ the net dc voltage across the sheath can be given by

$$\frac{\bar{V}}{T_e} = -\frac{1}{2} + \frac{1}{2}\Bigg[1 + \frac{1}{2e\omega^2 T_e\varepsilon_0 n_0}\Bigg\{\sum_{p=1}^{N}\sum_{\substack{q=1 \\ q\ne p}}^{N}\frac{\bar{J}_p\bar{J}_q}{p}\left(\frac{1}{(p+q)}\cos(p+q)\pi\right.$$

$$\left.-\frac{1}{(p-q)}\cos(p-q)\pi\right) + \frac{3}{2}\sum_{p=1}^{N}\sum_{\substack{q=1 \\ q=p}}^{N}\frac{\bar{J}_p^2}{p^2}\Bigg\}\Bigg]^2 \qquad (5\ 26)$$

Now, the instantaneous electric field is given by (5 15) Integrating the electric field with respect to x, we obtain the instantaneous voltage $V(t)$ from the plasma to the electrode across the sheath as

$$V(t) = \int_S^{S_m} E(x,t)\, dx = \int_{\omega t}^{\pi} \sum_{p=1}^{N} \frac{\bar{J}_p}{p\omega\varepsilon_0}\left[cos(p\omega t) - cos(p\varphi)\right]\frac{dx}{d\varphi}\, d\varphi \tag{5 27}$$

Using (5 19) and (5 20) and inserting into (5 27) we obtain the equation for the instantaneous sheath voltage $V(t)$, for $0 < \omega t < \pi$, as

$$e\omega^2\varepsilon_0 n_0 V(t) = \int_{\omega t}^{\pi} \sum_{p=1}^{N}\sum_{q=1}^{N} \frac{\bar{J}_p\bar{J}_q}{p}\left\{cos(p\omega t) - cos(p\varphi)\right\}sin(q\varphi)d\varphi - \frac{1}{e\omega^2 T_e\varepsilon_0\pi n_0}$$

$$\int_{\omega t}^{\pi}\left[\sum_{p=1}^{N}\sum_{\substack{q=1\\q\neq p}}^{N}\sum_{r=1}^{N}\sum_{s=1}^{N} \frac{\bar{J}_p\bar{J}_q\bar{J}_r\bar{J}_s}{ps}\left\{\frac{2p+q}{2p(p+q)^2}sin(p+q)\varphi - \frac{2p-q}{2p(p-q)^2}sin(p-q)\varphi\right.\right.$$

$$\left.- \frac{1}{2(p+q)}\varphi\,cos(p+q)\varphi + \frac{1}{2(p-q)}\varphi\,cos(p-q)\varphi\right\}\left\{cos(s\omega t) - cos(s\varphi)\right\}sin(r\varphi)$$

$$+ \sum_{p=1}^{N}\sum_{\substack{q=1\\q=p}}^{N}\sum_{r=1}^{N}\sum_{s=1}^{N} \frac{J_p^2\bar{J}_r\bar{J}_s}{ps}\left\{\frac{3}{8p^2}sin(2p\varphi) - \frac{\varphi}{4p}cos(2p\varphi) - \frac{\varphi}{2p}\right\}$$

$$\left.\left\{cos(s\omega t) - cos(s\varphi)\right\}sin(r\varphi)\right]d\varphi$$

Or,

$$e\omega^2\varepsilon_0 n_0 V(t) = \sum_{p=1}^{N}\sum_{q=1}^{N} \frac{\bar{J}_p\bar{J}_q}{p}I_1^{pq} - \frac{1}{e\omega^2 T_e\varepsilon_0\pi n_0}\left[\sum_{p=1}^{N}\sum_{\substack{q=1\\q\neq p}}^{N}\sum_{r=1}^{N}\sum_{s=1}^{N} \frac{\bar{J}_p\bar{J}_q\bar{J}_r\bar{J}_s}{ps}\right.$$

$$\left\{\frac{2p+q}{4p(p+q)^2}cos(s\omega t)\left(I_2^{pqr} - I_3^{pqr}\right) - \frac{2p-q}{4p(p-q)^2}cos(s\omega t)\left(I_4^{pqr} - I_5^{pqr}\right) - \frac{1}{4(p+q)}\right.$$

$$cos(s\omega t)\left(I_6^{pqr} - I_7^{pqr}\right) + \frac{1}{4(p-q)}cos(s\omega t)\left(I_8^{pqr} - I_9^{pqr}\right) - \frac{2p+q}{8p(p+q)^2}$$

$$\left(I_{10}^{pqrs} + I_{11}^{pqrs} - I_{12}^{pqrs} - I_{13}^{pqrs}\right) + \frac{2p-q}{8p(p-q)^2}\left(I_{14}^{pqrs} + I_{15}^{pqrs} - I_{16}^{pqrs} - I_{17}^{pqrs}\right)$$

$$\left.+ \frac{1}{8(p+q)}\left(I_{18}^{pqrs} + I_{19}^{pqrs} - I_{20}^{pqrs} - I_{21}^{pqrs}\right) - \frac{1}{8(p-q)}\left(I_{22}^{pqrs} + I_{23}^{pqrs} - I_{24}^{pqrs} - I_{25}^{pqrs}\right)\right\}$$

$$+ \sum_{p=1}^{N} \sum_{\substack{q=1 \\ q=p}}^{N} \sum_{r=1}^{N} \sum_{s=1}^{N} \frac{J_p^2 \bar{J}_r \bar{J}_s}{ps} \left\{ \frac{3}{16p^2} cos(s\omega t)\left(I_{26}^{pr} - I_{27}^{pr}\right) - \frac{1}{8p} cos(s\omega t)\left(I_{28}^{pr} - I_{29}^{pr}\right) \right.$$

$$- \frac{1}{2p} cos(s\omega t) I_{30}^{r} + \frac{1}{4p}\left(I_{31}^{rs} + I_{32}^{rs}\right) - \frac{3}{32p^2}\left(I_{33}^{prs} + I_{34}^{prs} - I_{35}^{prs} - I_{36}^{prs}\right)$$

$$\left. + \frac{1}{16p}\left(I_{37}^{prs} + I_{38}^{prs} - I_{39}^{prs} - I_{40}^{prs}\right) \right\} \Bigg]$$

<div align="right">(5 28)</div>

where,

$$I_1^{pq} = cos(p\omega t)\frac{1}{q}\left\{cos(q\omega t) - cos(q\pi)\right\} - \frac{1}{2(p+q)}\left\{cos(p+q)\omega t - cos(p+q)\pi\right\}$$

$$+ \frac{1}{2(p-q)}\left\{cos(p-q)\omega t - cos(p-q)\pi\right\}, \qquad p \neq q$$

$$= cos(p\omega t)\frac{1}{q}\left\{cos(q\omega t) - cos(q\pi)\right\} - \frac{1}{2(p+q)}\left\{cos(p+q)\omega t - cos(p+q)\pi\right\},$$

<div align="center">$p = q$</div> <div align="right">(5 28i)</div>

$$I_2^{pqr} = -\frac{1}{p+q-r} sin(p+q-r)\omega t, \qquad p+q-r \neq 0$$

$$= \pi - \omega t, \qquad p+q-r = 0 \qquad \text{(5 28ii)}$$

$$I_3^{pqr} = -\frac{1}{p+q+r} sin(p+q+r)\omega t \qquad \text{(5 28iii)}$$

$$I_4^{pqr} = -\frac{1}{p-q-r} sin(p-q-r)\omega t, \qquad p-q-r \neq 0$$

$$= \pi - \omega t, \qquad p-q-r = 0 \qquad \text{(5 28iv)}$$

$$I_5^{pqr} = -\frac{1}{p-q+r} sin(p-q+r)\omega t, \qquad p-q+r \neq 0$$

$$= \pi - \omega t, \qquad p-q+r = 0 \qquad \text{(5 28v)}$$

$$I_6^{pqr} = \frac{\omega t}{p+q+r} cos(p+q+r)\omega t - \frac{\pi}{p+q+r} cos(p+q+r)\pi$$

<div align="center">157</div>

$$-\frac{1}{(p+q+r)^2}sin(p+q+r)\omega t \qquad\qquad\qquad (5\ 28\text{vi})$$

$$I_7^{pqr} = \frac{\omega t}{p+q-r}cos(p+q-r)\omega t - \frac{\pi}{p+q-r}cos(p+q-r)\pi$$

$$-\frac{1}{(p+q-r)^2}sin(p+q-r)\omega t\ , \qquad\qquad p\text{+}q\text{-}r \neq 0$$

$$= 0, \qquad\qquad p\text{+}q\text{-}r = 0 \qquad (5\ 28\text{vii})$$

$$I_8^{pqr} = \frac{\omega t}{p-q+r}cos(p-q+r)\omega t - \frac{\pi}{p-q+r}cos(p-q+r)\pi$$

$$-\frac{1}{(p-q+r)^2}sin(p-q+r)\omega t\ , \qquad\qquad p\text{-}q\text{+}r \neq 0$$

$$= 0, \qquad\qquad p\text{-}q\text{+}r = 0 \qquad (5\ 28\text{viii})$$

$$I_9^{pqr} = \frac{\omega t}{p-q-r}cos(p-q-r)\omega t - \frac{\pi}{p-q-r}cos(p-q-r)\pi$$

$$-\frac{1}{(p-q-r)^2}sin(p-q-r)\omega t\ , \qquad\qquad p\text{-}q\text{-}r \neq 0$$

$$= 0, \qquad\qquad p\text{-}q\text{-}r = 0 \qquad (5\ 28\text{ix})$$

$$I_{10}^{pqrs} = -\frac{1}{p+q-r+s}sin(p+q-r+s)\omega t\ , \qquad p\text{+}q\text{-}r\text{+}s \neq 0$$

$$= \pi - \omega t\ , \qquad\qquad p\text{+}q\text{-}r\text{+}s = 0 \qquad (5\ 28\text{x})$$

$$I_{11}^{pqrs} = -\frac{1}{p+q-r-s}sin(p+q-r-s)\omega t\ , \qquad p\text{+}q\text{-}r\text{-}s \neq 0$$

$$= \pi - \omega t\ , \qquad\qquad p\text{+}q\text{-}r\text{-}s = 0 \qquad (5\ 28\text{xi})$$

$$I_{12}^{pqrs} = -\frac{1}{p+q+r+s}sin(p+q+r+s)\omega t \qquad\qquad (5\ 28\text{xii})$$

$$I_{13}^{pqrs} = -\frac{1}{p+q+r-s}sin(p+q+r-s)\omega t\ , \qquad p\text{+}q\text{+}r\text{-}s \neq 0$$

$$= \pi - \omega t, \qquad\qquad p+q+r-s = 0 \qquad\qquad (5\ 28\text{xiii})$$

$$I_{14}^{pqrs} = -\frac{1}{p-q-r+s}\sin(p-q-r+s)\omega t, \qquad p\text{-}q\text{-}r\text{+}s \neq 0$$

$$= \pi - \omega t, \qquad\qquad p\text{-}q\text{-}r\text{+}s = 0 \qquad\qquad (5\ 28\text{xiv})$$

$$I_{15}^{pqrs} = -\frac{1}{p-q-r-s}\sin(p-q-r-s)\omega t, \qquad p\text{-}q\text{-}r\text{-}s \neq 0$$

$$= \pi - \omega t, \qquad\qquad p\text{-}q\text{-}r\text{-}s = 0 \qquad\qquad (5\ 28\text{xv})$$

$$I_{16}^{pqrs} = -\frac{1}{p-q+r+s}\sin(p-q+r+s)\omega t, \qquad p\text{-}q\text{+}r\text{+}s \neq 0$$

$$= \pi - \omega t, \qquad\qquad p\text{-}q\text{+}r\text{+}s = 0 \qquad\qquad (5\ 28\text{xvi})$$

$$I_{17}^{pqrs} = -\frac{1}{p-q+r-s}\sin(p-q+r-s)\omega t, \qquad p\text{-}q\text{+}r\text{-}s \neq 0$$

$$= \pi - \omega t, \qquad\qquad p\text{-}q\text{+}r\text{-}s = 0 \qquad\qquad (5\ 28\text{xvii})$$

$$I_{18}^{pqrs} = \frac{\omega t}{p+q+r+s}\cos(p+q+r+s)\omega t - \frac{\pi}{p+q+r+s}\cos(p+q+r+s)\pi$$

$$- \frac{1}{(p+q+r+s)^2}\sin(p+q+r+s)\omega t \qquad\qquad (5\ 28\text{xviii})$$

$$I_{19}^{pqrs} = \frac{\omega t}{p+q+r-s}\cos(p+q+r-s)\omega t - \frac{\pi}{p+q+r-s}\cos(p+q+r-s)\pi$$

$$- \frac{1}{(p+q+r-s)^2}\sin(p+q+r-s)\omega t, \qquad p\text{+}q\text{+}r\text{-}s \neq 0$$

$$= 0, \qquad\qquad p\text{+}q\text{+}r\text{-}s = 0 \qquad\qquad (5\ 28\text{xix})$$

$$I_{20}^{pqrs} = \frac{\omega t}{p+q-r+s}\cos(p+q-r+s)\omega t - \frac{\pi}{p+q-r+s}\cos(p+q-r+s)\pi$$

$$- \frac{1}{(p+q-r+s)^2}\sin(p+q-r+s)\omega t, \qquad p\text{+}q\text{-}r\text{+}s \neq 0$$

$$= 0, \qquad\qquad p\text{+}q\text{-}r\text{+}s = 0 \qquad\qquad (5\ 28\text{xx})$$

$$I_{21}^{pqrs} = \frac{\omega t}{p+q-r-s}\cos(p+q-r-s)\omega t - \frac{\pi}{p+q-r-s}\cos(p+q-r-s)\pi$$

$$- \frac{1}{(p+q-r-s)^2}\sin(p+q-r-s)\omega t, \qquad p+q-r-s \neq 0$$

$$= 0, \qquad\qquad p+q-r-s = 0 \qquad\qquad (5\ 28\text{xxi})$$

$$I_{22}^{pqrs} = \frac{\omega t}{p-q+r+s}\cos(p-q+r+s)\omega t - \frac{\pi}{p-q+r+s}\cos(p-q+r+s)\pi$$

$$- \frac{1}{(p-q+r+s)^2}\sin(p-q+r+s)\omega t, \qquad p-q+r+s \neq 0$$

$$= 0, \qquad\qquad p-q+r+s = 0 \qquad\qquad (5\ 28\text{xxii})$$

$$I_{23}^{pqrs} = \frac{\omega t}{p-q+r-s}\cos(p-q+r-s)\omega t - \frac{\pi}{p-q+r-s}\cos(p-q+r-s)\pi$$

$$- \frac{1}{(p-q+r-s)^2}\sin(p-q+r-s)\omega t, \qquad p-q+r-s \neq 0$$

$$= 0, \qquad\qquad p-q+r-s = 0 \qquad\qquad (5\ 28\text{xxiii})$$

$$I_{24}^{pqrs} = \frac{\omega t}{p-q-r+s}\cos(p-q-r+s)\omega t - \frac{\pi}{p-q-r+s}\cos(p-q-r+s)\pi$$

$$- \frac{1}{(p-q-r+s)^2}\sin(p-q-r+s)\omega t, \qquad p-q-r+s \neq 0$$

$$= 0, \qquad\qquad p-q-r+s = 0 \qquad\qquad (5\ 28\text{xxiv})$$

$$I_{25}^{pqrs} = \frac{\omega t}{p-q-r-s}\cos(p-q-r-s)\omega t - \frac{\pi}{p-q-r-s}\cos(p-q-r-s)\pi$$

$$- \frac{1}{(p-q-r-s)^2}\sin(p-q-r-s)\omega t, \qquad p-q-r-s \neq 0$$

$$= 0, \qquad\qquad p-q-r-s = 0 \qquad\qquad (5\ 28\text{xxv})$$

$$I_{26}^{pr} = -\frac{1}{2p-r}\sin(2p-r)\omega t, \qquad\qquad 2p-r \neq 0$$

$$= \pi - \omega t, \qquad\qquad 2p-r = 0 \qquad\qquad (5\ 28\text{xxvi})$$

$$I_{27}^{pr} = -\frac{1}{2p+r}\sin(2p+r)\omega t \qquad (5\ 28\text{xxvii})$$

$$I_{28}^{pr} = \frac{\omega t}{2p+r}\cos(2p+r)\omega t - \frac{\pi}{2p+r}\cos(2p+r)\pi - \frac{1}{(2p+r)^2}\sin(2p+r)\omega t \qquad (5\ 28\text{xxviii})$$

$$I_{29}^{pr} = \frac{\omega t}{2p-r}\cos(2p-r)\omega t - \frac{\pi}{2p-r}\cos(2p-r)\pi$$

$$- \frac{1}{(2p-r)^2}\sin(2p-r)\omega t, \qquad\qquad 2p\text{-}r \neq 0$$

$$= 0, \qquad\qquad 2p\text{-}r = 0 \qquad (5\ 28\text{xxix})$$

$$I_{30}^{r} = \frac{\omega t}{r}\cos(r\omega t) - \frac{\pi}{r}\cos(r\pi) - \frac{1}{r^2}\sin(r\omega t) \qquad (5\ 28\text{xxx})$$

$$I_{31}^{rs} = \frac{\omega t}{r+s}\cos(r+s)\omega t - \frac{\pi}{r+s}\cos(r+s)\pi - \frac{1}{(r+s)^2}\sin(r+s)\omega t \qquad (5\ 28\text{xxxi})$$

$$I_{32}^{rs} = \frac{\omega t}{r-s}\cos(r-s)\omega t - \frac{\pi}{r-s}\cos(r-s)\pi - \frac{1}{(r-s)^2}\sin(r-s)\omega t, \qquad r\text{-}s \neq 0$$

$$= 0, \qquad\qquad r\text{-}s = 0 \qquad (5\ 28\text{xxxii})$$

$$I_{33}^{prs} = -\frac{1}{2p-r+s}\sin(2p-r+s)\omega t, \qquad\qquad 2p\text{-}r\text{+}s \neq 0$$

$$= \pi - \omega t, \qquad\qquad 2p\text{-}r\text{+}s = 0 \qquad (5\ 28\text{xxxiii})$$

$$I_{34}^{prs} = -\frac{1}{2p-r-s}\sin(2p-r-s)\omega t, \qquad\qquad 2p\text{-}r\text{-}s \neq 0$$

$$= \pi - \omega t, \qquad\qquad 2p\text{-}r\text{-}s = 0 \qquad (5\ 28\text{xxxiv})$$

$$I_{35}^{prs} = -\frac{1}{2p+r+s}\sin(2p+r+s)\omega t \qquad (5\ 28\text{xxxv})$$

$$I_{36}^{prs} = -\frac{1}{2p+r-s}\sin(2p+r-s)\omega t, \qquad\qquad 2p\text{+}r\text{-}s \neq 0$$

$$= \pi - \omega t , \qquad\qquad 2p+r\text{-}s = 0 \qquad\qquad (5\ 28\text{xxxvi})$$

$$I_{37}^{prs} = \frac{\omega t}{2p+r+s}\cos(2p+r+s)\omega t - \frac{\pi}{2p+r+s}\cos(2p+r+s)\pi$$

$$- \frac{1}{(2p+r+s)^2}\sin(2p+r+s)\omega t \qquad\qquad (5\ 28\text{xxxvii})$$

$$I_{38}^{prs} = \frac{\omega t}{2p+r-s}\cos(2p+r-s)\omega t - \frac{\pi}{2p+r-s}\cos(2p+r-s)\pi$$

$$- \frac{1}{(2p+r-s)^2}\sin(2p+r-s)\omega t , \qquad\qquad 2p+r\text{-}s \neq 0$$

$$= 0, \qquad\qquad 2p+r\text{-}s = 0 \qquad\qquad (5\ 28\text{xxxviii})$$

$$I_{39}^{prs} = \frac{\omega t}{2p-r+s}\cos(2p-r+s)\omega t - \frac{\pi}{2p-r+s}\cos(2p-r+s)\pi$$

$$- \frac{1}{(2p-r+s)^2}\sin(2p-r+s)\omega t , \qquad\qquad 2p\text{-}r\text{+}s \neq 0$$

$$= 0, \qquad\qquad 2p\text{-}r\text{+}s = 0 \qquad\qquad (5\ 28\text{xxxix})$$

$$I_{40}^{prs} = \frac{\omega t}{2p-r-s}\cos(2p-r-s)\omega t - \frac{\pi}{2p-r-s}\cos(2p-r-s)\pi$$

$$- \frac{1}{(2p-r-s)^2}\sin(2p-r-s)\omega t , \qquad\qquad 2p\text{-}r\text{-}s \neq 0$$

$$= 0, \qquad\qquad 2p\text{-}r\text{-}s = 0 \qquad\qquad (5\ 28\text{xl})$$

5 3 1 1 Sheath capacitance

$V(t)$ in Eqn (5 28) is an even, periodic function of ωt with period 2π For $-\pi < \omega t < 0$, we find that $V(t)$ is given by Eqn (5 28) with ωt at the right hand side of the equation replaced by $-\omega t$ Expanding $V(t)$ in a Fourier series we have,

$$V(t) = \overline{V}_0 + \sum_{k=1}^{\infty} \overline{V}_k \cos(k\omega t) \qquad\qquad (5\ 29)$$

where, $\overline{V_0} = \frac{1}{\pi} \int_0^\pi V(\omega t)\, d\omega t$ (5 29i)

$$\overline{V_k} = \frac{2}{\pi} \int_0^\pi V(\omega t) \cos(k\omega t)\, d\omega t \qquad (k=1,2,3, \ ) \qquad (5\ 29\mathrm{ii})$$

It is evident from Eqn (5 28) that it is almost impossible to perform manually the analytical Fourier transforms given by Eqn (5 29) But using a personal computer it is very easy to perform these calculations numerically using any routine programming language, such as FORTRAN, Pascal, C etc

Defining the effective capacitance per unit area using the relation,

$$-\overline{J_k} \sin(k\omega t) = C_k \frac{d}{dt}\left[\overline{V_k} \cos(k\omega t)\right] \qquad (5\ 30)$$

we obtain the sheath capacitance (in $Farad/m^2$) for k-th harmonic frequency,

$$C_k = \frac{\overline{J_k}}{k\omega \overline{V_k}} \qquad (5\ 31)$$

5 3 1 2 Sheath conductance

The RF conductance of the sheath is due to stochastic heating of the electrons by the oscillating sheath An electron that is reflected from a moving sheath experiences a change of energy If the sheath moves toward the electron, then the energy increases, if the sheath moves away, then the energy decreases For an oscillating sheath, some electrons gain energy and others lose energy However, avaraging over an oscillation period, the net effect is an energy gam, corresponding to a dissipation of heat in the sheath [12, 30, 162-164]

Electrons reflecting from the large decelerating fields of a moving high-voltage sheath can be approximated by assuming that the reflected velocity is that which occurs in an elastic collision of a ball with a moving wall

$$u_r = -u + 2u_s \qquad (5\ 32)$$

where u and u_r are the incident and reflected electron velocities parallel to the time-varying electron sheath velocity u_s For a uniform density model we let $f_s(u,t)$ be the electron velocity distribution at s, normalized as

$$\int_{-\infty}^{\infty} f_s(u,t)du = n_i(s(t)) = n_s(t) \tag{5 33}$$

In a time interval dt and for a speed interval du, the number of electrons per unit area that collide with the sheath is given by $(u - u_s)f_s(u,t)dudt$ This results in a power transfer per unit area,

$$dP_{stoc} = \frac{1}{2}m\left(u_r^2 - u^2\right)\left(u - u_s\right)f_s(u,t)du \tag{5 34}$$

Using $u_r = -u + 2u_s$ and integrating over all incident velocities, we obtain

$$P_{stoc} = -2m\int_{u_s}^{\infty} u_s\left(u - u_s\right)^2 f_s(u,t)du \tag{5 35}$$

To determine f_s, we first note that the sheath is oscillating because the electrons in the bulk plasma are oscillating in response to a time-varying electric field If the velocity distribution function within the plasma at the ion sheath edge $x = 0$ in the absence of the electric field is a Maxwellian $f_m(u)$ having density n_0, then the distribution within the plasma at the sheath edge is $f_0(u,t)=f_m(u-u_0)$, where $u_0(t)$ is the time-varying oscillation velocity of the plasma electrons [30] At the moving electron sheath edge, because $n_s < n_0$, not all electrons having $u > 0$ at $x = 0$ collide with the sheath at s Many electrons are reflected within the region $0 < x < s$ where the ion density drops from n_0 to n_s This reflection is produced by a weak electric field whose value maintains $n_e \approx n_i$ at all times The transformation of f_0 across this region to obtain f_s is complicated However, the essential features to determine the stochastic heating are seen if we approximate [30]

$$f_s = \frac{n_s}{n_0}f_m(u - u_0), \qquad u > 0 \tag{5 36}$$

Inserting (5 36) into (5 35) and transforming to a new variable $u' = u - u_0$, we obtain

$$P_{stoc}(t) = -\frac{2m}{n_0}\int_{u_s-u_0}^{\infty} u_s n_s\left[u'^2 - 2u'(u_s - u_0) + (u_s - u_0)^2\right]f_m(u')du' \tag{5 37}$$

From Eqn (5 10) we have

$$n_s u_s = n_0 \sum_{p=1}^{N} \bar{u}_p \sin(p\varphi) = n_0 u_0 \tag{5 38}$$

where, $\bar{u}_p = \frac{J_p}{en_0}$

From Eqns (5 19) and (5 20) we obtain,

$$
e\omega n_0 \frac{dx}{d\varphi} = \sum_{p=1}^{N} \bar{J}_p \sin(p\varphi) - \frac{1}{e\omega^2 T_e \varepsilon_0 \pi n_0} \left[\sum_{p=1}^{N} \sum_{\substack{q=1 \\ q \neq p}}^{N} \frac{\bar{J}_p \bar{J}_q}{p} \left\{ \frac{2p+q}{2p(p+q)^2} \sin(p+q)\varphi \right. \right.
$$

$$
\left. - \frac{2p-q}{2p(p-q)^2} \sin(p-q)\varphi - \frac{1}{2(p+q)} \varphi \cos(p+q)\varphi + \frac{1}{2(p-q)} \varphi \cos(p-q)\varphi \right\}
$$

$$
\left. + \sum_{p=1}^{N} \sum_{\substack{q=1 \\ q=p}}^{N} \frac{\bar{J}_p^2}{p} \left\{ \frac{3}{8p^2} \sin(2p\varphi) - \frac{\varphi}{4p} \cos(2p\varphi) - \frac{\varphi}{2p} \right\} \right] \sum_{p=1}^{N} \bar{J}_p \sin(p\varphi) \qquad (5\ 39)
$$

Using $\varphi = \omega t$ from the above equation we obtain

$$
e n_0 u_s = e n_0 u_0 - \frac{1}{e\omega^2 T_e \varepsilon_0 \pi n_0} \left[\sum_{p=1}^{N} \sum_{\substack{q=1 \\ q \neq p}}^{N} \frac{\bar{J}_p \bar{J}_q}{p} \left\{ \frac{2p+q}{2p(p+q)^2} \sin(p+q)\varphi - \frac{2p-q}{2p(p-q)^2} \right. \right.
$$

$$
\left. \sin(p-q)\varphi - \frac{1}{2(p+q)} \varphi \cos(p+q)\varphi + \frac{1}{2(p-q)} \varphi \cos(p-q)\varphi \right\}
$$

$$
\left. + \sum_{p=1}^{N} \sum_{\substack{q=1 \\ q=p}}^{N} \frac{\bar{J}_p^2}{p} \left\{ \frac{3}{8p^2} \sin(2p\varphi) - \frac{\varphi}{4p} \cos(2p\varphi) - \frac{\varphi}{2p} \right\} \right] \sum_{p=1}^{N} \bar{J}_p \sin(p\varphi)
$$

Or,

$$
u_s - u_0 = - \frac{1}{e^2 \omega^2 T_e \varepsilon_0 \pi n_0^2} \left[\sum_{p=1}^{N} \sum_{\substack{q=1 \\ q \neq p}}^{N} \sum_{r=1}^{N} \frac{\bar{J}_p \bar{J}_q \bar{J}_r}{p} \left\{ \frac{2p+q}{4p(p+q)^2} \left\{ \cos(p+q-r)\varphi \right. \right. \right.
$$

$$
\left. - \cos(p+q+r)\varphi \right\} - \frac{2p-q}{4p(p-q)^2} \left\{ \cos(p-q-r)\varphi - \cos(p-q+r)\varphi \right\}
$$

$$
- \frac{1}{4(p+q)} \varphi \left\{ \sin(p+q+r)\varphi - \sin(p+q-r)\varphi \right\} + \frac{1}{4(p-q)} \varphi \left\{ \sin(p-q+r)\varphi \right.
$$

$$
\left. - \sin(p-q-r)\varphi \right\} \right\} + \sum_{p=1}^{N} \sum_{\substack{q=1 \\ q=p}}^{N} \sum_{r=1}^{N} \frac{\bar{J}_p^2 \bar{J}_r}{p} \left\{ \frac{3}{16p^2} \left\{ \cos(2p-r)\varphi - \cos(2p+r)\varphi \right\} \right.
$$

$$-\frac{\varphi}{8p}\left\{sin(2p+r)\varphi - sin(2p-r)\varphi\right\} - \frac{\varphi}{2p}sin(r\varphi)\right\}\right] = F(\varphi)$$ (5 40)

$F(\varphi)$ must be an odd function of φ which is valid for $0 < \varphi < \pi$ For $-\pi < \varphi < 0$ we will use $-F(\varphi)$ instead of $F(\varphi)$ We find from Eqns (5 37) and (5 38) that the average stochastic power for a single sheath is

$$\overline{P}_{stoc} = -\frac{2m}{2\pi}\int_{-\pi}^{\pi}\int_{u_s-u_0}^{\infty}\left[u'^2 - 2u'(u_s - u_0) + (u_s - u_0)^2\right]u_0 f_m(u')du'd\varphi$$

$$= -\frac{m}{\pi}\int_{-\pi}^{\pi}\sum_{p=1}^{N}u_p sin(p\varphi)d\varphi\int_{F(\varphi)}^{\infty}u'^2 f_m(u')du'$$

$$+\frac{2m}{\pi}\int_{-\pi}^{\pi}F(\varphi)\sum_{p=1}^{N}u_p sin(p\varphi)d\varphi\int_{F(\varphi)}^{\infty}u' f_m(u')du'$$

$$-\frac{m}{\pi}\int_{-\pi}^{\pi}F^2(\varphi)\sum_{p=1}^{N}u_p sin(p\varphi)d\varphi\int_{F(\varphi)}^{\infty}f_m(u')du'$$

$$= \overline{P}_1 + \overline{P}_2 + \overline{P}_3$$ (5 41)

Since $F(\varphi)$ is an odd function, the $\overline{P}_1$ and $\overline{P}_3$ integrands integrate to zero, with the $\overline{P}_2$ integral yielding

$$\overline{P}_{stoc} = \overline{P}_2 = \frac{2m}{\pi}\int_{-\pi}^{\pi}F(\varphi)\sum_{p=1}^{N}u_p sin(p\varphi)d\varphi\int_{F(\varphi)}^{\infty}u' f_m(u')du'$$ (5 42)

For a Maxwellian distribution we have the incident flux [62,66],

$$\Gamma_s = \int_0^{\infty}u' f_m(u')du' = \frac{1}{4}n_0 u_e$$ (5 43)

where, the mean electron speed $u_e = \left(\frac{8eT_e}{\pi m}\right)^{\frac{1}{2}}$ If the assumption is made that the sheath motion is much slower than the electron thermal velocity, we can take the lower limit of the u' integral in Eqn (5 42) to be zero So from Eqn (5 43) we obtain

$$\int_{F(\varphi)}^{\infty}u' f_m(u')du' \approx \int_0^{\infty}u' f_m(u')du' = \frac{1}{4}n_0 u_e = \Gamma_s$$ (5 44)

Since $F(\varphi)$ is an odd function, inserting Eqn (5 44) into Eqn (5 42) and putting

$$\overline{u}_p = \frac{\overline{J}_p}{en_0} \text{ we obtain}$$

$$\overline{P}_{stoc} = \frac{4m}{\pi en_0}\Gamma_s \int_0^\pi F(\varphi) \sum_{p=1}^N \overline{J}_p \sin(p\varphi)d\varphi \tag{5 45}$$

Inserting Eqns (5 40) into Eqn (5 45) and performing the integration we obtain

$$\overline{P}_{stoc} = -\frac{4m\Gamma_s}{e^3\omega^2 T_e \varepsilon_0 \pi^2 n_0^3}\left[\sum_{p=1}^N \sum_{\substack{q=1\\q\neq p}}^N \sum_{r=1}^N \sum_{s=1}^N \frac{\overline{J}_p \overline{J}_q \overline{J}_r \overline{J}_s}{p}\left\{\frac{2p+q}{8p(p+q)^2}\right.\right.$$

$$\left(I_1^{stoc} - I_2^{stoc} - I_3^{stoc} + I_4^{stoc}\right) - \frac{2p-q}{8p(p-q)^2}\left(I_5^{stoc} - I_6^{stoc} - I_7^{stoc} + I_8^{stoc}\right)$$

$$\left. -\frac{1}{8(p+q)}\left(I_9^{stoc} - I_{10}^{stoc} - I_{11}^{stoc} + I_{12}^{stoc}\right) + \frac{1}{8(p-q)}\left(I_{13}^{stoc} - I_{14}^{stoc} - I_{15}^{stoc} + I_{16}^{stoc}\right)\right\}$$

$$+ \sum_{p=1}^N \sum_{\substack{q=1\\q=p}}^N \sum_{r=1}^N \sum_{s=1}^N \frac{\overline{J}_p^2 \overline{J}_r \overline{J}_s}{p}\left\{\frac{3}{32p^2}\left(I_{17}^{stoc} - I_{18}^{stoc} - I_{19}^{stoc} + I_{20}^{stoc}\right)\right.$$

$$\left.\left. -\frac{1}{16p}\left(I_{21}^{stoc} - I_{22}^{stoc} - I_{23}^{stoc} + I_{24}^{stoc}\right) - \frac{1}{4p}\left(I_{25}^{stoc} - I_{26}^{stoc}\right)\right\}\right] \tag{5 46}$$

where,

$$I_1^{stoc} = \frac{1}{p+q-r+s}\left\{1 - \cos(p+q-r+s)\pi\right\}, \qquad p+q-r+s \neq 0$$

$$= 0, \qquad\qquad\qquad\qquad\qquad\qquad\qquad p+q-r+s = 0 \tag{5 46i}$$

$$I_2^{stoc} = \frac{1}{p+q-r-s}\left\{1 - \cos(p+q-r-s)\pi\right\}, \qquad p+q-r-s \neq 0$$

$$= 0, \qquad\qquad\qquad\qquad\qquad\qquad\qquad p+q-r-s = 0 \tag{5 46ii}$$

$$I_3^{stoc} = \frac{1}{p+q+r+s}\left\{1 - \cos(p+q+r+s)\pi\right\} \tag{5 46iii}$$

$$I_4^{stoc} = \frac{1}{p+q+r-s}\left\{1 - cos(p+q+r-s)\pi\right\}, \qquad p+q+r-s \neq 0$$

$$= 0, \qquad\qquad\qquad p+q+r-s = 0 \qquad\qquad \text{(5 46iv)}$$

$$I_5^{stoc} = \frac{1}{p-q-r+s}\left\{1 - cos(p-q-r+s)\pi\right\}, \qquad p-q-r+s \neq 0$$

$$= 0, \qquad\qquad\qquad p-q-r+s = 0 \qquad\qquad \text{(5 46v)}$$

$$I_6^{stoc} = \frac{1}{p-q-r-s}\left\{1 - cos(p-q-r-s)\pi\right\}, \qquad p-q-r-s \neq 0$$

$$= 0, \qquad\qquad\qquad p-q-r-s = 0 \qquad\qquad \text{(5 46vi)}$$

$$I_7^{stoc} = \frac{1}{p-q+r+s}\left\{1 - cos(p-q+r+s)\pi\right\}, \qquad p-q+r+s \neq 0$$

$$= 0, \qquad\qquad\qquad p-q+r+s = 0 \qquad\qquad \text{(5 46vii)}$$

$$I_8^{stoc} = \frac{1}{p-q+r-s}\left\{1 - cos(p-q+r-s)\pi\right\}, \qquad p-q+r-s \neq 0$$

$$= 0, \qquad\qquad\qquad p-q+r-s = 0 \qquad\qquad \text{(5 46viii)}$$

$$I_9^{stoc} = \frac{1}{(p+q+r-s)^2}\left\{cos(p+q+r-s)\pi - 1\right\}, \qquad p+q+r-s \neq 0$$

$$= \frac{\pi^2}{2}, \qquad\qquad\qquad p+q+r-s = 0 \qquad\qquad \text{(5 46ix)}$$

$$I_{10}^{stoc} = \frac{1}{(p+q+r+s)^2}\left\{cos(p+q+r+s)\pi - 1\right\} \qquad\qquad\qquad\qquad \text{(5 46x)}$$

$$I_{11}^{stoc} = \frac{1}{(p+q-r-s)^2}\left\{cos(p+q-r-s)\pi - 1\right\}, \qquad p+q-r-s \neq 0$$

$$= \frac{\pi^2}{2}, \qquad\qquad\qquad p+q-r-s = 0 \qquad\qquad \text{(5 46xi)}$$

168

$$I_{sinc}^{12} = \frac{1}{(p+q-r+s)^2}\{\cos(p+q-r+s)\pi - 1\}, \qquad p+q-r+s \neq 0$$

$$= \frac{\pi^2}{2}, \qquad\qquad\qquad\qquad\qquad p+q-r+s = 0 \qquad (5.46\ \text{xii})$$

$$I_{sinc}^{13} = \frac{1}{(p-q+r-s)^2}\{\cos(p-q+r-s)\pi - 1\}, \qquad p-q+r-s \neq 0$$

$$= \frac{\pi^2}{2}, \qquad\qquad\qquad\qquad\qquad p-q+r-s = 0 \qquad (5.46\ \text{xiii})$$

$$I_{sinc}^{14} = \frac{1}{(p-q+r+s)^2}\{\cos(p-q+r+s)\pi - 1\}, \qquad p-q+r+s \neq 0$$

$$= \frac{\pi^2}{2}, \qquad\qquad\qquad\qquad\qquad p-q+r+s = 0 \qquad (5.46\ \text{xiv})$$

$$I_{sinc}^{15} = \frac{1}{(p-q-r-s)^2}\{\cos(p-q-r-s)\pi - 1\}, \qquad p-q-r-s \neq 0$$

$$= \frac{\pi^2}{2}, \qquad\qquad\qquad\qquad\qquad p-q-r-s = 0 \qquad (5.46\ \text{xv})$$

$$I_{sinc}^{16} = \frac{1}{(p-q-r+s)^2}\{\cos(p-q-r+s)\pi - 1\}, \qquad p-q-r+s \neq 0$$

$$= \frac{\pi^2}{2}, \qquad\qquad\qquad\qquad\qquad p-q-r+s = 0 \qquad (5.46\ \text{xvi})$$

$$I_{sinc}^{17} = \frac{1}{2p-r+s}\{1 - \cos(2p-r+s)\pi\}, \qquad 2p-r+s \neq 0$$

$$= 0, \qquad\qquad\qquad\qquad\qquad\quad 2p-r+s = 0 \qquad (5.46\ \text{xvii})$$

$$I_{sinc}^{18} = \frac{1}{2p-r-s}\{1 - \cos(2p-r-s)\pi\}, \qquad 2p-r-s \neq 0$$

$$= 0, \qquad\qquad\qquad\qquad\qquad\quad 2p-r-s = 0 \qquad (5.46\ \text{xviii})$$

$$I_{19}^{stoc} = \frac{1}{2p+r+s}\left\{1 - cos(2p+r+s)\pi\right\}$$

(5 46xɪx)

$$I_{20}^{stoc} = \frac{1}{2p+r-s}\left\{1 - cos(2p+r-s)\pi\right\}, \qquad 2p+r-s \neq 0$$

$$= 0, \qquad 2p+r-s = 0$$

(5 46xx)

$$I_{21}^{stoc} = \frac{1}{(2p+r-s)^2}\left\{cos(2p+r-s)\pi - 1\right\}, \qquad 2p+r-s \neq 0$$

$$= \frac{\pi^2}{2}, \qquad 2p+r-s = 0$$

(5 46xxɪ)

$$I_{22}^{stoc} = \frac{1}{(2p+r+s)^2}\left\{cos(2p+r+s)\pi - 1\right\}$$

(5 46xxɪɪ)

$$I_{23}^{stoc} = \frac{1}{(2p-r-s)^2}\left\{cos(2p-r-s)\pi - 1\right\}, \qquad 2p-r-s \neq 0$$

$$= \frac{\pi^2}{2}, \qquad 2p-r-s = 0$$

(5 46xxɪɪɪ)

$$I_{24}^{stoc} = \frac{1}{(2p-r+s)^2}\left\{cos(2p-r+s)\pi - 1\right\}, \qquad 2p-r+s \neq 0$$

$$= \frac{\pi^2}{2}, \qquad 2p-r+s = 0$$

(5 46xxɪv)

$$I_{25}^{stoc} = \frac{1}{(r-s)^2}\left\{cos(r-s)\pi - 1\right\}, \qquad r-s \neq 0$$

$$= \frac{\pi^2}{2}, \qquad r-s = 0$$

(5 46xxv)

$$I_{26}^{stoc} = \frac{1}{(r+s)^2}\left\{cos(r+s)\pi - 1\right\}$$

(5 46xxvɪ)

Eqn (5 46) gives the total power dissipated in the plasma sheath by the stochastic heating mechanism It is evident from the equation that it is impossible to separate the amount of heating corresponding to a particular harmonic component of the RF current In our model we will consider only one harmonic component of RF current in operation at a time to calculate the stochastic heating corresponding to that harmonic frequency This is a good approximation, because, we will show in a later part of this chapter (see section 5 7) that the difference between the total stochastic power determined by adding all the stochastic power components using our modelled equation when only one RF harmonic current is consdered, and that determined using the Eqn (5 46) is very small

Considering only the k-th harmonic component of RF current and using a subcript k in Eqn (5 9) we have

$$J_k(t) = -\bar{J}_k \, sin(k\omega t)$$ (5 47)

Similarly, removing the Σ sign from Eqns (5 38), (5 40) and (5 45), and replacing p, q, r and s by k, we have

$$n_s u_s = n_0 \bar{u}_k \, sin(k\varphi) = n_0 u_0$$ (5 48)

$$u_s - u_0 = -\frac{1}{e^2 \omega^2 T_e \varepsilon_0 \pi n_0^2} \frac{\bar{J}_k^3}{k} \left[\frac{3}{16k^2} \{cos(k\varphi) - cos(3k\varphi)\} \right.$$

$$\left. -\frac{\varphi}{8k} \{sin(3k\varphi) - sin(k\varphi)\} - \frac{\varphi}{2k} sin(k\varphi) \right] = F_1(\varphi)$$ (5 49)

$$\bar{P}_{stoc\,k} = \frac{4m}{\pi e n_0} \Gamma_s \int_0^\pi F_1(\varphi)\bar{J}_k \, sin(k\varphi)d\varphi,$$ (5 50)

where $\bar{P}_{stoc\,k}$ is the average stochastic power for a single sheath corresponding to the k-th harmonic component of RF current Inserting Eqn (5 49) in Eqn (5 50) and performing the integration we have

$$\bar{P}_{stoc\,k} = \frac{3m\bar{J}_k^4}{8k^2 e^3 \omega^2 T_e \varepsilon_0 n_0^3} \Gamma_s$$ (5 51)

where Γ_s = the incident electron flux on the sheath, is given by Eqn (5 43)

The sheath conductance per unit area is,

$$G_k = \frac{1}{2} \frac{\bar{J}_k^2}{\bar{P}_{stoc\,k}}$$ (5 52)

Equating (5 51) and (5 52), we obtain

$$G_k = \frac{4k^2}{3J_k^2}\frac{e^3\omega^2 T_e \varepsilon_0 n_0^3}{m\Gamma_s}$$

(5 53)

5 3 2 Bulk Plasma Impedance

In the calculation of the bulk plasma impedance the following assumptions were made

a) The plasma outside the two sheaths can be represented as a solid cylinder of length d, with a linearly varying cross-sectional radius from plate A to plate B (Figure 5 2) [161]

b) The plasma density n_0 is inversly proportional to the cross sectional area of the plasma This is a good approximation if we assume that the RF current is constant at any distance from either of the plates, because, the current density becomes inversely proportional to the cross-sectional area and the plasma density increases almost linearly with the current density [72]
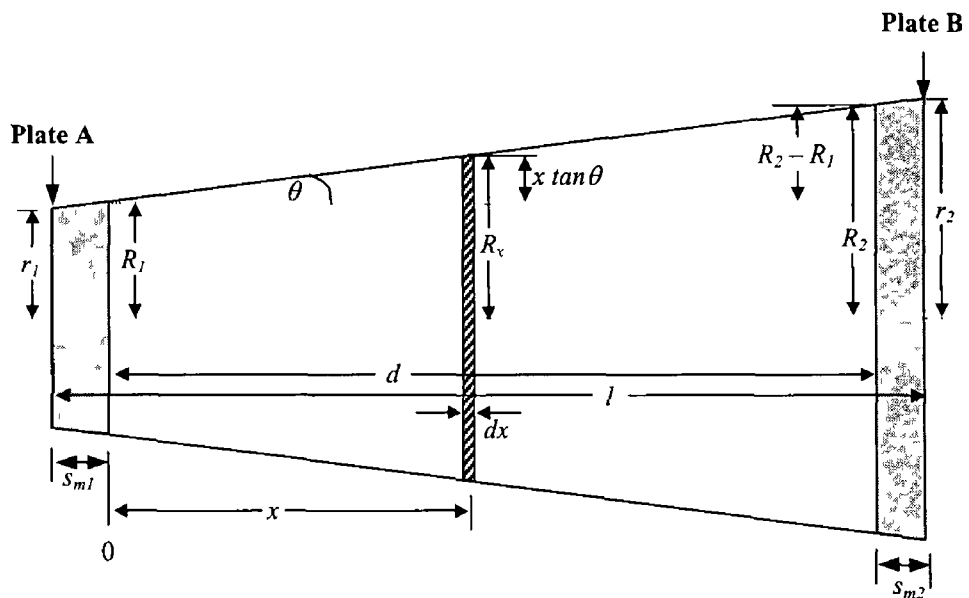
Figure 5 2 The schematic diagram of the plasma

The k-th harmonic impedance (Ohm) of a bulk plasma slab of thickness dx and cross-sectional area A_x, at a distance x from the ion sheath edge of plate A can be written as [62]

$$dZ_k = \frac{dx}{jk\omega\varepsilon_{px}A_x}$$ (5 54)

where,

$$\varepsilon_{px} = \varepsilon_0\left[1 - \frac{\omega_{pe\,x}^2}{k\omega(k\omega - jv_m)}\right]$$ (5 55)

In this case, the electron plasma frequency,

$$\omega_{pe\,x} = \left(\frac{e^2 n_{0x}}{\varepsilon_0 m}\right)^{\frac{1}{2}}$$ (5 56)

and v_m = electron-neutral collision frequency Here n_{0x} is the plasma density at a position x which is also equal to the electron density at that position From Fig 5 2,

$$A_x = \pi R_x^2 = \pi(R_1 + x\tan\theta)^2$$ (5 57)

and,

$$\tan\theta = \frac{R_2 - R_1}{d} = \frac{r_2 - r_1}{l}$$ (5 58)

Here, r_1 and r_2 are the radii of the plates A and B, respectively R_1 and R_2 are the radii of the plasma cylinder at the two ion sheath edges From Fig 5 2 we obtain

$$R_1 = r_1 + s_{m1}\tan\theta$$ (5 59)

$$R_2 = r_1 + (l - s_{m2})\tan\theta$$ (5 60)

The relation between the effective bulk plasma length, d and the separation between the two plates, l can be found as,

$$d = l - s_{m1} - s_{m2}$$ (5 61)

where, s_{m1} and s_{m2} are the ion sheath thicknesses at plate A and B respectively Assuming that the plasma density is inversely proportional to the cross sectional area of the plasma cylinder we have

$$n_{01}A_1 = n_{0x}A_x = n_{02}A_2$$ (5 62)

We have used subscripts 1, x and 2 for the positions at the ion sheath edge of plate A, at a distance x from the ion sheath edge of plate A and at the ion sheath edge of plate B, respectively Inserting Eqns (5 56) and (5 62) in Eqn (5 55) we obtain

$$\varepsilon_{px} = \varepsilon_0\left[1 - \frac{e^2 A_1 n_{01}}{k\omega\varepsilon_0 m(k\omega - jv_m)A_x}\right]$$ (5 63)

Using Eqns (5 54) and (5 63) and integrating from $x = 0$ to $x = d$ we have

$$Z_k = \int_0^d \frac{dx}{jk\omega\varepsilon_0\pi\left[(R_1 + x\tan\theta)^2 - \dfrac{e^2 R_1^2 n_{01}}{k\omega\varepsilon_0 m(k\omega - jv_m)}\right]}$$

(5 64)

Substituting $z = R_1 + x\tan\theta$ we have from Eqn (5 64)

$$Z_k = \frac{\cot\theta}{jk\omega\varepsilon_0\pi}\int_{R_1}^{R_2}\frac{dz}{[z^2 - a^2]}$$

$$= \frac{\cot\theta}{jk\omega\varepsilon_0\pi}\frac{1}{2a}\log_e\left[\frac{(R_2 - a)(R_1 + a)}{(R_2 + a)(R_1 - a)}\right]$$

$$= \frac{l}{(r_2 - r_1)jk\omega\varepsilon_0\pi}\frac{1}{2a}\log_e\left[\frac{(R_2 - a)(R_1 + a)}{(R_2 + a)(R_1 - a)}\right]$$

(5 65)

Here,

$$a = eR_1\sqrt{\frac{n_{01}}{k\omega\varepsilon_0 m(k\omega - jv_m)}}$$

$$= eR_1\sqrt{\frac{n_{01}}{k\omega\varepsilon_0 m\sqrt{k^2\omega^2 + v_m^2}}e^{j\phi}}, \qquad \phi = \tan^{-1}\left(\frac{v_m}{k\omega}\right)$$

$$= eR_1\left(\frac{n_{01}}{k\omega\varepsilon_0 m}\right)^{\frac{1}{2}}\left(k^2\omega^2 + v_m^2\right)^{-\frac{1}{4}}e^{j\frac{\phi}{2}}$$

$$= eR_1\left(\frac{n_{01}}{k\omega\varepsilon_0 m}\right)^{\frac{1}{2}}\left(k^2\omega^2 + v_m^2\right)^{-\frac{1}{4}}[\cos(\phi/2) + j\sin(\phi/2)]$$

$$= D_1 + jD_2$$

(5 66)

where,

$$D_1 = eR_1\left(\frac{n_{01}}{k\omega\varepsilon_0 m}\right)^{\frac{1}{2}}\left(k^2\omega^2 + v_m^2\right)^{-\frac{1}{4}}\cos(\phi/2)$$

(5 66i)

$$D_2 = eR_1\left(\frac{n_{01}}{k\omega\varepsilon_0 m}\right)^{\frac{1}{2}}\left(k^2\omega^2 + v_m^2\right)^{-\frac{1}{4}}\sin(\phi/2)$$

(5 66ii)

Inserting Eqn (5 66) into Eqn (5 65) we have

$$Z_k = \frac{l}{(r_2 - r_1)jk\omega\varepsilon_0\pi} \frac{1}{2a} log_e \left[\frac{(R_2 - D_1 - jD_2)(R_1 + D_1 + jD_2)}{(R_2 + D_1 + jD_2)(R_1 - D_1 - jD_2)} \right]$$

$$= \frac{l}{(r_2 - r_1)jk\omega\varepsilon_0\pi} \frac{1}{2a}$$

$$log_e \left[\frac{\sqrt{\{(R_2 - D_1)(R_1 + D_1) + D_2^2\}^2 + \{D_2(R_2 - R_1 - 2D_1)\}^2}}{\sqrt{\{(R_2 + D_1)(R_1 - D_1) + D_2^2\}^2 + \{D_2(R_1 - R_2 - 2D_1)\}^2}} e^{j(\alpha_1 - \alpha_2)} \right]$$

$$= \frac{l}{(r_2 - r_1)jk\omega\varepsilon_0\pi} \frac{1}{2a} [D_3 + jD_4] \tag{5 67}$$

where, $D_3 = \frac{1}{2} log_e \left[\frac{\{(R_2 - D_1)(R_1 + D_1) + D_2^2\}^2 + \{D_2(R_2 - R_1 - 2D_1)\}^2}{\{(R_2 + D_1)(R_1 - D_1) + D_2^2\}^2 + \{D_2(R_1 - R_2 - 2D_1)\}^2} \right]$ \hfill (5 67i)

$$D_4 = \alpha_1 - \alpha_2 \tag{5 67n}$$

$$\alpha_1 = tan^{-1} \frac{D_2(R_2 - R_1 - 2D_1)}{(R_2 - D_1)(R_1 + D_1) + D_2^2} \tag{5 67111}$$

$$\alpha_2 = tan^{-1} \frac{D_2(R_1 - R_2 - 2D_1)}{(R_2 + D_1)(R_1 - D_1) + D_2^2} \tag{5 67iv}$$

Again, inserting Eqn (5 66) into Eqn (5 67) we obtain

$$Z_k = \frac{l}{(r_2 - r_1)jk\omega\varepsilon_0\pi} \frac{1}{2(D_1 + jD_2)} [D_3 + jD_4]$$

$$= \frac{l}{2(r_2 - r_1)k\omega\varepsilon_0\pi} \frac{\sqrt{D_3^2 + D_4^2}}{\sqrt{D_1^2 + D_2^2}} e^{j\left(\alpha_3 - \frac{\phi}{2} - \frac{\pi}{2}\right)}$$

$$= Z_{real} + jZ_{imag} \tag{5 68}$$

where,

$$Z_{real} = \frac{l}{2(r_2 - r_1)k\omega\varepsilon_0\pi} \frac{\sqrt{D_3^2 + D_4^2}}{\sqrt{D_1^2 + D_2^2}} cos\left(\alpha_3 - \frac{\phi}{2} - \frac{\pi}{2}\right) \tag{5 68i}$$

$$Z_{imag} = \frac{l}{2(r_2 - r_1)k\omega\varepsilon_0\pi} \frac{\sqrt{D_3^2 + D_4^2}}{\sqrt{D_1^2 + D_2^2}} sin\left(\alpha_3 - \frac{\phi}{2} - \frac{\pi}{2}\right) \tag{5 68ii}$$

$$\alpha_3 = \tan^{-1} \frac{D_4}{D_3}$$

(5 68iii)

If the value of D_3 becomes negative, the value of α_3 in Eqn (5 68iii) should be chosen such that $\pi/2 < \alpha_3 < 3\pi/2$ In Eqn (5 68) Z_{real} and Z_{imag} are the real and imaginary parts of the bulk impedance, respectively

5 3 3 Overall RF impedance between the two electrodes

To determine the overall impedance between the two electrodes we need to include three components i) the sheath impedance at plate A, ii) the bulk plasma impedance and iii) the sheath impedance at plate B For an asymmetrically driven, parallel plate RF discharge (non-equal area plates), there are two RF sheaths in series – one on plate A and the other on plate B The sheath equations for plate B will be identical to those for plate A, except that the harmonics of the current density considered for calculation at plate A will be multiplied by a factor $b = \frac{A_A}{A_B}$, where A_A and A_B are the cross-sectional areas of plate A and B, respectively The sheath voltage on plate B will be similar to that of plate A but shifted by a phase angle π We let $V_{Ak}(\omega t)$ and $V_{Bk}(\omega t)$ be the k-th harmonic voltages on plates A and B, respectively, with respect to the plasma, then from Eqn (5 29) we can write,

$$V_{Ak}(\omega t) = \overline{V}_{Ak} \cos(k\omega t)$$

(5 69)

$$V_{Bk}(\omega t) = \overline{V}_{Bk} \cos[k(\omega t + \pi)]$$
$$= (-1)^k \overline{V}_{Bk} \cos(k\omega t)$$

(5 70)

where, $\overline{V}_{Ak}$ and $\overline{V}_{Bk}$ are the k-th harmonic RF voltage coefficients for the sheath at plates A and B, respectively, given by Eqn (5 29ii) Since the phase direction of $V_{Bk}(\omega t)$ is opposite to $V_{Ak}(\omega t)$ and the sheath capacitances are directly related to the sheath voltages, it can be seen from Eqns (5 31), (5 69) and (5 70) that the equation for the equivalent sheath capacitance (in *Farad*) is,

$$C_{es\,k} = \frac{\overline{I}_k}{k\omega \left(\overline{V}_{Ak} - (-1)^k \overline{V}_{Bk} \right)}$$

(5 71)

where, $\overline{I}_k$ is the total RF current (in *Amperes*) The equivalent sheath resistance (in *Ohms*) can be written as

$$r_{esk} = \frac{1}{A_A G_{Ak}} + \frac{1}{A_B G_{Bk}} \tag{5 72}$$

where, G_{Ak} and G_{Bk} are the sheath conductances (mho/m^2) of Plates A and B, respectively Here G_{Ak} and G_{Bk} are given by Eqn (5 53) except that the current density, $\bar{J}_k$, should be replaced by $\bar{J}_{kA}$ and $\bar{J}_{kB}$, respectively From Eqns (5 53) and (5 72) and using $\bar{J}_{kB} = b \bar{J}_{kA}$ we obtain

$$r_{esk} = \frac{1}{A_A} \frac{3\bar{J}_{kA}^2 m \Gamma_s}{4k^2 e^3 \omega^2 T_e \varepsilon_0 n_0^3} + \frac{1}{A_B} \frac{3\bar{J}_{kA}^2 m \Gamma_s b^2}{4k^2 e^3 \omega^2 T_e \varepsilon_0 n_0^3}$$

$$= \frac{3\bar{J}_{kA}^2 m \Gamma_s}{4k^2 e^3 \omega^2 T_e \varepsilon_0 n_0^3 A_A} \left(1 + b^3\right) \tag{5 73}$$

where, $\bar{J}_{kA}$ is the k-th harmonic current density at plate A Now, from Eqns (5 71), (5 73) and (5 68), and using $\bar{I}_k = A_A \bar{J}_{kA}$ we obtain the overall k-th harmonic impedance (in *Ohms*) between the two plates

$$Z_{ok} = \left[Z_{real} + \frac{3\bar{I}_k^2 m \Gamma_s}{4k^2 e^3 \omega^2 T_e \varepsilon_0 n_0^3 A_A^3} \left(1 + b^3\right) \right] + j\left[Z_{imag} - \frac{\left\{\bar{V}_{Ak} - (-1)^k \bar{V}_{Bk}\right\}}{\bar{I}_k} \right] \tag{5 74}$$

For a symmetrical discharge, $b = 1$ and $\bar{V}_{Ak} = \bar{V}_{Bk}$ Thus, replacing $\bar{V}_{Ak}$ and $\bar{V}_{Bk}$ by $\bar{V}_k$, and A_A by A we can re-write Eqn (5 74) as

$$Z_{ok} = \left[Z_{real} + \frac{3\bar{I}_k^2 m \Gamma_s}{2k^2 e^3 \omega^2 T_e \varepsilon_0 n_0^3 A^3} \right] + j\left[Z_{imag} - \left\{1 - (-1)^k\right\} \frac{\bar{V}_k}{\bar{I}_k} \right] \tag{5 75}$$

From Eqn (5 75) it is evident that there is no sheath capacitance effect on the overall impedance for even harmonic frequencies

5 3 4 The overall RF voltage

The overall k-th harmonic RF voltage at the powered electrode with respect to the ground can be obtained as,

$$\bar{V}_{RFk} = \bar{I}_k Z_{ok} \tag{5 76}$$

where, $\bar{I}_k$ is the k-th harmonic RF current and $Z_{o\,k}$ is the overall RF impedance of the same harmonic frequency, given by Eqns (5 74) and (5 75)

It is important to note here that in the Lieberman model there is no even harmonic overall voltage and hence no even harmonic overall impedance This was an obvious problem with this model, as our measurements (see Chapter 3) have always observed even harmonic components But we have found that the even harmonic components of RF voltage and impedance never become zero in the present model This is because the sheath resistance associated with the stochastic heating in both the sheaths and the bulk plasma impedance are always present, even for a symmetrical discharge From Eqn (5 75) we see that in a symmetrical discharge only the sheath capacitance effect is diminished in overall voltage and impedance

5 4 Experiments

To verify the validity of the present model and make some comparisons with the Lieberman model [30] we carried out a number of experiments A short description of the experimental equipment and the experimental procedure is given below

5 4 1 Experimental equipment

The equipment used for the experiment was the same as described in section 3 2 except that a replaceable hollow circular shaped anodized aluminium plate was placed above the powered electrode (Fig 5 3) This anodized plate provided a variable effective area for the powered electrode The word 'effective' is used here because the anodized plate acts as an insulator and thus, only the exposed part of the powered electrode comes in contact with the plasma

5 4 2 Experimental procedure

Before the main experiments the plasma chamber was cleaned as usual by running the system for an hour in RIE mode with Ar gas at 8 6 sccm flow rate while the RF power and the chamber pressure were maintained at 200 Watts and 72 mTorr,
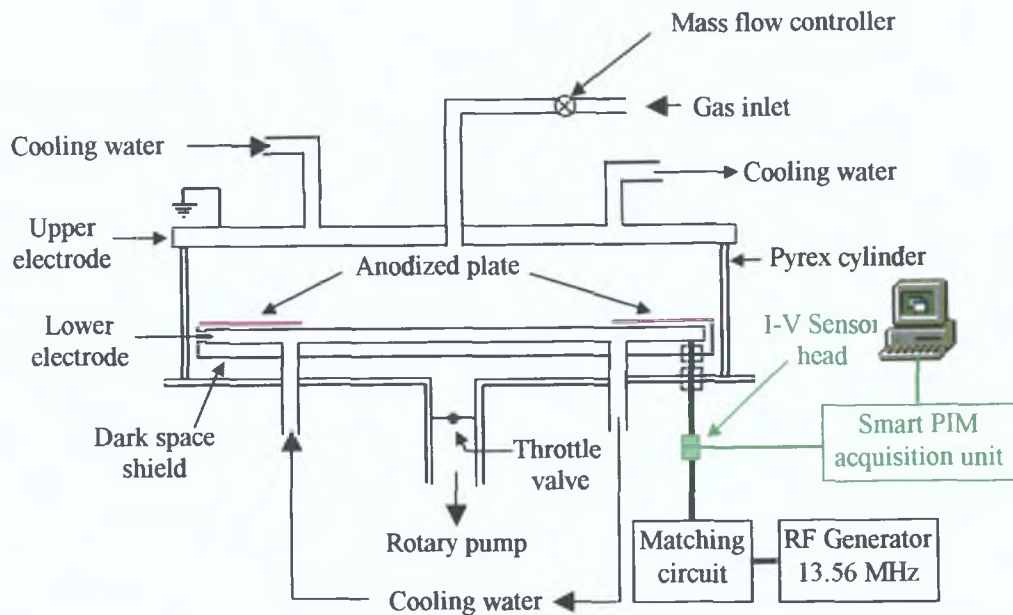
Figure 5.3 *Schematic diagram of the capacitively driven, parallel plate, RIE system with the Plasma Impedance Monitoring system. The system is now in "variable effective area" mode.*

respectively. Then the system was run in RIE mode with Ar gas at 180 Watts RF power, 30 mTorr chamber pressure and 4.35 sccm gas flow rate. The experiment was repeated for the same operating condition but different effective diameters of the powered electrode. The harmonic components of RF current, voltage and impedance were recorded up to the fifth harmonic of the fundamental frequency for each set of experiments.

5.5 Comparison of the Present Model with the Lieberman Model

In the Lieberman model [30] the RF source current was assumed to be purely sinusoidal containing the fundamental frequency given by

$$J_{RF}(t) = -\bar{J}_1 \sin(\omega t) \tag{5.77}$$

The Eqn. (5.77) can also be obtained from Eqn. (5.9) by simply removing the summation sign and replacing p by 1 where the subscript 1 is used to indicate the fundamental component of RF current. That means that the sheath equations for the Lieberman model can easily be obtained from the present model by removing the summation signs from the respective equations and replacing p, q, r and s by 1.

179

In reality the RF source current always contains harmonic components. The magnitudes of these harmonics depends upon the operating condition of plasma system, i.e., RF power, chamber pressure, type of plasma used, gas flow rate, chamber geometry etc. But the Lieberman model excludes all the harmonic components except the fundamental. As a result the effect of the harmonic currents were not included in that model. In the following subsections we contrast and compare a number of important sheath parameters obtained from the present model and the Lieberman model. The Lieberman equations obtained here are the same as the equations described in his publication [30]. In comparision we calculate each of the sheath parameters using both models and plotted these on the same graph so that the difference between the values obtained from the two models can be clearly visualized. We also calculate the percentage difference in the sheath parameters determined by the two models as

$$\%Diff = \frac{Y_L - Y_P}{Y_P} \times 100 \tag{5.78}$$

where, Y_L and Y_P indicate a particular sheath parameter determined by the Lieberman and the present model, resepectively. The sheath formed near the powered electrode is considered for comparision. We use the RF currents given by Table 5.1, recorded in a particular experiment described in section 5.4.2, as parameters for the calculations. We assume that the magnitudes of the higher harmonics (beyond 5th) of RF current were very small and can be neglected as they were beyond the scope of our measurements. Only the fundamental component of RF current given in Table 5.1 was used while the calculation was performed for the Lieberman model. Since there was no scope to experimentally measure some characteristics of the plasma, i.e., the plasma density n_0, electron temperature T_e, and the electron-neutral-atom collision frequency v_m (as there was no facility for probe measurement in our plasma system), typical values of these parameters were used in the calculations [62]. The assumed values of n_0, T_e and v_m are shown in Table 5.2. These assumed parameters may not yield quantitatively exact results, but they will nonetheless allow for an analysis of trends of sheath parameters and comparision between the two models.

Table 5.1 *Harmonic components of RF current recorded in the experiment while the effective diameter of the powered electrode was set to 18 cm.*

I_1 (A)	I_2 (A)	I_3 (A)	I_4 (A)	I_5 (A)
9.9394	0.2011	0.1841	0.0491	0.0375

Table 5 2 *Typical values of plasma characteristics used for calculations*

n_0	T_e	v_m
1×10^{12} cm^{-3}	3 5 Volt	2×10^7 s^{-1}

5 5 1 The non-linear motion of the electron sheath

Putting $x=s(t)$ and $\varphi=\omega t$ in Eqn (5 21) we obtain the nonlinear motion of the electron sheath as

$$e\omega n_0 s(t) = \sum_{p=1}^{N} \frac{\bar{J}_p}{p} \left\{ 1 - cos(p\omega t) \right\}$$

$$- \frac{1}{e\omega^2 T_e \varepsilon_0 m n_0} \left[\sum_{p=1}^{N} \sum_{\substack{q=1 \\ q \neq p}}^{N} \sum_{r=1}^{N} \frac{\bar{J}_p \bar{J}_q \bar{J}_r}{p} F_1^{pqr} + \sum_{p=1}^{N} \sum_{\substack{q=1 \\ q=p}}^{N} \sum_{r=1}^{N} \frac{\bar{J}_p^2 \bar{J}_r}{p} F_2^{pqr} \right] \qquad (5\ 79)$$

where,

$$F_1^{pqr} = \frac{2p+q}{4p(p+q)^2} \left\{ \frac{1}{p+q-r} sin(p+q-r)\omega t - \frac{1}{p+q+r} sin(p+q+r)\omega t \right\}$$

$$- \frac{2p-q}{4p(p-q)^2} \left\{ \frac{1}{p-q-r} sin(p-q-r)\omega t - \frac{1}{p-q+r} sin(p-q+r)\omega t \right\}$$

$$+ \frac{1}{4(p+q)} \left\{ \frac{\omega t}{p+q+r} cos(p+q+r)\omega t - \frac{1}{(p+q+r)^2} sin(p+q+r)\omega t \right.$$

$$\left. - \frac{\omega t}{p+q-r} cos(p+q-r)\omega t + \frac{1}{(p+q-r)^2} sin(p+q-r)\omega t \right\}$$

$$- \frac{1}{4(p-q)} \left\{ \frac{\omega t}{(p-q+r)} cos(p-q+r)\omega t - \frac{1}{(p-q+r)^2} sin(p-q+r)\omega t \right.$$

$$\left. - \frac{\omega t}{p-q-r} cos(p-q-r)\omega t + \frac{1}{(p-q-r)^2} sin(p-q-r)\omega t \right\}$$

, when $p+q-r \neq 0$, $p-q+r \neq 0$ and $p-q-r \neq 0$ (5 79a)

181

$$F_1^{pqr} = \frac{2p+q}{4p(p+q)^2}\left\{\omega t - \frac{1}{2r}\sin(2r\omega t)\right\} - \frac{2p-q}{4p(p-q)^2}\left\{\frac{1}{2q}\sin(2q\omega t) - \frac{1}{2p}\sin(2p\omega t)\right\}$$

$$+ \frac{1}{4(p+q)}\left\{\frac{\omega t}{2r}\cos(2r\omega t) - \frac{1}{4r^2}\sin(2r\omega t)\right\} - \frac{1}{4(p-q)}\left\{\frac{\omega t}{2p}\cos(2p\omega t)\right.$$

$$\left. - \frac{1}{4p^2}\sin(2p\omega t) + \frac{\omega t}{2q}\cos(2q\omega t) - \frac{1}{4q^2}\sin(2q\omega t)\right\}$$

$$\text{, when } p+q-r = 0 \qquad (5\ 79\text{b})$$

$$F_1^{pqr} = \frac{2p+q}{4p(p+q)^2}\left\{\frac{1}{2p}\sin(2p\omega t) - \frac{1}{2q}\sin(2q\omega t)\right\} - \frac{2p-q}{4p(p-q)^2}\left\{\frac{1}{2r}\sin(2r\omega t) - \omega t\right\}$$

$$+ \frac{1}{4(p+q)}\left\{\frac{\omega t}{2q}\cos(2q\omega t) - \frac{1}{4q^2}\sin(2q\omega t) - \frac{\omega t}{2p}\cos(2p\omega t) + \frac{1}{4p^2}\sin(2p\omega t)\right\}$$

$$- \frac{1}{4(p-q)}\left\{\frac{\omega t}{2r}\cos(2r\omega t) - \frac{1}{4r^2}\sin(2r\omega t)\right\}$$

$$\text{, when } p-q+r = 0 \qquad (5\ 79\text{c})$$

$$F_1^{pqr} = \frac{2p+q}{4p(p+q)^2}\left\{\frac{1}{2q}\sin(2q\omega t) - \frac{1}{2p}\sin(2p\omega t)\right\} - \frac{2p-q}{4p(p-q)^2}\left\{\omega t - \frac{1}{2r}\sin(2r\omega t)\right\}$$

$$+ \frac{1}{4(p+q)}\left\{\frac{\omega t}{2p}\cos(2p\omega t) - \frac{1}{4p^2}\sin(2p\omega t) - \frac{\omega t}{2q}\cos(2q\omega t) + \frac{1}{4q^2}\sin(2q\omega t)\right\}$$

$$- \frac{1}{4(p-q)}\left\{\frac{\omega t}{2r}\cos(2r\omega t) - \frac{1}{4r^2}\sin(2r\omega t)\right\}$$

$$\text{, when } p-q-r = 0 \qquad (5\ 79\text{d})$$

and,

$$F_2^{pqr} = \frac{3}{16p^2}\left\{\frac{1}{2p-r}\sin(2p-r)\omega t - \frac{1}{2p+r}\sin(2p+r)\omega t\right\}$$

$$+ \frac{1}{8p}\left\{\frac{\omega t}{2p+r}\cos(2p+r)\omega t - \frac{1}{(2p+r)^2}\sin(2p+r)\omega t - \frac{\omega t}{(2p-r)}\cos(2p-r)\omega t\right.$$

$$\left. + \frac{1}{(2p-r)^2}\sin(2p-r)\omega t\right\} + \frac{1}{2p}\left\{\frac{\omega t}{r}\cos(r\omega t) - \frac{1}{r^2}\sin(r\omega t)\right\}$$

$$F_2^{pqr} = -\frac{7}{128p^3}\sin(4p\omega t) + \frac{\omega t}{32p^2}\cos(4p\omega t) - \frac{1}{8p^3}\sin(2p\omega t)$$

$$+ \frac{\omega t}{4p^2}\cos(2p\omega t) + \frac{3\omega t}{16p^2} \qquad\qquad \text{, when } 2p-r = 0 \qquad (5\ 79f)$$

Figures 5 4(a) and 5 4(b) show the calculations for the position of the electron sheath as measured from the powered electrode as a function of the phase angle ωt while Fig 5 4(c) shows the difference in the sheath position determined by the Lieberman model compared to that determined by the present model The position of the electron sheath (distance between the electron sheath and the powered electrode) can be calculated as

$$s_m\text{-}s(t) \qquad\qquad (5\ 80)$$

The sheath position $s(t)$ is given by Eqn (5 79) and the ion sheath thickness s_m can be obtained by putting $s(t) = s_m$ and $\omega t = \pi$ in Eqn (5 79)

The Lieberman equation for the distance between the electron sheath and the powered electrode is also same as Eqn (5 80) The sheath position $s(t)$ for the Lieberman model can be obtained from Eqn (5 79) by removing the Σ signs and replacing p, q and r by 1 as

$$e\omega n_0 s(t) = \bar{J}_1\{1 - \cos(\omega t)\} - \frac{\bar{J}_1^3}{e\omega^2 T_e \varepsilon_0 \pi n_0}\left[\frac{3}{16}\left\{\sin(\omega t) - \frac{1}{3}\sin(3\omega t)\right\}\right.$$

$$\left. + \frac{1}{8}\left\{\frac{\omega t}{3}\cos(3\omega t) - \frac{1}{9}\sin(3\omega t) - \omega t\cos(\omega t) + \sin(\omega t)\right\} + \frac{1}{2}\left\{\omega t\cos(\omega t) - \sin(\omega t)\right\}\right]$$

Or,

$$e\omega n_0 s(t) = \bar{J}_1\{1 - \cos(\omega t)\} + \frac{\bar{J}_1^3}{8e\omega^2 T_e \varepsilon_0 \pi n_0}\left[\frac{3}{2}\sin(\omega t) + \frac{11}{18}\sin(3\omega t)\right.$$

$$\left. - 3\omega t\cos(\omega t) - \frac{\omega t}{3}\cos(3\omega t)\right] \qquad (5\ 81)$$

and the corresponding ion sheath thickness s_m can be obtained by putting $s(t) = s_m$ and $\omega t = \pi$ in Eqn (5 81)

(a)

(b)
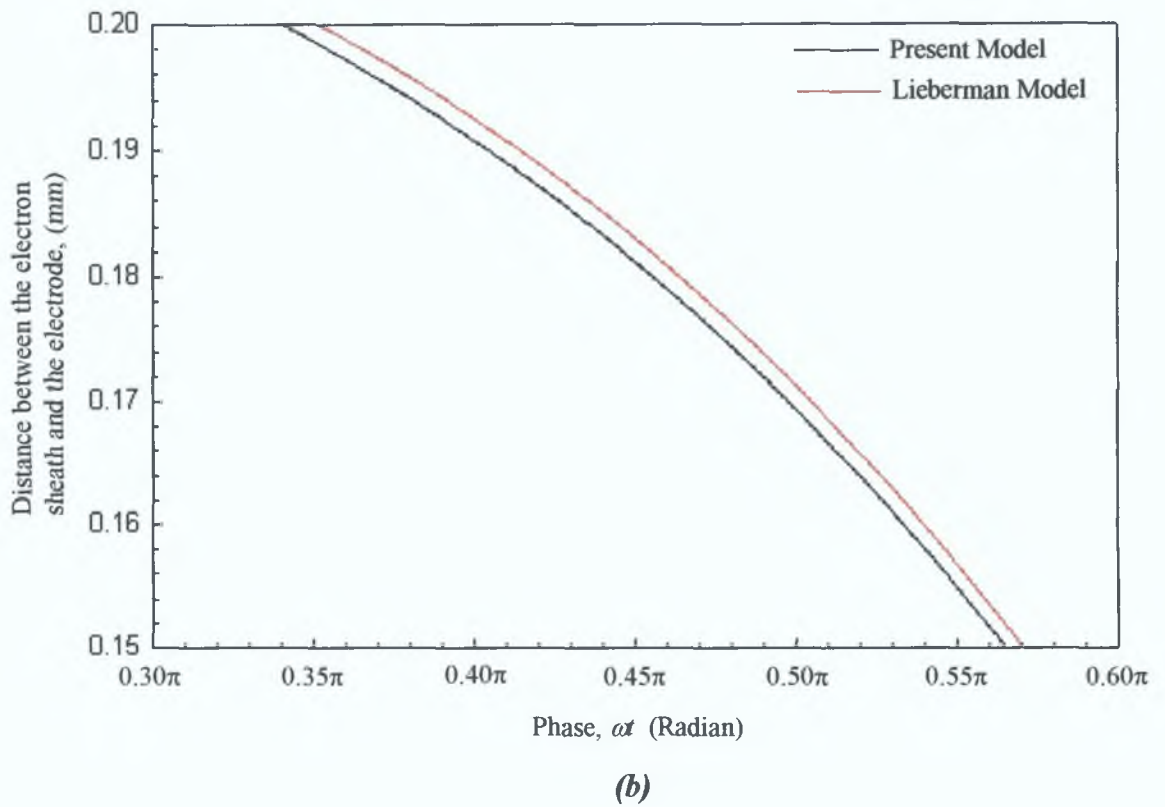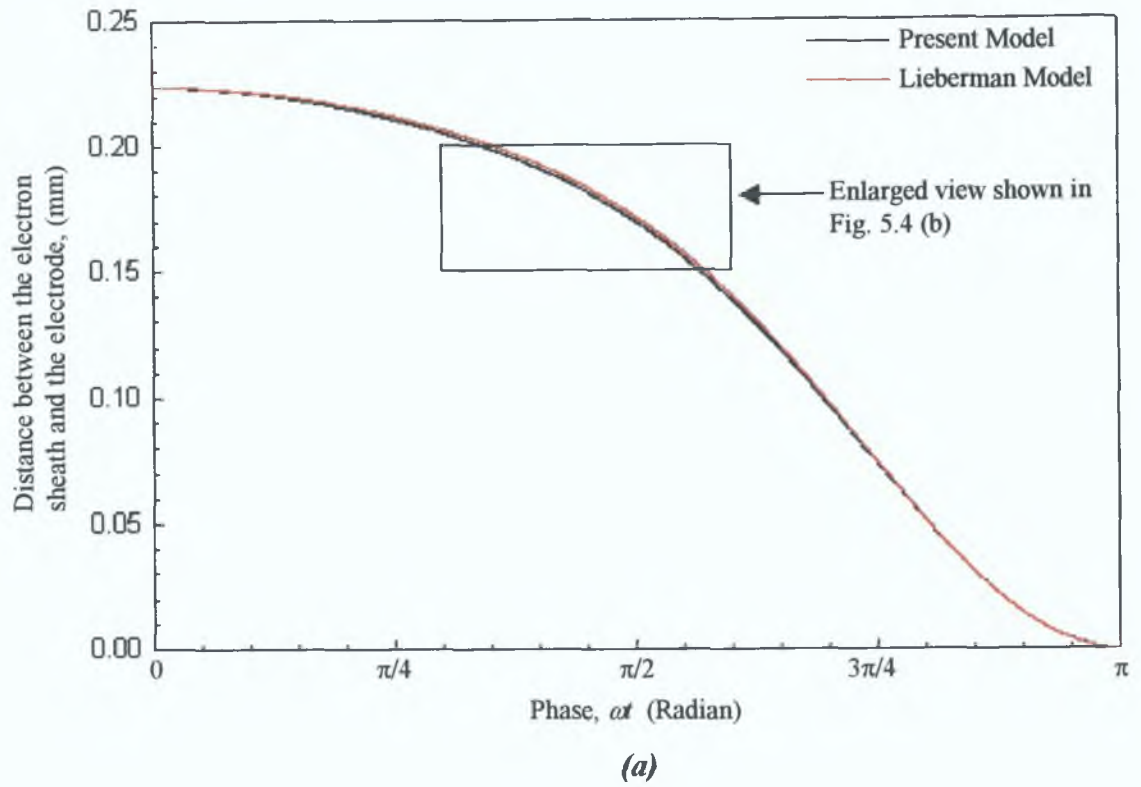
Figure 5.4 (a) *Position of the electron sheath measured from the powered electrode as a function of phase,* ω*t.* ***(b)*** *Enlarged view of the area enclosed by the rectangle shown in (a).*
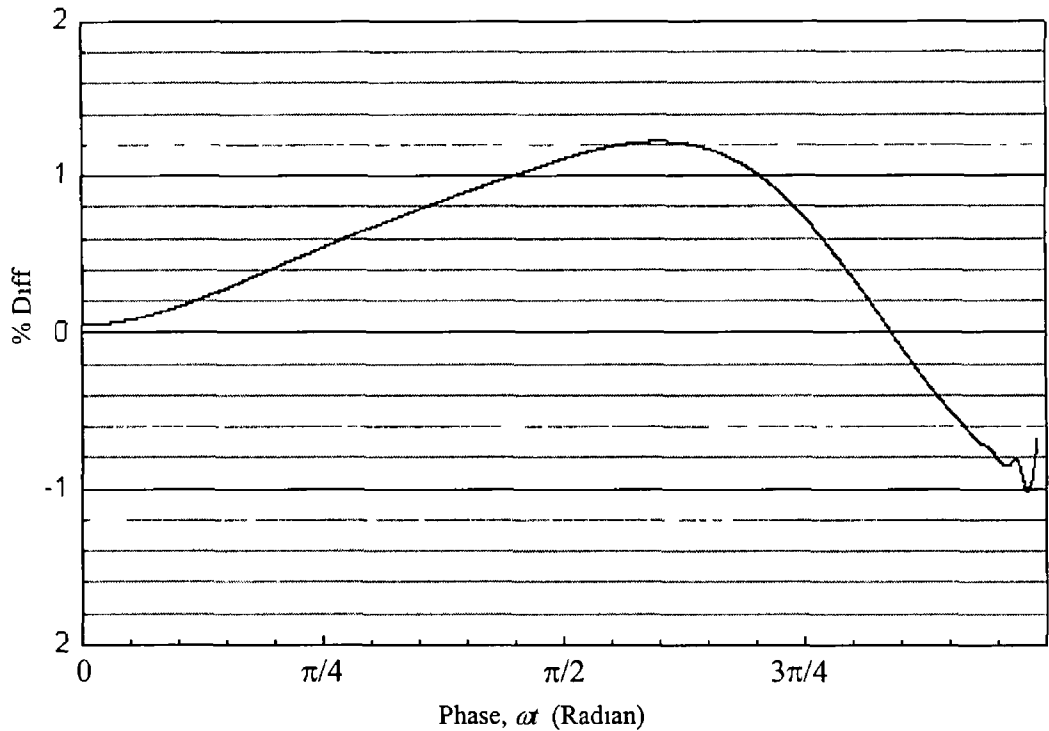
Figure 5 4(c) *Percentage difference in electron sheath positions determined by the two models*

We see from the Figs 5 4(a), 5 4(b) and 5 4(c) that the electron sheath starts moving (at ωt=0) from almost the same position for both the present and the Lieberman models That means that the ion sheath thickness is approximately same for both the models But starting from ωt=0 the difference between the electron sheath positions determined by the two models increases up to $\omega t \approx 0$ 6π radians while the electron sheath position is overestimated by the Lieberman model compared to that of the present model After $\omega t \approx 0$ 6π radians the difference decreases and at $\omega t \approx 0$ 84π radians it reaches to zero From $\omega t \approx 0$ 84π radians the difference again increases up to $\omega t \approx 0$ 98π radians while the electron sheath position is underestimated by the Lieberman model After $\omega t \approx 0$ 98π radians the difference again starts to decrease and both the models estimate the same value at ωt=π radians That means that up to $\omega t \approx 0$ 6π radians the electron sheath determined by the present model moves faster than that of the Lieberman model towards the electrode and after that it moves slower than that of the Lieberman model up to $\omega t \approx 0$ 98π radians At $\omega t \approx 0$ 84π radians the electron sheath positions determined by both the models become the same After $\omega t \approx 0$ 98π radians the

electron sheath of the present model moves again faster than that of the Lieberman model because the sheath positions determined by both the models must reach the electrode at $\omega t = \pi$

From Fig 5 4(c) it is evident that the maximum difference in determining the electron sheath position by the Lieberman model is ~1 2% Off course, this difference between the electron sheath positions determined by the two models arises from the non-presence and the presence of the harmonic currents in the two models However, it is interesting that the contribution from the harmonics have such a small influence on the sheath position

5 5 2 The time-average electric field within the sheath

We obtained the time-average electric field from Eqn (5 17) as

$$\overline{E}(x) = \sum_{p=1}^{N} \frac{\overline{J}_p}{p\omega\varepsilon_0\pi}\left[\frac{1}{p}sin(p\varphi) - \varphi cos(p\varphi)\right]$$
(5 82)

Figures 5 5(a) and 5 5(b) show the time-average electric field as a function of the position measured from the powered electrode while Fig 5 5(c) shows the difference in the electric field determined by the Lieberman model compared to that of the present harmonic model The electron sheath position as a function of φ is given by

$$s_m - x$$
(5 83)

where $x(\varphi)$ is given by Eqn (5 21) The ion sheath thickness s_m can be calculated as described in section 5 5 1 For a particular value of φ the time-average electric field and the corresponding position can be calculated using Eqns (5 82) and (5 83), respectively

The Lieberman equation for the time average electric field can be obtained from Eqn (5 82) by removing the summation sign and replacing p by 1 as

$$\overline{E}(x) = \frac{\overline{J}_1}{\omega\varepsilon_0\pi}\left[sin(\varphi) - \varphi cos(\varphi)\right]$$
(5 84)

The corresponding position can be calculated using equation (5 83), where $x(\varphi)$ is obtained from Eqn (5 21) (removing summation sign and replacing p, q and r by 1) as

186
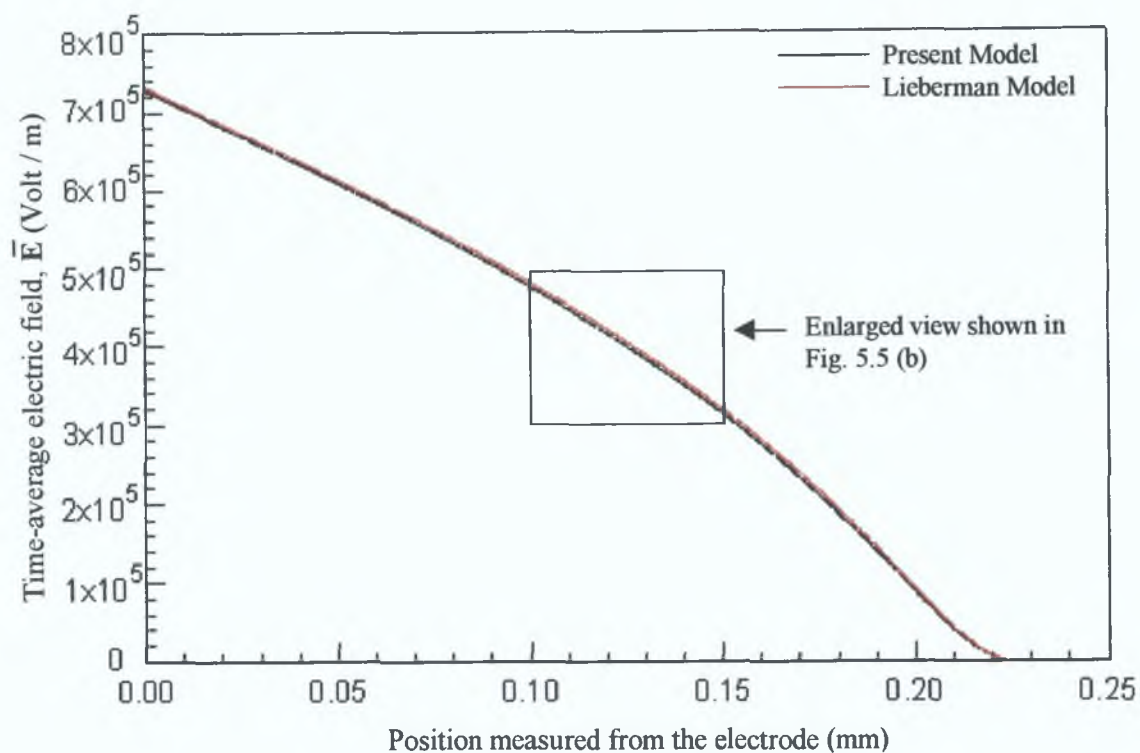
(a)
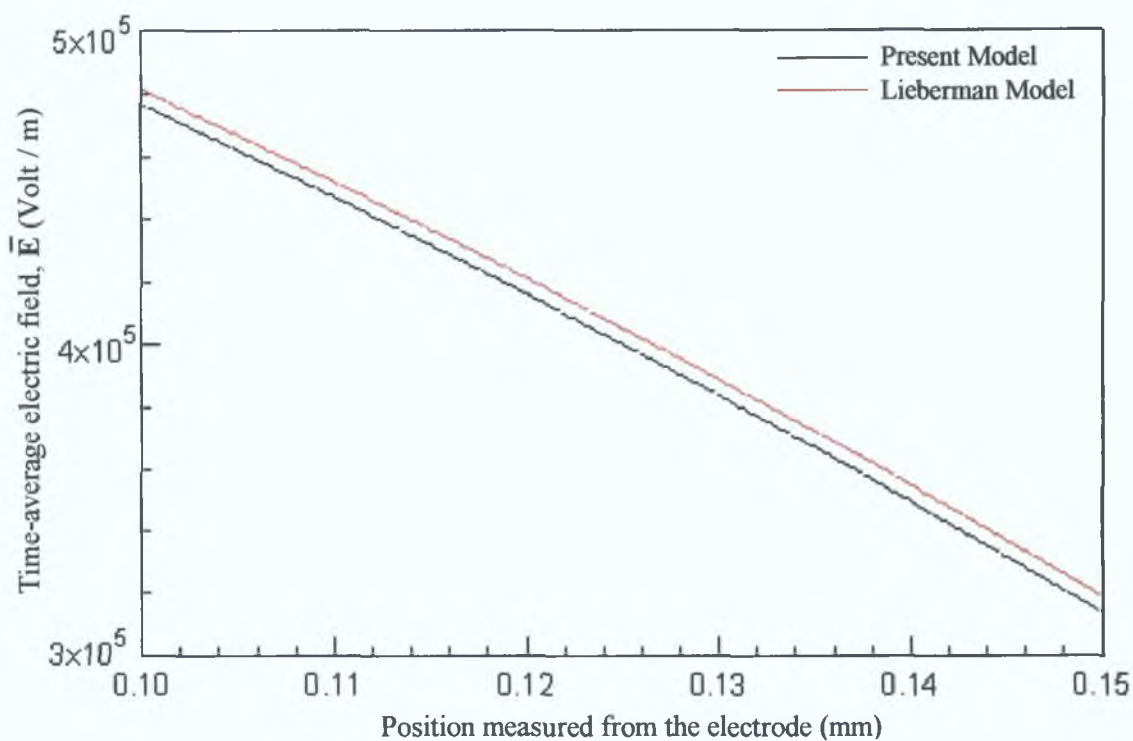
(b)

Figure 5.5 *(a) Time-average electric field as a function of position measured from the powered electrode. (b) Enlarged view of the area enclosed by a rectangle shown in (a).*
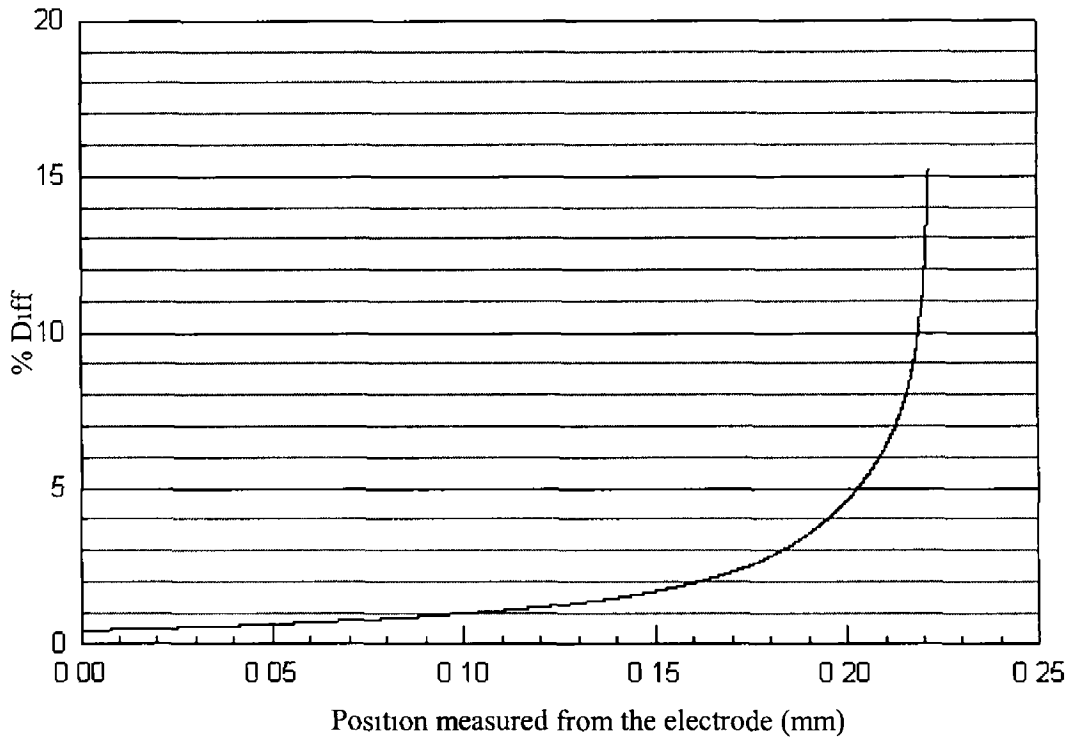
Figure 5 5(c) *Percentage difference in time-average electric fields determined by the two models*

$$e\omega n_0 x = \overline{J}_1\{1 - cos(\varphi)\} + \frac{\overline{J}_1^3}{8e\omega^2 T_e \varepsilon_0 \pi n_0}\left[\frac{3}{2}sin(\varphi) + \frac{11}{18}sin(3\varphi)\right.$$

$$\left. -3\varphi cos(\varphi) - \frac{\varphi}{3}cos(3\varphi)\right] \qquad (5\ 85)$$

The value of s_m for the Lieberman model can be calculated by putting $x = s_m$ and $\varphi = \pi$ in Eqn (5 85) (also described in section 5 5 1)

From Figs 5 5(a), 5 5(b) and 5 5(c) we can see that the Lieberman model always over-estimates the time-average electric field compared to that of the present model The difference is much worse near the ion-sheath edge This is due to the fact that the time average electric field is very small near the ion-sheath edge but the difference is not too small compared to that Therefore, when the difference is expressed as a percentage of the time average electric field determined by the present model it becomes very high near the ion-sheath edge

188

A lower time-average electric field, as obtained by the present model, assumes a lower time-average sheath voltage and hence a lower energy of ions striking the electrode

5 5 3 The ion density and the time-average electron density within the sheath

The ion density and the time-average electron density for the present model can be calculated using Eqns (5 22) and (5 24) From Eqn (5 22) we have the Lieberman equation for ion density within the sheath as

$$n_i = n_0 \left[1 - \frac{\bar{J}_1^2}{e\omega^2 T_e \varepsilon_0 \pi n_0} \left(\frac{3}{8} \sin(2\varphi) - \frac{\varphi}{4} \cos(2\varphi) - \frac{\varphi}{2} \right) \right]^{-1} \tag{5 86}$$

The Lieberman equation for electron density is same as Eqn (5 24) except that the ion density n_i in Eqn (5 24) is given by Eqn (5 86)

Figures 5 6(a), 5 6(b) and 5 6(c) show the ion density and the time-average electron density as functions of position as measured from the powered electrode while Fig 5 6(d) shows the differences in both the densities determined by the Lieberman model compared to those of the present model For each particular value of φ the corresponding position for the ion/electron density was calculated as described in section 5 5 2

From the figures we can see that both the ion and time-average electron densities are underestimated by the Lieberman model compared to those of the present model That means, as obtained by the present model, a higher number of ions will strike the electrode in a particular period of time Again, higher densities of electrons and ions need a comparatively lower sheath field to sustain the plasma for a given input power which is in agreement with the result shown in section 5 5 2

5 5 4 Charge density within the sheath

Figures 5 7(a), 5 7(b) and 5 7(c) show the time-average charge density within the sheath as a function of position as measured from the powered electrode while Fig 5 7(d) shows the percentage difference in the charge density determined by the

189
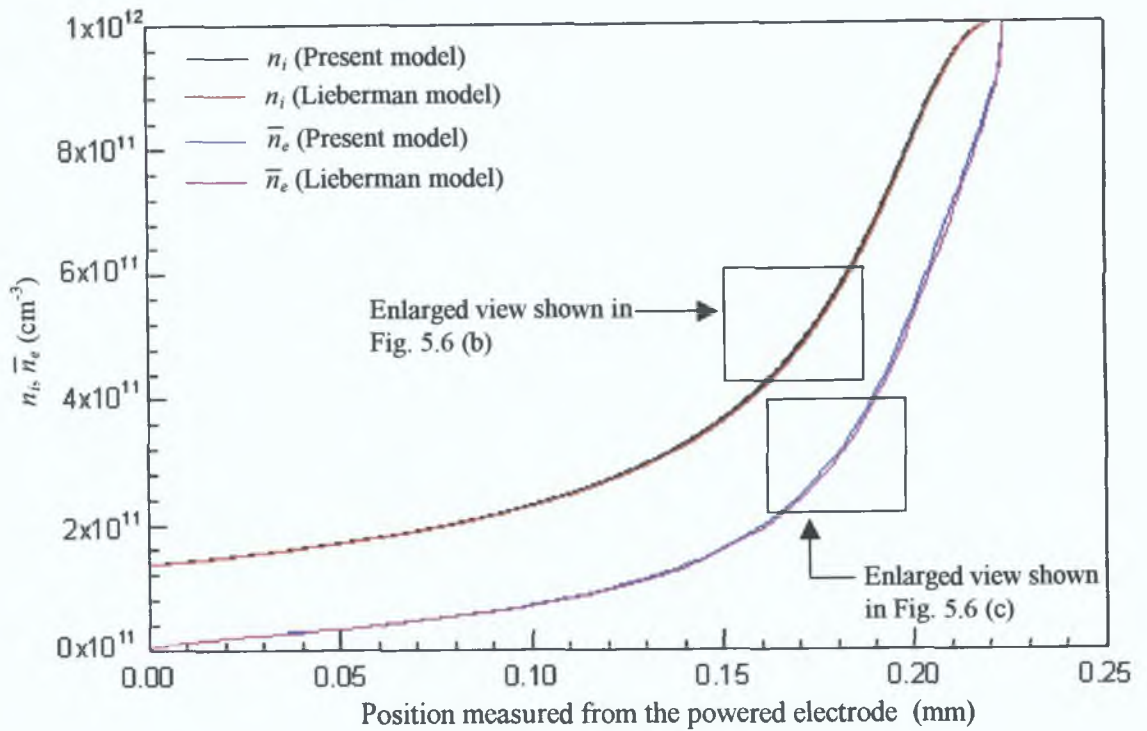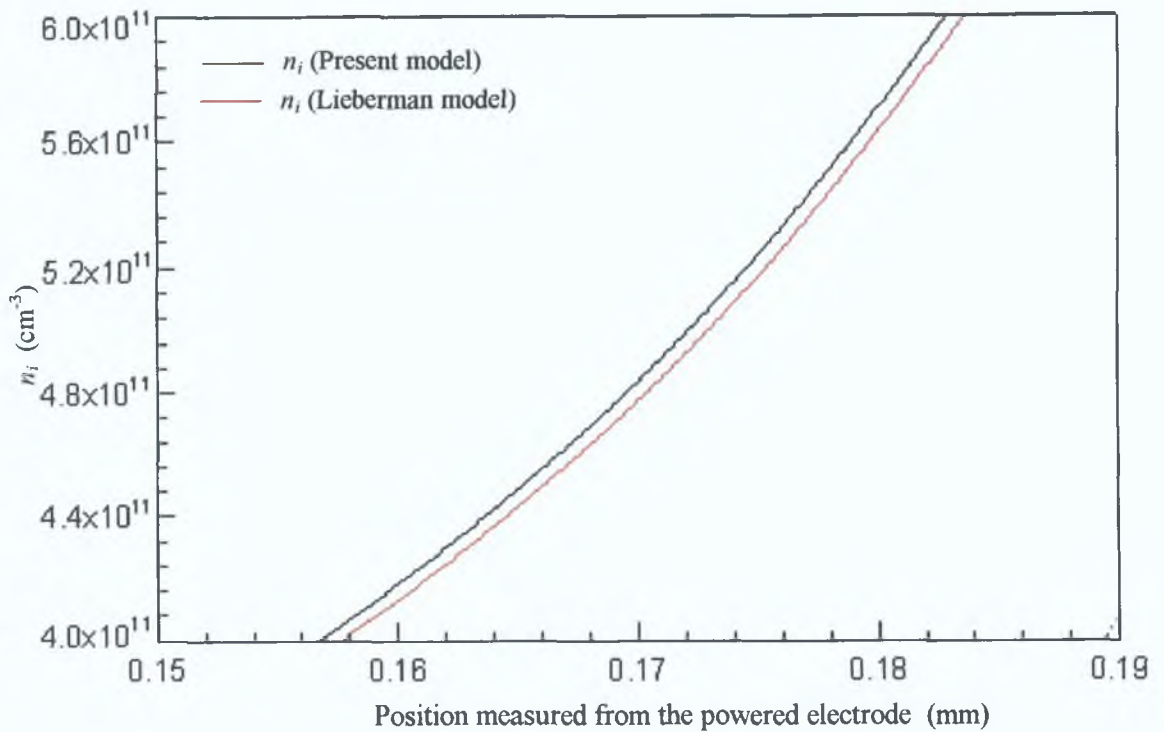
Figure 5.6 **(a)** *Ion density and time-average electron density as a function of position measured from the powered electrode.* **(b)** *Enlarged view of the area enclosed by a rectangle shown in (a).*
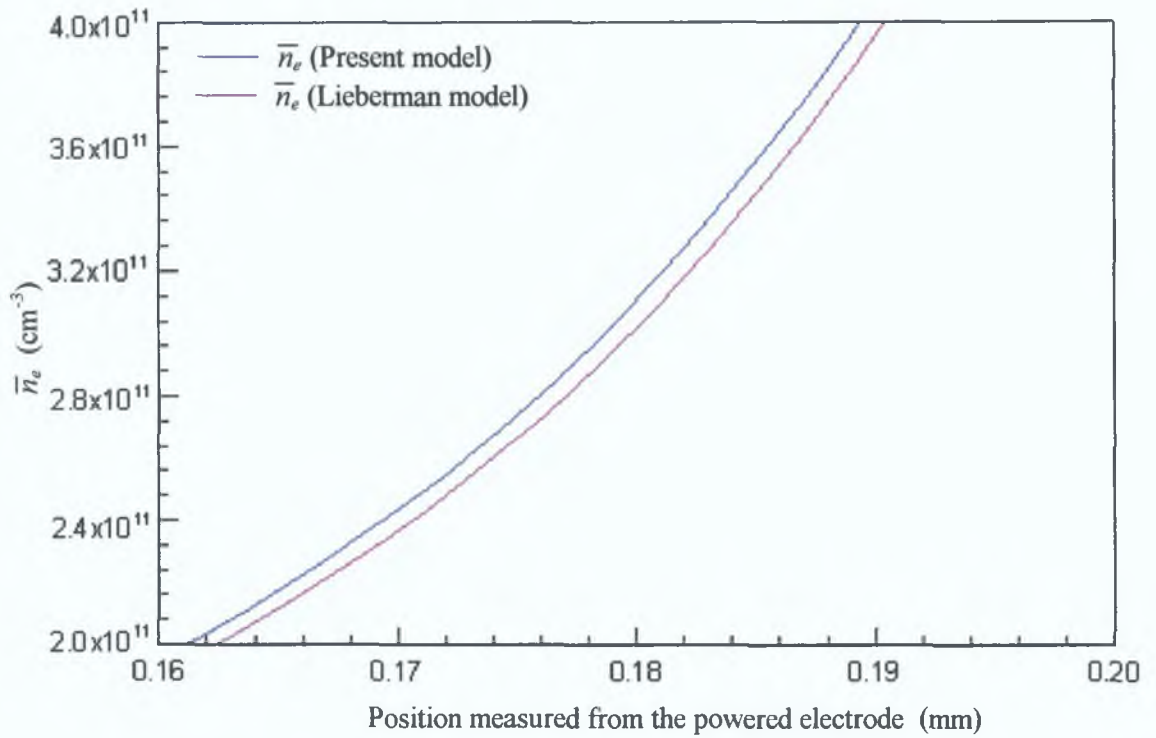
Figure 5.6(c) Enlarged view of the area enclosed by a rectangle shown in Fig. 5.6 (a).
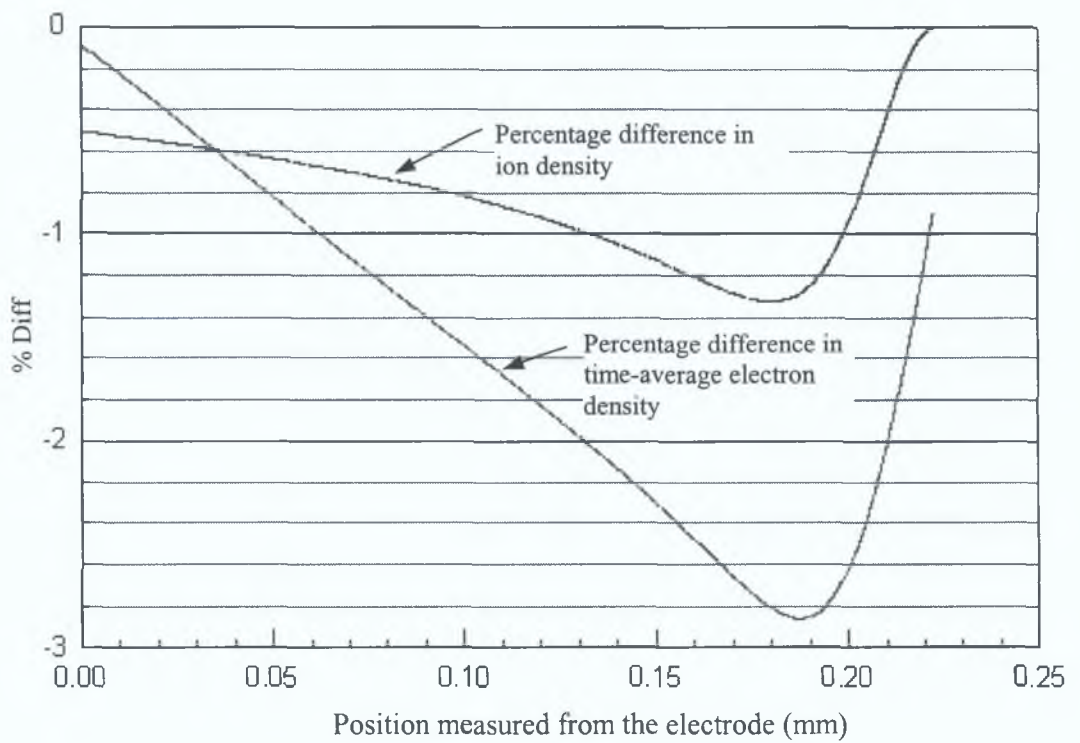
Figure 5.6(d) Percentage difference in ion and time-average electron densities determined by the two models.
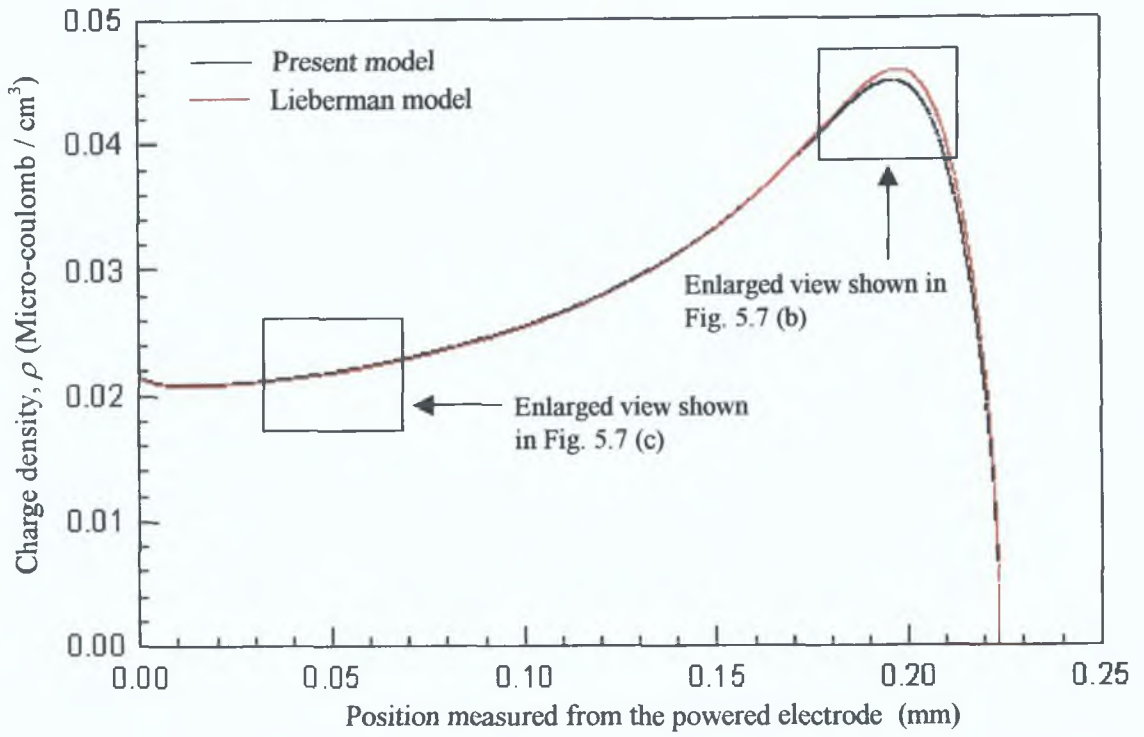
Figure 5.7(a) *Charge density as a function of position measured from the powered electrode.*
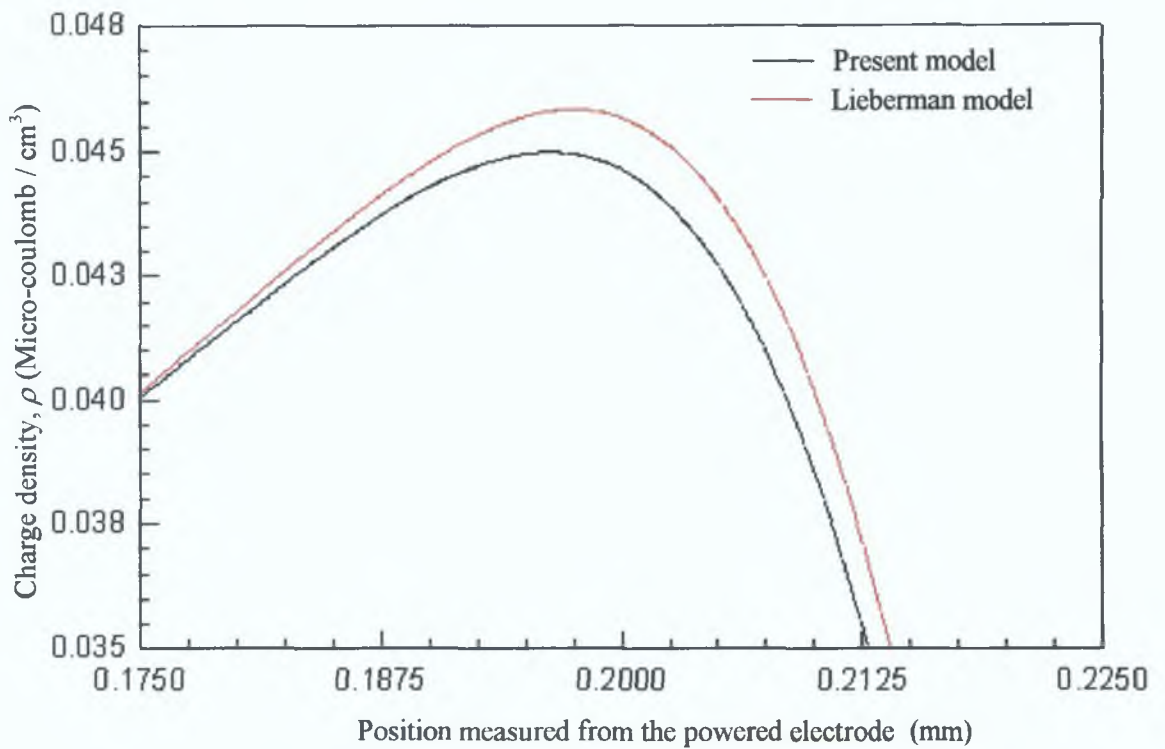
Figure 5.7(b) *Enlarged view of the area enclosed by a rectangle shown in Fig.5.7(a).*
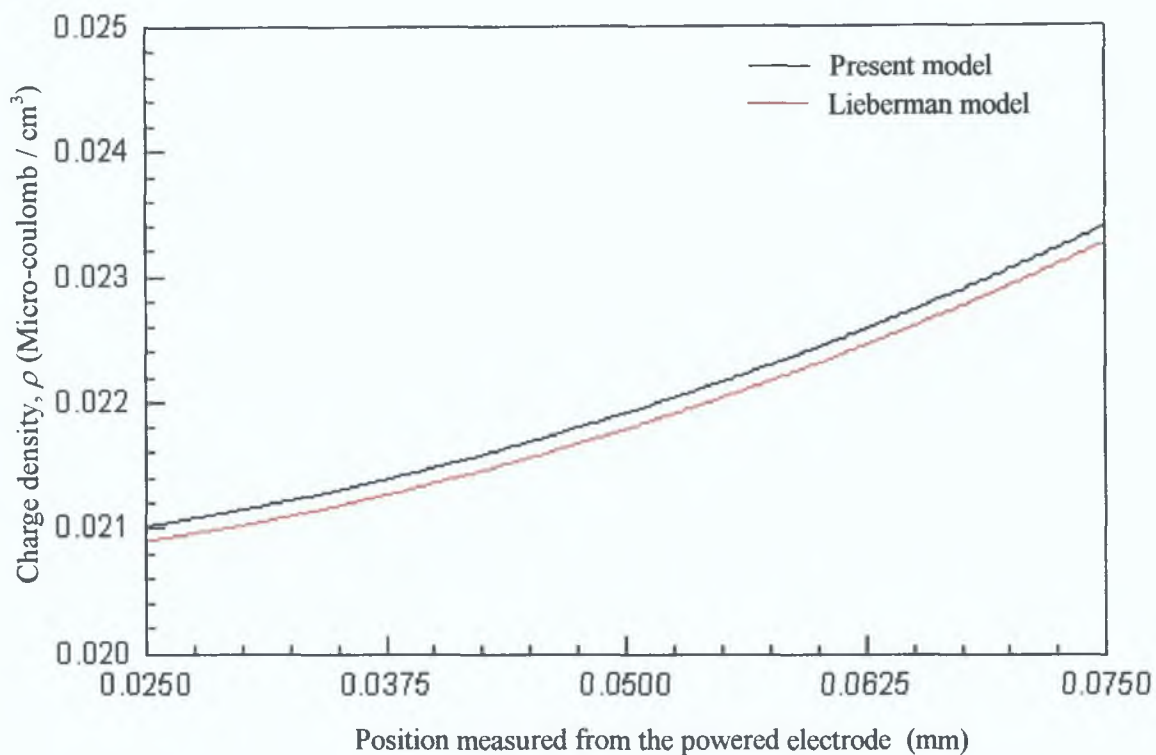
Figure 5.7(c) *Enlarged view of the area enclosed by a rectangle shown in Fig.5.7(a).*
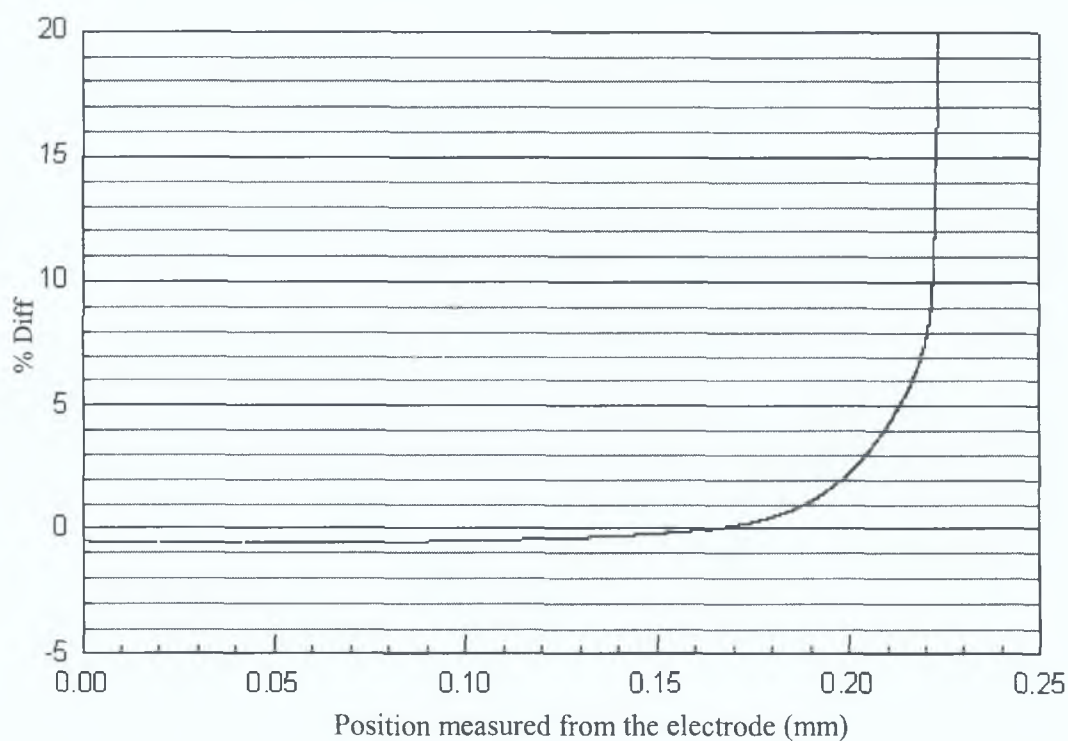
Figure 5.7(d) *Percentage difference in charge densities determined by the two models.*

Lieberman model compared to that of the present model For both models the charge density is given by Eqn (5 23) but the value of n_i in Eqn (5 23) should be evaluated differently as described in section 5 5 3

From the figures we see that the charge density is a little underestimated by the Lieberman model near the electrode (up to ~0 165 mm from the electrode) but it is much overestimated near the bulk plasma Since we know that the slope of the time-average electric field curve is directly proportional to the charge density, the time-average electric field curve obtained from the present model will be steeper than that of the Lieberman model up to ~0 165mm from the electrode and after that it will be more gradual compare to that of the Lieberman model This is also verified by the Fig 5 5(a)

5 5 5 The time-average potential within the sheath

The time-average potential $\overline{\Phi}$ within the sheath is given by the Eqn (5 25) From Eqn (5 25) we have the Lieberman equation for $\overline{\Phi}$ as

$$\frac{\overline{\Phi}}{T_e} = \frac{1}{2} - \frac{1}{2}\left[1 - \frac{J_1^2}{e\omega^2 T_e \varepsilon_0 \pi n_0}\left(\frac{3}{8}\sin(2\varphi) - \frac{\varphi}{4}\cos(2\varphi) - \frac{\varphi}{2}\right)\right]^2 \quad (5\ 87)$$

Figures 5 8(a) and 5 8(b) show the time-average potential with respect to the bulk plasma as a function of position as measured from the powered electrode while Fig 5 8(c) shows the percentage difference in time-average potential determined by the Lieberman model compared to that of the present model The corresponding positions, as functions of φ, were calculated as described in section 5 5 2

It is clear from the figures that the time-average sheath potential is always overestimated by Lieberman model compared to that of the present model The lower time-average sheath potential as determined by the present model is a result of lower time-average electric field within the sheath (also mentioned in section 5 5 2) The lower time-average potential will result in lower energy ions which will strike the electrode
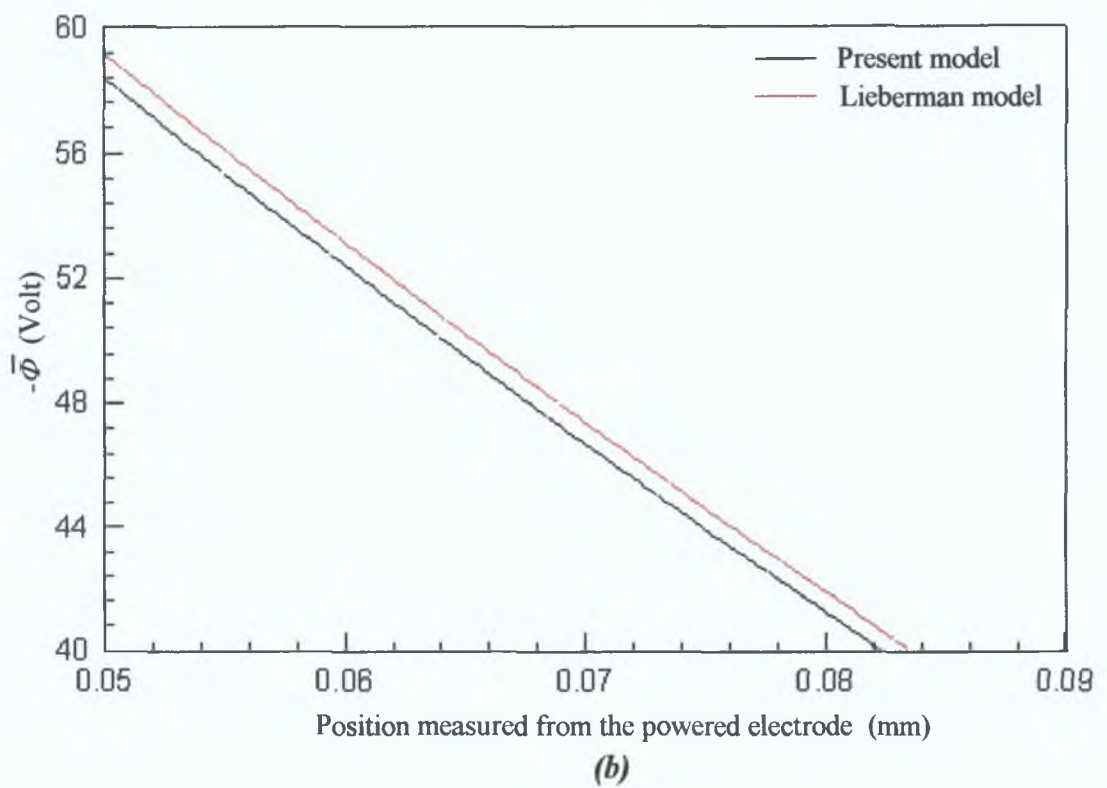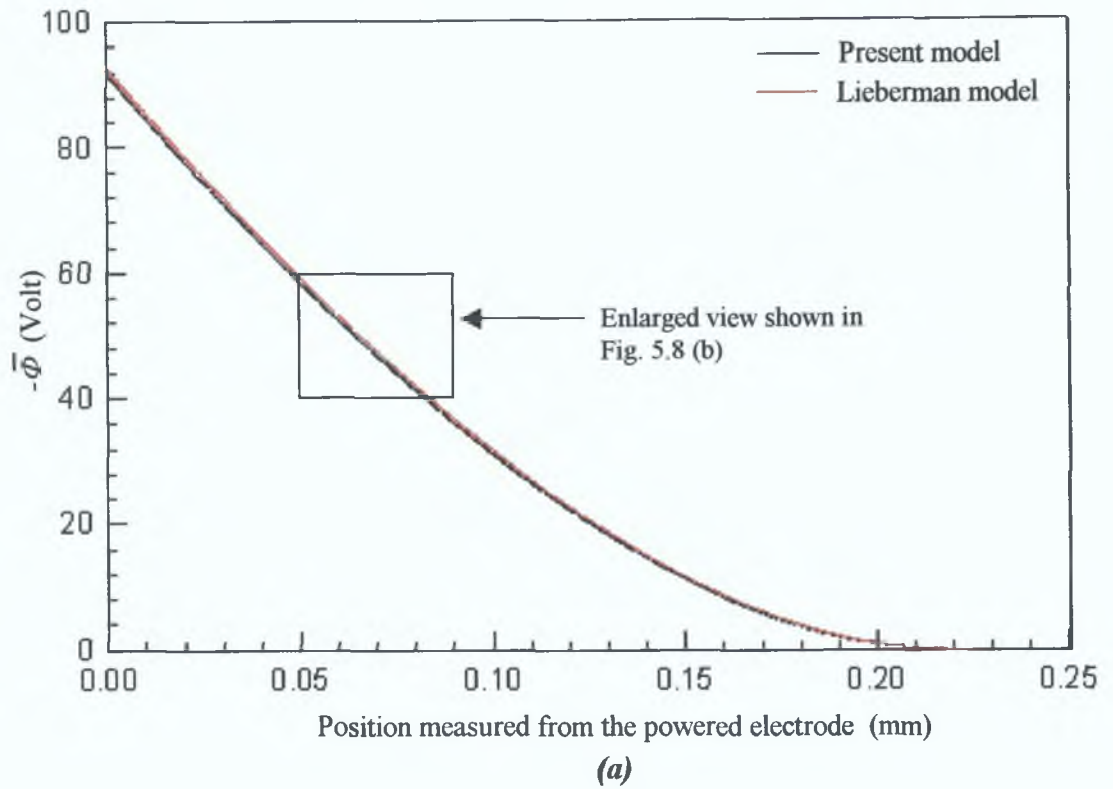
Figure 5.8 (a) Time time-average sheath potential as a function of position measured from the powered electrode. *(b)* Enlarged view of the area enclosed by the rectangle shown in (a).
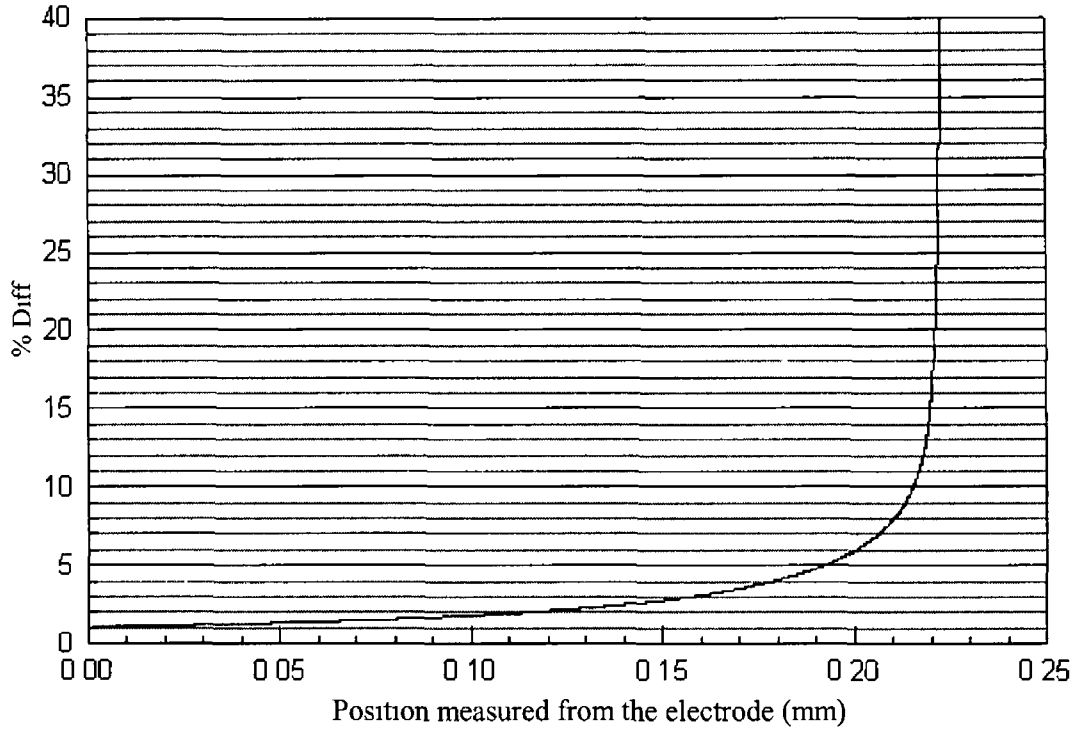
Figure 5 8(c) *Percentage difference in time-average sheath potentials determined by the two models*

5 5 6 The time-varying sheath voltage

The time-varying sheath voltage $V(t)$ for the present model is given by Eqn (5 28) From Eqn (5 28) we can obtain the Lieberman equation for $V(t)$ as

$$e\omega^2 \varepsilon_0 n_0 V(t) = \bar{J}_1^2 I_1 - \frac{\bar{J}_1^4}{e\omega^2 T_e \varepsilon_0 \pi n_0} \left\{ \frac{3}{16} cos(\omega t)(I_{26} - I_{27}) - \frac{1}{8} cos(\omega t)(I_{28} - I_{29}) \right.$$

$$-\frac{1}{2} cos(\omega t) I_{30} + \frac{1}{4}(I_{31} + I_{32}) - \frac{3}{32}(I_{33} + I_{34} - I_{35} - I_{36})$$

$$\left. + \frac{1}{16}(I_{37} + I_{38} - I_{39} - I_{40}) \right\}$$ (5 88)

where,

$$I_1 = cos(\omega t)\{cos(\omega t) + 1\} - \frac{1}{4}\{cos(2\omega t) - 1\}$$ (5 88i)

$$I_{26} = -sin(\omega t)$$ (5 88ii)

$$I_{27} = -\frac{1}{3} sin(3\omega t)$$ (5 88iii)

196

$$I_{28} = \frac{\omega t}{3} \cos(3\omega t) + \frac{\pi}{3} - \frac{1}{9} \sin(3\omega t)$$ (5 88iv)

$$I_{29} = \omega t \cos(\omega t) + \pi - \sin(\omega t)$$ (5 88v)

$$I_{30} = \omega t \cos(\omega t) + \pi - \sin(\omega t)$$ (5 88vi)

$$I_{31} = \frac{\omega t}{2} \cos(2\omega t) - \frac{\pi}{2} - \frac{1}{4} \sin(2\omega t)$$ (5 88vii)

$$I_{32} = 0$$ (5 88viii)

$$I_{33} = -\frac{1}{2} \sin(2\omega t)$$ (5 88ix)

$$I_{34} = \pi - \omega t$$ (5 88x)

$$I_{35} = -\frac{1}{4} \sin(4\omega t)$$ (5 88xi)

$$I_{36} = -\frac{1}{2} \sin(2\omega t)$$ (5 88xii)

$$I_{37} = \frac{\omega t}{4} \cos(4\omega t) - \frac{\pi}{4} - \frac{1}{16} \sin(4\omega t)$$ (5 88xiii)

$$I_{38} = \frac{\omega t}{2} \cos(2\omega t) - \frac{\pi}{2} - \frac{1}{4} \sin(2\omega t)$$ (5 88xiv)

$$I_{39} = \frac{\omega t}{2} \cos(2\omega t) - \frac{\pi}{2} - \frac{1}{4} \sin(2\omega t)$$ (5 88xv)

$$I_{40} = 0$$ (5 88xvi)

Eqn (5 88) can be re-arranged as

$$e\omega^2 \varepsilon_0 n_0 V(t) = \frac{\bar{J}_1^2}{4} \left[4\cos(\omega t) + \cos(2\omega t) + 3 - \frac{\bar{J}_1^2}{e\omega^2 T_e \varepsilon_0 \pi n_0} \right.$$

$$\left\{ \frac{15}{16} \pi + \frac{5}{3} \pi \cos(\omega t) + \frac{3}{8} \omega t + \frac{1}{3} \omega t \cos(2\omega t) + \frac{1}{48} \omega t \cos(4\omega t) \right.$$

$$\left. \left. - \frac{5}{18} \sin(2\omega t) - \frac{25}{576} \sin(4\omega t) \right\} \right]$$ (5 89)

Figures 5 9(a), 5 9(b), 5 9(c) and 5 9(d) show the time-varying sheath voltage as a function of phase angle ωt while Fig 5 9(e) shows the percentage difference in the time-varying sheath voltage determined using the Lieberman model compared to that of the present model From these figures it is evident that, compared to the present model,

197
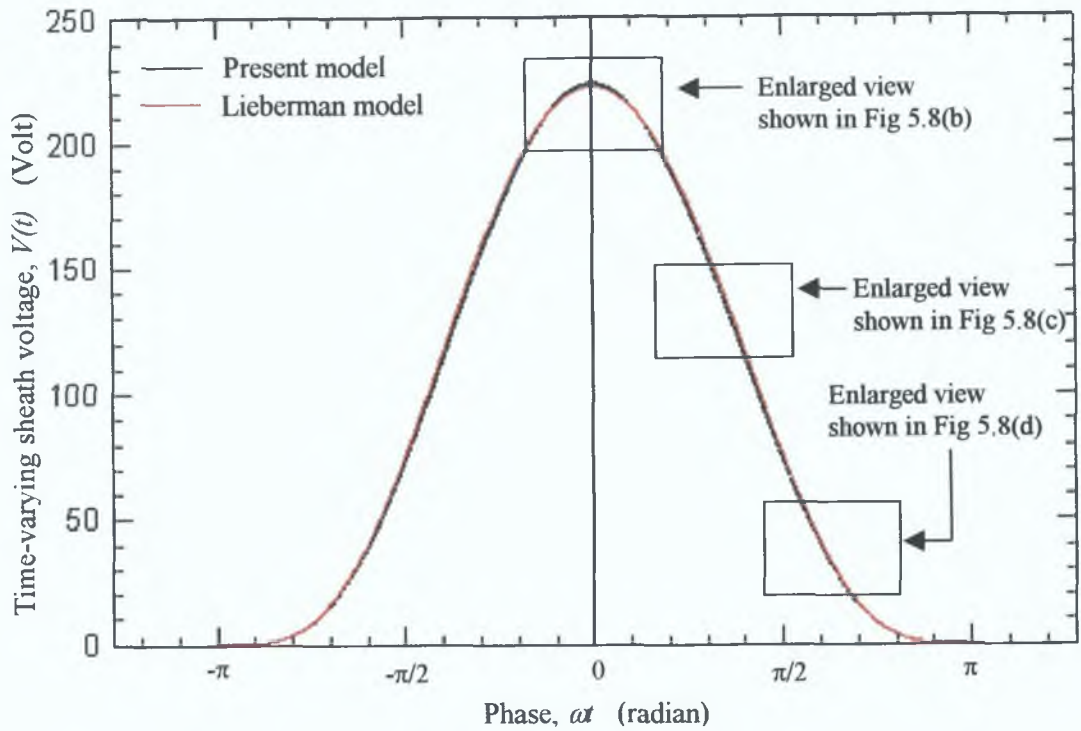
Figure 5.9(a) *Time-varying sheath voltage as a function of phase, ωt.*
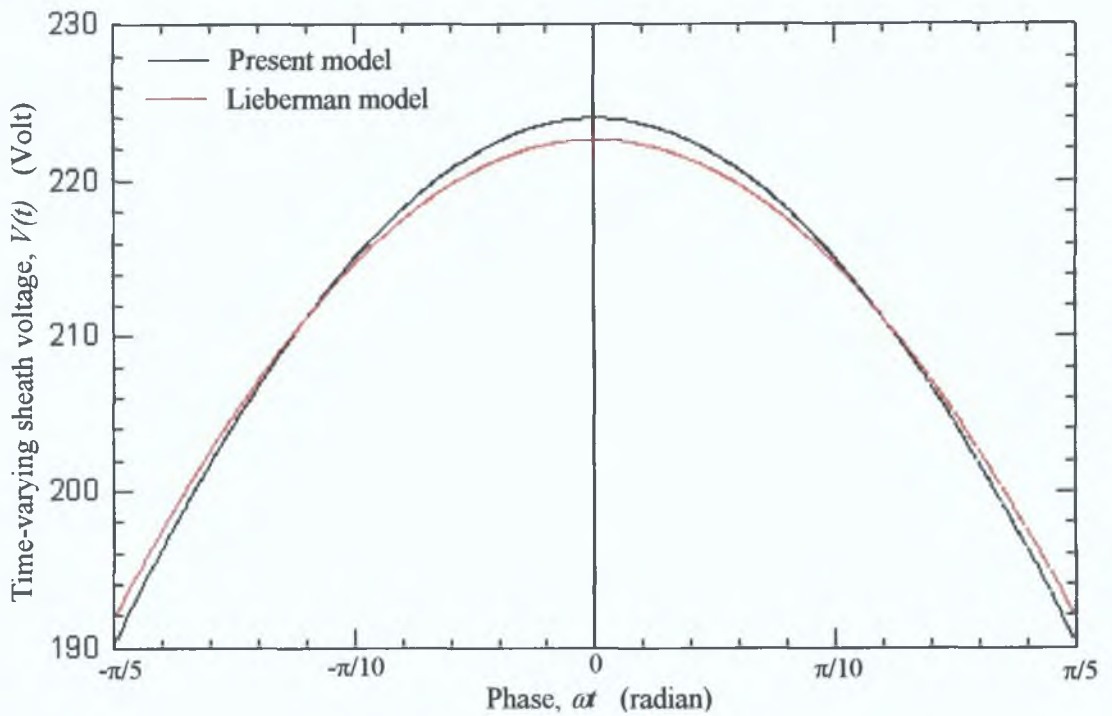
Figure 5.9(b) *Enlarged view of the area enclosed by a rectangle shown in Fig. 5.9(a).*
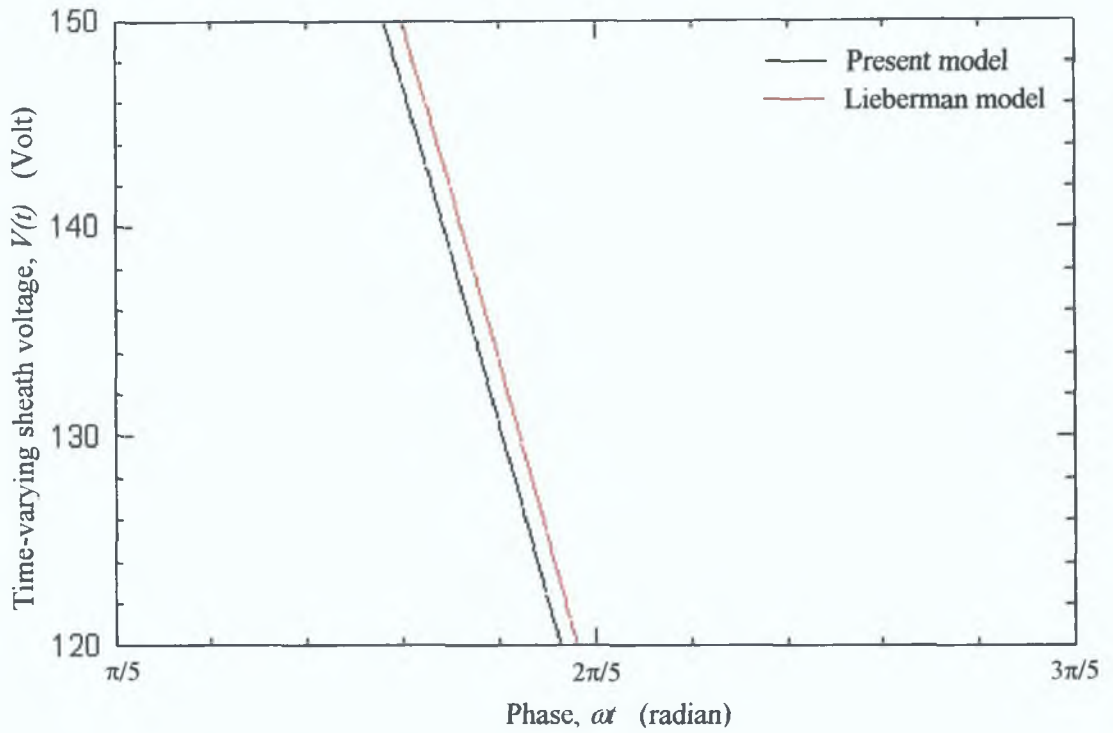
Figure 5.9(c) *Enlarged view of the area enclosed by a rectangle shown in Fig. 5.9(a).*
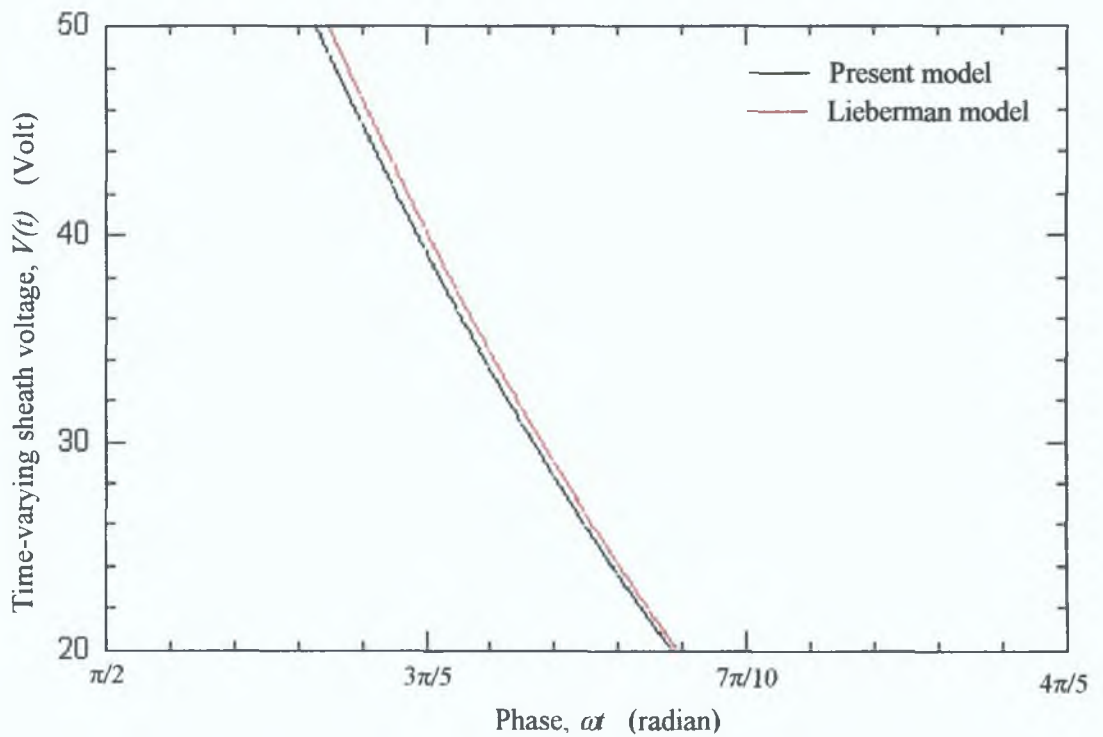
Figure 5.9(d) *Enlarged view of the area enclosed by a rectangle shown in Fig. 5.9(a).*
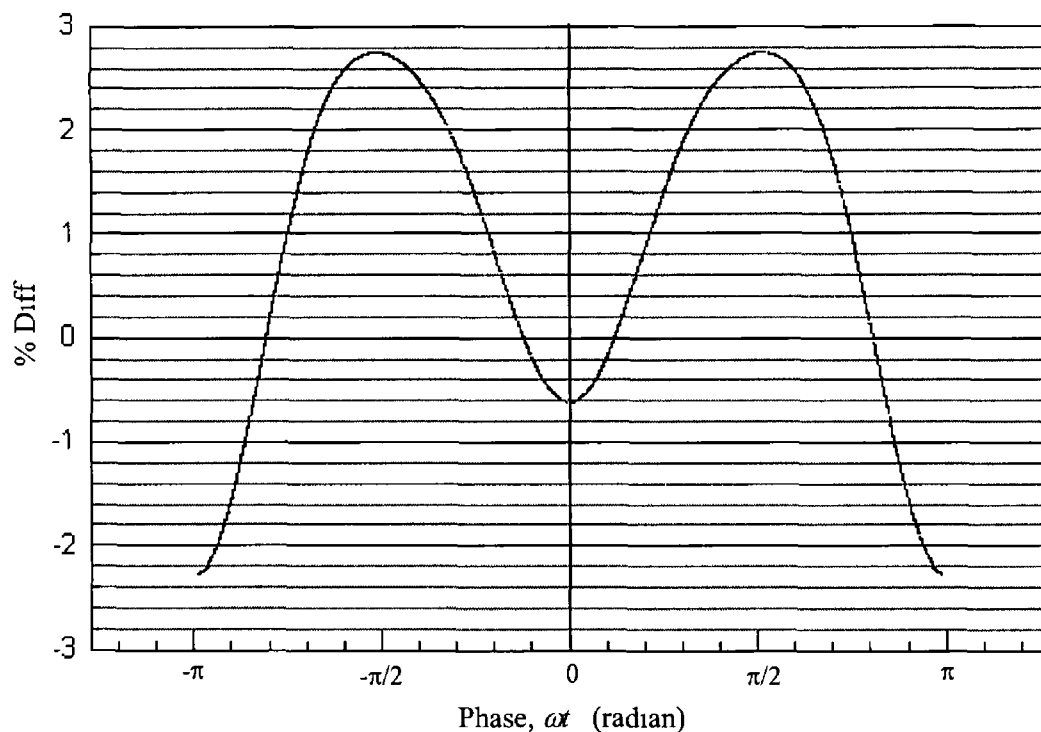
Figure 5 9(e) *Percentage difference in time-varying sheath voltages determined by the two models*

the time-varying sheath voltage is overestimated by the Lieberman model for $0\ 12\pi < |\omega t| < 0\ 81\pi$ and it is underestimated for the rest of the time We also see that the maximum difference in determining the time-varying sheath voltage by the Lieberman model is about 2 8% The ranges of ωt where the Lieberman model overestimates or underestimates the potential and the percentage difference in potential determined by the Lieberman model do not have fixed values—they are dependent upon the magnitudes of the harmonic currents and the other parameters used in the calculations Off course, the difference in the time-varying sheath voltages (as in other parameters described in previous sections) determined by the two models arises due to the exclusion of harmonic currents in the Lieberman model

5 5 7 Sheath resistance, sheath capacitance and the overall RF voltage

The sheath resistance r_k and sheath capacitance C_k of a single sheath can be estimated by the present model as (also see eqns 5 31 and 5 53),

$$r_k = \frac{3\bar{J}_k^2}{4k^2} \frac{m\Gamma_s}{e^3\omega^2 T_e \varepsilon_0 n_0^3}$$ (5 90)

$$C_k = \frac{\bar{J}_k}{k\omega\bar{V}_k}$$ (5 91)

where, $\bar{J}_k$ = k-th harmonic component of current density and $\bar{V}_k$ = k-the harmonic Fourier component of the time-varying sheath voltage given by eqn (5 29ii) It is clear from eqns (5 90) and (5 91) that the Lieberman model fails to relate either the sheath resistance or the sheath capacitance to the harmonic frequencies (other than the fundamental frequency), as there is no harmonic current present in that model But in the present model both of these parameters are present for all the harmonic frequencies

Figure 5 10 shows the percentage differences between the harmonic components of the time-varying sheath voltage ($\bar{V}_k$) at the powered electrode determined by the two models The result shows that the difference is small while estimating the fundamental component (less than 1%) but it increases very rapidly as the harmonic frequency increases For example, the percentage difference for the 5th harmonic component of the time-varying sheath voltage is ~200% Since the sheath voltage is the major part of the overall RF voltage, the Lieberman model will thus produce a huge error in the estimate of the overall RF voltage for higher harmonic frequencies

5 6 Comparison of Analytically Obtained I-V Parameters with the Experimental Results

To analyze the validity of the present model we conducted the same experiment as described in section 5 4 2 for two different effective diameters of the powered electrode The I-V parameters measured by the PIM were recorded for each of the effective diameter conditions of the powered electrode The RF voltage and the RF impedance were calculated using the present model and compared with the corresponding measured data We used the current harmonics measured in the experiments as parameters for calculation The typical values of three plasma characteristics (n_0, T_e and v_m) given by Table 5 2 were also used for this calculation
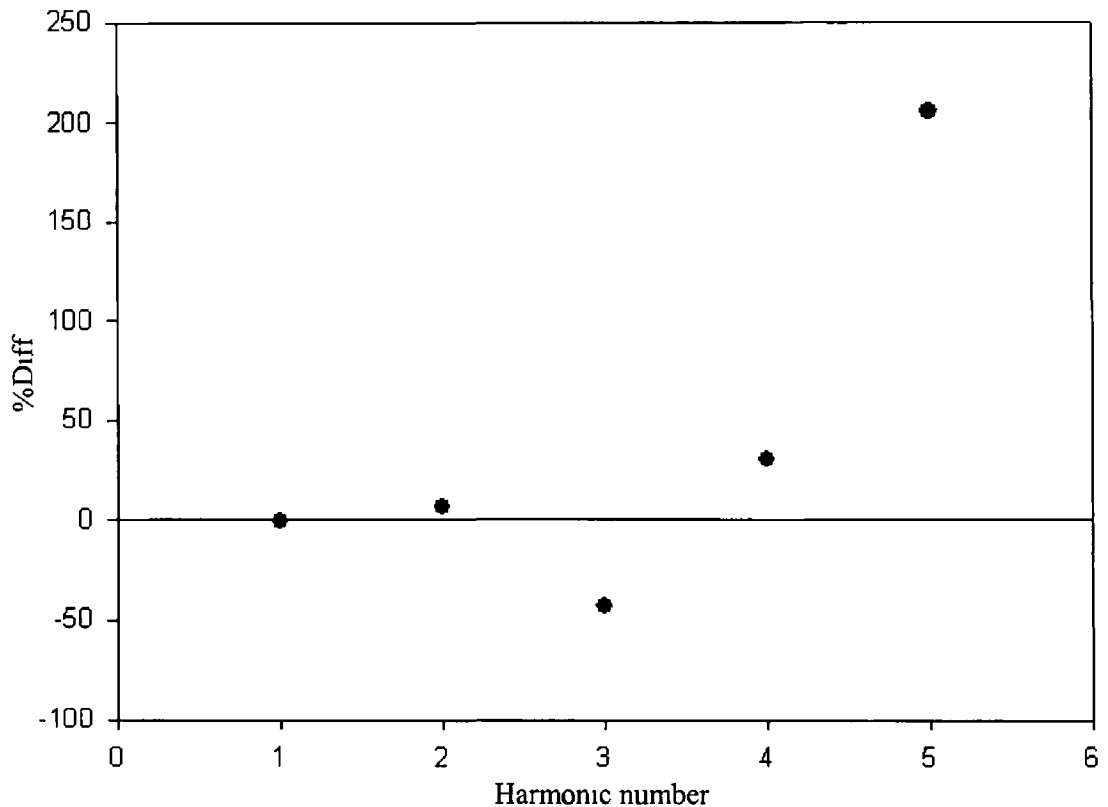
Figure 5 10 Percentage difference in the harmonic coefficients of the time-varying sheath voltage at the powered electrode determined by the two models

We saw in the previous sections that the modelled equations are strongly dependent upon three plasma characteristics, i e , n_0, T_e and v_m It would be best if we could measure these parameters in experiments and use the exact values in calculations But we already mentioned that there was no scope to measure experimentally these characteristic parameters as there was no facility for probe or similar measurements in our plasma system We mentioned earlier that the values of these parameters depend upon the operating conditon of the plasma system (i e , discharge power, operating pressure, the gas flow rate and the geometry of the plasma chamber) and change drastically for small changes in these For this reason it is very difficult to assume the exact values of these parameters and hence the calculated values of the different parameters may vary significantly in absolute value from the measured values In this work we used typical values of the three plasma characteristics just to elucidate *trends in the data* such as the relative contributions of each harmonic component of RF voltage or impedance

202

To analyze the trends in the data the measured and the calculated values of the RF parameters were normalized with respect to their fundamental components and plotted on the same graph Figures 5 11 and 5 12 show the comparisions between the measured and the calculated values of the RF voltage and the RF impedance, respectively, while the comparisons are made for the effective diameter of the powered electrode set to both 18 cm and 20 cm, respectively It is clear from the figures that the relative magnitudes of the RF voltage harmonics and RF impedance harmonics calculated using the present model follow qualitatively the values measured in the experiment In the previous sections we saw that the plasma equations are non-linear in behaviour and they depend on the above mentioned three plasma characteristics very much non-linearly That is a major factor in the reason why the calculated impedance and voltage harmonics, when they are normalized with respect to their fundamental component, do not match exactly with the measured values but follow the trend of relative magnitudes of each of the harmonic components To obtain improved results one should use the exact values of three plasma characteristics mentioned previously

Figures 5 13 and 5 14 show a comparision between the calculated and measured values of RF voltage and RF impedance harmonics, respectively, for the effective diameter of the powered electrode, D_l, set to 16 cm, 18 cm and 20 cm, respectively From these figures we again see that the overall qualitative trends are similar for measured and calculated values But the values of both RF voltage and impedance move to lower values as the effective diameter of the powered electrode, D_l, increases This can be explained in the following way We saw in the analytical sections (see sections 5 3 3 and 5 3 4) that there is no sheath capacitance effect on the even harmonic components of RF voltage and impedance for a symmetric discharge (i e , when the areas of both the electrodes are same) That means the harmonic phenomenon is reduced as the asymmetry of the system is reduced In other words, the fundamental component will be more prominent in less asymmetric systems When the harmonic components are normalized with respect to the fundamental, they will be of lower value than those of more asymmetric systems Now, an increase in the diameter of the powered electrode reduces the asymmetry of the system, as the diameter of the grounded electrode is fixed (28 5 cm) This is the main reason why the normalized curves of the RF voltage and impedance harmonics shift downward for higher D_l
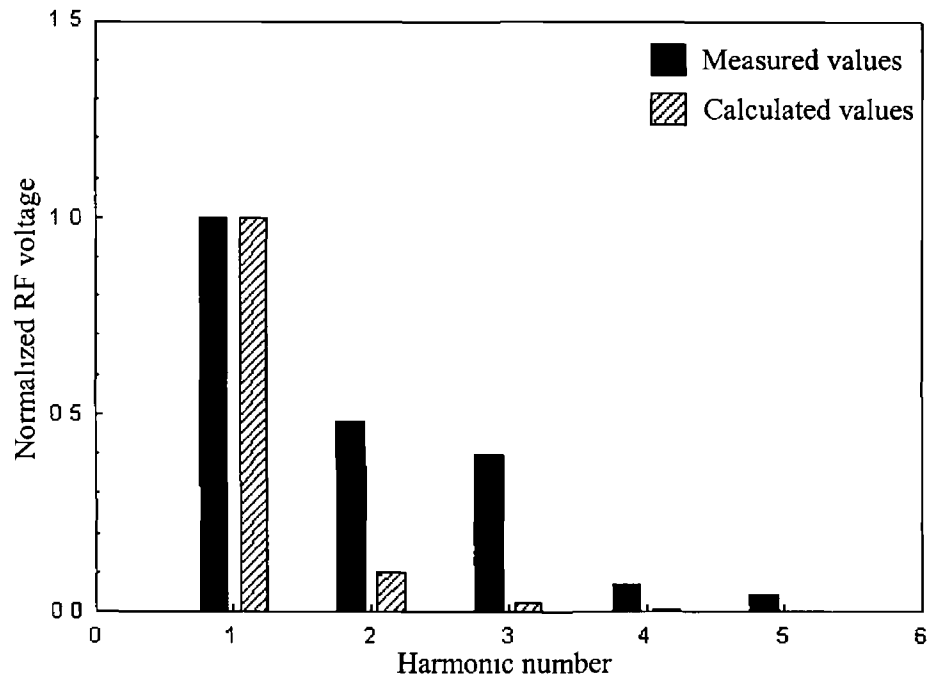
(a)
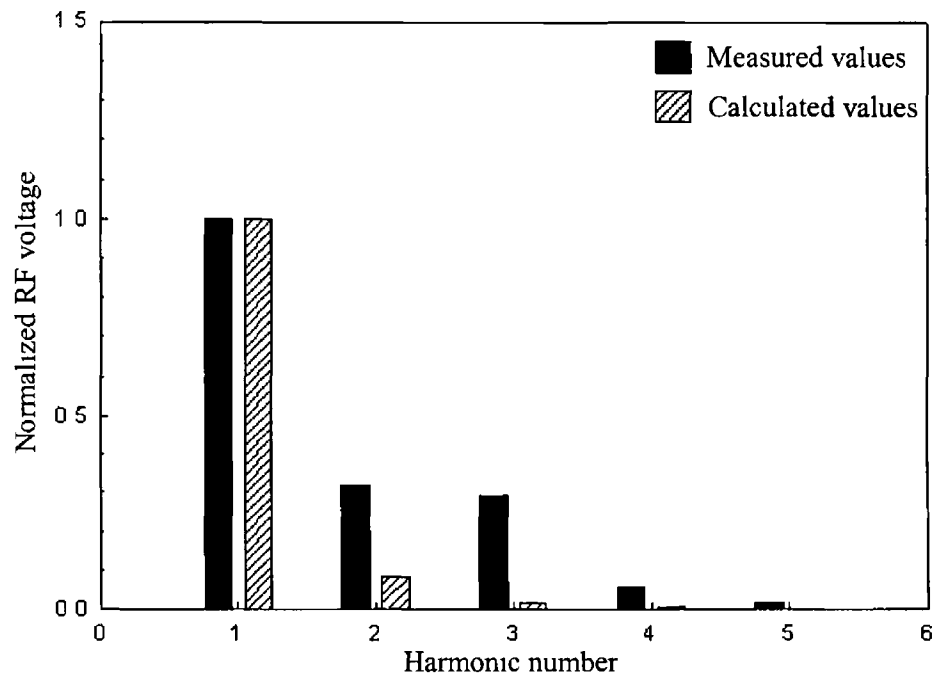
(b)

Figure 5 11 *Normalized RF voltage as a function of the harmonic number for two different effective diameters of the powered electrode, D_1, (a) $D_1 = 18$ cm, (b) $D_1 = 20$ cm*
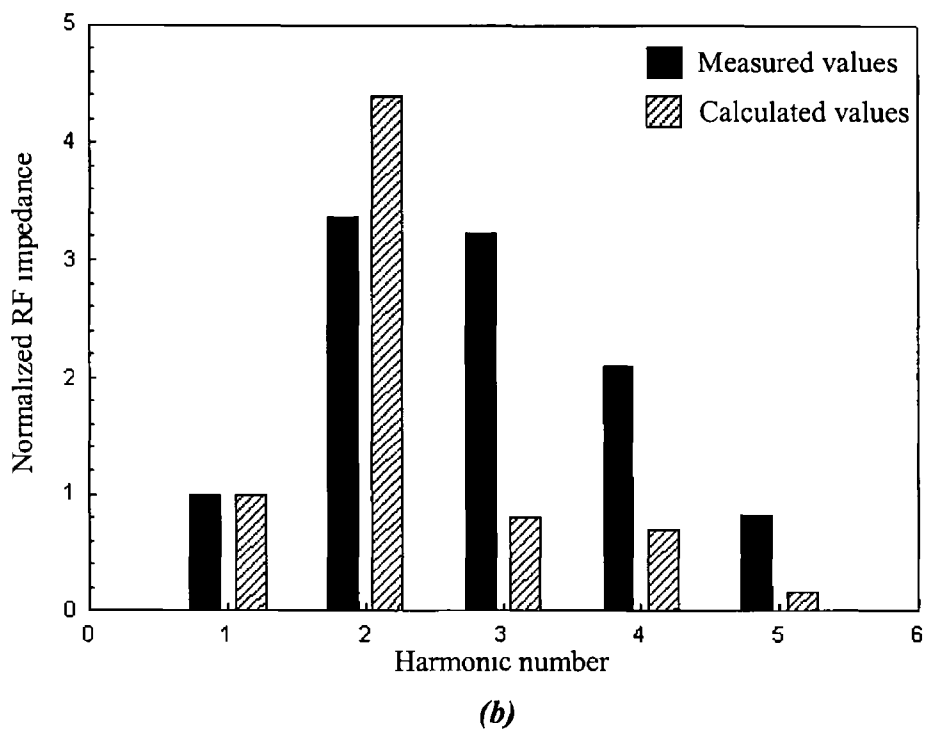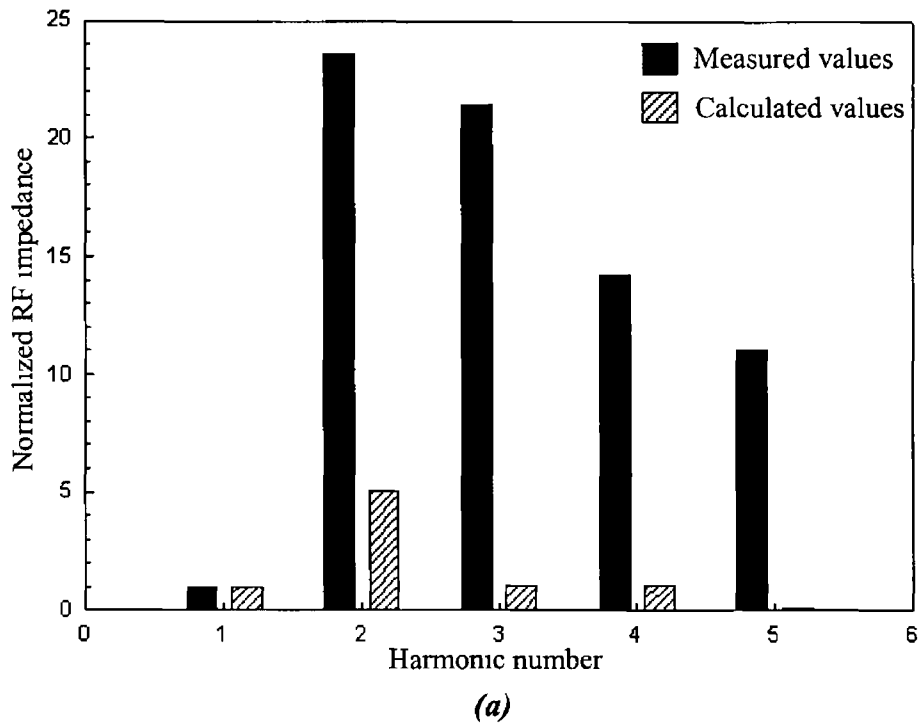
Figure 5 12 Normalized RF impedance as a function of the harmonic number for two different effective diameters of the powered electrode, D_1, (a) D_1 =18 cm, (b) D_1 =20 cm
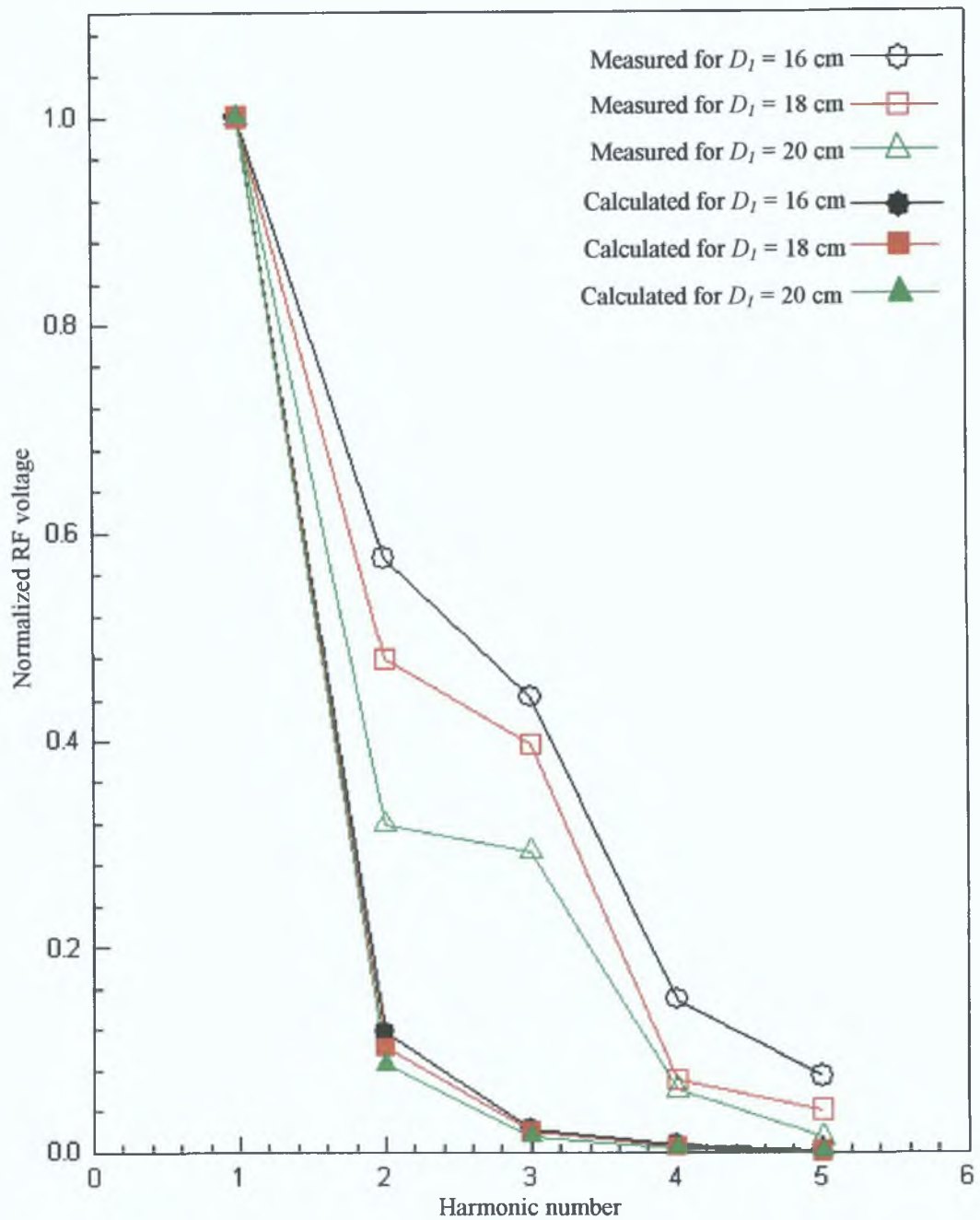
Figure 5.13 Comparison of calculated and measured values of normalized RF voltage for the effective diameter of the powered electrode, $D_1 = 16$ cm, 18 cm and 20 cm, respectively.
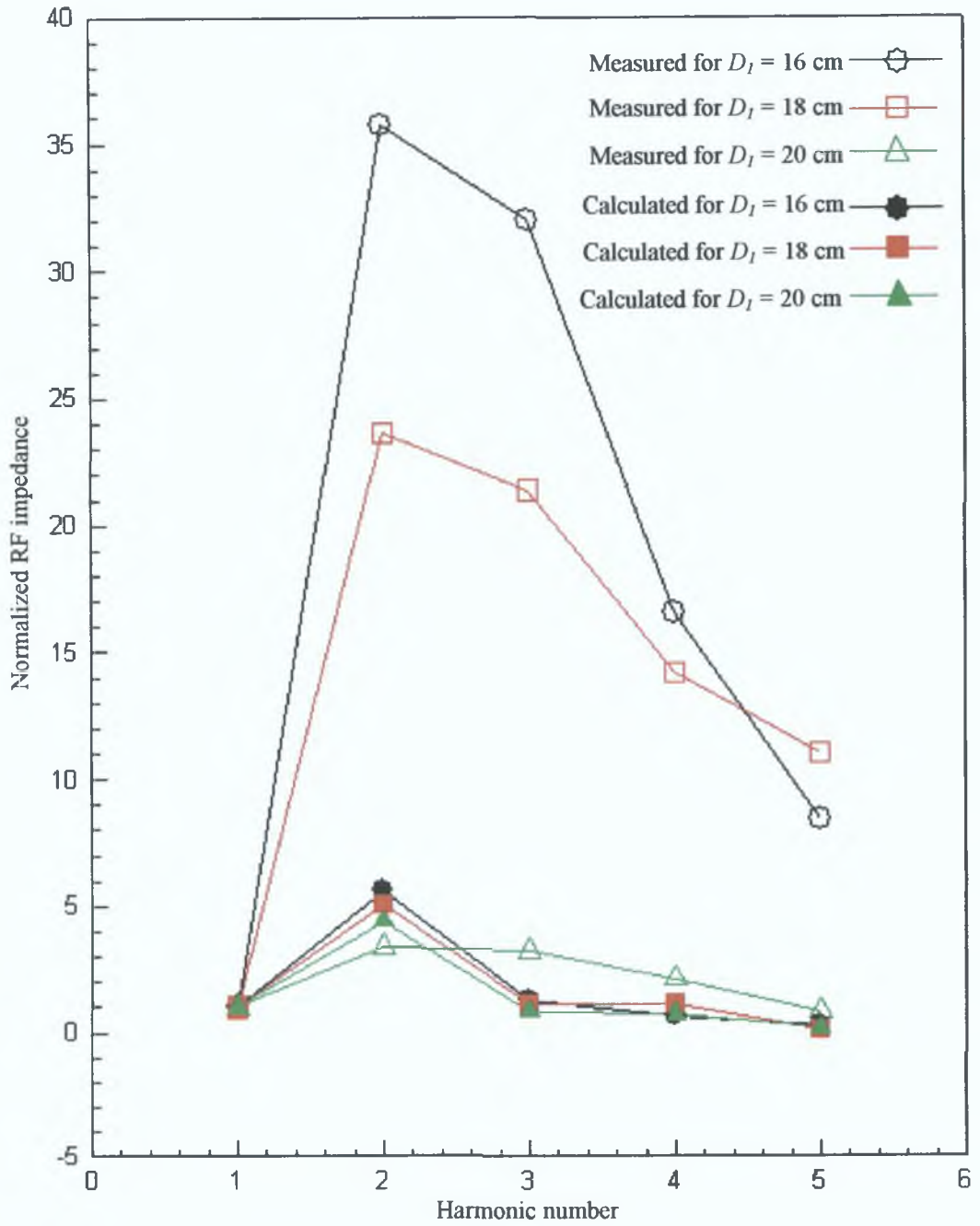
Figure 5.14 *Comparison of calculated and measured values of normalized RF impedance for the effective diameter of the powered electrode, $D_1 = 16$ cm, 18 cm and 20 cm, respectively.*

5 7 Sources of Error

We already mentioned that the three basic plasma characteristics (i e , n_0, T_e and $v_{m)}$ used in our calculation depend greatly on the operating conditions of the plasma and the geometry of the plasma system The assumption of typical values for these parameters rather than using the exact values is a major source of error Furthermore, in our calculation we used the same values of these three parameters (given by Table 5 2) for all settings of the powered electrode diameter (D_I) The values of these parameters would tend to be different for different diameters of the powered electrode But it is difficult to know the relative change of these parameters with the change in D_I without proper measurement

Throughout the modelling and derivations we had to make several assumptions for the sake of simplicity Most of these assumptions are not perfectly true and can incorporate at least a small error in the calculations For example, we assumed that the bulk plasma can be represented as a solid cylinder with a linearly varying radius and there is no transverse variation in the current and the plasma densities at a particular distance from either of the electrodes This assumption is not strictly true because the current flux will never follow a straight line exactly and it will bend outward near the middle of the bulk yielding a lower current density than that we assumed This error would be minimum for the condition $l << \sqrt{A}$, where l and A are the separation between the two electrodes and the electrode areas, respectively But the separation of the electrodes in our system was 6 cm which is quite high compared to the electrode areas (16 cm, 18 cm, 20 cm or 28 5 cm) and could give some error in the calculations

We assumed that there were only five harmonic components present in the source current We made this assumption because we could not measure the higher harmonic components due to the limitation of the Plasma Impedance Monitoring system But there could be one or more higher harmonic components of RF current of considerable amplitude that we neglected in our calculation Exclusion of any harmonic current having large amplitude will incorporate an error

In the calculation of stochastic heating related to each of the harmonic frequencies we assumed that only one harmonic of RF current is in operation at a time (see section 5 3 1 2) This assumption was not exactly perfect because all the current harmonics are in operation simultaneously and each harmonic component of RF current contributes to the stochastic heating corresponding to each of the harmonic frequencies To find out how great an error emerges in the calculations we calculated the total stochastic power generated by all the current harmonics using Eqn (5 46) This gives the correct amount of total stochastic power Again, the approximated stochastic power generated by each of the current harmonics was calculated separately using Eqn (5 51) Then all of the approximated stochastic power was summed to estimate the total approximated stochastic power The percentage error in the total approximated stochastic power was calculated as

$$Percentage\ Error = \frac{\sum_{k=1}^{N}\overline{P}_{stoc\ k} - \overline{P}_{stoc}}{\overline{P}_{stoc}}x100 \qquad (5\ 92)$$

where, $\overline{P}_{stoc}$ and $\overline{P}_{stoc\ k}$ are given by Eqns (5 46) and (5 51), respectively The error was determined for both the data sets used for Figs 5 11 and 5 12 (i e , D_l=18 cm and 20 cm) and they were 1 68% and 1 58%, respectively These errors are very small and hence we can conclude that error in the determination of sheath conductance given by Eqn (5 53) was not very significant

5 8 Conclusion

We presented an analytical solution for a high voltage, collisionless, capacititve RF discharge driven by a non-sinusoidal RF current source, assuming that the RF current contains a finite number of harmonic components whose frequencies are integer multiples of the fundamental frequency We obtained analytical expressions for some important sheath parameters, for example, the time-average ion and electron densities, electrical field and electric potential within the sheath, nonlinear oscillation motion of the electron sheath boundary, ion sheath thickness, the effective sheath impedance etc The Lieberman model [30] for the sheath parameters is also obtainable from the present work if we assume that all the harmonic components of the RF current, except the fundamental, equal to zero

209

We made a comparison between the sheath parameters calculated using the present and the Lieberman models We also calculated the difference in sheath parameters determined by the two models We used a set of RF current harmonics measured in an Ar reactive ion etching experiment as parameters for the calculations We also used typical values for three basic plasma characteristics i e , the plasma density n_0, electron temperature T_e and the electron-neutral-atom collision frequency v_m, as there was no facility to measure these values in our laboratory The sheath parameters are sometimes overestimated and sometimes they are underestimated by the Lieberman model depending upon the location within the sheath The errors in the Lieberman model for the electron sheath position, time-average ion and electron densities and the time-varying sheath voltage are up to ~ ±3% but the error is even higher (more than 10%) for the charge density, the time-average electric filed and the time-average sheath potential The error is bigger near the ion sheath-plasma boundary as the difference in those parameters determined by the two models are high compared to their actual magnitudes

We determined the overall RF impedance and the RF voltage for each of the harmonic frequencies considering an asymmetric discharge (unequal electrode areas) We also obtained equations for the same quantities for a symmetric discharge assuming the same electrode areas In the calculation of the overall impedance we included the bulk plasma impedance together with the two sheath impedances The present model always found the even harmonic components of RF voltage and hence the RF impedance whereas Lieberman found no even harmonic component of RF voltage This is because the sheath resistance effect, associated with the stochastic heating in the two sheaths, and the bulk plasma impedance never become zero even in a symmetric discharge Only the sheath capacitance effect is cancelled at the even harmonic frequencies when the discharge is symmetric

This analysis proved that the Lieberman model fails to relate either the sheath resistance or the sheath capacitance while considering the harmonic frequencies This previous model produces a large error while estimating the higher harmonic components of the time-varying sheath voltage though the error is insignificant while estimating the fundamental component Since the sheath voltage is the major part of the

overall RF voltage the Lieberman model will also produce a large error during the calculation of the higher harmonic components of the overall RF voltage

The RF voltage and the impedance harmonics were determined for different diameter settings of the powered electrode while the grounded electrode diameter was fixed The calculated values were compared with the values measured in experiments The same typical values of the three plasma characteristics (mentioned earlier) and the current harmonics measured in experiments were used as parameters for the above calculations For better comparisons the RF voltage and impedance harmonics determined using the present model and those measured in experiments were normalized with respect to their fundamental component and plotted on the same graphs From the graphs we can conclude that the relative magnitudes of RF voltage and impedance harmonics determined using the present model follow qualitatively the values measured in the experiment as they follow the trend of the relative magnitudes of each of the harmonic components

It has been observed (Figs 5 13 and 5 14) that the values of the normalized RF voltage and impedance harmonics shift downward (assume lower values) both for calculated and measured quantities as the asymmetry of the plasma chamber decreases This means that harmonic phenomenon increases with the increase of asymmetry of the chamber

There were different sources of error for which the calculated values of I-V parameters determined using the present model do not exactly match with the experimental values, though they follow the trend of the relative magnitudes of the harmonic components measured experimentally The different assumptions we had to make in our modelling for simplicity will always incorporate at least some error in the calculations As the modelled equations strongly depend on the three basic plasma characteristics (i e , n_0, T_e and V_m), it is most likely the main source of error in the calculations Again these parameters can vary with the operating conditions of the plasma and the geometry of the chamber The use of the same values of these parameters for all diameter settings of the powered electrode could incorporate another error in the calculations

In the calculation of the stochastic heating (associated with the sheath resistance) corresponding to a particular harmonic frequency we assumed that only one harmonic component of RF current of the same harmonic frequency is in operation, though, all the harmonic components are present simultaneously in normal operation To see how much error emerged in the calculations we analyzed the error in the total stochastic power given by the summation of all the stochastic power related to each of the harmonic frequencies The errors were found to be 1 68% and 1 58% for the effective diameter settings of the powered electrode of 18 cm and 20 cm, respectively Thus the error in the sheath resistance calculation was not very significant

Since the RF source current of a plasma processing system always contains some harmonics the present model will always give more accurate results in determining the plasma parameters, compared to the Lieberman model which does not consider the harmonics of RF current Although, the harmonics of RF current measured in the present work are very small compared to the fundamental, they have a significant effect on the plasma parameters and can themselves be used to monitor the state of the plasma The magnitudes of harmonic currents depend on the operating condition of the plasma system and the geometry of the chamber In real industrial plasma systems, where higher power is used for operation, the magnitudes of the harmonic currents may have much higher values than the data given in the present work Therefore the contribution of current harmonics to plasma parameters will be even more significant Again, in the calculation of the present work we neglected any harmonic current above the 5th harmonic frequency because of the limitations of the measurement equipment In industrial plasmas the harmonic components of RF current above the 5th harmonic frequency may have considerable magnitude compared to the fundamental component In those cases all the harmonic currents must be measured accurately for better results

CONCLUSIONS AND SUGGESTIONS FOR FUTURE RESEARCH

6 1 Conclusions

The main objectives of this study were

(a) to investigate the usefulness of the Plasma Impedance Monitoring (PIM) system to monitor the RIE processes in a capacitively coupled parallel plate reactor,

(b) to investigate the effectiveness of the PIM for end point detection when a SiO_2 layer deposited on a Si substrate undergoes SF_6 RIE, and

(c) to develop a mathematical model for a simple argon plasma in a non-symmetric, parallel plate, capacitive discharge driven by a non-sinusoidal RF current

It is shown that the use of I-V harmonic measurements via the PIM is a useful technique for monitoring RIE processes The sensitivity of the PIM to the RIE process variations was investigated This sensitivity was tested by measuring the harmonic components of the I-V parameters (i e , RF discharged power, plasma impedance and the phase between RF voltage and current) in an SF_6 plasma at different RF source powers and comparing them with the same data for different silicon sample sizes inside the plasma chamber while the chamber pressure and the gas flow rates were kept identical It was observed that the PIM is sensitive to the presence of silicon inside the chamber but the sensitivity to differences in silicon sizes is probably not large enough to be useful This is because the presence of silicon in the chamber changes the plasma chemistry inside the chamber and hence the I-V characteristics However the variation of the size of the Si sample doesn't change the I-V characteristics very much This is possibly because the plasma chemistry inside the chamber does not vary significantly with the variation of the silicon size, and also the impedance of the lower electrode sheath is very little changed as the wafer covers a small fraction of this electrode The sensitivity is much better when P_2, Z_1 or ϕ_1 is used as the monitoring parameter rather than using P_1, Z_2 or ϕ_2 The higher harmonic components (beyond 2nd harmonic) of any

of the plasma parameters (i e, discharge power, plasma impedance and phase) were not found to be applicable for use as monitoring parameters, because the measured data of those parameters do not follow any particular trend as a function of Si wafer size inside the chamber However, the PIM showed some sensitivity to the presence of silicon while using P_3 and Z_3 as monitoring parameters but only in specific ranges of RF power It is also shown that if one uses the ratio of the discharged power to the plasma impedance of the same harmonic component while considering the first two harmonic frequencies (i e, P_1/Z_1 and P_2/Z_2), better PIM sensitivity can also be obtained at higher power levels The different sensitivity behaviours of the PIM to the different I-V parameters mentioned above are not clearly understood These sensitivities can again be different if the plasma environments (i e, type of gas and/or material inside the chamber) are changed

The effectiveness of the PIM for the detection of end points is tested by running a SF$_6$ RIE on Si samples covered with a 1 32 μm SiO$_2$ layer at different operating conditions (i e, discharged power, chamber pressure and gas flow rate) The end point of each experiment was confirmed by observing the plasma colour during the experiment and using the Infra-Red (IR) spectroscopy technique on the sample after the RIE It is shown that monitoring the fundamental component of phase (ϕ_1) is a good tool for observing the endpoint of SiO$_2$ etching on a Si wafer using SF$_6$ RIE At the end point when the SiO$_2$ overlayer is completely and preferentially etched away and the silicon layer starts to be etched, the plasma chemistry inside the chamber is changed completely from one state to another and so also is the value of ϕ_1 The PIM can easily detect the change in the ϕ_1 value and hence the end point of the process The fundamental component of plasma impedance (Z_1) also appears to give good end point detection but only for specific ranges of operating conditions for RF power, chamber pressure and gas flow rate The other I-V parameters or harmonic components were found to be of little use for this kind of end point detection

The plasma species and their concentrations change from one steady-state condition to another at the end point, forcing the value of ϕ_1 (or Z_1) to be altered The transition of ϕ_1 (or Z_1) value to the next steady-state requires a finite amount of time as the plasma species and their concentrations need a finite amount time to reach their next

steady-state condition This transition time increases as the areal non-uniformity in the etching increases It can be reduced by cutting the sample into many pieces and placing them at approximately the same radial position of the electrode during the RIE because the etch uniformity is improved in this way

To reliably detect the end point of a process it is necessary to predict the value of the monitoring parameter used as the end point detector when the end point is reached Using the *Box-Behnken* methodology the I-V parameters were empirically modelled as polynomial equations of the input factors (i e, RF power, chamber pressure and gas flow rate) for a fixed range of their values It is shown that the prediction becomes more accurate when the operating input workspace considered for the modelling is smaller It has been shown in this study that while the Si-SiO$_2$ interface is reached during an SF$_6$ RIE of a Si wafer covered with a SiO$_2$ layer, the predicted shift of ϕ_I ($\Delta\phi_{I\,pred}$) is always close to the actual shift ($\Delta\phi_{I\,act}$) Therefore, using the modelled equation for ϕ_I it is possible to detect the end point of the RIE of SiO$_2$ lying on a Si substrate using the PIM In general, it can be concluded that the PIM may detect the end point when a material lying on a dissimilar substrate undergoes RIE For this end point detection process to work the monitoring parameter should be chosen such that the value of this parameter changes significantly when the end point is reached

A mathematical model for a simple argon plasma in a non-symmetric, parallel plate, capacitive discharge was developed on the premise that the main plasma is divided into three separate zones—two sheaths near the two electrodes and the bulk plasma The solution for the sheath was considered for a high voltage, collisionless RF sheath driven by an RF current, which is not sinusoidal any more The expressions for the different sheath parameters (i e, the time-average ion and electron densities, electrical field and electric potential within the sheath, nonlinear oscillation motion of the electron sheath boundary, ion sheath thickness, the effective sheath impedance etc) were derived Assuming typical values of the three plasma characteristics (i e, the plasma density n_0, electron temperature T_e, and the electron-neutral-atom collision frequency, ν_m) some important sheath parameters (i e, (i) the nonlinear oscillation motion of the electron sheath boundary, (ii) the time-average electric field within the sheath, (iii) the ion and the time average-electron densities within the sheath, (iv) the

215

charge density within the sheath, (v) the time-average potential within the sheath, (vi) the time varying sheath voltage) were calculated and compared with those obtained from the Lieberman model The harmonic components of the RF current measured in the experiment were used in all the calculations Finally, with the inclusion of the properties of the bulk plasma, the overall plasma impedance and the overall RF voltage were estimated for the first five harmonic frequencies These were then compared with the experimental values Equations for the same quantities were also obtained for a symmetric discharge

The sheath parameters are always overestimated or underestimated by the Lieberman model compared to those obtained from the present model depending upon the location within the sheath The difference is as small as ~ ±3% for the electron sheath position, time-average ion and electron densities and the time-varying sheath voltage, whereas it is more than 10% for the charge density, the time-average electric field and the time-average sheath potential The errors in the sheath parameters obtained by the Lieberman model are larger near the ion sheath-plasma boundary

In the calculation of the overall impedance the bulk plasma impedance was included together with the two sheath impedances, whereas the bulk impedance was not included in the Lieberman model Thus, Lieberman found no even harmonic component of RF voltage and overall impedance, whereas they are always present in our improved model even in a symmetric discharge This is because the sheath resistance effect, associated with the stochastic heating in the two sheaths, and the bulk plasma impedance never vanish In this case of a symmetric discharge only the sheath capacitance effect is cancelled at the even harmonic frequencies Again, the sheath resistance and the sheath capacitance estimated by the Lieberman model are always zero at the harmonic frequencies, whereas they never become zero for the present model The Lieberman model produces a large error while estimating the higher harmonic components of the time-varying sheath voltage, though the error is insignificant in estimating the fundamental component Therefore, the Lieberman model will also produce a large error during the calculation of the higher harmonic components of the overall RF voltage, as the sheath voltage is the major part of the overall RF voltage

It is shown that the relative magnitudes of RF voltage and impedance harmonics determined by the present model follow qualitatively the values measured in the experiment as they follow the trend of the relative magnitudes of each of the harmonic components The values of the normalized RF voltage and impedance harmonics assume lower values both for calculated and measured quantities as the asymmetry of the plasma chamber decreases This is possibly because the harmonic phenomenon increases with the increase of asymmetry of the chamber

As the RF source current of any plasma processing system always contains harmonics the present model will give more accurate results in determining the plasma parameters In real industrial plasma systems, where higher power is used for operation, the magnitudes of the harmonic currents may have much higher values than the data given in the present work Therefore the contribution of current harmonics to plasma parameters will be even more significant In the present work any harmonic current above the 5th harmonic was neglected, as they could not be measured due to the limitations of the experimental equipment Any harmonic component of RF current having a considerable magnitude compared to the fundamental component must be taken into account for better results

6 2 Suggestions for Future Research

For future research with PIM and plasma modelling the following suggestions are made

(a) In a real semiconductor chip fabrication process there are many types of materials (e g , semiconductor, oxide, polysilicon, metal, photoresist etc) lying on a dissimilar material, which need to be removed by RIE at different stages of the actual fabrication Removal of these materials requires different operating conditions i e , power, pressure and gas flow rate and type of gases The best monitoring parameter to be used as an end point detector may not be the same for all of the RIE operations even if the operating conditions are similar, because the plasma chemistry will not be the same while etching different materials Further investigations could be carried out to find the best monitoring parameters to be used as end point detectors for the etch of a variety of materials and operating conditions of the plasma

217

(b) In the present work we have seen that by using the Box-Behnken modelled polynomial equation of the monitoring parameter for end point detection, the PIM can predict and detect the end point when one material lying on a dissimilar material undergoes a RIE process Again, the RIE equipment could be controlled using control circuitry and a microcomputer (using suitable software) interfaced with the equipment Thus an investigation could be carried out as to whether the complete RIE operation could be automatically controlled so that the RIE operation automatically ceased when the end point is reached A semi-automatic operation is tested in this study and is described in Appendix A

(c) A more sophisticated model could be used for modelling the end point monitoring parameter

(d) In the mathematical modelling of the plasma (Chapter 5) we used typical values for the three plasma characteristics (i e n_0, T_e, and v_m) in our all of our calculations due to the lack of a measurement facility to acquire these These values could be measured in a real experiment and used in the calculations to have better results

(e) The present model described in Chapter 5 is not totally self-consistent as we had to use the harmonic components of the RF current measured in the experiment as parameters for the calculations A self-consistent model could be developed so that calculations could be performed without using the RF current harmonics measured in the experiments

(f) The same type of modelling described in Chapter 5 could also be developed for collisional RF sheaths

REFERENCES

[1]   J Proud, R A Gottscho, J A Bondur, A Garscadden, J V Heberlein, G K Herb, M J Kushner, J E Lawler, M A Lieberman, T M Mayer, A V Phelps, W Roman, H H Sawin and H F Winters, *Plasma Processing of Materials Scientific Opportunities and Technological Challenges*, Washington DC National Academy Press, 1991

[2]   R A Gottscho, M E Barone and J M Cook, *MRS Bulletin*, vol 21, p 38, 1996

[3]   D M Manos and D L Flamm, *Plasma Etching*, New York Academic, 1989

[4]   S R Schmidt and R G Launsby, *Understanding Industrial Designed Experiments*, Colorado Air Academy Press, 1997

[5]   F Schneider, *Zschr Angew Phys* vol 6, p 456, 1954

[6]   H S Butler and G S Kino, *Phys Fluids*, vol 6, p 1346, 1963

[7]   R W Gould, *Phys Lett*, vol 11, p 236, 1964

[8]   H R Koenig and L I Maissel, *IBM J Res Dev*, vol 14, p 168, 1970

[9]   J H Keller and W B Pennebaker, *IBM J Res Dev*, vol 23, p 3, 1979

[10]   W E Mlynko and D W Hess, *J Vac Sci Technol A*, vol 3, p 499, 1985

[11]   W C Roth, R N Carlile and J F O'Hanlon, *J Vac Sci Technol A*, vol 15, p 2930, 1997

[12]   V A Godyak, *Sov Phys Tech Phys*, vol 16, p 1973, 1972

[13]   A Metze, D W Ernie and H J Oskam, *J Appl Phys*, vol 60, p 3081, 1986

[14]   C B Zarowin, *J Electrochem Soc*, vol 130, p 1144, 1983

[15]   C B Zarowin, *J Vac Sci Technol A*, vol 2, p 1537, 1984

[16]   A J van Roosmalen, W G M van den Hoek and H Kalter, *J Appl Phys*, vol 58, p 653, 1985

[17]   D L Flamm and V M Donnelly, *J Appl Phys*, vol 59, p 1052, 1986

[18]   V M Donnelly, D L Flamm and R H Bruce, *J Appl Phys* vol 58, p 2135, 1985

[19]   B E Thompson and H H Sawin, *J Electrochem Soc*, vol 133, p 1887, 1986

[20] B E Thompson, K D Allen, A D Richards and H H Sawin, *J Appl Phys*, vol 59, p 1980, 1986

[21] P Bletzinger and M J Flemming, *J Appl Phys*, vol 62, p 4688, 1987

[22] V A Godyak, *Sov J Plasma Phys*, vol 2, p 78, 1976

[23] V A Godyak and O A Popov, *Sov J Plasma Phys*, vol 5, p 227, 1979

[24] W B Pennebaker, *IBM J Res Develop*, vol 23, p 16, 1979

[25] V A Godyak and Z K Ganna, *Sov J Plasma Phys*, vol 6, p 372, 1980

[26] V Vahedi, C K Birdsall, M A Lieberman, G DiPeso and T D Rognlien, *Plasma Sources Sci Technol*, vol 2, p 273, 1993

[27] M J Grapperhaus and M J Kushner, *J Appl Phys*, vol 81, p 569, 1997

[28] P A Miller and M E Riley, *J Appl Phys*, vol 82, p 3689, 1997

[29] D Vender and R W Boswell, *J Vac Sci Technol A*, vol 10, p 1331, 1992

[30] M A Lieberman, *IEEE Trans Plasma Sci*, vol 16, p 638, 1988

[31] K E Orlov and A S Smirnov, *Plasma Sources Sci Technol*, vol 8, p 37, 1999

[32] M Chandhok and J W Grizzle, *IEEE Trans Plasma Science*, vol 26, p 181, 1998

[33] V A Godyak, R B Piejak and B M Alexandrovich, *IEEE Trans Plasma Sci*, vol 19, p 660, 1991

[34] H Kawata, T Kubo and K Murata, *Jpn J Appl Phys*, vol 33, p 4365, 1994

[35] S Bushman, T F Edgar and I Trachtenberg, *J Electrochem Soc*, vol 144, p 721, 1997

[36] A T -C Koh, N F Thornhill and V J Law, *Elec Lett*, vol 35, p 1383, 1999

[37] I Batty, M Cooke and V J Law, *Vaccum*, vol 52, p 509, 1999

[38] V J Law, A J Kenyon, N F Thornhill, V Srigengan and I Batty, *Vaccum*, vol 57, p 351, 2000

[39] L Tonks and I Langmuir, *Phys Rev*, vol 33, p 195, 1929

[40] V E Golant, A P Zhilinsky and I E Sakharov, *Fundamentals of Plasma Physics*, New York John Wiley & Sons, 1980

[41] N A Krall and A W Trivelpiece, *Principles of Plasma Physics*, New York McGraw-Hill, 1973

[42] S M Rossnagel, J J Cuomo and W D Westwood, *Handbook of Plasma processing Technology*, New Jersey Noyes Publications, 1990

[43] H O Pierson, *Handbook of Chemical Vapor Deposition (CVD)*, New Jersey Noyes Publications, 1992

[44] K Popova, E Spassova, I Zhivkov and G Danev, *Thin Solid Films*, vol 274, p 31, 1996

[45] J Park, H J Lee, J T Kong, S H Lee, "Modeling of polymer neck generation and its effects on the etch profile for oxide contact hole etching using Ar, CHF_3, and CF_4 gases," presented at the *International Conference on Simulation of Semiconductor Processes and Devices*, Sep 1997

[46] A R Remberg, *Circuits Manufacturing*, vol 19, p 25, 1979

[47] R A Heinecke, *Solid State Electron*, vol 18, p 1146, 1975

[48] J A Thornton and A Penfold, *Thin Film Processes*, ed By J L Vossen and W Kern, New York Academic, 1987

[49] I Lin, D C Hinson, W H Class and R L Sandstrom, *Appl Phys Lett*, vol 44, p 185, 1984

[50] J M Moran and D Maydan, *Bell System Tech J*, vol 58, p 1027, 1979

[51] D E Rosner and H D Allendorf, *J Chem Phys* vol 75, p 308, 1971

[52] K Suzuki, S Okudain, N Sakudo and I Kanomata, *J Appl Phys* vol 16, p 1979, 1977

[53] S Matatsuo and Y Adachi, *Jpn J Appl Phys*, vol 21, p L4, 1982

[54] S C Brown, *Introduction to Electrical Discharges in Gases*, New York John Wiley and Sons, 1966

[55] F F Chen, *Introduction to plasma physics and controlled fusion*, New York Plenum Press, 1983

[56] E W Holt and R E Haskell, *Foundations of Plasma Dynamics*, New York Macmillian, 1965

[57] R O Dendy, *Plasma Dynamics*, New York Oxford University Press, 1990

[58] T H Stix, *The Theory of Plasma Waves*, New York McGraw-Hill, 1962

[59]   S C Brown, *Basic Data of Plasma Physics*, New York John Wiley and Sons, 1959

[60]   B E Cherrington, *Gaseous Electronics and Gas Lasers*, Oxford Pergammon, 1979

[61]   M Gryzinski, *Phys Rev Lett*, vol 24, p 45, 1970

[62]   M A Lieberman and A J Lichtenberg, *Principles of Plasma Discharges and Materials Processing*, New York John Wiley & Sons Inc , 1994

[63]   B Chapman, *Glow Discharge Processes*, New York John Wiley and Sons, 1980

[64]   B G Streerman, *Solid State Electronic Devices*, 3rd ed , New Jersey Prentice Hall, Inc , 1990

[65]   C M Ferreira and J Loureiro, *J Phys D Appl Phys* , vol 17, p 1175, 1984

[66]   A Beiser, *Concept of Modern Physics*, 4th ed , New York McGraw-Hill, 1987

[67]   R A Ruth, *An experimental study of low pressure parallel plate radio frequency discharge*, Ph D Thesis, Dublin Dublin City University, 1994

[68]   T J Sommerer, W N G Hitchon and J E Lawler, *Phys Rev Lett* , vol 63, p 2361, 1989

[69]   T J Sommerer, W N G Hitchon, R E P Harvey and J E Lawler, *Phys Rev A* , vol 43, p 4452, 1991

[70]   D E Golden and H W Brandel, *Phys Rev* , vol 149, p 58, 1966

[71]   M Surendra and D B Graves, *Phys Rev Lett* , vol 66, p 1469, 1991

[72]   V A Godyak, R B Piejak and B M Alexandrovich, *Plasma Sources Sci Technol* , vol 1, p 36, 1992

[73]   V A Godyak and R B Piejak, *Phys Rev Lett* , vol 65, p 996, 1992

[74]   M M Turner and M B Hopkins, *Phys Rev Lett* , vol 69, p 3511, 1992

[75]   M M Turner, R A Doyle and M B Hopkins, *Appl Phys Lett* , vol 62, p 3247, 1993

[76]   J V Scanlan, *Langmuir Probe Measurements in 13 56MHz Discharges*, Ph D Thesis, Dublin Dublin City University, 1991

[77]   V A Godyak, R B Piejak and B M Alexandrovich, *Phys Rev Lett* , vol 68, p 40, 1992

[78] F Llewellyn-Jones, *Ionisation and Breakdown in gases*, London Methuen & Co Ltd, 1966

[79] J L Vossen and J J Cuomo, *Thin Film Processes,* ed by J L Vossen and W Kern, Orlando Academic, 1978

[80] E Naser, *Fundamentals of Gaseous Ionization and Plasma Electronics*, New York Wiley InterScience, 1971

[81] V M Donnelly, D L Flamm and G Collins, *J Vac Sci Technol*, vol 21, p 817, 1982

[82] A von Engel, *Ionized Gases*, London Oxford Univresity Press, 1965

[83] D B Graves and K F Jensen, *IEEE Trans on Plasma Sci*, vol PS-14, p 78, 1986

[84] W D Davis and T A Vanderslice, *Phys Rev*, vol 131, p 219, 1963

[85] W Kiyotaka, *Handbook of sputter deposition technology principles, technology, and applications*, New Jersey Noyes Publications, 1992

[86] A S Penfold in *Handbook of Thin Film Processes Technology*, ed by D A Glocker and S I Shah, Bristol IOP Publishing, 1995

[87] D L Flamm, *J Vac Sci Technol A*, vol 4, p 729, 1986

[88] M R Werrtheimer, *J Vac Sci Technol A*, vol 3, p 2643, 1985

[89] H Curtins, N Wyrsch and A V Shah, *Electron Lett*, vol 23, p 228, 1987

[90] D L Flamm and V M Donnelly, *Plasma Chemistry and Plasma Processing*, vol 1, p 317, 1981

[91] J D Chin, I Adeside, E D Wolf and R C Tiberio, *J Vac Sci Technol*, vol 19, p 1418, 1981

[92] K Kohler, J W Coburn, D E Horne, E Kay and J H Keller, *J Appl Phys*, vol 57, p 59, 1985

[93] C M Horwitz, *J Vac Sci Technol A*, vol 1, p 60, 1983

[94] M J Kushner, *IEEE Trans Plas Sci*, vol PS-14, p 188, 1986

[95] D Graves, *AIChE J*, vol 35, p 1, 1989

[96] E Gogolides, J P Nicolai and H H Sawin, *J Vac Sci Techol A*, vol 7, p 1001, 1989

[97] M J Kushner, *J Appl Phys*, vol 54, p 4958, 1983

[98] J P Boeuf, *Phys Rev A*, vol 36, p 2782, 1987

[99] D B Graves, K F Jensen, *IEEE Trans Plasma Sci*, vol 14, p 78, 1986

[100] X Li, T Abe and M Esashi, *Sensors and Actuators A Physical*, vol 87, p 139, 2001

[101] M Reiche, U Goesele and M Wiegand, *Crystal Research and Technology*, vol 35, p 807, 2000

[102] M C Peignon, G Turban, C Charles and R W Boswell, *Surface and Coatings Technology*, vol 97, p 465 1997

[103] N Lee K, W Lee J, C R Abernathy, S J Pearton, W S Hobson and F Ren, *Solid-State Electron*, vol 41, p 401 1997

[104] M S Feng, Y M Lu, E Y Chang and J D Guo, *Materials Chem Phys*, vol 45, p 80, 1996

[105] M Mieth and A Barker, *J Vac Sci Technol A*, vol 1, p 629, 1983

[106] M Mieth, A Barker and G Corn, *Semicond Int*, p 222, 1984

[107] W Beinvogl and B Hasler, *Solid State Technol*, vol 26, p 125, 1983

[108] R H Huddlestone and S L Leonard (eds), *Plasma Diagnostic Techniques*, New York Academic, 1965

[109] M A Heald and C B Wharton, *Plasma Diagnostics with Microwaves*, New York J Wiley, 1965

[110] H R Griem, *Plasma Spectroscopy*, New York McGraw-Hill, 1964

[111] H R Griem and R H Lovberg (eds) *Methods of Experimental Physics Plasma Physics*, part A, New York Academic, 1970

[112] C Almgren, *Semiconductor International*, vol August, p 99, 1997

[113] M N A Dewan, P J McNally and P A F Herbert, "The Use of RF Fundamental & Harmonic I-V Characteristics for Semiconductor Plasma Process Monitoring", presented at the *Fourteenth European Conference on the Atomic and Molecular Physics of Ionised Gases (ESCAMPIG'98)*, August 1998

[114] http //www scisys com/, Scientific Systems Ltd, 2000

[115] I Langmuir and H Mott-Smith, *Gen Elec Rev*, vol 27, p 449, 1924

[116] W H Bennett, *Phys Rev*, vol 45, p 890, 1934

[117] D Albares, N A Krall and C L Oxley, *Phys Fluids*, vol 4, p 1031, 1961

[118] V A Gribkov, O N Kronin, V I Mikhailov and V Ya, Nikulin, *Sov Phys - Lebedev Institute Reports*, p 20, 1984

[119] X Y Chen, Z C Wu, Z G Liu, X Y Lei and Z S Sha, *Appl Phys A*, vol 67, p 331, 1998

[120] E H Putley, *Appl Opt*, vol 4, p 649, 1965

[121] A J Lichtenberg, S Sesnic and A W Trivelpiece, *Phys Rev Lett*, vol 13, p 387, 1964

[122] G A Cottrell, *Nuclear Fusion*, v 23, p 1689, 1983

[123] V N Garbuzov, G L Iosel'son, V A Leikin, L A Nazarenko and A S Rivtsis, *High Temp*, vol 24, p 257, 1986

[124] G Bekefi, *Radiation Processes in Plasmas*, New York Wiley, 1966

[125] W Lochte-Holtgreven (ed), *Plasma Diagnostics*, Amsterdam North Holland Publishing Company, 1968

[126] G Ward, R E Pechacek and A W Trivelpiece, *Phys Rev*, vol A3, p 1721, 1971

[127] M Sternheim, W Van Gelder and A Hartman, *J Electrochem Soc Solid-State Sci Technol*, vol 130, p 655, 1983

[128] B J Curtis and H Brunner, *J Electrochem Soc*, vol 13, p 829, 1978

[129] W Harshbarger, T Miller, P Norton and R Porter, *Appl Spectrosc*, vol 31, p 201, 1977

[130] G Buyard and B Ruby, *Solid State Technol*, vol 20, p 53, 1977

[131] H Busta and R E Lajos, *IEEE 1977 International Electron Devices Meeting (IEDM)*, p 12, 1977

[132] G Fortunato, *J Phys*, vol 20, p 1051, 1987

[133] A Tretola, *Electrochem Soc Proc*, vol 81, p 295, 1981

[134] K Ukai and K Hanazawa, *J Vac Sci Technol*, vol 16, p 385, 1979

[135] V Patel, B Singh and J H Thomas III, *Appl Phys Lett*, vol 61, p 1912, 1992

[136] V Patel, M Patel, S Ayyagari, W Kosonocky, D Misra and B Singh, *Appl Phys Lett*, vol 59, p 1299, 1991

[137] H C Sun, V Patel, E A Whittaker, B Sing and J H Thomas, *J Vac Sci & Technol A*, vol 11, p 1193, 1993

[138] M A Sobolewski, *IEEE Trans Plasma Sci*, vol 23, p 1006, 1995

[139] M A Sobolewski and J K Olthoff, "Electrical Sensors for monitoring RF Plasma Sheaths," *Proc SPIE*, vol 2091, p 290, 1994

[140] P J Hargis, K E Greenberg, P A Miller, J B Gerardo, J R Torczynski, M E Riley, G A Hebner, J R Roberts, J K Olthoff, J R Whetstone, R J Vanbrunt, M A Sobolewski, H M Anderson, M P Splichal, J L Mock, P Bletzinger, A Garscadden, R A Gottscho, G Selwyn, M Dalvie, J E Heidenreich, J W Butterbaugh, M L Brake, M L Passow, J Pender, A Lujan, M E Elta, D B Graves, H H Sawin, M J Kushner, J T Verdeyen, R Horwath, T R Turner, "The Gaseous Electronics Conference Radiofrequency Reference Cell A Defined Parallel-Plate Radiofrequency System for Experimental and Theoretical-Studies of Plasma-Processing Discharges," *Rev Sci Instrum*, vol 65, p 140, 1994

[141] P A Millar, "Dependence on Excitation Symmetry of Electrical Parameters and Radial Currents in a Parallel Plate RF Discharge," *45th Annu Gaseous Electron Conf, Amer Phys Soc*, Boston, 1992

[142] *Scientific Systems Smart PIM Installation and Software Manual*, Dublin Scientific Systems Ltd, 1997

[143] K Nakamoto, *Infrared and Raman Spectra of Inorganic and Coordination Compunds*, 4th edn, New York John Wiley & Sons, 1986

[144] M A M Palazon, *Carbon nitride deposition by magnetron sputtering structural, mechanical, electrical and optical properties*, Ph D Thesis, Dublin Dublin City University, 2000

[145] Bomem, *FT-IR User's Guide, Michelson series*, 1989

[146] K O'Dwyer, *Development of infrared evanescent wave fibre sensors using an FTIR spectrum*, M Sc Thesis, Dublin Dublin City University, 1993

[147] E O Brighan, *The Fast Fourier Transform*, New Jersey Prentice-Hall, 1974

[148] F L Pedrotti and L S Pedrotti, *Introduction to Optics*, New Jersey Prentice-Hall Inc, 1987

[149] J W Cooley, P A W Lewis and P D Welch, "The fast Fourier transform and its applications," presented at *IEEE international convention*, 1968

[150] K Mishikida, *Infrared Software Note #25*, Norwalk, CT Perkin-Elmer Corporation, 1988

[151] G R Wilkinson, *Laboratory Methods in Infrared Spectroscopy*, ed by R G S Miller and B C Stace, London Heyden & Sons, Ltd, 1972

[152] R A Nuquist and R O Kagel, *Handbook of Infrared and Raman Spectra of Inorganic Compounds and Organic Salts, (a 4-Volume set)*, NewYork Academic Press Inc , 1997

[153] G Lucovsky, M J Manitini, J K Srivastava and E A Irene, *J Vac Sci Technol B,* vol 5, p 530, 1987

[154] I W Boyd and J I B Wilson, *J Appl Phys* , vol 53, p 4166, 1982

[155] J E Dial, R E Gong and J N Fordemwalt, *J Electrochem soc* , vol 115, p 327, 1968

[156] J Wong, *J Appl Phys* , vol 44, p 5629, 1973

[157] E Gogolides, *Jpn J Appl Phys* , vol 36, p 2435, 1997

[158] G E P Box and D W Behnken, *Technometrics,* vol 2, p 455, 1960

[159] *The Quality Edge*, User's Guide, Colorado Springs Mike Bishop and Schmidt/Launsby Consulting, 1991

[160] K –U Riemann, *J Phys D Appl Phys* , vol 24, p 493, 1991

[161] M N A Dewan, Patrick J McNally and P A F Herbert, "Modelling of Harmonic Contributions to Non-Symmetrical RF Plasmas", presented at *International Conference on Advances in Materials and Processing Technology, AMPT'99*, August 1999

[162] E Fermi, *Phys Rev* , vol 75, p 1169, 1949

[163] A I Akiezer and Z K Bakai, *Sov Phys Dokl* , vol 16, p 1065, 1971

[164] A J Lichtenberg and M A Lieberman, *Regular and Stochastic Motion*, New York Springer-Verlag, 1983

AUTOMATIC OPERATION OF REACTIVE ION ETCHING: A SMALL AND SIMPLE PROPOSAL

A 1 Introduction

The growth in the use of RIE processes has led to the need for real-time, *in situ* techniques to detect endpoints These techniques are needed to increase tool use and process uniformity instead of depending on off-line wafer inspections In semiconductor industries accurate endpoint detection offers a greater opportunity for the control of the plasma process, reduces the wastage of materials used for IC fabrication and increases the total throughput In the previous chapters we saw that the PIM can accurately detect the endpoint when a SiO_2 layer lying on a Si base undergoes SF_6 reactive ion etching Here the fundamental component of phase proved to be the best monitoring parameter for the endpoint detection It is well understood that when any material lying on a dissimilar material undergoes an RIE process, and the endpoint occurs, the plasma constituents always change from one state to another even though the operating conditions (RF power, chamber pressure, type of gas, gas flow rate etc) remain identical This change can radically alter the value of any of the I-V parameter harmonics which can be easily detected by the PIM using some appropriate modelling (e g , *Box-Behnken*) Again, most of the RIE equipment used in the semiconductor industry is partially or completely computer controlled By combining the software used for the RIE equipment and for the PIM it should be possible to operate the RIE equipment where the computer will automatically detect the endpoint and turn the system off so that the etching process will no longer continue

The RIE equipment in our laboratory is totally manually controlled But there are some interface cables connected to various components of this equipment which could be used for computer control This is a brief discussion chapter Here we tested the automatic turning on and off of the RIE operation using a computer and some auxiliary

circuitry. Then we demonstrate a simple method for automatic control of this equipment when any material lying on a dissimilar material undergoes an RIE process.

A.2 Automatic Operation of the RIE Equipment

The RIE equipment in our laboratory is a PLASMALAB^{TM}, model PE80 [A1] provided by Plasma Technology (UK) Ltd. Figure A.1 shows the main RIE equipment including all other accessories (see section 3.2 for details) whereas figure A.2 and A.3 show the front panel and the back panel of the main equipment.

Figure A.1 Capacitively driven, parallel plate, RIE system with the Plasma Impedance Monitoring monitor.

If we look at the front panel of the equipment we will see that there are three power selectors for the three process channels at the top of the panel. Only one of the three channels becomes active during the actual operation. The power selector button allows selection of the RF power level to be used for the operation. This is actually a potentiometer which regulates a variable dc voltage used as an input to the control circuitry of the RF power supply unit. The RF power supplied by the power supply unit is directly proportional to this dc voltage input which is regulated by the power selector. All of the electronic communications between the main plasma equipment and the RF power supply unit is performed by an interface cable shown in figure A.3.
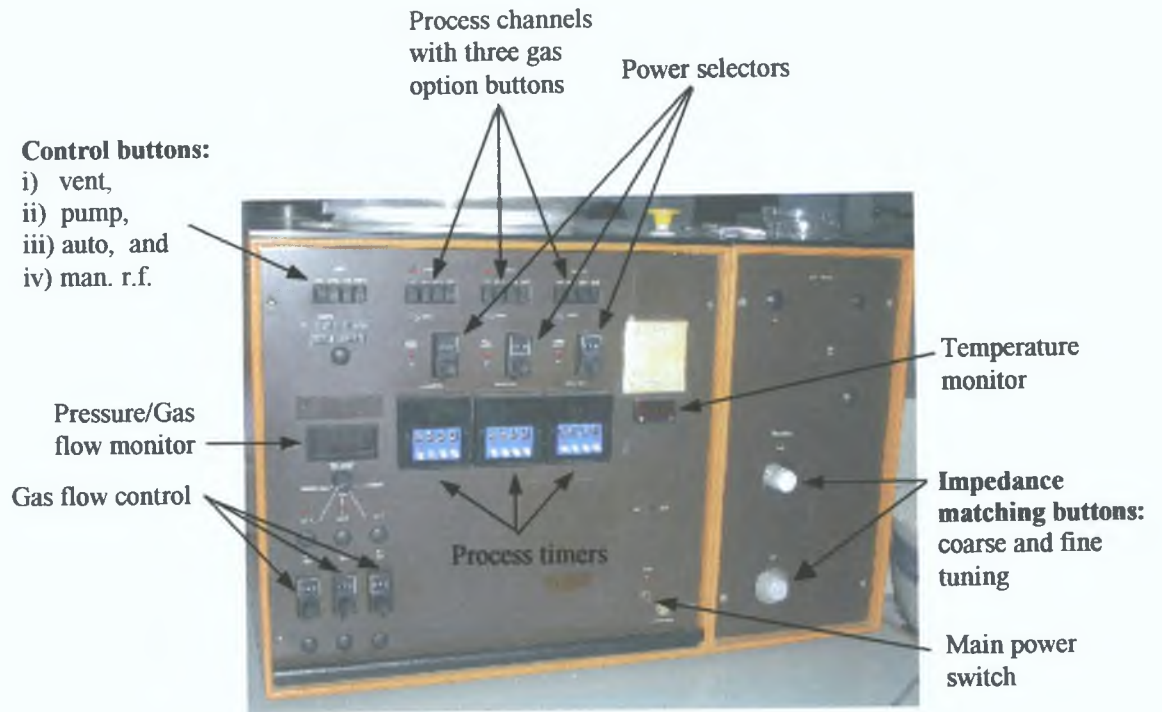
Figure A.2 Front panel of the main RIE equipment.

Figure A.3 Back panel of the main RIE equipment.

The internal configuration of the interface cable (for normal operation) is shown in figure A 4 The cable is connected by a 25 pin female socket named **SKT18** to a 25 pin male port on the RIE equipment, whereas it is connected by a 15 pm male socket named **PL41** to a 15 pm female port on the RF power supply unit The pin configuration of the two ports are shown in figure A 5 As shown in figure A 4 the dc voltage (0-10 Volt) selected by the power selector in the RIE equipment becomes available at pin number 9 of **SKT18** which is directly connected to pin number 5 of **PL41** This voltage controls the control circuitry of the RF power supply unit which activates a corresponding amount of RF power via a co-axial cable connected at **PL42** and **SKT42**, respectively (see figure A 4), to the RIE chamber The RF power supplied by the unit is directly proportional to the voltage applied at pin number 5 of socket **PL41** That means that it is also possible to control the RF power supply by externally applying a voltage (0-10 Volt) at pin number 5 of **PL41** Now, during an RIE operation if the connection between pin 5 of **PL41** and pin 9 of **SKT18** is somehow broken the etching process will cease as the voltage at pin 5 of **PL41** becomes zero Keeping this fact in mind we reconfigured the connection between the above mentioned pins as in figure A 6 Here the connection between the aforementioned two pins is established via a switching transistor which is operated directly by a signal coming from the computer For practical operation of the switching transistor we needed to use some auxiliary circuit between the computer and the base of the transistor shown in figure A 6 When the signal from the computer is 'low' (0 Volt dc) the relay coil remains inactivated and the relay switch S maintains the normal position at '1' At this moment the base of the transistor becomes connected to the 5 volt dc supply via a 95 KΩ base resistor and the transistor becomes ON allowing an electronic connection between pm 5 of **PL41** and pin 9 of **SKT18** When the signal from the computer is 'high' (5 Volt dc) the relay coil becomes activated changing the position of the switch S to '2' The position '2' is grounded and applying a zero voltage to the base turns the transistor OFF Upon this situation pin 5 of **PL41** and pin 9 of **SKT18** are electronically disconnected Thus it becomes clear that by sending an appropriate signal to the control circuitry the connection between pin 5 of **PL41** and pin 9 of **SKT18** can be easily controlled by the computer
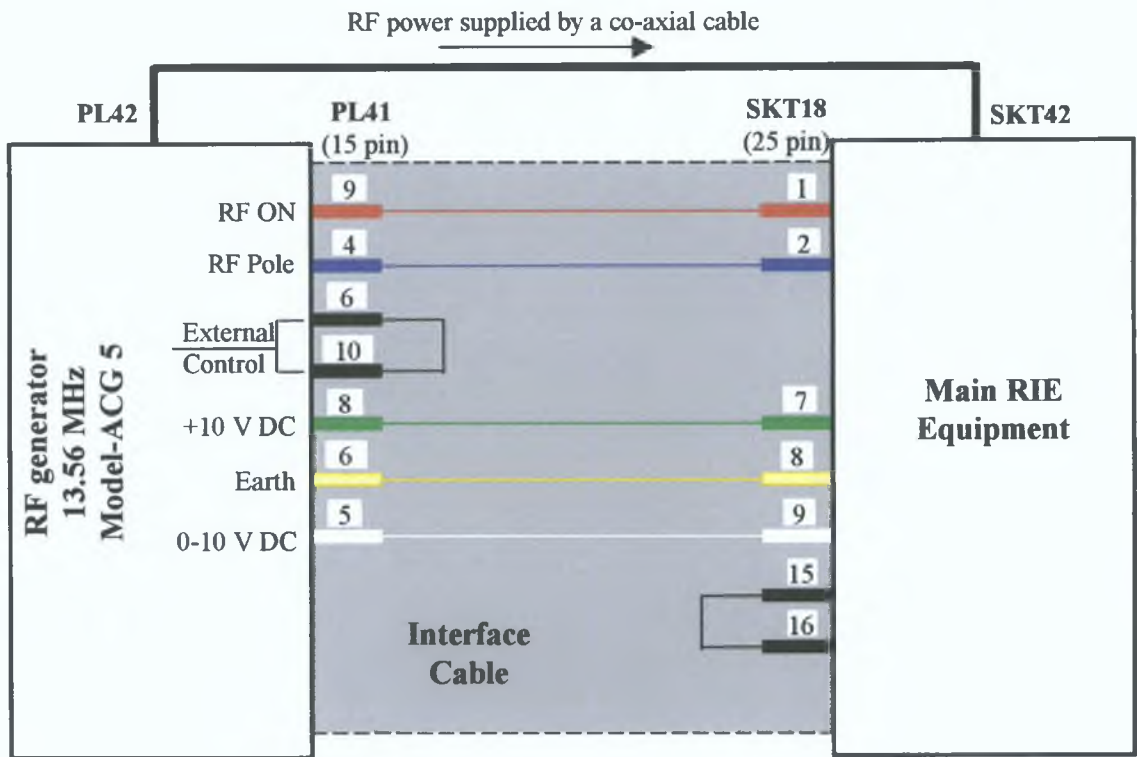
Figure A.4 *Internal configuration of interface cable between the main RIE equipment and the RF power supply unit.*
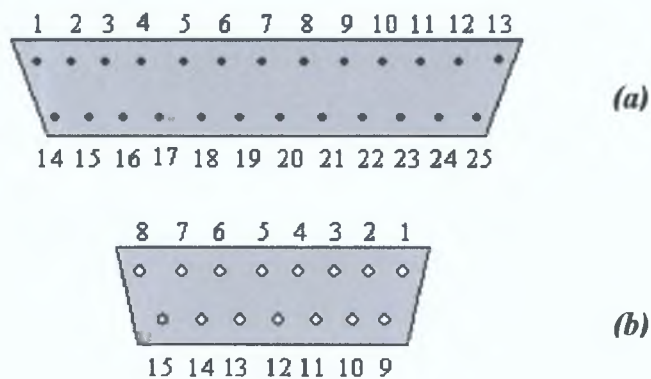
Figure A.5 *Pin configurations of the two interface ports:* **(a)** *male port of the RIE equipment and* **(b)** *female port of the RF power supply unit.*
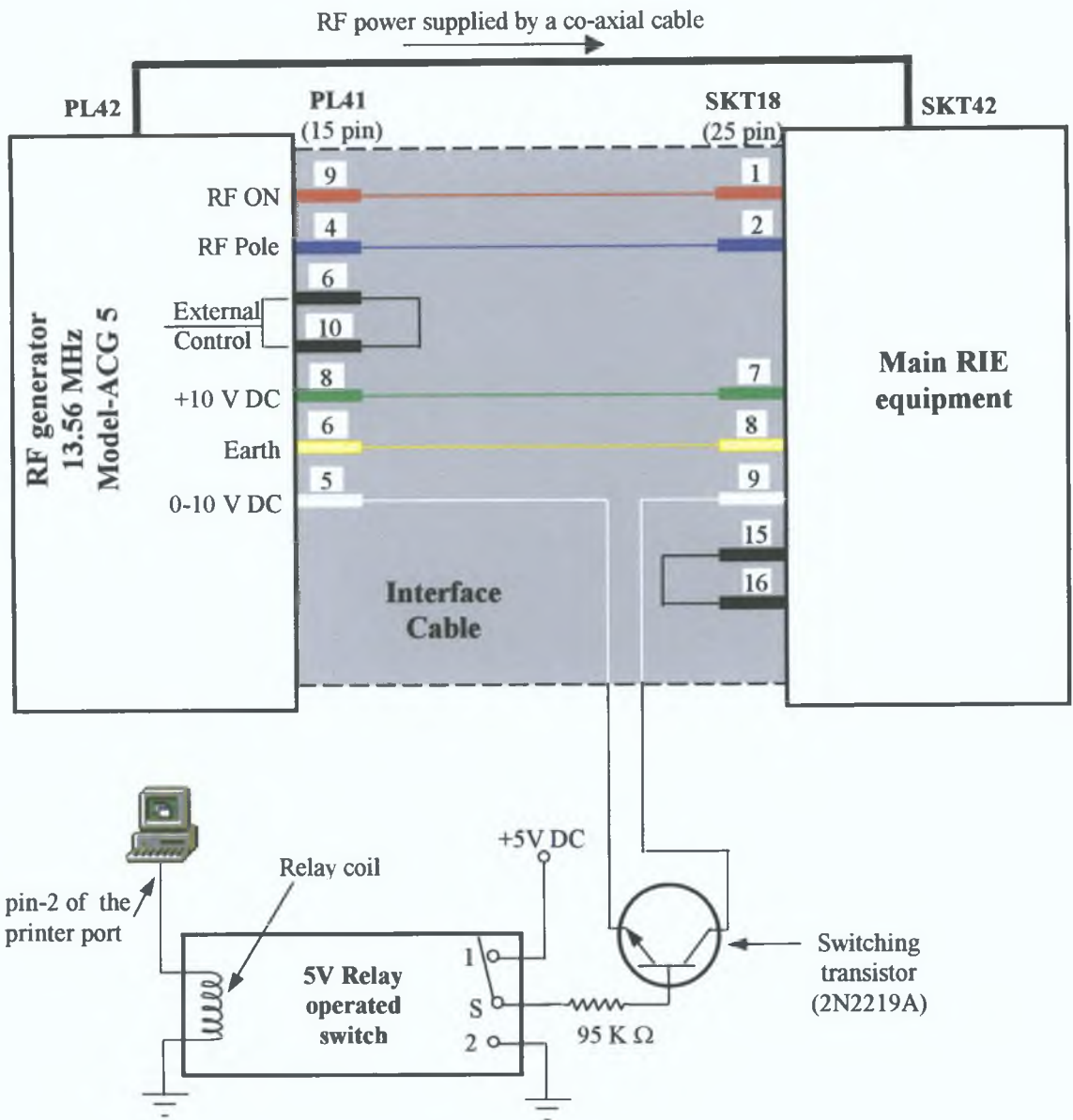
Figure A.6 *Computer controlled RIE operation using an auxiliary circuit.*

During normal RIE operation the computer must maintain the connection between pin 5 of **PL41** and the pin 9 of **SKT18** sending a 'low' signal at the relay input terminal until the end point is reached. As soon as the computer detects the end point the computer will send a 'high' signal to the relay input which will break the connection between the two pins. As a result the RF power supply will go to zero Volts and further etching will be stopped. That means it is possible to detect the RIE endpoint and turn the process off automatically by the computer. Together with the switching circuit shown in figure A.6 it is also possible to set an alarm circuit shown in figure A.7 which

is operated by another computer signal The alarm will facilitate any further action which can be taken immediately after the RIE end point is reached and the RF power supply is stopped by the computer
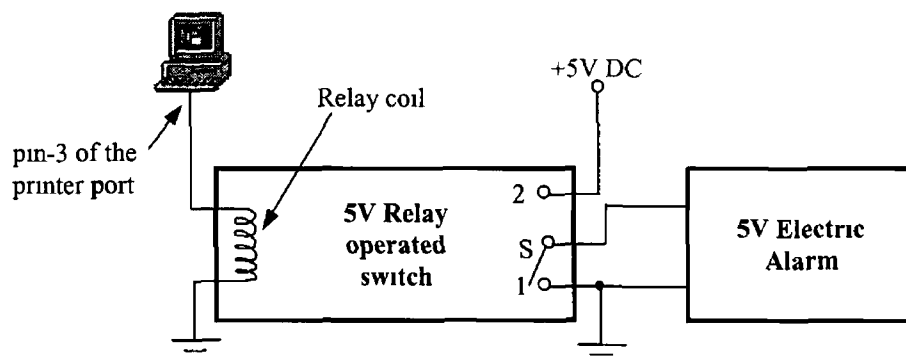
Figure A 7 The alarm circuit for the computer controlled RIE operation

A 3 Software for the Proposed Automatic RIE Operation

For automatic control of the RIE operation the computer needs software to perform three specific operation

i) to predict the end point by predicting the value of monitoring parameter used for end point detection,

ii) to detect the end point by comparing the measured value of the monitoring parameter with the predicted value, and

iii) to turn the RIE operation off by sending the appropriate signal to the control circuitry discussed in section A 2

Using the Plasma Impedance Monitor and its own software, PIMSoft™, the computer can easily measure the monitoring parameter during RIE operation This software can be modified so that it allows one to predict the value of the monitoring parameter used for the end point detection by using the modelled equation and the values of input factors (i e , RF power, chamber pressure, gas flow rate etc) Thus, the computer will be able to detect the end point comparing the predicted value of the monitoring parameter

A7

with the measured value As soon as the computer detects the end point it needs to send an appropriate signal to the control circuitry For this purpose the software needs some special commands which will send the 'low' or 'high' signal to any of the computer ports (i e , parallel or serial port) which is directly connected to the relay input of the control circuitry Since, the state of the computer output signal ('high' or 'low') depends on whether the end point is reached or not the original software should contain some logical operational block which will continuously check whether the end point is reached or not and decide whether the output signal would be 'low' or 'high'

A 3 1 Parallel port and the corresponding command

The command to send a 'low' or 'high' signal to the port varies depending upon which programming language (e g , C++, Pascal, BASIC etc) is used to create the software and which output port of the computer is used to send the signal In our laboratory we used the C++ programming to create only a simple block of the program which allowed us to send 'low' or 'high' signal to the output pins of the printer port (LPT1) of the computer This was an independent program which was used to test the operation of the control circuitry described in section A 2

The LPT1 printer port of the computer is a female port consisting of 25 pins as shown in figure A 8
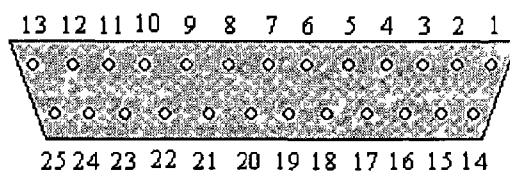
Figure A 8 Pin configuration of the LPT1 printer port of a computer

Pin-2 (bit-0) to pin-9 (bit-7) are the output pins and pin 25 is the ground The address of this output pins in C++ code is 0x378 The C++ code to pass the binary equivalent of 3 to the output pins is Outportb(0x378, 3) This means that the corresponding binary number of decimal 3 (i e , 00000011) will be sent to pin-2 to 9 as a byte Pins 2 and 3 of the computer printer port were connected to the relay inputs of the control circuitry and the alarm circuit, respectively, whereas pin 25 was connected

to the common ground of the circuit shown in figures A 6 and A 7 The C++ codes used in our experiment are given below

```
#include <conio h>
#include <stdio h>
#include <dos h>
#include <fstream h>
void main() {
outportb(0x378, 0),
cout<<"'0' has been sent to pins 2 and 3 of the parallel port
Press any key when you are ready to sent '1' to both pins "<<endl,
getch(),
outportb(0x378, 3),
cout<<"'1' has been sent to pins 2 and 3 of the parallel port
Press any key to quit this program "<<endl,
getch(),  }
```

Before applying any RF power to the RIE chamber we run the above C++ program At the start of the program it confirms 'low' signals at both pins (pin 2 and 3) and sends a message to the computer screen as,

```
'0' has been sent to pins 2 and 3 of the parallel port  Press any key
when you are ready to sent '1' to both pins
```

After that we applied the RF power to the RIE chamber which started the etching operation Now to test the operation of the control circuitry we pressed any of the keyboard buttons Instantly, the computer sent 'high' signals to both pins which activated the controlled circuitry and stopped the RF power supply It also activated the alarm shown in figure A 7 At the same time the program gives a message on the computer screen as,

```
'1' has been sent to pins 2 and 3 of the parallel port  Press any key
to quit this program
```

To quit this program any of the keyboard buttons was pressed Before quitting this program it was made sure that the RIE system was manually turned off Otherwise, the

RF power could again be turned on as the control circuitry would be inactivated while the program was terminated

A 4 Conclusion

It becomes clear from the above discussions that by adding two additional program blocks in the original software, PIMSoft^{TM}, the three operations i e ,

i)   prediction of the end point by predicting the value of the monitoring parameter,

ii)   detection of the end point by comparing the measured value of the momtoring parameter with the predicted value, and

iii)   turning the RF power supply off by sending an appropriate signal to the control circuitry,

when the end point is reached, could be performed using the same software and the plasma impedance monitor It is thus possible to automatically control the RIE operation by a computer and the plasma impedance monitor when any material lying on a dissimilar material needs to be completely etched away

Reference

[A1] *PLASMALAB^{TM} Installation & Operating Manual*, vol 1, Bristol, UK Plasma Technology (UK) Ltd

PUBLICATIONS FROM THIS RESEARCH

1   M N A Dewan, P J McNally and P A F Herbert, "The use of RF fundamental and harmonic I-V characteristics for semiconductor plasma process monitoring", Proc XIVth Europhysics Conference on Atomic & Molecular Physics of Ionized Gases (ESCAMPIG XIV), Vol 22H, pp 378-379, Malahide, Ireland, 26-29 August, 1998

2   M N A Dewan, P J McNally and P A F Herbert, "Modelling of harmonic contributions to non-symmetrical rf plasmas", Proc Int Conf On Advances in Materials & Processing Technologies (AMPT '99), Vol II, pp 939-949, Dublin, Ireland, 3-6 August, 1999

3   M N A Dewan, P J McNally and P A F Herbert, "Modelling of harmonic contributions to non-symmetrical rf plasmas", J Mater Proc Technol, accepted for publication, 2001

4   M N A Dewan, P J McNally and P A F Herbert, "Plasma modelling for a non-symmetric capacitive discharge driven by a non-sinusoidal rf current", submitted to J Appl Phys, 2001

5   M N A Dewan, P J McNally, T Perova and P A F Herbert, "Determination of SF_6 reactive ion etching end point of the SiO_2/Si system by plasma impedance monitoring", submitted to Plasma Sources Sci & Technol, 2001

6   M N A Dewan, P J McNally, T Perova and P A F Herbert, "Use of plasma impedance monitoring for the determination of SF_6 reactive ion etching process end points in a SiO_2/Si system, submitted to Mater Res Innov, 2001